Spectroelectrochemical graphene-silver/zinc oxide nanoparticulate phenotype biosensors for ethambutol and pyrazinamide

Thesis by

Siphokazi Tshoko

A thesis submitted in fulfilment of the requirements for the degree of

Magister Scientiae in Chemical Sciences

Faculty of Science, University of the Western Cape

Supervisor: Dr R.F. Ajayi

Co-supervisor (s): Prof E.I. Iwuoha, Dr T. Mulaudzi-Masuku

January 2019

ABSTRACT

Tuberculosis (TB), a deadly disease second to HIV/AIDS, is a global health problem. Diagnosis of active tuberculosis is tedious and requires expensive procedures since there is no recognizable method for sole detection of active TB. Although this is a deadly disease, treatment drug toxicity is also an issue that also causes fatalities in diagnosed patients. Therefore, a rapid sensitive and specific diagnostic method is imperative for TB drug management. In this study spectroscopic and/or electrochemical biosensors were developed for the detection and quantification of TB treatment drugs. The biosensors were constructed with electroactive layers of graphene oxide coupled to silver nanoparticles and/or zinc oxide nanoparticles. These nanoparticles coupled with graphene oxide sheets were covalently attached onto the enzymes such as Cytochrome P450-2D6 to achieve the electrochemical detection of the TB treatment drugs and obtain the required electron transfer between the electrode surface and enzyme. The surface morphology of graphene oxide, nanoparticles as well as the green synthesized nanocomposites were achieved using High-Resolution Transmission Electron Microscopy (HRTEM), Atomic Force Microscopy (AFM), and High-Resolution Scanning Electron Microscopy (HRSEM) while the elemental analysis were obtained using Fourier Transform Infrared Spectroscopy (FTIR), Energy Dispersive X-Ray (EDX), Raman spectroscopy and X-Ray diffraction (XRD). Additionally, the optical properties of the developed nanocomposites where further characterised using Small Angle X-ray Scattering (SAXS), Photoluminescence Spectroscopy (PL) and Ultraviolet Spectroscopy (UV-vis). The electrochemical studies were obtained using cyclic voltammetry (CV) and showed an increase in electron conductivity for the green synthesized zinc oxide nanoparticles coupled with graphene oxide (ZnONPs/GO) and silver nanoparticles coupled with graphene oxide (AgNPs/GO) nanocomposite which was an indication that they were

suitable as platforms towards biosensor development. Furthermore, amperometric technique was also used for biotransformation of the TB treatment drugs (Ethambutol and Pyrazinamide) in standard solutions of 0.1 M phosphate buffer (pH 7.0). Furthermore, the sensitivity value of 0.0748 μA/μM was determined for the ethambutol biosensor while a value of 0.1715 μA/μM was determined for the pyrazinamide biosensors. Very good detection limits were obtained for the standard solutions of ethambutol and pyrazinamide where a value of 0.02057 nM was determined for ethambutol at concentration linear range of 50 μM – 400 μM. Additionally, a value of 0.8975 x 10^{-2} nM was determined for pyrazinamide at the concentration linear range of 100 μM – 300 μM. The determined limit of detections have provided a clear indication that these biosensors have potential of being used in human samples since these values are below the peak serum concentrations of these drugs in TB diagnosed patients as reported in literature. This was further confirmed by the limit of quantification values determined for each biosensor where a value of 0.8975 x 10^{-2} nM was determined for pyrazinamide and a value of 0.02057 nM was determined for ethambutol.

KEY WORDS

Ethambutol

Pyrazinamide

Tuberculosis

Green extract

Biosensor

Graphene oxide

Silver nanoparticles

Cytochrome P450 2D6

Zinc oxide nanoparticles

DECLARATION

I declare that ***''Spectroelectrochemical graphene-silver/zinc oxide nanoparticulate phenotype biosensors for ethambutol and pyrazinamide''*** is my own work, that it has not been submitted before for any degree or examination in any other university, and that all the sources I have used or quoted have been indicated or acknowledged as complete references.

Siphokazi Tshoko **Signed:** 

ACKNOWLEDGEMENTS

First and foremost I would like to thank **God** for the wisdom and strength he has given me along this journey. It was not an easy journey but it was worthwhile.

I wish to extend my gratitude to my supervisor **Dr Rachel Fanelwa Ajayi** for endless support, guidance, advice, encouragement and for believing in me when I did not believe in myself.

I will also like to thank my co-supervisors Prof. **Emmanuel Iwuoha** and **Dr Takalani** for their guidance and support.

I wish to thank the staff of the **Chemistry Department** of the University of the Western Cape for their technical and academic assistance.

I would also like to express my sincerest gratefulness to **SensorLab** colleagues especially **Dr Masikini** for their insights and guidance they shared with me.

A special thanks to Council for Scientific and Industrial Research (CSIR) and National Research Foundation (NRF) for financial support.

A gigantic thank you to **Campus France** for giving me an opportunity of a lifetime of funding my research at the University of Cergy Pontoise which lasted for four months.

To my mother **Nomsa Tshoko**, if it was not for your love, guidance and sacrifices I would not be where I am today. Thank you for giving me an opportunity to educate myself and believing in me for that I will forever be grateful. To my precious daughter **Ligugu Tshoko,** thank you for bringing light and joy in my life. To **Zolani Mandlakazi** and **Khanya Mooi** thank you for all your love, support and advices you have given me along the journey.

TABLE OF CONTENTS

List of Abbreviations

Ag - Silver

ZnO - Zinc oxide

TB - Tuberculosis

EMB - Ethambutol

NPs - Nanoparticles

GO - Graphene oxide

GrO - Graphite oxide

PZA – Pyrazanamide

CE - Counter electrode

WE -Working electrode

RE - Reference electrode

XRD - X-Ray diffraction

CV - Cyclic voltammetry

CH - Conventional heating

MI - Microwave irradiation

PBS - Phosphate buffer solution

WHO -World Health Organization

CYP2D6 - Cytochrome P450-2D6

AFM - Atomic Force Microscopy

PL - Photoluminescence Spectroscopy

SAXS - Small-Angle X-ray Scattering

UV-vis - Ultraviolet Visible Spectroscopy

FTIR - Fourier Transform Infra-Red Spectroscopy

DOTS - Directly Observed Treatment Short Course

HRTEM - High-Resolution Scanning Electron Microscopy

HRSEM - High-Resolution Transmission Electron Microscopy

List of Tables

List of Figures

Figure 4.10: (a) Graphite oxide AFM topography image with 3-D representation and cross sectional analysis (b) Graphene oxide topography image with 3-D representation of the selected area and cross sectional analysis of the selected individual.

Figure 4.11: CV of bare Glassy carbon electrode (GCE) (black curve), Graphite oxide (red curve) and graphene oxide (blue curve) in phosphate buffer solution (pH 7.4) at 30 mV s^{-1}.

Figure 4.12: CV of (a) graphite oxide and (b) graphene oxide in 0.1 M phosphate buffer solution (pH 7.4) at 10-100 mV s^{-1}.

Figure 4.13: Plots of log current versus log scan rate of (a) graphite oxide and (b) graphene oxide.

Figure 4.14: Fourier transform infrared spectrum (FTIR) of conventional green synthesized silver nanoparticles (Black line) microwave green synthesized silver nanoparticles (Red line) and Tomato and apple extract (Blue line).

Figure 4.15: Ultraviolet-visible spectrum of (a) microwave green synthesized silver nanoparticles and (b) conventional green synthesized silver nanoparticles.

Figure 4.16: HRTEM images of (a) microwave green synthesized silver nanoparticles and (b) conventional green synthesized silver nanoparticles.

Figure 4.17: Particle size distribution of (a) microwave green synthesized silver nanoparticles and (b) conventional green synthesized silver nanoparticles.

Figure 4.18: (a) Conventional green synthesized silver nanoparticles (AgNPs) and (b) microwave green synthesized silver nanoparticles (AgNPs) at 2.1 nm scale view. Insert SAED pattern.

Figure 6.10: Calibration curve of pyrazinamide for the AgNPs/GO/CYT2D6/GCE biosensor

CHAPTER 1

Introduction

Summary

This chapter gives a brief idea on the background on Tuberculosis and its treatment regime as well as a detailed description of the drugs used during treatment. In addition, this chapter focuses briefly on other aspects involved in this project namely; Graphene oxide, silver nanoparticles, zinc oxide, biosensors and the enzymes responsible for the metabolism of tuberculosis treatment drugs. Also, included herein is the relationship between the above mentioned aspects and their contribution towards the success of this study. Finally, this chapter also includes the project's rationale and motivation, the aim and specific objectives of the study and the thesis outline.

1.1 Background

Tuberculosis (TB) is an ancient infectious disease known to mankind and notorious worldwide. **(Srivastava *et al*., 2016)** This disease is known to be chronic disease and caused by the bacillus *Mycobacterium tuberculosis* (Mtb) which spreads from one human being to another through air. TB usually affects most parts of the human body mainly the lungs and other parts such as the liver, spine, kidneys, brains or intestines. TB symptoms mostly depend on a specific body part where TB bacteria are growing. For instance, in pulmonary TB it causes symptoms such as weight loss, flu, night sweats, weakness or fatigue, haemoptysis, pain in the chest and chronic cough. **(Zaman., 2010)** Tuberculosis still remains one of the most significant social and economic global diseases with high mortality and infection rates. It has been reported by the World Health Organization (WHO) in 2015 that there are 1.5 million patients' deaths annually and 10.4 million people infected with TB. **(WHO., 2015)** Hence, early diagnosis and the immediate start of treatment are significant for effective TB control programs. **(El Dim *et al*., 2015)**

At the present moment, the WHO recommends the Directly Observed Therapy Short-course (DOTS) approach for treating entirely drug-susceptible TB. The DOTS program is a 6-months therapeutic regimen, starting with an intensive treatment phase for 2-months using a combination of the first line drugs namely; pyrazinamide (PZA), isoniazid (INH), ethambutol (EMB) and rifampicin (RIF), followed by a maintenance phase for 4-months using only RIF and INH. When the bacterial strain becomes resistant to one or more of these drugs, second-line drugs are used. These include streptomycin, kanamycin, fluoroquinolones, ethionamide, and p-aminosalicylic acid. Generally, second-line drugs are less effective and more toxic compared to the first-line drugs. **(Sarkar *et al*., 2016)**

Furthermore, in TB treatment each drug dose is consumed under direct observation and supervision of medical trained professionals. This effort is made to improve therapeutic adherence because when the DOTS program is completely adhered to, the turnout is a high cure rate in patients with drug-susceptible TB; though there are still some TB cases reported annually that are treated unsuccessfully. **(Luies *et al*., 2017)** Nevertheless, TB treatment is termed quite different from other disease treatment plans due to the unique characteristics of Mtb. **(Sarkar *et al*., 2016)**. It is unique because of the presence of mycolic acid and the high lipid content of the cell wall. **(Meena *et al*., 2011)**

Accordingly**,** after Mtb inhalation, alveolar macrophages mainly capture all these bacteria which evade the host immune system and continue to be dominant for quite some time where at some point they are reactivated to a virulent form under immunocompromised conditions of the host. This can likely occur because Mtb can persist in both fast and slow growing bacteria stages which makes treatment challenging. Nearly all the drugs that are possibly used to treat TB work thoroughly when bacteria are dividing. In the first phase of TB treatment (the intensive phase), the drugs kills mainly the fast growing bacteria which causes the eradication of clinical symptoms and rapid sputum conversion. However, in order to kill the slow and some persistent growing strains of Mtb, a second phase of TB treatment is essential (the continuation phase). **(Jnawali., 2013)** The majority of the infectious bacilli are killed during the intensive stage thus reducing clinical symptoms. **(Carnetti., 1962)** Some first line drugs like Ethambutol (EMB) are highly effective for the first intensive phase **(Sarkar *et al*., 2016)** and plays an important role in the chemotherapy of drug-resistant TB and it is a bacteriostatic agent that is active for growing bacilli and has no effect on non-replicating bacilli. Additionally, Pyrazinamide (PZA) is a strong sterilizing agent and has the ability to inhibit semi dormant bacilli residing in acidic environments. **(Jnawali., 2013)**

Fundamentally, the main aim of TB treatment is to prevent death, cease transmission, cure patients, and prevent drug resistant persistently positive sputum smears despite treatment. TB treatment failure is attributed to a variety of factors which include; the lack of TB-education among patients; poor life quality and poverty resulting more in transport problems to the sites of treatment administration; biochemical associated factors contributing to poor treatment results, such as: non-adherence to the treatment program, mainly due to the related side effects, adjustable individual metabolism of the anti-TB drugs (which includes drug absorption, drug-drug interactions and variation in xenobiotic metabolism) and finally, pathogenicity and drug resistance by the infectious organism. **(De Villiers *et al*. 2013)**

According to WHO reports, there are 10.4 million new TB cases reported annually of which 15 % are multidrug-resistant TB (MDR-TB) cases. The case of multidrug-resistant TB (MDR-TB) is estimated to be almost four times higher than usual an indication of the drastic growth in unsuccessful treatment. **(Krasniqi *et al*., 2017)** This unexpected rise in numbers of drug-resistant infectious strains of *Mycobacterium tuberculosis* is due to poor patient adherence in community and hospital settings and inappropriate use of antibiotics. **(Mani *et al*., 2014)** Multidrug resistant TB (MDR-TB) is harder to treat because second-line drugs are less effective, more toxic and more expensive than first-line drugs and require prolonged treatment courses **(Leibert *et al*. 2010)** added to the fact that they cause severe side effects.

Therefore, the focus of this study was to improve the detection and the quantification of clinically first-line TB treatment drugs (mainly ethambutol and Pyrazinamide). The goal was to develop a device to study the metabolic profiles of these drugs geared at a better understanding of the role of drugs taken by TB diagnosed patients who as we know have different metabolic profiles and drug metabolic rates. For those who are slow metabolizers, the effects are worse because they are more prone to hepatotoxicity and experience severe

side effects. This study was focused on fabricating electrochemical biosensors using nanocomposites of green method synthesized silver or zinc oxide modified graphene sheets in the absence and presence of the enzymes cytochrome P450-2D6 (CYP2D6).

Thus far, nanoscience has provided a vital platform to develop and explore minuscule, high specific and high sensitive sensors for more effective treatment regimens. Biosensor devices used in previous studies have shown to have the ability to provide rapid, specific and cost effective reliable qualitative and quantitative analysis. **(Tothill., 2011)** The electrochemical biosensors used in this study generally consist of two parts; one part for information acquisition and another part where the requisite chemical or physical processes are performed. **(Muchindu *et al*., 2010**)

According to the International Union of Pure and Applied Chemistry (IUPAC), "biosensors are devices that use specific biochemical reactions mediated by isolated enzymes, immunosystems, tissues, organelles or whole cells to detect chemical compounds usually by optical, thermal or electrical signals". Additionally, biosensors are also endorsed for label free measurements of certain analytes, real time and preferably reversible. **(Srivastava., 2014)** The developed biosensors were constructed with electroactive layers of graphene oxide (GO) coupled to silver nanoparticles or zinc oxide nanoparticles. GO was used due to its large surface area and unique ability to disperse in aqueous medium. GO is known to be involved in the detection of different analytes. **(Nurunnabi *et al*., 2015)**

As for the nanoparticles, two types of syntheses were explored in this study namely; microwave-assisted green synthesis and one-pot green synthesis. The electrochemical and structural properties of these nanoparticles were compared to one another before the fabrication of the biosensor of interest. The choice to carry out green synthesis for

nanoparticles explored in this study was based on the fact they are eco-friendly and they have a simple reaction pathway using plant extracts among other organic materials. This synthesis route allows for particle reduction, control and capping with well-defined shaped and sized nanoparticles on completion. **(Patil *et al*., 2016)** While for microwave-assisted green synthesis, products are prepared within a short period of time with same desired effects upon completion. **(Kahrilas *et al*., 2013)**

In this study two noble metal nanoparticles (silver and zinc oxide nanoparticles) were extensively studied due to their wide applications in sensors, detectors and antibacterial agents. Silver has been described as therapeutic agent for many diseases, antifungal agent and an efficacious antibacterial **(Isaac *et al*., 2013)** while zinc oxide is well known as an easily available Lewis acid catalyst that gained much interest in sensors, surface acoustic-wave devices, various organic transformations and transparent conductors. **(Patil *et al*., 2016)**

However, the use of nanoparticles as a single electrode modifier in electrochemical biosensors has not been well established since they behave as n-type semiconductors whereby; the dopant atoms are capable of providing extra conduction electrons to the host material. This creates an excess of negative (n-type) electron charge carriers that causes difficulties in direct electron transfer, reduced operation speed and fast recombination of the generated Electron Hole pairs. So instead of implementing and the use of artificial electron shuttles to liberate the captured-(stored)-electrons which are highly recommended in some studies; for this study graphene oxide was merged to these nanoparticles to form nanocomposites such as silver nanoparticles/graphene oxide (AgNPs/GO) or zinc oxide nanoparticles/graphene oxide (ZnONPs/GO). **(Salih *et al*., 2016)**

Of these two nanocomposites (AgNPs/GO and ZnONPs/GO), only one was selected and used towards the fabrication of novel electrochemical sensors for the detection of TB treatment drugs. This choice as discussed later was based on which platform possess a larger electrochemically active surface area for the adsorption and effective acceleration of electron transfer between the electrode and the chosen solution which will lead to a more rapid and sensitive current response.

Most importantly the enzyme Cytochrome P450-2D6 (CYP2D6) was covalently attached onto AgNPs/GO or ZnONPs/GO nanocomposites to achieve the electrochemical detection of the TB treatment drugs. Additionally, the platforms were also used to achieve the required electron transfer between the electrode surface and enzyme. The attachment of enzyme and nanocomposite were the main sensing elements of the biosensor towards Ethambutol and Pyrazinamide.

1.2 Problem statement

It is significant to carry out this study in order to improve the outcomes of inappropriate dosing of treatment and inadequate treatment administration. Although the treatment of TB is available, highly effective, achieving cure rates up to 95 % if taken as prescribed and even boosts the immune system; it still fails to meet the individual required doses of patients. This is clearly because different individuals have different drug metabolic profiles which affect the manner in which medication is bio-transformed. Hence the purpose of this study is to reduce the mortality and infection rate which occurs in patients infected with TB caused by poor treatment results. These include non-adherence to the treatment programs caused by related side effects, adjustable individual metabolism of the anti-TB drugs and lastly drug resistance

by the infectious organism. However, the most viable solution to this problem is the development of biosensor systems which can be utilised at point-of-care by healthcare practitioners to quantify TB treatment drugs of patients suspected of experiencing side effects. Additionally, these devices will be assistance in the identification of poor, intermediate and rapid metabolizers based on the amount of drug quantified after drug administration. The aim is to eventually encourage health care practitioners to individualize treatment based on each patient's metabolic profile. This study has successfully developed such a biosensor for the quantification of the TB treatment drugs namely ethambutol and pyrazinamide.

1.3 Rational and motivation

This study sought to address the issues caused by mortal side effects which resulted from administration of TB treatment by constructing biosensors which aimed at quantifying the level of TB drugs so as to individualize treatment regimens for TB diagnosed patients. The motive behind this study is driven by the ever increasing amount of patients experiencing drug resistance towards first-line drugs. Through the Directly Observed Treatment Short Course (DOTS) program which combines the drugs (isoniazid, ethambutol, pyrazinamide and rifampicin), a great deal of positivity has been observed towards human health, but sever effects caused by side effects and the improper use of first-line TB drugs has led to the more serious issue of multi-drug resistance in diagnosed patients. On the other hand, the incomplete application of the DOTS campaign has been the main cause of high incidences of the drug resistant strains of Mycobacterium tuberculosis followed by the spread of HIV/Aids in tuberculosis-endemic regions thus increasing the number of fatalities among TB diagnosed patients. Additionally, fully susceptible tuberculosis develops secondary resistance during

therapy due to non-adherence to the prescribed regimen or using low quality medication, inappropriate dosing of treatment and inadequate treatment.

There are however methods that are now available to quantify the levels of TB treatment drugs but they are relatively expensive, time consuming and they require large sample sizes. These methods include high performance liquid chromatography, mass spectrometry and liquid chromatography. Therefore, there is an immediate need to develop new analytical devices that are easy to use, inexpensive and which can allow the quantification of substrate turnover.

Hence in this research work an appropriate biosensor was used due to its capability of continuous measurements, its small size and its ability to measure analytes faster and at lower costs than traditional methods. **(Srivastava *et al*., 2016)** This study presents the development of biosensors for the quantification of ethambutol and pyrazinamide using zinc oxide nanopartiles/graphene oxide (ZnONPs/GO) or silver nanoparticles/graphene oxide (AgNPs/GO) nanocomposites coupled to Cytochrome P450-2D6 immobilized on glassy carbon electrodes. The attraction to the use of the AgNPs/GO or ZnONPs/GO nanocomposite is due to their synergistic effect and novel properties which are further discussed in the following chapter. The drug testing analyses was achieved using cyclic voltammetry (CV) or Ultraviolet Visible Spectroscopy (UV-vis) while the surface morphology studies of the nanocomposites were achieved using High-Resolution Transmission Electron Microscopy (HRTEM), Atomic Force Microscopy (AFM) and High-Resolution Scanning Electron Microscopy (HRSEM). Elemental analyses were accomplished using Fourier Transform Infrared Spectroscopy (FTIR), Energy Dispersive X-Ray (EDX), Raman spectroscopy and X-Ray diffraction (XRD)**.** The optical properties were obtained using Ultraviolet Visible

Spectroscopy (UV-vis), Photoluminescence Spectroscopy (PL) and Small-Angle X-ray Scattering (SAXS).

1.4 Aims and objectives

Research aim:

The aim of this study was to develop biosensor systems for the detection of the TB treatment drugs namely ethambutol and pyrazinamide. The biosensor(s) was developed using graphene modified silver or zinc oxide nanocomposites coupled to Cytochrome P450-2D6 (CYP2D6) immobilized on glassy carbon electrode surfaces.

In this research study a quantitative research approach was applied and the aim was achieved through the following objectives:

1. The synthesis of amine terminated graphene sheets using Hummers method.
2. The one-pot green conventional and green microwave-assisted synthesis of zinc oxide nanoparticles (ZnNPs).
3. The one-pot green conventional and green microwave-assisted synthesis of silver nanoparticles (AgNPs).
4. The development and optimization of (AgNPs/GO) and (ZnONPs/GO)nanocomposite electroactive platforms
5. The study of the physical characterization of GO, ZnONPs, AgNPs, ZnONPs/GO and AgNPs/GO using FTIR, PL, RAMAN, UV-vis, AFM, HRSEM, HRTEM, XRD, EDX, CV and SAXS

6. The electrochemical, spectroscopically and optical characterization of the developed platforms using CV and UV-vis spectroscopy.
7. To covalently attach the enzyme Cytochrome P450-2D6 (CYP2D) onto the zinc oxide or silver nanoparticles graphene electroactive platforms for develop the desired biosensors.
8. To electrochemically and optically detect and quantify ethambutol and pyrazinamide in standard solutions.

1.5 Research framework

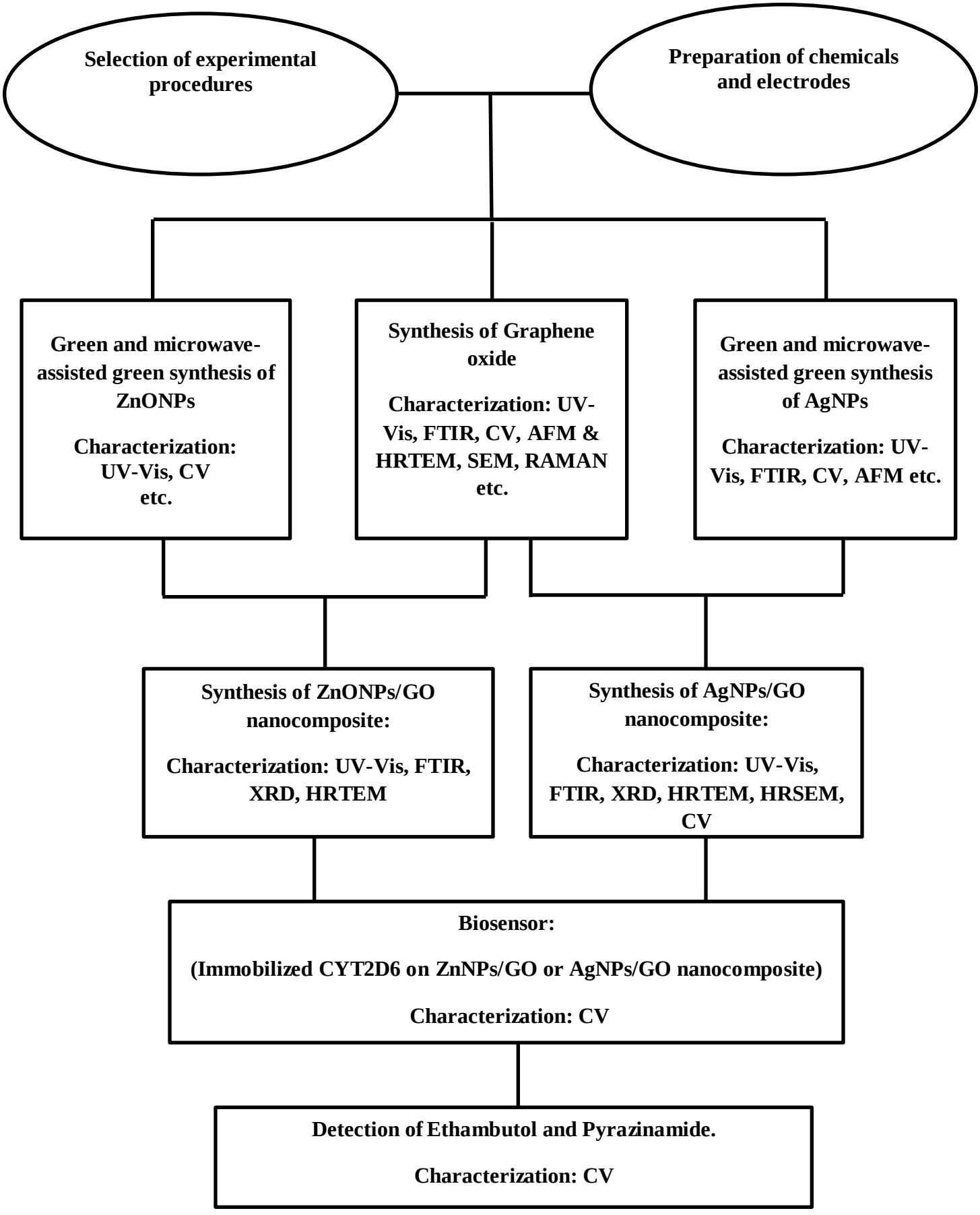

1.6 Thesis outline

The work presented in this thesis describes the development of a variety of different bio-sensing methods towards the goal of the detection of TB drugs in patients as outlined below.

Chapter 1 presents a brief background on Tuberculosis and its treatment regime as well as a detailed description of the drugs used during treatment, rationale and motivation, as well as the research aim and objectives.

Chapter 2 provides detailed current literature including substantive findings, as well as theoretical and methodological contributions towards this study.

Chapter 3 consists of detailed procedures used for the success of this work. Also included in this chapter are the lists of materials and instruments used.

Chapter 4 provides the morphological and amperometric results obtained from the nanomaterials; GO, ZnONPs and AgNPs synthesized in this work while

Chapter 5 consists of green synthesized AgNPs/GO and ZnONPs/GO morphological and amperometric results obtained.

Chapter 6 illustrates the morphological and amperometric results for the developed AgNPs/GO/CYP2D6 or ZnONPs/GO/CYP2D6 biosensors and also consists of results on the detection of ethambutol and pyrazinamide using the developed biosensors.

Chapter 7 illustrates general conclusion, recommendations and future work.

1.7 References

Carnetti G, 1962. The eradication of tuberculosis: theatrical problems and practical solutions. Tubercle 43: 301-321

De Villiers, L. and Toit Loots, D., 2013. Using metabolomics for elucidating the mechanisms related to tuberculosis treatment failure. Current Metabolomics, 1(4), pp.306-317.

El Din, M.A.T., El Maraghy, A.A. and Hay, A.H.R.A., 2015. Adverse reactions among patients being treated for multi-drug resistant tuberculosis at Abbassia Chest Hospital. Egyptian Journal of Chest Diseases and Tuberculosis, 64(4), pp.939-952.

Isaac, R.S., Sakthivel, G. and Murthy, C.H., 2013. Green synthesis of gold and silver nanoparticles using Averrhoa bilimbi fruit extract. Journal of Nanotechnology, 2013.

Jnawali, H.N. and Ryoo, S., 2013. First–and Second–Line Drugs and Drug Resistance. In Tuberculosis-Current Issues in Diagnosis and Management. InTech.

Kahrilas, G.A., Wally, L.M., Fredrick, S.J., Hiskey, M., Prieto, A.L. and Owens, J.E., 2013. Microwave-assisted green synthesis of silver nanoparticles using orange peel extract. ACS Sustainable Chemistry & Engineering, 2(3), pp.367-376

Krasniqi, S., Jakupi, A., Daci, A., Tigani, B., Jupolli-Krasniqi, N., Pira, M., Zhjeqi, V. and Neziri, B., 2017. Tuberculosis Treatment Adherence of Patients in Kosovo. Tuberculosis research and treatment, 2017.

Leibert, E. and Rom, W.N., 2010. New drugs and regimens for treatment of TB. Expert review of anti-infective therapy, 8(7), pp.801-813.

Li, J., Kuang, D., Feng, Y., Zhang, F., Xu, Z., Liu, M. and Wang, D., 2013. Green synthesis of silver nanoparticles–graphene oxide nanocomposite and its application in electrochemical sensing of tryptophan. Biosensors and Bioelectronics, 42, pp.198-206.

Luies, L., du Preez, I. and Loots, D.T., 2017. The role of metabolomics in tuberculosis treatment research. Biomarkers in medicine, 11(11), pp.1017-1029.

Mani, V., Wang, S., Inci, F., De Libero, G., Singhal, A. and Demirci, U., 2014. Emerging technologies for monitoring drug-resistant tuberculosis at the point-of-care. Advanced drug delivery reviews, 78, pp.105-117.

Meena, R. and Meena, L.S., 2011. Unique Characteristic Features of Mycobacterium tuberculosis in Relation to Immune System. American Journal of Immunology, 7(1).

Nurunnabi, M., Parvez, K., Nafiujjaman, M., Revuri, V., Khan, H.A., Feng, X. and Lee, Y.K., 2015. Bioapplication of graphene oxide derivatives: drug/gene delivery, imaging,

polymeric modification, toxicology, therapeutics and challenges. RSC advances, 5(52), pp.42141-42161.

Obeid, K.M. and Saravolatz, L., 2009. Tuberculosis: a comprehensive clinical reference. JAMA, 302(22), pp. 676–688.

Patil, B.N. and Taranath, T.C., 2016. Limonia acidissima L. leaf mediated synthesis of zinc oxide nanoparticles: A potent tool against Mycobacterium tuberculosis. International journal of mycobacteriology, 5(2), pp.197-204.

Salih, E., Mekawy, M., Hassan, R.Y. and El-Sherbiny, I.M., 2016. Synthesis, characterization and electrochemical-sensor applications of zinc oxide/graphene oxide nanocomposite. Journal of Nanostructure in Chemistry, 6(2), pp.137-144.

Sarkar, S., Ganguly, A. and Sunwoo, H.H., 2016. Current Overview of Anti-Tuberculosis Drugs: Metabolism and Toxicities. Mycobact Dis, 6(209), pp.2161-1068.

Srivastava, S.K., 2014. Biosensor based detection of tuberculosis biomarkers. Wageningen University.

Srivastava, S.K., Van Rijn, C.J. and Jongsma, M.A., 2016. Biosensor-based detection of tuberculosis. RSC advances, 6(22), pp.17759-17771.

Tothill, I., 2011. Biosensors and nanomaterials and their application for mycotoxin determination. World Mycotoxin Journal, 4(4), pp.361-374.

World Health Organization and World Health Organization, 2015. Global tuberculosis report 2015. 2015. Geneva: World Health Organization.

Zaman, K., 2010. Tuberculosis: a global health problem. Journal of health, population, and nutrition, 28(2), p.111.

CHAPTER 2

Literature review

Summary

This chapter gives a comprehensive explanation of all the concepts stated in Chapter 1.It also indicates that the topic at hand is thoroughly understood and that literature has been consulted thoroughly in order to aid in the successful completion of this study. The subject matters discussed herein are Green synthesis, Nanomaterials, Graphene oxide, Biosensors, Enzymes, Pyrazinamide, Ethambutol and Tuberculosis.

2.1 Green synthesis of Nanomaterials

2.1.1 Introduction

Nanomaterials are the leading edge of the rapid development of nanotechnology. They have unique size-dependent properties which make them indispensable and superior in many areas of human activity. **(El-Rafie *et al*., 2012)** Although physical and chemical methods could successfully produce pure, well-defined metal based nanomaterials such as gold, zinc oxide and silver nanoparticles, these methods are quite expensive and potentially dangerous to the environment. **(Salata., 2014)** Hence the use of biological organisms such as plant extract, microorganisms, or plant biomass are preferable as alternatives to chemical and physical methods for the production of nanoparticles in an eco-friendly manner. **(Rao *et al*., 2013)**

Nanomaterials are known to have a long list of applicability that improves human life and its environment because of their optical and magnetic properties. **(Kotakadi *et al*., 2014)** These materials are usually used to describe materials with one or more components that have at least one dimension in the range of 1 to 100 nm that includes nanotubes, nanoparticles, composite materials, nanofibres and nano-structured surfaces. The nanoparticles are usually a subset of nanomaterials currently well-defined by consensus as single particles with a diameter less than 100 nm. **(Borm *et al*., 2006)**

At present, there are two main approaches for fabrication of nanostructure and synthesis of nanomaterials: “bottom up” and “top down” approaches as shown below in **Figure 2.1**.

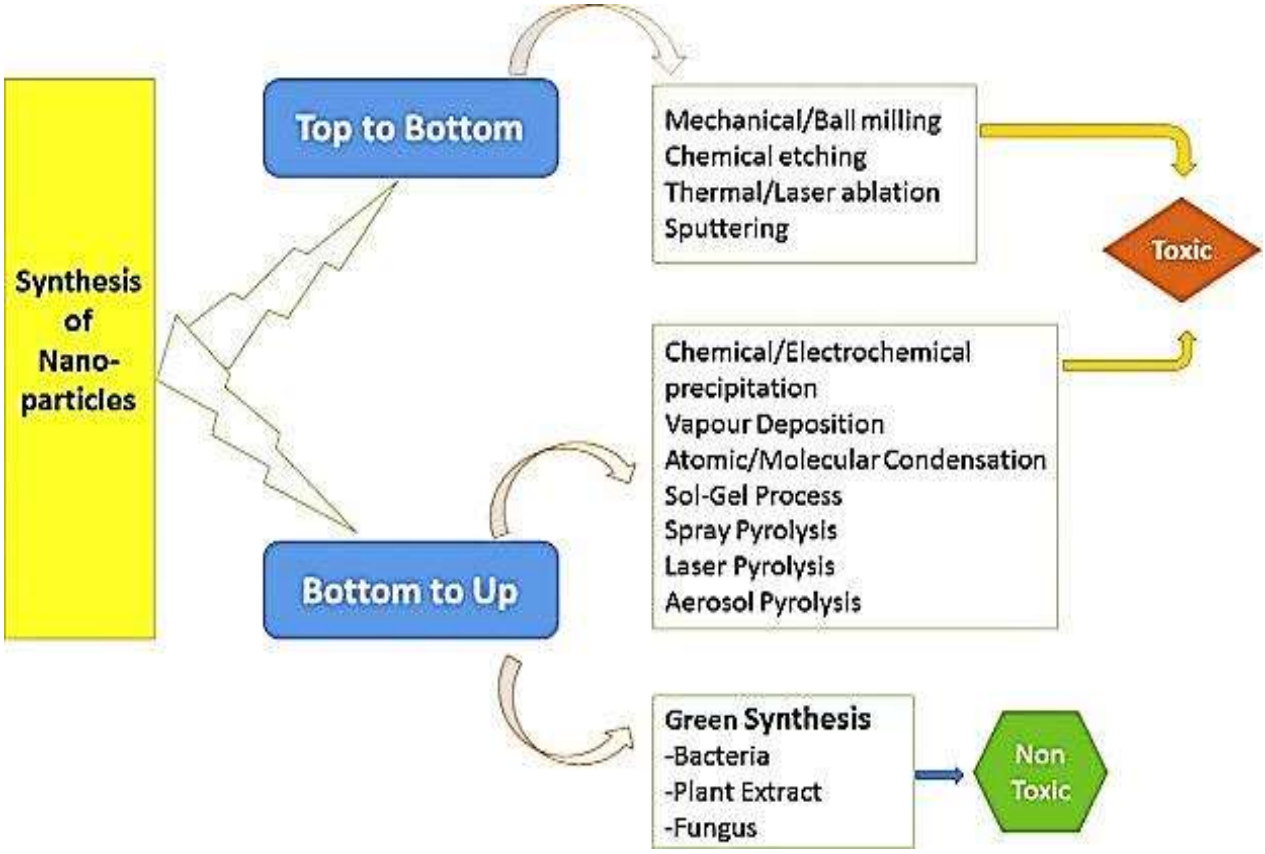

Figure 2.1: Schematic diagram illustrating the synthesis of nananomaterials. (Ahmed *et al*., 2016)

The top-down approach is a physical method known as micro-fabrication method where suitable bulks materials break down into fine particles by size reduction with various lithographic techniques e.g. milling, thermal/laser ablation, grinding and sputtering. **(Singh *et al*, 2016)** However, the operative and acceptable method for nanoparticle preparation is the bottom up approach, where nanoparticles can be synthesized using either biological or chemical methods through the self-assembling of atoms to new nuclei which grow into particles at the nanoscale. **(Ahmed *et al*., 2016)** This particular approach is further categorized into biological and chemical processes, in which the chemical synthesis process massively consumes expensive organic solvents, reducing agents and non-renewable solvents

which lead to environmental pollution. Henceforward the biological paths of nanoparticle synthesis processes are developing as greener and novel strategies. **(Sathiyanarayanan *et al*., 2017)**

Currently the development of green processes for nanoparticles synthesis is developing into a central branch of nanotechnology. Most metal based nanomaterials have drawn attention to scientist due to their extensive application in the development of new technologies in the areas of material sciences, electronics and medicine at the nanoscale. **(Banu *et al*., 2013)** Nanocomposite materials containing nanoparticles such as silver, zinc oxide etc. have also recently attracted a lot of attention because of their chemical stability, catalysis and good conductivity and they are extensively used in construction materials, food industries as anti-bacterial agents in food packing and food industries as anti-bacterial agents in food packing. **(Bai *et al*., 2012)**

As a result, these nanoparticles have exceptional properties and they are promising in new areas of research due to their size and highly active performance caused by their large surface areas yet, there are also some problems observed in the use of nanoparticles such as; high degree of agglomeration between nanoparticles. **(Haghparasti *et al*., 2018)** Silver and zinc oxide nanoparticles seem to have a wide range of potential applications in various areas of science hence they were preferred in this study. **(Sangeetha *et al*., 2011)** Moreover, expansion of green syntheses over chemical and physical methods is due to properties such as; non-toxicity, the use of safe reagents, lack for the need to use high pressure, energy, temperature and toxic chemicals and are generally environmental friendly. **(Grodowska and Parczewski., 2010)** Nanoparticles synthesized using green technology or biological methods have great stability, are diverse in nature and have proper dimensions since they are synthesized using a one-step method. **(Parveen *et al*., 2016)**

2.2 Methods used in green synthesis of nanomaterials

2.2.1 Microwaves irradiation (MI)

Microwave irradiation (MI) method denotes a major invention in synthetic chemical methodologies; a dramatic change in the way green synthesis is performed. **(Grewal *et al*., 2013)** This method holds a great significance in the regime of nanoparticle synthesis as it controls high temperature enhancing the nucleation process by which nanoparticles are initially formed. MI forms nanoparticles that provide greater control over the shape and morphology of the nanostructures produced and has higher degrees of crystallinity. **(Parveen *et al*,. 2016)** This method consists of magnetic and electric fields and thus represents electromagnetic energy during synthesis.

The electromagnetic energy performs as a nonionizing radiation that causes rotation of the dipoles and molecular motions of ions, but does not affect molecular structures. The internal heating in MI is much more homogeneous than the classical heating. **(Majumder *et al*., 2013)** MI is commonly used in agrochemical, pharmaceutical and related industries in development processes and in initial discoveries. Its principal interest concerns the saving of energy for heating by focusing efficient energy on the sample, enhancing product purities avoiding possible side reactions, the increase in product yields and dramatic reduction of reaction times and amount of solvents. **(Veitía *et al*., 2015)**

2.2.2 Ultrasound

The ultrasound method has steadily been introduced as a green synthetic approach in the field of chemistry as it is safe for the environment. This method is known to be one of the rapid techniques for the synthesis of metal nanoparticles due to its high pressure and temperature.

(Popov *et al*., 2015) This extreme condition from ultrasound irradiation can possibly produce reactive free radical species and it will be followed in producing of metal nanoparticle in short time. One of its greatest advantages is that it improves the yield, produces nanoparticles that are nontoxic, environmental friendly and simple**. (Faried *et al*.,2016)** Currently, the ultrasonic-assisted synthesis of nanoparticles has been found to be affective in size distribution of the particles in a narrower range by thermal convection due to penetration property of ultrasonic irradiation through solution, causing uniform activation energy for the reaction solution. The synthesis of this method can also control the morphology and size distribution of the nanoparticles. **(Suib., 2013)** This technique presently is widely used in environmental and fine chemistry. Also, ultrasound avoids the addition of phase transfer agents, reduces reaction times and allows activation energy. **(Grewal *et al*., 2013)**

2.2.3 Photocatalysis

Photocatalysis synthesis method plays a significant role in green process since it provides an alternative to classic chemistry. **(Guo *et al*., 2009)** It offers suitable tools for industrial reactions using cells and enzymes which can be carried out under mild conditions, with a great control over chemo-, regio- and stereoselectivity by using appropriate enzymes and with the use of heavy metals. **(Hernaiz *et al*., 2010)** Additionally, in fine chemistry the activation by photocatalysis under visible light could be another method. This innovative approach is very attractive due to circumvents of the use of heavy metals. In this method, light can be considered as an ideal reagent which is environmentally friendly in green chemical synthesis. **(Anastas and Kirchhoff., 2002)** Dissimilar too many conventional reagents, light generate no waste; it is non-toxic and abundant. These days, the advancement

of photo redox catalysis originated by visible light is of real significance. The reaction of this method is usually carried out by photo redox catalysts, organometallic complexes containing iridium and ruthenium. **(Grewal *et al*., 2013)**

2.2.4 Biotransformation

Biotransformation is a widely used method in green chemistry and it massively contributes to the development of chiral chemistry in aqueous medium merging the constraints enforced by the efficient synthesis with the constraints related in respect to the environment. **(Veitía *et al*., 2015)** This method deals with the use of a biocatalyst for the mediation of a chemical reaction and for the synthesis of an organic chemical. Biotransformation is currently playing a crucial role in many industries, including animal feed stock, chiral drug formation and vitamin production. Even the use of microbes and enzyme for synthesis is expected to grow enormously since the industries are being forced by the public to shift toward ‘‘green chemistry,’’ which uses safer and cleaner chemicals in their manufacturing processes and produces less toxic effluents. **(Doble *et al*., 2004)**

2.2.5 Conventional heating (CH)

Conventional heating is the most frequently used method to obtain green synthesis and usually it involves the use of oil baths or furnace which heats the walls of the reactors by conduction or convection. In this particular method the process initiates from the source where heat is generated and it then gets transferred from the external to the internal part of the material used through convection, conduction and radiation steadily. **(Jin *et al*., 2017)** CH can be used to produce nanoparticles in enormous quantities with defined shape and sizes in a

short period of time; however it is also inefficient, outdated and complicated. In recent years, there has been rising concern in synthesis of nanoparticles which need to be environmentally friendly and should produce non-toxic waste products during the manufacturing process. **(Moghimi *et al*., 2001)** Recent studies have started succeeding that through benign synthesis techniques of a biological nature using biotechnological tools that are considered safe and ecologically sound for nanomaterial fabrication as a substitute to conventional chemical and physical methods. This has certainly given rise to the concept of green nano-biotechnology or green technology. **(Patra and Baek., 2014)**

2.3 Types of green synthesized nanomaterials

2.3.1 Metal Based Nanomaterials

Metal based materials are commonly regarded as nanoparticles (nano silver, nano gold etc.), quantum dots and oxides with metal bases. Nanoparticles of metals and metal oxides are identified to exhibit improved chemical activities and unique reactivity because of the presence of different surface crystal planes, high density of surface atoms as well as surface relaxation between layers. **(Mody *et al*., 2010)** Most recently the major focus has been the development of green chemical methods for the synthesis of metal nanoparticles hence a majority of researchers have gained interest to investigate mechanisms of metal ions application and bio-reduction and to understand the possible mechanisms of metal nanoparticle formation.

However, green chemistry has been studied in order to find an eco-friendly method for production of well-characterized nanoparticles. One of the ultimate considered techniques is the production of metal nanoparticles using organisms. Amongst these organisms, plants

appear to be the greatest media and they are appropriate for large scale biosynthesis of nanoparticles. **(Taheriniya and Behboodi., 2016)** The rates of nanoparticles produced by plants are faster and have a wider variety in size and shape as compared to those produced by other organisms such as prokaryotic bacterial cells and eukaryotic fungi. **(Makarov *et al*., 2014)** Nanoparticles prepared by green methods have low toxicity and are more stable. Thus, the preparation of nanoparticles using plants provide a best environment while the nanoparticles prepared by chemical method have been reported to be less suitable for biological activities because of their toxicity. Chemical methods are not only toxic but are also costly and potentially hazardous not to mention their difficult separation procedures, energy requirement and high pressure they have. **(Taheriniya and Behboodi., 2016)**

In this study, a green chemistry approach was used to prepare metal nanoparticles namely; silver (Ag) and zinc oxide (ZnO) using aqueous solutions of tomato and apple extracts as reducing and stabilising agents. Most studies has also used plants to synthesis similar metals such as **Khalil *et al*., 2014** who synthesized silver using hot water olive leaf extracts (OLE) as a reducing and stabilizing agent for the evaluation of antibacterial activity against drug resistant bacterial isolates**. Singh et al., 2016** also synthesized silver (AgNPs), gold (AuNPs), and gold–silver bimetallic (Au–AgNPs) nanoparticles from medicinal plants such as *Barleria prionitis, Plumbago zeylanica* and *Syzygium cumini* where the nanoparticles where tested against Mycobacterium tuberculosis. **(Singh *et al*., 2016)**

2.3.2 Carbon Based Nanomaterials

Carbon is one of the most versatile and plentiful elements in creation because of its allotropic characteristics capability to form compounds that are entirely different in properties

depending on the arrangement of the adjacent carbon atoms. Graphite, nanotubes, fullerene, graphene and diamond are typical examples as shown in **Figure 2.2**. **(Siqueira and Oliveira., 2017)** Carbon exhibits exceptional characteristics such as superior hardness, high density and high strength. Its development, innovation and research are taking place in various fields. Studies have provided exertion in the development of carbon-based materials which have presented numerous positive results for a wide variety of structures which has permitted the development of several materials with different applications. **(dos Santos *et al*., 2014)** Carbon nanomaterials have provided new functionalities in biomedical applications, such as controlling delivery of drugs, pharmaceuticals as well as sensing. **(Siqueira and Oliveira., 2017)**

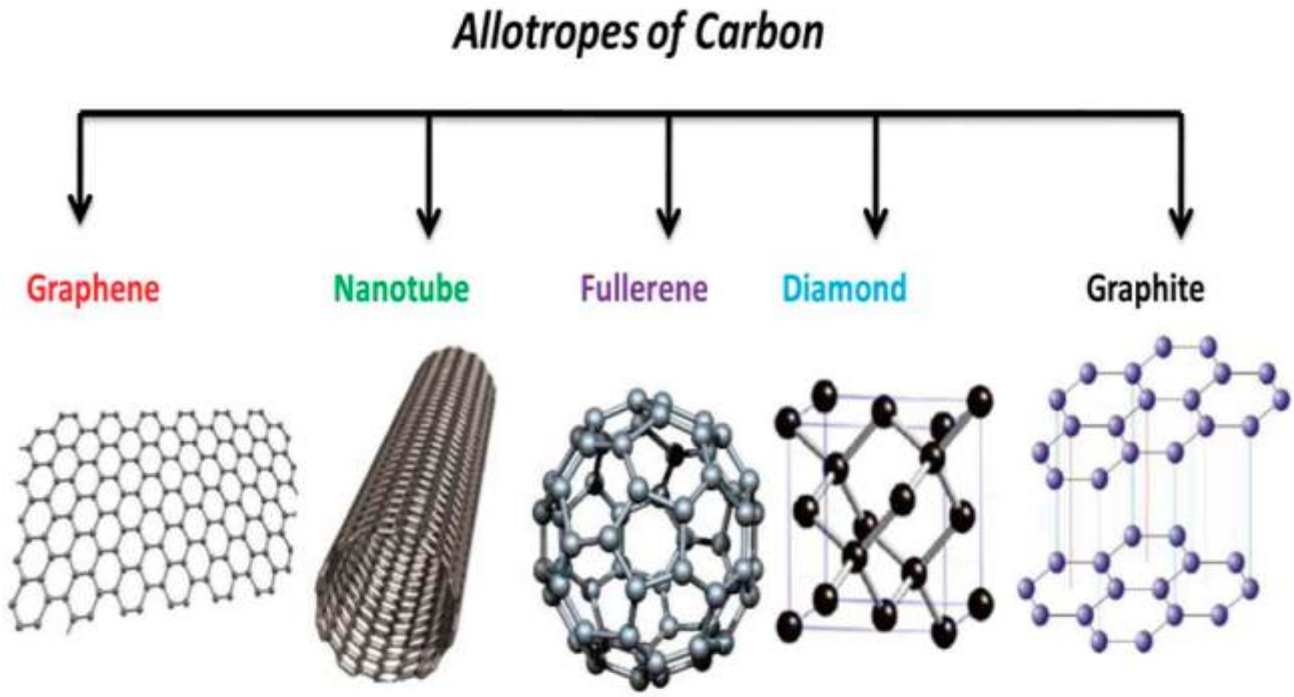

Figure 2.2: Allotropes of carbon and their crystal structures. (Movlaee *et al*, 2017)

In recent times, a variety of methods have been developed to synthesize carbon-based nanomaterials with improved performance for various applications. These nanomaterials are believed to be suitable and promising to cushion the threat. As a result, the remarkable properties of these materials and ultimate potentials towards environment friendly synthesis methods and industrial scale production of carbon nanostructured materials are most certainly necessary and can then be seen as the focal point of many researchers in science and technology of late. **(Nasir *et al*., 2018)**

Currently carbon-based nanomaterials are mostly formed in chemical processes, but nanotechnology has started to focus on the materials themselves for use of green synthesis methods, rather than their respective syntheses in order to check impacts associated with these nanomaterials. This is based on the incredible future that lies ahead with these smart nanomaterials even their objectives represents a huge research opportunity that can improve the environmental and economic efficiencies and can also enable enhanced synthetic control at the lower temperatures which need to realize some of the presently unattainable materials. **(Gilbertson *et al*., 2015)**

2.3.3 Composites

Composites are a class of materials made up of several elements with nanoscale dimensions embedded in a polymer matrix, metal or ceramic. Their main goal is to create synergistic effect such as electrical conductivity, compatibility or catalytic activity between various materials. However, the properties of nanocomposites rely on shape, size, range of variable, particularly the degree of dispersion and orientation of the nanoscale second phase and interactions between second phase and the matrix. **(Monticelli *et al*., 2012)**

Furthermore, several methods have been developed for the synthesis of composites using both chemical and physical approaches such as electrochemical methods, microwave irradiation, thermal decomposition, sonochemical and laser ablation although they are related in terms of their limitations because they require high operational costs, energy needs and toxic chemicals. **(Quyen *et al*., 2017)** Due to these limitations a substantial interest has been given for the preparation of composites using green synthesis. As widely known, green synthesis is a well-known as environment friendly processes in chemistry, engineering and in chemical technology that has gain popularity and much needed since the global concern is about environmental problems at the moment. **(Iravani *et al*., 2014)**

Literature suggests that green methods has been used as a new alternative for the synthesis of composite using reductions and capping agents such as natural polymers, plant extracts, enzymes, microorganisms and , sugars. The greatest advantages of using green methods are; they use more stable materials, one simple step processes, cost-effective, environment friendly and energy efficient. **(Quyen *et al*., 2017)**

In the present research work graphene oxide and zinc oxide or silver nanocomposites (AgNPS/GO and ZnONPs/GO) was synthesized using tomato and apple extract. Numerous studies have reported on these nanocomposites; **Patil *et al.*, 2017** synthesized silver nanoparticles (AgNPs)/graphene nanocomposite using *sapodilla* peel extract under photochemical irradiation while **Sutradhar and Saha., 2016** demonstrated series of ZnO nanocomposites with titanium dioxide nanoparticles (TiO_2) and graphene oxide (GO) by using the aqueous extract of tomatoes as non-toxic and ecofriendly reducing material.

2.4 Green synthesized based paltforms/nanomaterials

2.4.1 Synthesis of graphene oxide (GO)

Graphene oxide (GO) is a monolayer of graphite oxide that is produced by exfoliating graphite oxide into layered sheets through mechanical or sonication stirring. **(Zaaba *et al*., 2017)** Graphene oxide consists of graphene sheets covered with hydroxyl and epoxide groups. During the exfoliation process the rapid heating of graphene oxide results in delamination and expansion because of evolution of gases and evaporation of the intercalated water from pyrolysis of the oxygen containing functional groups. **(Paulchamy *et al*., 2015)**

Initially the functional groups on the graphene oxide surface act as effective fastening sites to immobilize several active species and it also possesses tunable electronic properties. Usually graphene oxide is insulating because of its large portion of sp^3 hybridized carbon atoms bonded with oxygen containing groups. **(Li *et al*., 2015)** GO is extremely suitable for use in biological and chemical sensors due to the nature of the alignment of atoms on its surface, controllable surface defect density that modulates the sensor sensitivity and specificity and lastly, due to its scalable solution-based preparation process.**(Li *et al*.,2013)**

The properties and structure of graphene oxide depend on the degree of oxidation and the chosen synthesis method. The commonly used method for the synthesis of GO is the chemical method called Hummer's method as illustrated in **Figure 2.3**. This method of synthesis is diverse and appropriate for oxidizing agents used to exfoliate graphite flakes. **(Paulchamy *et al*., 2015)**

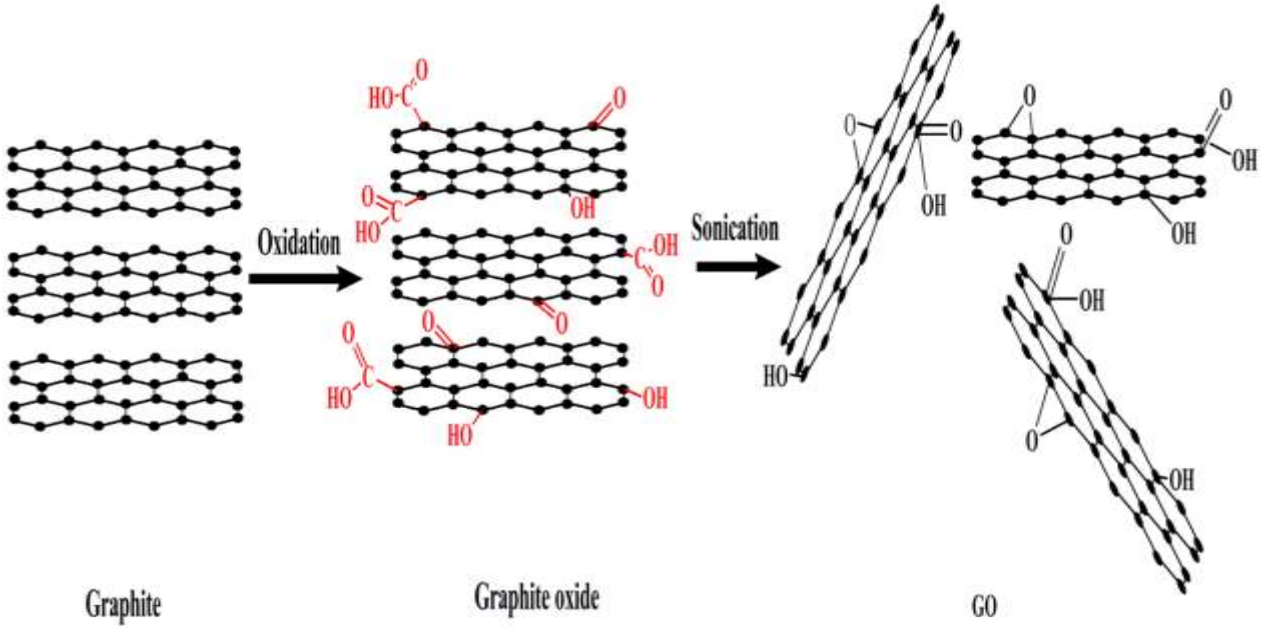

Figure 2.3: Preparation of graphene oxide (GO). (Li *et al*., 2014)

2.4.2 Synthesis of graphene oxide based nanocomposites

Graphene based nanocomposites are materials with unique structures and superb properties and they have emerged as one class of the fascinating materials with promising applications in the field of electrochemistry. For graphene oxide based nanocomposites, the exceptional properties of the graphene oxide nanosheets make them predominantly useful as supports for nanoparticles. The high surface area of GO is also important for the dispersion of the nanoparticles in order to sustain their electrochemical activities. **(Chen *et al*., 2012)**

Nanoparticles supported by graphene oxide are not only to maximize the accessibility of the nanosized surface area for electron transfer, but they also create enhanced mass transport of the reactants to the electroactive sites on the electrode surface of interest. Furthermore, the conductive graphene oxide support enables the well-organized collection and transfer of electrons to the collecting electrode surface. Nonetheless, the functionalization of graphene

oxide with nanoparticles has made the consciousness of nanoscale composite electrode modification promising. **(Zhang *et al*.,2011)**

In electrochemical applications, graphene oxide based nanocomposite modified electrodes has shown an uncommon advantage over macroelectrodes. These include excellent catalytic activities, enhancement of mass transport, high effective surface areas and control over the electrode micro-environment. In addition, the combination of GO with nanoparticles may prove capable of contributing additional performance in some functional electrochemical applications. **(Chen *et al*., 2012)**

Of late, the trends of applying green reductants in the synthesis of nanomaterials have grown widely **(Adil *et al*., 2015)**. For example, a variety of green reductants have been useful for the synthesis of metallic nanoparticles, such as microorganisms, glucose, plant extracts, mino acids, vitamin C, ascorbic acid and bovine serum albumin **(Hebbalalu *et al*., 2013)**. As mentioned before, amongst these green reductants, plant extracts are the only one that has received great attention because of its easy availability, cost effectiveness and bulk amounts **(Akhtar *et al*., 2013)**. Additionally, plant extracts function as both reducing and stabilizing agents thus limiting the use of additional chemical stabilizers. Due to that, most recently plant extract have also been effectively used for the reduction of graphene oxide (GO) too. **(Khan *et al*., 2014)** However a sequence of metallic nanoparticles have been prepared using plant extracts as reducing agents and their application in the synthesis of graphene based nanocomposites has so far been admirable (**Sedki *et al*., 2015)**.

As mentioned before, in this study AgNPs/GO or ZnONPs/GO nanocomposites were successfully synthesized using tomato and apple extracts which served as both stabilizing and reducing agents. Previously reported study has successfully demonstrated a simple, one-step approach for the preparation of AgNPs/GO nanocomposites (**Al-Marri *et al*., 2015**) through

the simultaneous reduction of both graphene oxide (GO) and silver ions using *Pulicaria glutinosa plant extract (PE)* as a reducing agent. **(Al-Marri *et al*., 2015)** Additionally, graphene nanosheets have also been employed already as supports to stabilize and disperse various nanoparticles such as; Gold (Au) **(Liu *et al*., 2011)**, zinc oxide (ZnO) **(Li *et al*., 2012)**, manganese dioxide (MnO_2) **(Li *et al*., 2010)** and titanium dioxide (TiO_2). **(Zhang and Choi., 2011)** These methods can be easily prepared because of the abundant surface functional groups (–OH,C–O–C,and–COOH) on graphene oxide which provide reactive sites for the binding of metal nanoparticles **(Zhang *et al*., 2011)**.

2.5 Enzymes

Enzymes are proteins that aim to accelerate particular life essential biochemical reactions through many orders of magnitude. For a long period of time they have been used to assess concentrations of diverse analytes to aim compounds such as pathogens, hormones and drugs. This is as a result of their selectivity towards specific substrates. **(Callender and Dyer., 2014)** Once an enzyme (E) binds to a substrate (S) an enzyme-substrate complex is formed and the substrate is converted to products (P). **(Agarwal., 2006)**

$$E + S \leftrightarrow ES \leftrightarrow E + P \qquad (1)$$

Enzymes have countless functional features. At the molecular level, enzymes catalyze biochemical reacts by accelerating the change of substrates into products in a repressed pocket within the active site of the enzyme. Most reactions would be too slow to be useful for

life without enzyme catalysis. **(Milanowski *et al*., 2013)** However, the pioneering studies by **Krebs., 1970** on the citric acid cycle have realized that enzymes do not act independently but modulate collectively metabolic networks and pathways. Enzymes carry out their molecular function in a specific cell compartment. Lastly, there is great variety in the fraction of enzymes in different organisms and variations at tissue levels, cell type and organelle have also been perceived. **(Cuesta *et al*., 2015)** In this study the enzyme of interest and which was utilized for the sensor construction was Cytochrome P450 2D6.

2.5.1 Cytochrome P450-2D6

Cytochrome P450-2D6 (CYP2D6) is a heme-containing enzyme that is in control of the metabolism of at least 20 % of known drugs. **(Owen *et al*., 2009)** Substrates of CYP2D6 normally contain a planar aromatic ring and basic nitrogen. The crystal structure of human CYP2D6 has been resolved and advanced to a 3.0 Å resolutions. As shown below in **Figure 2.4**, the structure illustrates the characteristic of P450 fold and other members of the family with orientations and lengths of the individual secondary structural elements being very similar to each other. **(Rowland *et al*., 2006)**

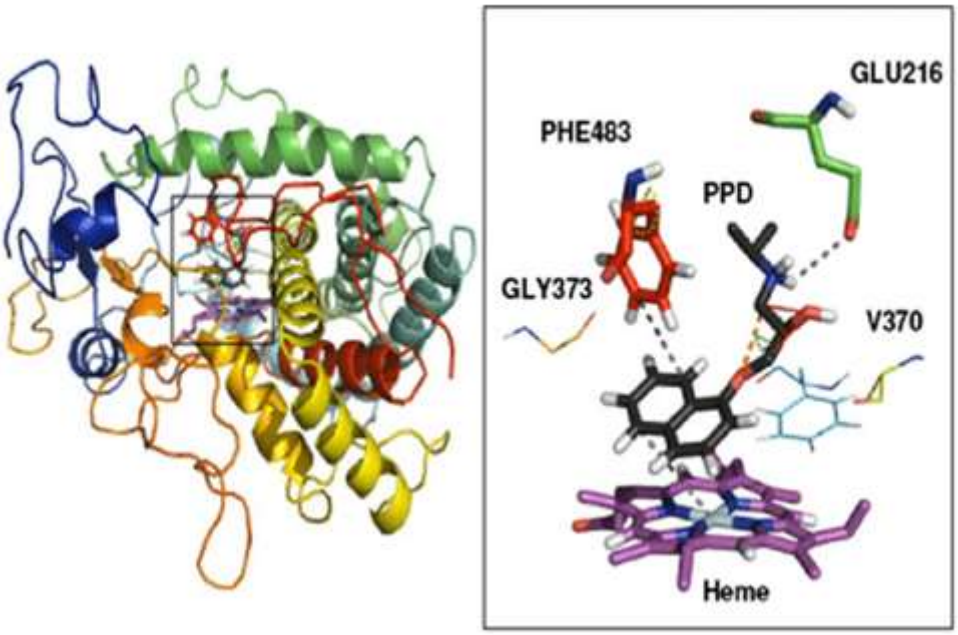

Figure 2.4: Crystal structure of human Cytochrome P450 2D6. (**Nagy and Oostenbrink., 2012)**

CYP2D6 is primarily a hepatic enzyme which constitutes only about 2 % of the total cytochrome protein in the liver. It has been revealed that it has contributed significantly towards the metabolism of over 30 recommended drugs such as; Amiodarone, cimetidine and diphenhydramine (Benadryl). **(Ingelman-Sundberg., 2005)** Great deals of drugs are CYP2D6 inhibitors and taking an inhibitory drug along with a CYP2D6 substrate can change the obvious phenotype of the patient. This phenomenon is well-known as phenocopying. When an instance like this occurs, wide metabolizers appear to be poor metabolizers or intermediate metabolizers due to a majority of available enzyme that are being inhibited by a confounding drug. An associated phenotype that can occur with chronic dosing of a CYP2D6 drug is called autophenocopying where a CYP2D6 substrate can inhibit its own metabolism

over a period of time as the concentration of the drug approaches stable state. The pharmacokinetic profile of repeated dosing or single dose drugs exhibit phenocopying that can differ significantly. **(Owen *et al*., 2009)** Cytochrome P450 2D6 (CYP2D6) induction and inhibition are the key mechanisms mediating drug–drug interaction (DDI) in clinical pharmacotherapy. During tuberculosis chemotherapy there is a high probability of DDIs caused by the inhibition or induction of the drug-metabolizing enzymes, especially cytochrome isoforms. The effect and safety of anti-tuberculosis drugs has been investigated on cytochrome P450 2D6 (CYP2D6). **(Lee *et al*., 2014)**

In this research study, the direct electron transfer between CYP2D6 and modified electrodes was investigated based on the as-constructed electrochemical platform which was nanomaterial and graphene oxide. Previous studies have proven that CYP2D6 immobilized on nanocomposites consisting of graphene oxide and nanostructured materials have excellent electrocatalytic metabolic behaviours and electrochemistry such as; **Ajayi *et al*., 2016** who studied the competitive inhibition by paroxetine of CYP2D6 encapsulated in a nanostructured materials and **Cui *et al*., 2014** who reported an electrochemical platform for the investigation of drug metabolism in vitro which was constructed by immobilizing cytochrome P450 2D6 with cyt P450 reductase (CPR) on graphene modified glass carbon electrode.

The fabricated electrochemical platform with CYP2D6 and modified electrodes in this study was then used for detection of the tuberculosis drugs; Pyrazinamide and Ethambutol.

2.6 Tuberculosis

Tuberculosis (TB) remains one of the major worldwide health threats leading to mortality and morbidity. **(Cruz-Knigh and Blake-Gumbs., 2013)** It is an infection caused by the non–spore-forming, rod-shaped, aerobic bacterium *Mycobacterium tuberculosis* (Mtb). *Mycobacterium tuberculosis* that measure 0.5 μm by 3 μm are typically classified as acid-fast bacilli and have a distinctive cell wall structure essential to their existence. Mycobacterium tuberculosis spreads from one human being to another by small airborne droplets called droplet nuclei, generated by talking, sneezing, coughing, or singing of a person with laryngeal or pulmonary tuberculosis. **(Knechel., 2009)**

According to the World Health Organisation (WHO), one third of the world's population is likely to have dormant tuberculosis with 10 million people who fell ill with this disease and 1.6 million died from the disease (including 0.3 million among people with HIV) in 2017. Additionally, 75 % of cases are in the most economically productive age group (15 - 54 years), where over 90 % of global TB cases and deaths occur in developing countries. **(World Health Organization, 2017)** Co-infection with human immunodeficiency virus (HIV) significantly increases the risk of developing TB because of the compromised immune systems. Sub-Saharan Africa countries with a high popularity of HIV are witnessing an increase in TB and South Africa is one of the countries with the highest problem of TB which is in the top ten amongst Indonesia, Kenya and India where the estimated rate of new infections occurs at a rate of one per second. **(Lawn and Churchyard., 2009)**

However, at the moment TB treatment is administered through the highly recommended and most effective therapy program recommended by the WHO; the Directly Observed Therapy Short-course (DOTS). **(Moonan *et al*., 2011)** The DOTS program is a 6-months therapeutic regimen, which starts with an intensive treatment phase for 2-months using a combination of

the first line drugs namely; pyrazinamide (PZA), isoniazid (INH), ethambutol (EMB) and rifampicin (RIF), followed by a maintenance phase for 4-months using only RIF and INH. **(Sarkar *et al*., 2016)** Though, the usefulness of this regimen is threatened by the escalating resistance to these first line drugs. **(Moonan *et al*., 2011)**

A current report by few researchers have shown emergence in *Mycobacterium tuberculosis* strains that were found to be resistant to antibiotics. **(Müller *et al*., 2013)** *Mycobacterium tuberculosis* possesses a crowd of resistance mechanisms contrary to antibiotics as far as its intrinsic mechanisms which can be categorized into specialized and passive resistance. **(Smith *et al*., 2012)** Specialized resistance mechanisms assists to detoxify drug molecules that manage to reach the cytoplasmic space, while the mycobacterial cell wall slows down antibiotic penetration. Passive resistance mechanism on the other hand controls the strong connection between antibiotic resistance and mycolic acid content. Also, passive resistance mechanism creates a space that resembles the periplasm of Gram-negative bacteria, another piece of evidence supporting the impermeability of the mycobacterial cell wall. **(Symeonidism and Marangos., 2012)**

2.7 Tuberculosis treatment regimen

There are four basic treatment regimens endorsed for treating adults with tuberculosis disease namely; pyrazinamide (PZA), isoniazid (INH), ethambutol (EMB) and rifampicin (RIF). Each of these treatment regimens consists of an initial two months treatment phase followed by a continuation phase of either four or seven months. **(Horsburgh *et al*., 2015)** There is normally a continuation phase of is four months for a majority of patients. All the drugs play a significant role in the initial regimen. In this study only pyrazinamide and ethambutol were investigated because they are reported as short-course regimens with high cure rates.

Pyrazinamide has strong sterilizing activity that can allow further shortening of the regimen from nine to six months while ethambutol assists in preventing the emergence of rifampicin resistance when primary isoniazid resistance is present. **(Fox *et al*., 1999)** However, EMB is not included when drug-susceptibility test results are known and the organisms are entirely at risk. It is also not recommended for children whose sharpness or clarity of vision cannot be monitored unless the risk of drug resistance is for children who have "adult-type" (cavity formation, upper lobe infiltration) or high tuberculosis infection. (**Zumla *et al*., 2015**) A schematic illustration of the sites of action of these principle anti-TB agents are shown below in **Figure 2.5** and are elucidated in each tuberculosis drug.

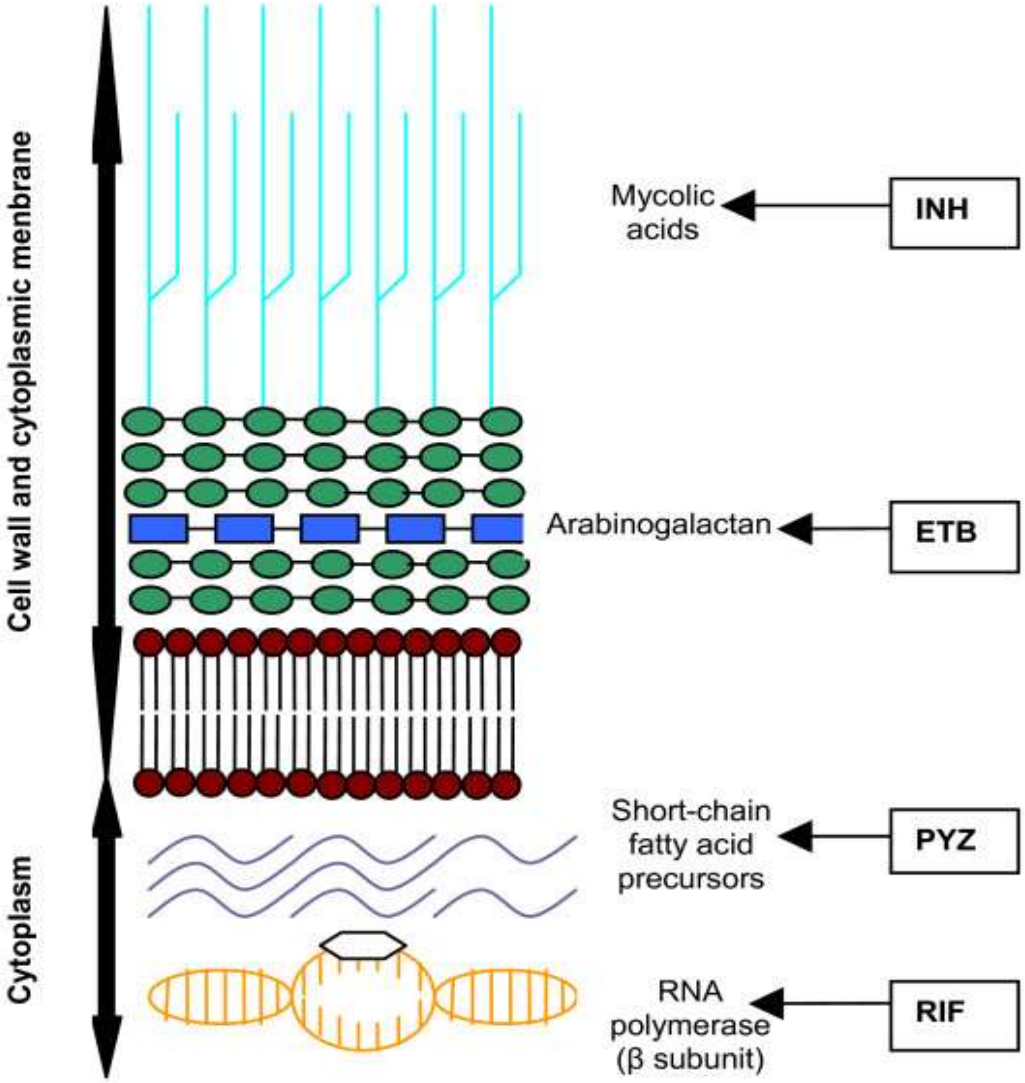

Figure 2.5: Sites of action of the principal anti-TB drugs. (Du Toit *et al*., 2006)

2.7.1 Ethambutol (EMB)

Ethambutol (EMB) is one of the most important first-line drugs against TB and it was discovered in 1961. This drug is believed to inhibit numerous metabolites crucial for the survival of the bacteria. EMB predominantly inhibits the synthesis of arabinogalacton; a significant component of the mycobacterial cell wall. **(Sarka *et al*., 2016)** The most common side effects observed with EMB are breathlessness, loss of appetite, blurred vision, stomach pain, nausea, dizziness, itching, headache, swelling of the face, lips or eyes, colour blindness, vomiting, numbness or tingling in the fingers or toes and rash. Patients taking this particular drug should have their color vision and visual acuity checked at least once a month. **(Jnawali and Ryoo., 2013).** EMB has a very simple structure as shown in **Figure 2.6** that is effective against *Mycobacterium tuberculosis* and some other mycobacteria.

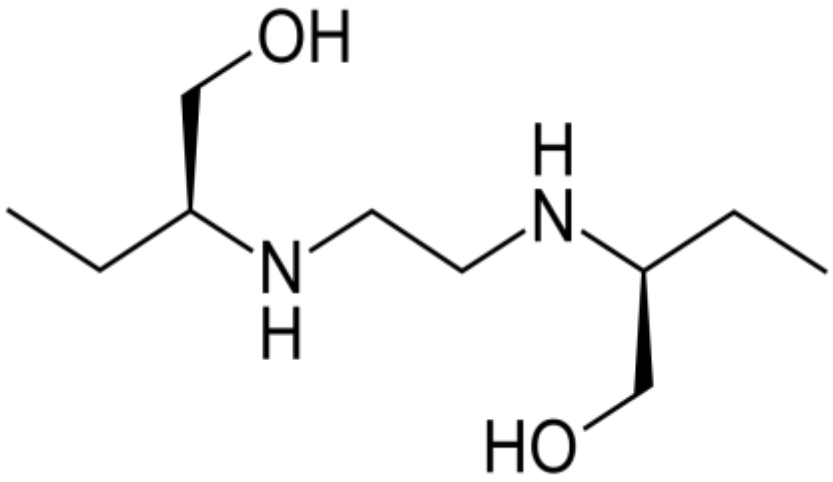

Figure 2.6: Structure of ethambutol.

(*https://en.wikipedia.org/wiki/Ethambutol*)

2.7.1.1 Mechanism of action

Ethambutol mechanism action occurs when it interferes with the biosynthesis of arabinogalactan, which is a leading polysaccharide on the mycobacterial cell wall. Normally EMB inhibits the arabinosyltransferase enzyme encoded by the embB gene that mediates the polymerization of arabinose into arabinogalactan. In vitro resistance to ethambutol grows gradually and is possibly because of mutations in the embB gene. **(Arbex *et al*., 2010)**

2.7.1.2 Mechanism of resistance to EMB

A well-known mechanism of resistance to EMB is related to mutations in the gene *embB* with mutations at position *embB*306 as the most predominant in most studies. Certain studies on the other hand, have also found mutations in *embB*306 in EMB susceptible isolates. **(Ahmad *et al*., 2007)** Besides, a study with a great number of *Mycobacterium tuberculosis* isolates brings into being that mutations in *embB*306 were not essentially related with resistance to EMB, but have a predisposition to develop resistance to cumulative number of drugs and to be transmitted. In detail, allelic altercation studies have revealed that individual mutations causing certain amino acid substitutions produced EMB resistance, whereas other amino acid such as Met306 of EmbB substitutions had slight or no effect on EMB resistance. **(El-Nima., 2011)**

Numerous researchers have stated that mutations in the decaprenylphosphoryl-B-D-arabinose (DPA) biosynthetic and utilization pathway genes, Rv3806c and Rv3792, together with mutations in *embB* and *embC* accumulate, providing growth to a range of EMB depending on mutation number type. **(Safi *et al*., 2013)** These outcomes could have an effect on the precise detection of EMB resistance by recent molecular methods such as; faster and simpler nucleic

acid amplification test (NAAT) and whole-genome sequencing (WGS). Mutations in *embB*306 then, cause variable degrees of EMB resistance however they are not sufficient to cause high-level resistance to EMB. There about 30 % EMB resistant strains remaining which do not present any mutation in *emb*B to stress the necessity to classify other possible mechanisms of drug resistance. **(Palomino and Martin., 2014)**

2.7.1.3 Pharmacokinetics

Pharmacokinetics for EMB is well immersed from the gastrointestinal tract and well spread in fluids and body tissues. **(Zhu *et al*., 2004)** Subsequently after oral administration of EMB, 75-80 % of the dose is absorbed and the peak drug serum levels are between 2 to 4 hours. Plasma concentrations of 2-5 μg/mL are produced by a single 25 mg/kg dose. The serum half-life of EMB is within the range of 3 to 4 hours and it can be extended to 10 hours in patients with severe kidney failure while part of the drug (20 -30 %) binds to plasma proteins. **(Safi *et al*., 2013)** This drug is usually circulated throughout the body with the immunity of the cerebrospinal fluid (CSF) in patients without meningitis. EMB is metabolized in the liver and the principal mechanism is oxidation to form an intermediate aldehyde, followed by conversion into dicarboxylic acid. Least of the drug approximately 20 % is excreted in faeces and most of the drug (50 - 80 %) is excreted in urine (and 8 -15 % is excreted as metabolites). **(Arbex *et al*., 2010)**

2.7.2 Pyrazinamide (PZA)

Pyrazinamide (PZA) is a significant bactericidal agent which was discovered in 1963 particularly for the slow growing strains of *Mycobacterium tuberculosis*. (**Kolyva and Karakousis., 2012)** PZA is a pro-drug converted by the bacterial enzyme pyrazinamidase to pyrazinoic acid (POA); thus it is normally used as an efficient and potent sterilizing agent. **(Yuan and Sampson., 2018)** PZA is active in acidic pH and POA inhibits fatty acid synthesis in the bacteria. Amongst all first-line of drug against tuberculosis, PZA is accountable for causing dose dependent hepatotoxicity. **(Sarkat *et al*., 2016)**

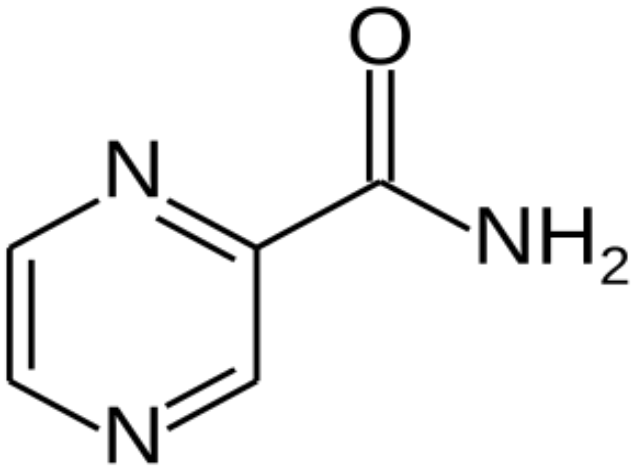

Figure 2.7: Structure of Pyrazinamide.

(*https://en.wikipedia.org/wiki/Pyrazinamide*)

2.7.2.1 Mechanism of action

Pyrazinamide is a pro-drug which requires conversion to be in its active form (pyrazinoic acid) using bacterial enzymes (pyrazinamidase / nicotinamidase). Up till now the mechanism

of action of PZA still needs to be fully understood. **(Wabale and Joshi., 2016)** It is supposed that PZA goes into the bacillus submissively it gets converted into pyrazinoic acid by pyrazinamidase and reaches high concentrations in the bacterial cytoplasm because of an ineffective efflux system. The increase of pyrazinoic acid decreases the intracellular pH to levels that cause the inactivation of enzymes such as fatty acid synthase I, that normally plays an essential role in synthesizing fatty acids and accordingly the impairment of mycolic acid biosynthesis. **(Arbex *et al*., 2010)**

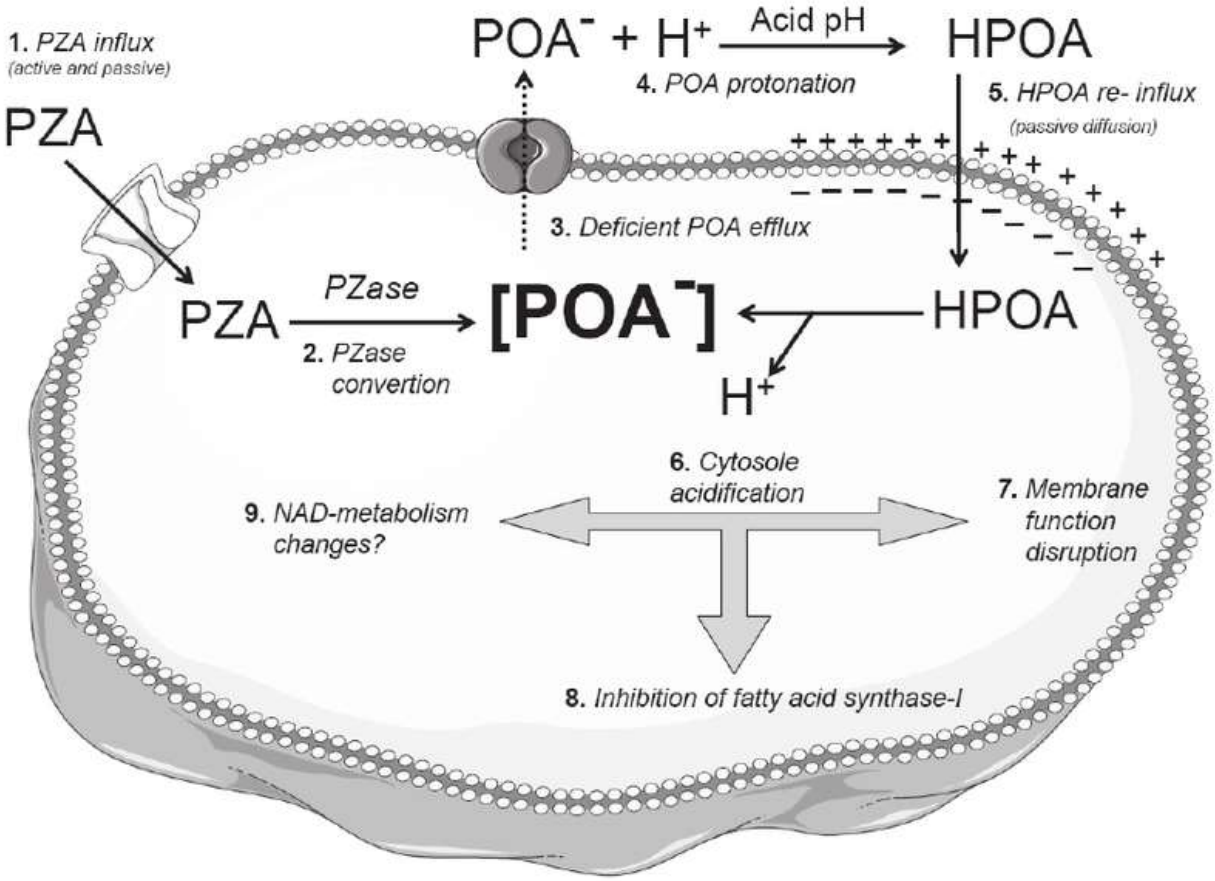

Figure 2.8: Mechanism of action of pyrazinamide. (Momekov *et al*., 2014)

2.7.2.2 Mechanism of Resistance to PZA

Resistance to PZA is caused by mutations in the *pnc*A gene that encodes the pyrazinamidase / nicotinamidase enzymes and stops PZA from being converted into its active form. **(Wabale and Joshi., 2016)** The comparatively high degree of variety in *pnc*A mutations in the midst of pyrazinamide-resistant clinical isolates have conveyed complication in development of molecular assays for the fast and cost-effective detection of pyrazinamide resistance. However, a slight percentage of isolates with high-level pyrazinamide resistance have no mutations in *pnc*A or its promoter proposing different mechanisms of resistance such as altered *pnc*A regulation, enhanced efflux or deficient uptake. **(Jnawali and Ryoo., 2013)**

2.7.2.3 Pharmacokinetics

Subsequent to oral administration full plasma concentrations of PZA are reached after duration of 1 to 2 hours. The oral bioavailability of PZA is nearly complete when increasing urinary excretion of PZA and its central metabolites after administration of a 27 mg/kg single oral dose to healthy matters is roughly 73 %. **(Bekker et al., 2016)** Also, food may interrupt the oral absorption of PZA but then again it does not have a substantial effect on the level of absorption. The plasma protein binding of PZA is small; values of 10 to 40 % have been reported. Its volume of distribution (V/F) is about 0.57 l/kg. **(Verbeeck *et al*., 2016)**

PZA is mostly removed by metabolism where only 3.2 % of an oral administered dose is recovered in unprocessed forms in the urine. The crucial metabolites recovered in urine are 5-OH-pyrazinoic acid (16.5 %), 5-OH-pyrazinamide (19.7 %) and 2-pyrazinoic acid (33.2 %). **(Bekker et al., 2016)** Succeeding oral administration of PZA to healthy matters, systemic exposure (area under the drug plasma concentration-time curve) to pyrazinoic acid is just

about 20 % of that of PZA. PZA, as similar to pyrazinoic acid, has a plasma half-life of around 10 hours. **(Drew., 2009)**

2.8 Biosensors for the detection of Tuberculosis treatment drugs

The developing world is facing a challenge of inappropriate dosing of treatment and inadequate treatment administration of first line drugs causing a problem in treatment and the difficulty of the disease is further increased by the emergence of multiple drug resistant (MDR) which resist multiple antibiotics. This is clearly due to different individuals who have different drug metabolic profiles which affect the manner in which medication is bio-transformed**. (Lange *et al.*, 2014)** Hence, it is important to carry out this study in order to develop a technique that will help in the identification of poor, intermediate and rapid metabolizers based on the amount of drug quantified after drug administration. In this way health care practitioners will have to individualize treatment based on each patient's metabolic profile. **(Samer *et al.*, 2016)** Similar studies have been done by **Mitchison and Davies., 2008** and **Ngece., 2011** over the last couple of years to develop effective drugs detective device that can be performed in rural areas and that are robust and cheap. However, they are still lacking on the market. The objective of this study is to evaluate currently available biosensing techniques that are either under development or already in use for detection of TB drugs. **(Srivastava *et al.*, 2016)**

Biosensors are analytical devices that transduce biochemical interactions/reactions of isolated enzymes, whole cells, tissues, antibodies, organelle, receptor proteins or nucleic acids with specific chemical compounds into an electrical , thermal or optical signal which can be

simply quantised and measured. **(Mehrotra., 2016)** Biosensors have greater advantages over conventional diagnostic techniques due to their:

- Quick response: response time is normally a few minutes for most biosensors allowing quick and better control over the measurement.
- Technical advantage: in biosensors often a high level of device and capture/detection integration is achieved allowing single step detection.
- Ease to use: many of the designed biosensors are personalized with user-friendly interfaces connecting them to advanced instrumentation. **(Srivastava *et al*., 2016)**

In this study an amperometric biosensor was developed and was used for detection of tuberculosis treatment drugs. Further details are discussed in detail in the section below.

2.8.1 Amperometric biosensors

Amperometric biosensors are driven by an external constant potential, through which an electrochemical redox reaction occur, and the resultant current is measured. **(Apetrei and Ghasemi-Varnamkhasti 2013)** This biosensor type can work in two or three electrode configurations but the disadvantage of using the two-electrode configuration is that it limits control of the potential on the working electrode surface with higher currents due to this a linear range may possibly be shortened. Thus the only plausible solution to this problem is to use a third auxiliary electrode is employed. The working electrode of the amperometric biosensor is normally either a screen-printed layer or a noble metal covered by the biorecognition component. **(Wang *et al*., 2018)** The signal of amperometric biosensors is produced through the electron exchange that occurs between the electrode and the biological system. The main advantages of using these biosensors are; their good sensitivity, excellent

specificity for the biological component which can be compromised by the partial selectivity of the electrode and it respond rapid. **(Zhang *et al*., 2014)**

2.9 References

Abbasi, E., Aval, S.F., Akbarzadeh, A., Milani, M., Nasrabadi, H.T., Joo, S.W., Hanifehpour, Y., Nejati-Koshki, K. and Pashaei-Asl, R., 2014. Dendrimers: synthesis, applications, and properties. Nanoscale Research Letters, 9(1), p.247.

Adil, S.F., Alabbad, S., Kuniyil, M., Khan, M., Alwarthan, A., Mohri, N., Tremel, W., Tahir, M.N., Siddiqui, M.R.H., 2015a. Vanadia supported on nickel manganese oxide nanocatalysts for the catalytic oxidation of aromatic alcohols. Nanoscale Res. Lett. 10, 52

Agarwal, P.K., 2006. Enzymes: An integrated view of structure, dynamics and function. Microbial cell factories, 5(1), p.2.

Ajayi, R.F., Nxusani, E., Douman, S.F., Jonnas, A., Baker, P.G.L. and Iwuoha, E.I., 2016. An Amperometric Cytochrome P450-2D6 Biosensor System for the Detection of the Selective Serotonin Reuptake Inhibitors (SSRIs) Paroxetine and Fluvoxamine. In Journal of Nano Research (Vol. 44, pp. 208-228). Trans Tech Publications.

Ahmed, S., Ahmad, M., Swami, B.L. and Ikram, S., 2016. Green synthesis of silver nanoparticles using Azadirachta indica aqueous leaf extract. Journal of Radiation Research and Applied Sciences, 9(1), pp.1-7.

Ahmad, S., Jaber, A.A. and Mokaddas, E., 2007. Frequency of embB codon 306 mutations in ethambutol-susceptible and-resistant clinical Mycobacterium tuberculosis isolates in Kuwait. Tuberculosis, 87(2), pp.123-129.

Akhtar, M.S., Panwar, J., Yun, Y.-S., 2013. Biogenic synthesis of metallic nanoparticles by plant extracts. ACS Sustain. Chem. Eng. 1, 591–602

Al-Marri, A.H., Khan, M., Shaik, M.R., Mohri, N., Adil, S.F., Kuniyil, M., Alkhathlan, H.Z., Al-Warthan, A., Tremel, W., Tahir, M.N. and Khan, M., 2016. Green synthesis of Pd@ graphene nanocomposite: Catalyst for the selective oxidation of alcohols. Arabian journal of chemistry, 9(6), pp.835-845.

Anastas, P.T. and Kirchhoff, M.M., 2002. Origins, current status, and future challenges of green chemistry. Accounts of chemical research, 35(9), pp.686-694.

Arbex, M.A., Varella, M.D.C.L., Siqueira, H.R.D. and Mello, F.A.F.D., 2010. Antituberculosis drugs: drug interactions, adverse effects, and use in special situations-part 1: first-line drugs. *Jornal Brasileiro de Pneumologia*, *36*(5), pp.626-640.

Bai, H., Li, C. and Shi, G., 2011. Functional composite materials based on chemically converted graphene. *Advanced Materials*, *23*(9), pp.1089-1115.

Banu, A. and Rathod, V., 2013. Biosynthesis of monodispersed silver nanoparticles and their activity against Mycobacterium tuberculosis. International Journal of Biomedical Nanoscience and Nanotechnology, 3(1-2), pp.211-220.

Bekker, A., Schaaf, H.S., Draper, H.R., van der Laan, L., Murray, S., Wiesner, L., Donald, P.R., McIlleron, H.M. and Hesseling, A.C., 2016. The pharmacokinetics of rifampicin, isoniazid, pyrazinamide and ethambutol in infants dosed at revised WHO-recommended treatment guidelines. Antimicrobial agents and chemotherapy, pp.AAC-02600.

Borm, P.J., Robbins, D., Haubold, S., Kuhlbusch, T., Fissan, H., Donaldson, K., Schins, R., Stone, V., Kreyling, W., Lademann, J. and Krutmann, J., 2006. The potential risks of nanomaterials: a review carried out for ECETOC. Particle and fibre toxicology, 3(1), p.11.

Callender, R. and Dyer, R.B., 2014. The dynamical nature of enzymatic catalysis. Accounts of chemical research, 48(2), pp.407-413.

Chamoli, P., Das, M.K. and Kar, K.K., 2017. Green synthesis of silver-graphene nanocomposite-based transparent conducting film. Physica E: Low-dimensional Systems and Nanostructures, 90, pp.76-84.

Chen, D., Feng, H. and Li, J., 2012. Graphene oxide: preparation, functionalization, and electrochemical applications. Chemical reviews, 112(11), pp.6027-6053.

Cui, D., Mi, L., Xu, X., Lu, J., Qian, J. and Liu, S., 2014. Nanocomposites of graphene and cytochrome P450 2D6 isozyme for electrochemical-driven tramadol metabolism. Langmuir, 30(39), pp.11833-11840.

Cruz-Knight, W. and Blake-Gumbs, L., 2013. Tuberculosis: an overview. Primary Care: Clinics in Office Practice, 40(3), pp.743-756.

Cuesta, S.M., Rahman, S.A., Furnham, N. and Thornton, J.M., 2015. The classification and evolution of enzyme function. Biophysical journal, 109(6), pp.1082-1086.

Dinesh N., Sharma S. and Balganesh M. Involvement of Efflux Pumps in the Resistance to Peptidoglycan Synthesis Inhibitors in Mycobacterium tuberculosis. Antimicrobial Agents and Chemotherapy. 2013, 57(4) pg 1941-1943

Doble, M., Kruthiventi, A.K. and Gaikar, V.G., 2004. Biotransformations and bioprocesses (p. 371). New York, NY, USA: Marcel Dekker.

dos Santos, M.C., Maynart, M.C., Aveiro, L.R., da Paz, E.C. and dos Santos Pinheiro, V., 2014. Carbon-Based Materials: Recent Advances, Challenges, and Perspectives.

Drew, R.H., Pyrazinamide: An overview.[homepage on the Internet]. 2009 [cited 2011 Oct 5]. Available from: Duke University Medical Center, Campbell University College of Pharmacy and Health Sciences Web site: http://www. uptodate. com/contents/pyrazinamide-an-ov erview.

Du Toit L.C., Pillay V. and Danckwerts M.P., Tuberculosis chemotherapy: current drug delivery approaches, Respiratory Research, 2006, 7 (118) pg 1-18.

El Harrad, L., Bourais, I., Mohammadi, H. and Amine, A., 2018. Recent advances in electrochemical biosensors based on enzyme inhibition for clinical and pharmaceutical applications. Sensors, 18(1), p.164.

El-Nima, E.A.I., 2011. Nuha Yousif Ibrahim Mohamed (Doctoral dissertation, University of Khartoum).

El-Rafie, M.H., Shaheen, T.I., Mohamed, A.A. and Hebeish, A., 2012. Bio-synthesis and applications of silver nanoparticles onto cotton fabrics. Carbohydrate polymers, 90(2), pp.915-920.

Faried, M., Shameli, K., Miyake, M., Zakaria, Z., Hara, H., Khairudin, N.A. and Etemadi, M., 2016. Ultrasound-assisted in the synthesis of silver nanoparticles using sodium alginate mediated by green method. Digest Journal of Nanomaterials and Biostructures, 11(2), pp.547-52.

Fox, W., Ellard, G.A. and Mitchison, D.A., 1999. Studies on the treatment of tuberculosis undertaken by the British Medical Research Council tuberculosis units, 1946–1986, with relevant subsequent publications. The International Journal of Tuberculosis and Lung Disease, 3(10), pp.S231-S279.

Gao, S., Li, Z. and Zhang, H., 2010. Bioinspired green synthesis of nanomaterials and their applications. Current Nanoscience, 6(5), pp.452-468.

Gilbertson, L.M., Zimmerman, J.B., Plata, D.L., Hutchison, J.E. and Anastas, P.T., 2015. Designing nanomaterials to maximize performance and minimize undesirable implications guided by the Principles of Green Chemistry. Chemical Society Reviews, 44(16), pp.5758-5777.

Grewal, A.S., Kumar, K., Redhu, S. and Bhardwaj, S., International Research Journal of Pharmaceutical and Applied Sciences (IRJPAS). chemistry, 6, p.8.

Grodowska, K. and Parczewski, A., 2010. Organic solvents in the pharmaceutical industry. Acta Pol Pharm, 67(1), pp.3-12.

Haghparasti, Z. and Shahri, M.M., 2018. Green synthesis of water-soluble nontoxic inorganic polymer nanocomposites containing silver nanoparticles using white tea extract and assessment of their in vitro antioxidant and cytotoxicity activities. Materials Science and Engineering: C, 87, pp.139-148.

Hebbalalu, D., Lalley, J., Nadagouda, M.N., Varma, R.S., 2013. Greener techniques for the synthesis of silver nanoparticles using plant extracts, enzymes, bacteria, biodegradable polymers, and microwaves. ACS Sustain. Chem. Eng. 1, 703–712.

Hernaiz, M.J., Alcantara, A.R., Garcia, J.I. and Sinisterra, J.V., 2010. Applied biotransformations in green solvents. Chemistry-A European Journal, 16(31), pp.9422-9437.

Horsburgh Jr, C.R., Barry III, C.E. and Lange, C., 2015. Treatment of tuberculosis. New England Journal of Medicine, 373(22), pp.2149-2160.

Ingelman-Sundberg, M., 2005. Genetic polymorphisms of cytochrome P450 2D6 (CYP2D6): clinical consequences, evolutionary aspects and functional diversity. The pharmacogenomics journal, 5(1), p.6.

Iravani, S., Korbekandi, H., Mirmohammadi, S.V. and Zolfaghari, B., 2014. Synthesis of silver nanoparticles: chemical, physical and biological methods. Research in pharmaceutical sciences, 9(6), p.385.

Jin, S., Guo, C., Lu, Y., Zhang, R., Wang, Z. and Jin, M., 2017. Comparison of microwave and conventional heating methods in carbonization of polyacrylonitrile-based stabilized fibers at different temperature measured by an in-situ process temperature control ring. Polymer Degradation and Stability, 140, pp.32-41.

Jnawali, H.N. and Ryoo, S., 2013. First–and Second–Line Drugs and Drug Resistance. In Tuberculosis-Current Issues in Diagnosis and Management. InTech.

Knechel, N.A., 2009. Tuberculosis: pathophysiology, clinical features, and diagnosis. Critical care nurse, 29(2), pp.34-43.

Kesrevani, R.K. and Sharma, A.K., 2016. Nanoarchitectured biomaterials: present status and future prospects in drug delivery. Nanoarchitectonics for Smart Delivery and Drug Targeting; Elsevier BV: Amsterdam, The Netherlands.

Khalil, M.M., Ismail, E.H., El-Baghdady, K.Z. and Mohamed, D., 2014. Green synthesis of silver nanoparticles using olive leaf extract and its antibacterial activity. Arabian Journal of Chemistry, 7(6), pp.1131-1139.

Khan, M., Khan, M., Kuniyil, M., Adil, S.F., Al-Warthan, A., Alkhathlan, H.Z., Tremel, W., Tahir, N.M., Siddiqui, M.R.H., 2014. Biogenic synthesis of palladium nanoparticles using Pulicaria glutinosa extract and their catalytic activity towards the Suzuki coupling reaction. Dalton Trans. 43, 9026–9031.

Kotakadi, V.S., Gaddam, S.A., Rao, Y.S., Prasad, T.N.V.K.V., Reddy, A.V. and Gopal, D.S., 2014. Biofabrication of silver nanoparticles using Andrographis paniculata. European journal of medicinal chemistry, 73, pp.135-140.

Krebs, H.A., 1970. The history of the tricarboxylic acid cycle. Perspectives in Biology and Medicine, 14(1), pp.154-172.

Lange, C., Abubakar, I., Alffenaar, J.W.C., Bothamley, G., Caminero, J.A., Carvalho, A.C.C., Chang, K.C., Codecasa, L., Correia, A., Crudu, V. and Davies, P., 2014. Management of patients with multidrug-resistant/extensively drug-resistant tuberculosis in Europe: a TBNET consensus statement. European Respiratory Journal, pp.erj01883-2013.

Lawn, S.D. and Churchyard, G., 2009. Epidemiology of HIV-associated tuberculosis running head: epidemiology of TB/HIV. Current Opinion in HIV and AIDS, 4(4), p.325.

Lee, S.Y., Jang, H., Lee, J.Y., Kwon, K.I., Oh, S.J. and Kim, S.K., 2014. Inhibition of cytochrome P450 by ethambutol in human liver microsomes. Toxicology letters, 229(1), pp.33-40.

Li, J., Zeng, X., Ren, T. and Van Der Heide, E., 2014. The preparation of graphene oxide and its derivatives and their application in bio-tribological systems. Lubricants, 2(3), pp.137-161.

Li, J., Kuang, D., Feng, Y., Zhang, F., Xu, Z., Liu, M. and Wang, D., 2013. Green synthesis of silver nanoparticles–graphene oxide nanocomposite and its application in electrochemical sensing oftryptophan. Biosensors and Bioelectronics, 42, pp.198-206.

Li, F., Jiang, X., Zhao, J. and Zhang, S., 2015. Graphene oxide: A promising nanomaterial for energy and environmental applications. Nano energy, 16, pp.488-515.

Majumder, A., Gupta, R. and Jain, A., 2013. Microwave-assisted synthesis of nitrogen-containing heterocycles. Green Chemistry Letters and Reviews, 6(2), pp.151-182.

Makarov, V.V., Love, A.J., Sinitsyna, O.V., Makarova, S.S., Yaminsky, I.V., Taliansky, M.E. and Kalinina, N.O., 2014. "Green" nanotechnologies: synthesis of metal nanoparticles using plants. Acta Naturae (англоязычная версия), 6(1 (20)).

Milanowski, P., Carter, T.J. and Weber, G.F., 2013. Enzyme catalysis and the outcome of biochemical reactions. Journal of Proteomics Bioinform, 6, pp.132-141.

Moghimi, S.M., Hunter, A.C. and Murray, J.C., 2001. Long-circulating and target-specific nanoparticles: theory to practice. Pharmacological reviews, 53(2), pp.283-318.

Ngece, R.F., 2011. Nanoparticulate of silver-modified poly (8-anilino-1-naphthalene sulphonic acid) nanobiosensor systems for the determination of Tuberculosis treatment drugs (Doctoral dissertation, University of the Western Cape).

Mody, V.V., Siwale, R., Singh, A. and Mody, H.R., 2010. Introduction to metallic nanoparticles. Journal of Pharmacy and Bioallied Sciences, 2(4), p.282.

Momekov, G., Ferdinandov, D., Voynikov, Y., Stavrakov, G. and Peykov, P., 2014. Pyrazinamide− Pharmaceutical, biochemical and pharmacological properties and reappraisal of its role in the chemotherapy of tuberculosis. Pharmacia, 61(1), pp.38-67.

Monticelli, O., Bocchini, S., Frache, A., Cozza, E.S., Cavalleri, O. and Prati, L., 2012. Simple method for the preparation of composites based on PA6 and partially exfoliated graphite. Journal of Nanomaterials, 2012, p.25.

Moonan, P.K., Quitugua, T.N., Pogoda, J.M., Woo, G., Drewyer, G., Sahbazian, B., Dunbar, D., Jost, K.C., Wallace, C. and Weis, S.E., 2011. Does directly observed therapy (DOT) reduce drug resistant tuberculosis? BMC public health, 11(1), p.19.

Movlaee, K., Ganjali, M.R., Norouzi, P. and Neri, G., 2017. Iron-based nanomaterials/graphene composites for advanced electrochemical sensors. Nanomaterials, 7(12), p.406.

Müller, B., Borrell, S., Rose, G. and Gagneux, S., 2013. The heterogeneous evolution of multidrug-resistant Mycobacterium tuberculosis. Trends in Genetics, 29(3), pp.160-169.

Nagy, G. and Oostenbrink, C., 2012. Rationalization of stereospecific binding of propranolol to cytochrome P450 2D6 by free energy calculations. European Biophysics Journal, 41(12), pp.1065-1076.

Nasir, S., Hussein, M.Z., Zainal, Z. and Yusof, N.A., 2018. Carbon-Based Nanomaterials/Allotropes: A Glimpse of Their Synthesis, Properties and Some Applications. Materials, 11(2), p.295.

Nguyen, L., 2016. Antibiotic resistance mechanisms in M. tuberculosis: an update. Archives of toxicology, 90(7), pp.1585-1604.

Nguyen, N.H., Padil, V.V.T., Slaveykova, V.I., Černík, M. and Ševců, A., 2018. Green Synthesis of Metal and Metal Oxide Nanoparticles and Their Effect on the Unicellular Alga Chlamydomonas reinhardtii. Nanoscale research letters, 13(1), p.159.

Owen, R.P., Sangkuhl, K., Klein, T.E. and Altman, R.B., 2009. Cytochrome P450 2D6. Pharmacogenetics and genomics, 19(7), p.559.

Palomino, J.C. and Martin, A., 2014. Drug resistance mechanisms in Mycobacterium tuberculosis. Antibiotics, 3(3), pp.317-340.

Parveen, K., Banse, V. and Ledwani, L., 2016, April. Green synthesis of nanoparticles: Their advantages and disadvantages. In AIP Conference Proceedings (Vol. 1724, No. 1, p. 020048). AIP Publishing.

Parveen, M., Ahmad, F., Malla, A.M. and Azaz, S., 2016. Microwave-assisted green synthesis of silver nanoparticles from Fraxinus excelsior leaf extract and its antioxidant assay. Applied Nanoscience, 6(2), pp.267-276.

Patil, A.G., Bafna, H.R., More, M.P., Deshmukh, P.K. and Patil, P.O., 2017. Green Synthesis of Graphene Based Silver Nanocomposite for Enhanced Antibacterial Activity against Dental Pathogens.

Patra, J.K. and Baek, K.H., 2014. Green nanobiotechnology: factors affecting synthesis and characterization techniques. Journal of Nanomaterials, 2014, p.219.

Paulchamy, B., Arthi, G. and Lignesh, B.D., 2015. A simple approach to stepwise synthesis of graphene oxide nanomaterial. Journal of Nanomedicine & Nanotechnology, 6(1), p.1.

Płotka-Wasylka, J., Szczepańska, N., de la Guardia, M. and Namieśnik, J., 2016. Modern trends in solid phase extraction: new sorbent media. TrAC Trends in Analytical Chemistry, 77, pp.23-43.

Popov, V., Hinkov, I., Diankov, S., Karsheva, M. and Handzhiyski, Y., 2015. Ultrasound-assisted green synthesis of silver nanoparticles and their incorporation in antibacterial cellulose packaging. Green Processing and Synthesis, 4(2), pp.125-131.

Quyen, T.T.B., Minh, T.A., Thuy, N.T.P. and Mai, T.T.X., A Green Approach Using River-Leaf Creeper Extract For Synthesis And Characterization Of Chitosan/Ag Nanocomposites And Study For Their Antibacterial Activity.

Rattan, A., Kalia, A. and Ahmad, N., 1998. Multidrug-resistant Mycobacterium tuberculosis: molecular perspectives. Emerging infectious diseases, 4(2), p.195.

Rao, Y.S., Kotakadi, V.S., Prasad, T.N.V.K.V., Reddy, A.V. and Gopal, D.S., 2013. Green synthesis and spectral characterization of silver nanoparticles from Lakshmi tulasi (Ocimum sanctum) leaf extract. Spectrochimica Acta Part A: Molecular and Biomolecular Spectroscopy, 103, pp.156-159.

Rowland, P., Blaney, F.E., Smyth, M.G., Jones, J.J., Leydon, V.R., Oxbrow, A.K., Lewis, C.J., Tennant, M.G., Modi, S., Eggleston, D.S. and Chenery, R.J., 2006. Crystal structure of human cytochrome P450 2D6. Journal of Biological Chemistry, 281(11), pp.7614-7622.

Safi, H., Lingaraju, S., Amin, A., Kim, S., Jones, M., Holmes, M., McNeil, M., Peterson, S.N., Chatterjee, D., Fleischmann, R. and Alland, D., 2013. Evolution of high-level ethambutol-resistant tuberculosis through interacting mutations in decaprenylphosphoryl-β-D-arabinose biosynthetic and utilization pathway genes. Nature genetics, 45(10), p.1190.

Salata, O.V., 2004. Applications of nanoparticles in biology and medicine. Journal of nanobiotechnology, 2(1), p.3.

Samer, C.F., Lorenzini, K.I., Rollason, V., Daali, Y. and Desmeules, J.A., 2013. Applications of CYP450 testing in the clinical setting. Molecular diagnosis & therapy, 17(3), pp.165-184.

Sathiyanarayanan, G., Dineshkumar, K. and Yang, Y.H., 2017. Microbial exopolysaccharide-mediated synthesis and stabilization of metal nanoparticles. Critical reviews in microbiology, 43(6), pp.731-752.

Sarkar, S., Ganguly, A. and Sunwoo, H.H., 2016. Current overview of anti-tuberculosis drugs: metabolism and toxicities. Mycobact Dis, 6(2), p.209.

Sedki, M., Mohamed, M.B., Fawzy, M., Abdelrehim, D.A., AbdelMottaleb, M.M., 2015. Phytosynthesis of silver–reduced graphene oxide (Ag–RGO) nanocomposite with an

enhanced antibacterial effect using Potamogeton pectinatus extract. RSC Adv. 5, 17358–17365.

Shangguan, L., Zhao, Y., Mi, L., Jiang, L. and Liu, S., 2016. Direct electrochemistry and electrocatalysis of cytochrome P450s immobilized on gold/graphene-based nanocomposites. *Journal of Electroanalytical Chemistry*, *772*, pp.46-51.

Singh, R., Nawale, L., Arkile, M., Wadhwani, S., Shedbalkar, U., Chopade, S., Sarkar, D. and Chopade, B.A., 2016. Phytogenic silver, gold, and bimetallic nanoparticles as novel antitubercular agents. International journal of nanomedicine, 11, p.1889.

Siqueira, J.R. and Oliveira, O.N., 2017. Carbon-Based Nanomaterials. In Nanostructures (pp. 233-249).

Smith, T., Wolff, K.A. and Nguyen, L., 2012. Molecular biology of drug resistance in Mycobacterium tuberculosis. In Pathogenesis of Mycobacterium tuberculosis and its Interaction with the Host Organism (pp. 53-80). Springer, Berlin, Heidelberg.

Srivastava, S.K., Van Rijn, C.J. and Jongsma, M.A., 2016. Biosensor-based detection of tuberculosis. RSC advances, 6(22), pp.17759-17771.

Suib, S.L. ed., 2013. New and future developments in catalysis: catalysis by nanoparticles. Newnes.

Symeonidis, A. and Marangos, M., 2012. Iron and microbial growth. In Insight and control of infectious disease in global scenario. IntechOpen.

Taheriniya, S. and Behboodi, Z., 2016. COMPARING GREEN CHEMICAL METHODS AND CHEMICAL METHODS FOR THE SYNTHESIS OF TITANIUM DIOXIDE NANOPARTICLES. International Journal of Pharmaceutical Sciences and Research, 7(12), pp.4927-4932.

Veitía, M.S.I. and Ferroud, C., 2015. New activation methods used in green chemistry for the synthesis of high added value molecules. International Journal of Energy and Environmental Engineering, 6(1), pp.37-46.

Verbeeck, R.K., Günther, G., Kibuule, D., Hunter, C. and Rennie, T.W., 2016. Optimizing treatment outcome of first-line anti-tuberculosis drugs: the role of therapeutic drug monitoring. European journal of clinical pharmacology, 72(8), pp.905-916.

Wabale, V.R. and Joshi, A.A., 2016. Pyrazinamide Drug Resistance in Mycobacterium Tuberculosis: A Minireview. J Bacteriol Mycol Open Access, 3(2), p.00054.

Yuan, T. and Sampson, N.S., 2018. Hit generation in TB drug discovery: from genome to granuloma. Chemical reviews, 118(4), pp.1887-1916.

Zaaba, N.I., Foo, K.L., Hashim, U., Tan, S.J., Liu, W.W. and Voon, C.H., 2017. Synthesis of graphene oxide using modified hummers method: solvent influence. Procedia engineering, 184, pp.469-477.

Zhang, L.,Li,Y.,Zhou,H.,Li,L.,Wang,Y.,Zhang,Y., 2012. Journalof Pharmaceutical and Biomedical Analysis66, 356–358.

Zhang, M., Liao, C., Mak, C.H., You, P., Mak, C.L. and Yan, F., 2015. Highly sensitive glucose sensors based on enzyme-modified whole-graphene solution-gated transistors. Scientific reports, 5, p.8311.

Zhu, M., Burman, W.J., Starke, J.R., Stambaugh, J.J., Steiner, P., Bulpitt, A.E., Ashkin, D., Auclair, B., Berning, S.E., Jelliffe, R.W. and Jaresko, G.S., 2004. Pharmacokinetics of ethambutol in children and adults with tuberculosis. The International Journal of Tuberculosis and Lung Disease, 8(11), pp.1360-1367.

Zumla, A., Chakaya, J., Centis, R., D'Ambrosio, L., Mwaba, P., Bates, M., Kapata, N., Nyirenda, T., Chanda, D., Mfinanga, S. and Hoelscher, M., 2015. Tuberculosis treatment and management—an update on treatment regimens, trials, new drugs, and adjunct therapies. The Lancet Respiratory Medicine, 3(3), pp.220-234.

CHAPTER 3

Experimental methods

Summary

This chapter gives detailed experimental procedures and instrumentation involved in this study. Drawn here are the methods involved in the microwave-assisted green synthesis and conventional green synthesis of silver and zinc oxide nanoparticles; chemical synthesized graphene oxide and graphene oxide/silver or zinc oxide nanocomposites, their characterization and their application in this study. Also included in this section is immobilization procedure used to attach the enzyme for the development of biosensor. Lastly, described here are the procedures used towards the detection of Tuberculosis treatment drugs by the biosensors. Techniques employed in this study were; Cyclic voltammetry (CV), Ultraviolet Visible Spectroscopy (UV-vis),High-Resolution Transmission Electron Microscopy (HRTEM), Atomic Force Microscopy (AFM), High-Resolution Scanning Electron Microscopy (HRSEM), Fourier Transform Infrared Spectroscopy (FTIR), Energy Dispersive X-Ray (EDX), Raman spectroscopy, X-Ray diffraction (XRD), Photoluminescence Spectroscopy (PL) and Small Angle X-ray Scattering (SAXS)

3.1 Reagents

Graphite powder, sulfuric acid 98 % (H_2SO_4), potassium permanganate, hydrogen peroxide 5 % (H_2O_2) and hydrochloric acid 5 % (HCl) were all purchased from Sigma-Aldrich and used for the synthesis of graphene oxide. Silver nanoparticles were achieved using silver nitrate ($AgNO_3$) which was purchased from Sigma-Aldrich in South Africa while apples and tomatoes were purchased from Spar supermarket in Bellville, South Africa. Additionally, during the preparation of the silver nanoparticles/graphene oxide nanocomposites; ammonia 99.98 % and ethanol 99.5 % were used also purchased from Sigma-Aldrich in South Africa. The biosensor was prepared using Cytochrome P450-2D6 (CYP2D6) human expressed in liver which was purchased from Biocom Africa (Pty) Ltd based in South Africa. The CYP2D6 was stored at -4 ºC under anhydrous conditions when not in use. The reaction medium, pH 7.4, 0.1 M phosphate buffer was prepared from sodium phosphate monobasic dihydrate 99 % ($H_2NaO_4P.2H_2O$) and sodium phosphate dibasic dehydrate 99.5% ($HNa_2O_4P.2H_2O$) that were purchase from Sigma Aldrich in South Africa. The biosensor substrates, ethambutol [(2S, 2′S)-2, 2′-(ethane-1,2-diyldiimino) dibutan-1-ol) -$C_{10}H_{20}N_2O_2$ (Sigma-Aldrich) and pyrazinamide [pyrazinecarboxamide - $C_5H_5N_3O$] from Biocom Africa (Pty) Ltd) were used without further purification dissolved in deionized water. De-ionized ultra-purified water used throughout these experiments was prepared with a Milli-Q water purification system.

3.2 Sample preparation

3.2.1 Preparation of buffer solutions

A concentration of 0.1 M phosphate buffer solution (PBS) with a pH of 7.4 was prepared from sodium phosphate monobasic dihydrate ($H_2NaO_4P.2H_2O$) and sodium phosphate dibasic

dehydrate ($HNa_2O_4P.2H_2O$); it was used as the electrolytic solution throughout the course of this study unless where stated otherwise. The PBS electrolyte solution was kept refrigerated at -4 ºC when not in use. This study made use of PBS buffer pH 7.4 for all the experiments after a series of experiments to determine the influence of different pH (from 3 to 8) and suitability for the biosensor characterization and for dryg detection. **(Beynon and Easterby., 2004)**

3.3 Methodology

3.3.1 Synthesis of graphite oxide (GrO)

Graphite oxide was synthesized from graphite using the modified Hummers method **(Sun *et al*., 2011)**. In a round-bottom flask, 2 g of graphite and 50 ml H_2SO_4 were mixed and stirred at room temperature for 30 minutes followed by subsequent mixing in an ice water bath for 20 minutes. Once the temperature inside the flask reached 1 ºC, 7 g of $KMnO_4$ powder was added in 1 g increments over a 30 minutes period with constant stirring causing the flask contents to turn a dark green colour. The flask was removed from the ice bath and the resultant solution was allowed to reach room temperature and thereafter brought to 35 ºC by using a water bath. As specified in the modified method, the reaction was run for 2 hours at this temperature after which the contents of the flask appeared as a dark brown sludge. The first step of quenching the reaction was to return the flask to the ice bath. The flask contents were then diluted by the addition of 150 ml of deionized water that had been kept in the ice water bath for 20 minutes. To consume any unreacted permanganate ions, refrigerated H_2O_2 was added in 10 ml increments. After adding a total amount of 30 ml H_2O_2, the temperature of the contents rapidly rose to 90 ºC accompanied by intense bubbling (evolution of steam and oxygen gas) and a yellow change in colour of the suspension was observed. A further 15

ml H_2O_2 were added which caused the bubbling to subside. The flask was removed from the ice bath and allowed to stir at room temperature overnight and later centrifuged for 20 minutes. Three washes with HCl solution (10 % in water) was performed followed by washing once with distilled water. The resulting product was dried for 48 hours in a vacuum oven resulting in the formation of graphite oxide powder.

3.3.2 Synthesis of graphene oxide (GO)

About 0.5 g graphite oxide was measured and dispersed in 100 mL of distilled water by ultrasonication for 1 hour. The obtained suspension of graphite oxide was centrifuged at 4000 rpm for 10 minutes. The recovered supernatant was obtained as a suspension of graphene oxide which was then filtered and dried to obtain graphene oxide. **(Marcano *et al*., 2010)**

3.3.3 Preparation of apple and tomato extracts

A novel synthesis of silver and zinc oxide nanoparticles were performed separately using green methods with the aid of apple and tomato extracts. At first, apple and tomato extract was prepared by cutting 50 g of apple and 50 g of tomato into small pieces which were then washed thoroughly with distilled water. Afterwards, the small cut apples and tomatoes were combined in a 500 ml conical flask with 200 ml of deionized water followed by heating and stirring for 1 hour at 80 ºC using an oil bath. The resultant solution in the flask was allowed to reach room temperature then filtered to obtain the extract. The apple and tomato extract was later used as a reducing and stabilizing agents for the synthesis of AgNPs and/or ZnONPs.

3.3.4 Synthesis of silver nanoparticles (AgNPs)

3.3.4.1 Conventional green synthesis

A novel synthesis of AgNPs was carried out in a dark place where the conical flask was covered in foil to avoid light that would oxidise the silver ions. The synthesis was prepared by using 20 mL of the apple and tomato extract in 180 mL of 0.1 M aqueous $AgNO_3$ solution. The mixture was stirred and heated at 80 ºC for 1 hour and was allowed to reach room temperature. The obtained AgNPs were stored at room temperature.

3.3.4.2 Microwave-assisted green synthesis

A novel synthesis was carried in Microwave Reaction System using (PRO) multiple 100 mL reaction vessels and septa designed for high temperature or pressure reactions in the microwave. Approximately 0,020 g of silver nitrate ($AgNO_3$) was added to each of the four vessels that were prepared along with 2 mL of apple and tomato extract 4 mL of deionized water and a stirrer bar. The reagent containing vessel was reacted in the PRO microwave at a temperature 90 ºC for 15 minutes with maximum temperature of 100 ºC.

3.3.5 Green synthesis of silver nanoparticles/graphene oxide nanocomposite

In this study GO was synthesized from natural graphite powder using the modified Hummers method. **(Sun *et al*., 2011)** Then an innovative AgNPs/GO nanocomposite was prepared by reducing silver ions directly on GO with the apple and tomato extract as a reducing and stabilizing agent. Initially, 15 mg of GO powder was dispersed in 15 mL of deionized water by ultrasonication for 60 minutes to form a stable GO colloid and then 20 mL of the apple and tomato extract was dissolved in this solution under stirring. Secondly, 1.1 mL of

ammonia (which forms a stable system) was added slowly to a 0.2 g of silver nitrate solution until the $AgOH/Ag_2O$ precipitate dissolved. Subsequently, the $Ag(NH_3)_2OH$ solution was mixed with the GO and apple and tomato extract containing solution and stirred for 30 minutes. The mixture was then allowed to sit undisturbed at room temperature for 2 hours followed by centrifugation of the slurry-like product which was washed with distilled water repeatedly to remove any impurities. Finally, the obtained product was dried overnight in an oven a 60 ºC indicating the formation of the AgNPs/GO nanocomposite.

3.3.6 Synthesis of zinc oxide nanoparticles (ZnONPs)

3.3.6.1 Green synthesis

A novel synthesis of ZnONPs was also performed by using 20 mL of the apple and tomato extract in 180 mL of distilled water with 3.4 g of zinc nitrate $Zn(NO_3)_2$ solution. The mixture was stirred and heated at 80 ºC for 1 hour and upon completion; it was allowed to reach room temperature. The obtained ZnONPs were then stored at room temperature.

3.3.6.2 Microwave-assisted green synthesis

In order to synthesize ZnONPs; 0.030 g zinc nitrate $Zn(NO_3)_2$ solution was mixed with 2 mL of the extract, 4 mL of deionized water and a stirrer bar in multiple 100 mL reaction vessels and then the synthesis was performed in Microwave Reaction System using (PRO) under high temperature (90 ºC) or pressure reactions for 15 minutes at a maximum temperature of 100 ºC.

3.3.7 Green synthesis of zinc oxide nanoparticles/graphene oxide nanocomposite

The zinc oxide nanoparticles/graphene oxide (ZnONPs/GO) nanocomposite was prepared by reducing zinc oxide directly on GO using the apple and tomato extract as reducing and stabilizing agent. Firstly, 15 mg of GO powder was dispersed in 15 mL of deionized water and ultrasonicated for 60 minutes to form a stable GO colloid followed by the addition of 20 mL of apple and tomato extract while stirring. Thereafter, 1.1 mL of ammonia (which forms a stable system) was added slowly to 0.54 g of zinc nitrate until the resultant precipitate dissolved. The nitrate solution was then mixed with the GO and extracts containing solution and allowed to stir for 30 minutes. The mixture was allowed to sit undisturbed at room temperature for 2 hours followed by centrifugation of the resultant slurry-like product. The product was then was washed with distilled water repeatedly to remove any impurities. Finally, the obtained product was dried overnight in an oven at a temperature of 60 ºC and thereafter the ZnO/GO nanocomposite was obtained.

3.3.8 Preparation of the AgNPs/GO/GCE or ZnONPs/GO/GCE platforms

Glassy carbon electrodes (GCE) were mechanically polished with 0.3 and 0.05 mm alumina slurry and then sequentially sonicated in anhydrous ethanol and distilled water for 15 min. The cleaned GCEs were dried under nitrogen stream followed by modification. 5.0 mg of AgNPs/GO or ZnONPs/GO nanocomposites were added to 2.5 mL DMF solution and then sonicated separately in an ultrasound bath for 30 min to form a stable suspension. From each suspension an amount of 5.0 µL was taken and drops casted onto the GCE surface using a micropipette. Thereafter, the suspensions were thoroughly dried under infrared lamps followed by rinsing using distilled water and further drying in air before use. The developed electrodes will be denoted and referred to as GCE/AgNPs/GO or GCE/ZnONPs/GO. For

comparison, the GO/GCE electrode and was prepared using GO dispersion using the same procedure as described above.

3.4 Preparation of TB Drugs biosensors

3.4.1 Preparation of CYP2D6:

5 µL aliquots of CYP2D6 were taken from the original stock and each dissolved in 5 µL of pH 7.4, 0.1 M phosphate buffer. The modified CYP2D6 solutions were stored in the refrigerator at -70 ºC when not in use and were used within 3 days of preparation.

3.4.2 Fabrication of CYP2D6/GCE platforms:

5 µL of 10 µg/µL CYP2D6 enzymes was drop coated onto a freshly prepared glassy carbon (GC) electrode. The enzyme-modified electrode was then covered with a tight fitting lid for about 30 seconds to form a uniform layer after which the lid was removed and the resultant electrode GCE/CYP2D6 was stored and refrigerated at 4 ºC for 24 hours.

3.4.3 Fabrication of GCE/AgNPs/GO-CYP2D6 or GCE/ZnONPs/GO-CYP2D6 biosensors:

0.1 M phosphate buffer with pH 7.4 was used for the preparation of CYP2D6 enzyme stock solutions which were stored at -70 ºC when not in use. 5 µL of 10 µg/µL enzyme was drop coated onto a freshly prepared AgNPs/GO/GCE electrode. The enzyme-modified electrode was then covered with a tight fitting lid for about 30 seconds to form a uniform layer, after which the lid was removed and the resultant electrode GCE/AgNPs/GO-CYP2D6 or GCE/ZnONPs/GO-CYP2D6 was stored refrigerated at 4 ºC for 24 hours.

3.4.4 Preparation of TB drug stock solutions

3.4.4.1 Ethambutol:

2.8 g of ethambutol (ETH) powder drug was placed in a 100 ml volumetric flask which was filled up to the mark with deionized water and the prepared ETH was 0.01M. The solution was used as the stock ethambutol solution from which all the other working solutions were prepared using appropriate dilutions with 0.1 M phosphate buffer solution with pH 7.4.

3.4.4.2 Pyrazinamide:

0.2 µL of pyrazanamide (PZA) drug was placed in a 10 ml volumetric flask which was filled up to the mark with deionized water and the concentration of prepared PZA was 0.01M. The solution was used as the stock pyrazinamide solution from which all the other working solutions were prepared using appropriate dilutions with 0.1 M phosphate buffer solution with pH 7.4.

3.4.5 Application of AgNP or ZnONPs/GO/CYP2D6 modified GCE as Amperometric TB Drug biosensors:

The modified electrodes used in this study namely; AgNPs or ZnONPs/GO/GCE AgNPs or ZnONPs/GO/CYP2D6 were detected for the amperometric sensing of the TB drugs namely; ethambutol (EMB) and pyrazinamide (PZA). Additionally, cyclic voltammetry (CV) experiments were performed at potential window of -1 V to 1 V, potential step of 0.005 V and at the scan rate of 50 mV/s at different concentrations of each drugs. Steady state amperometric determination of the drugs was performed at an applied potential of -250 mV with stirring maintained at 500 rpm in buffer solution as the supporting electrolyte. The

background current was allowed to reach a steady value before aliquots of standard drug solutions were successively added into the supporting electrolyte while steady-state current values were recorded as the response.

3.5 Stability and Reproducibility

The stability and reproducibility of the AgNPs or ZnONPs/GO/CYP2D6/GCE biosensor was studied in pH 7.4, 0.1 M phosphate buffer solution for a period of two weeks and the modified electrodes were stored at 4 ºC when not in use. Ten succeeding measurements of 2μM ethambutol or 2 μM pyrazanamide was carried out independently for two weeks. **(Ngece., 2011)**

3.6 Characterization techniques

3.6.1 Spectroscopic techniques

Spectroscopy is the study of interaction of electromagnetic radiation with matter. Spectroscopic techniques can be based on phenomena of absorption, emission, scattering or fluorescence. These techniques are normally used for quantitative and qualitative analysis of sample/s. Quantitative analysis is performed to estimate the concentration of analyte in sample while the qualitative analysis is performed to establish the identity of sample. **(Bumbrah *et al*., 2016)** Spectroscopic techniques are very attractive in the field of science due to their simplicity of procedures, accuracy and common availability of the instrumentation. Also, these techniques of analysis are simpler and more economic. **(Rojas and Ojeda., 2009)**

3.6.1.1 Ultraviolet Visible Spectroscopy (UV-vis)

The purpose of ultraviolet-visible spectroscopy is to measure the wavelength dependent absorbance of light from various chemical systems. That is achieved by controlling the wavelength of emitted light, resulting to investigation of optical properties of a system. A value for the absorbance can be calculated, from each wavelength of light that is transmitted through a liquid sample which is related to the concentration of the optically active compound in solution. The formula that is related the discussion above; the chemical concentration to optical absorbance is known as the Beer-Lambert law:

$$\mathbf{A(\lambda) = \log^{10}(I_0 I) = \varepsilon.c.l} \qquad \mathbf{(3.1)}$$

Where l is the path length of the light through the sample given in centimetres, c is the concentration of the solution in moles per litre, ε is the molar extinction coefficient in L mol^{-1} cm^{-1}, I_0 and I are the intensities of the light passing through the sample and lastly A is the absorbance value at a given wavelength (λ). By using of this formula, it is a possible to derive the concentration of a solution by measuring its absorbance in an ultraviolet-visible spectroscopy spectrometer. **(Collins., 2012)**

F the ground state to the excited state. **(Roberts *et al*., 2018)** The reason to use UV-Vis spectroscopy in research materials is mostly divided to two main categories; Firstly, it is for characterization of the electronic and optical properties of material and secondly for quantitative measurements of an analyte in the solid, gas and liquid phase. **(Tissue., 2002)**
In this work UV-vis spectroscopy was successfully used to characterize AgNPs, ZnONPs, ZnONPs/GO and AgNPs/GO nanocomposites dissolved respectively in phosphate buffer.

Instrumentation

In UV-Visible Spectrometer one can initially record the control spectrum and use that as internal reference for the sample spectrum. The latter tactic used has brought attention to scientist because numerous spectrometers in laboratories are computer controlled and baseline correction has a chance to be carried using the software by just taking off the control from sample spectrum. The visible part of spectrum has light source called tungsten filament bulb and the ultraviolet region has deuterium bulb. Meanwhile the emitted light consists of several different wavelengths, a monochromator, which contain of either a rotating metal grid or a prism of high accuracy called grating. The grating is positioned between the sample and light source. Moreover, using coloured filters as monochromators which absorb all but a certain limited range of wavelengths can accomplish wavelength selection. This limited range is called the bandwidth of the filter. **(Hofmann., 2010)**

Sample preparation is prepared by dissolving solute into the solvent (e,g water, ethanol, PBS etc.) to make a dilute sample solution. The diluted sample solution is then filled up to mark line of the sample cell. Thereafter, UV-visible absorption analyses can be performed using Shimadzu (Japan) 3100 PC spectrophotometer and Varian Cary 5E UV-Vis spectrophotometer. The spectrometer then records absorbance (A) against the wavelength (λ). **(Gullapalli and Barron., 2010)**

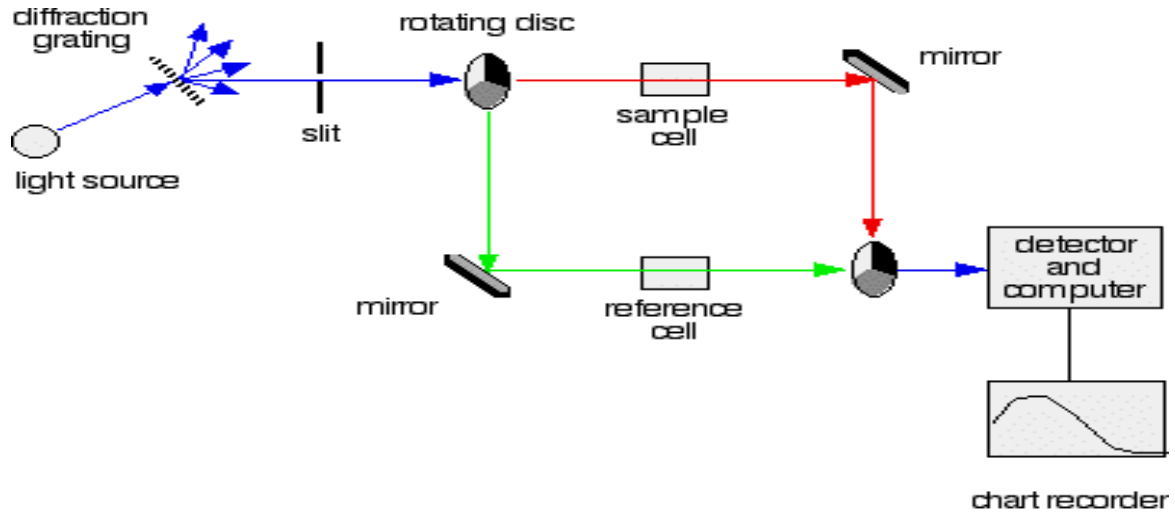

Figure 3.1: Schematic diagram of UV-Visible Spectrometer. (Gullapalli and Barron., 2010)

3.6.1.2 Photoluminescence Spectroscopy (PL)

Photoluminescence Spectroscopy (PL) is a photon emission process which occurs when molecules are relaxed from electronic excited states. A diagram that proposes a suitable representation of the relevant transitions and the excited state structure is called Jablonski diagram (as shown in **Figure 3.2**). **(So and Dong., 2001)** Photoluminescence Spectroscopy is one of the popular techniques because of its high level of specificity, sensitivity and simplicity and it can be used to observe, identify and quantify chemical activity. It is a spectroscopy technique used to analyze the photoluminescence properties of a sample that is done by determining the concentration of an analyte in a sample. This method is relatively an easy technique to perform and it is commonly used for measuring compounds in a solution.

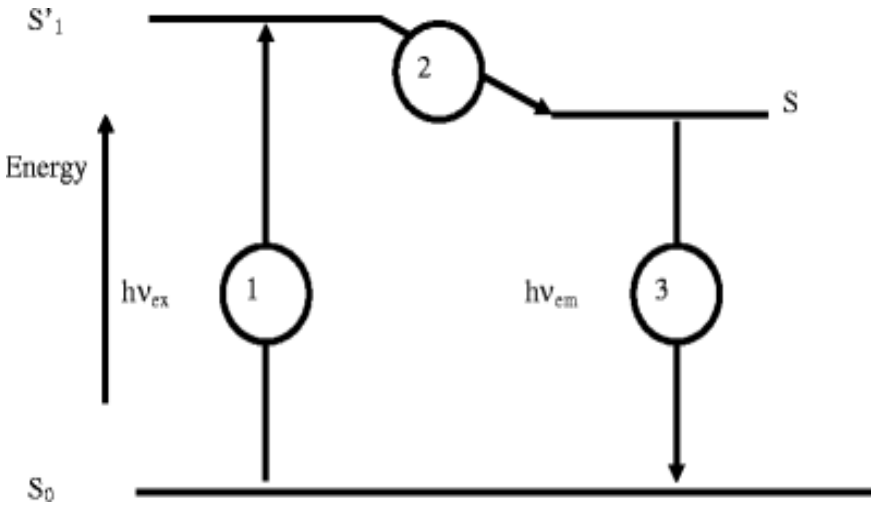

Figure 3.2: Jablonski diagram (Karoui and Blecker., 2011)

Elaborating more on the Jablonski diagram; (1) the initial step is the excitation, where a molecule absorbs light and is transferred to an electronically excited state, this means the electron moves from the ground singlet state (S_0) to an excited singlet state (S'_1). (2) The second step is an internal conversion or a vibrational relaxation, in this step molecule experiences a changeover from a higher electronically excited state to a lower one (S_1) this occur without any radiation. (3) The finally step is where the emission occurs usually just a few seconds after the excitation, when the electron goes back to its more stable ground state (S_0) emitting light at a wavelength according to the difference in energy between the two electronic states. **(Karoui and Blecker., 2011)**

In this study photoluminescence spectroscopy was productively used to characterize graphite oxide and graphene oxide dissolved in phosphate buffer respectively.

Instrumentation

A spectrofluorometer is an analytical device that is used to measure and records the photoluminescence of a sample. While the photoluminescence is recorded, the excitation, emission or both wavelengths can be scanned. The instrument of fluorescence consists of three basic items: a detector, a source of light and a sample holder. This type of device also consists of two monochromator where the first one selects excitation wavelength and the second one luminescence is observed. Normally the second monochromator is positioned 90 ◦ to the incident light to reduce intensity of scattered light reaching the detector. The emission spectrum is then produced if excitation wavelength is fixed and the emitted radiation is scanned. **(Sharma., 1999)**

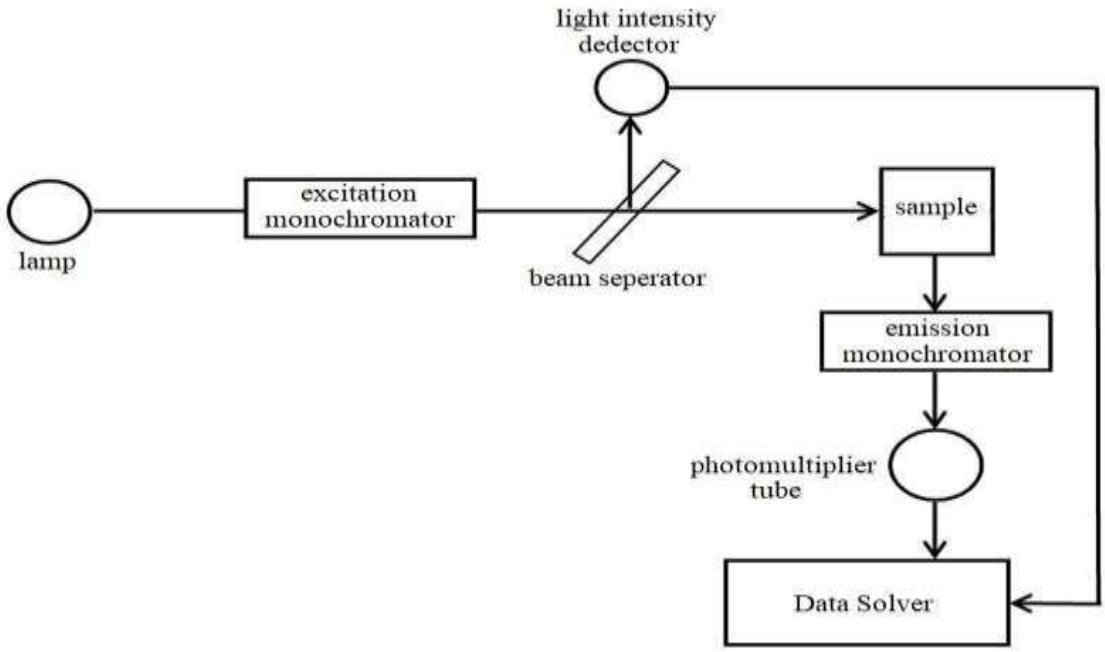

Figure 3.3: Schematic diagram of a characteristic photoluminescence spectrometer.

(PS, P.O.A.D. and Akaoğlu., 2017)

3.6.1.3 Raman Spectroscopy

Raman spectroscopy is a spectroscopic method constructed on inelastic scattering of monochromatic light, normally from a laser source. The denotation of inelastic scattering is that the frequency of photons in monochromatic light alters upon interaction with a sample. The sample absorbs these photons of the laser light and then reemits them. The reemitted photons frequency thereafter shifts up or down comparing the incident with original monochromatic frequency that is called Raman Effect. This shift gives detailed information about rotational, vibration and other low frequency transitions in molecules. This spectroscopy can be used to study samples in different phases for example in gaseous, liquid and solid form. **(Instruments., 2012**) It is mostly applicable to quantitative and qualitative analyses of covalently bonded molecules used to differentiate between different phases of the same material and can offer information on periodicity and strain in modulated structures. It is also used widely to characterize semiconductor surfaces. **(Vallikkodi., 2018)**

Raman spectroscopy was also successfully used in this study to characterize GO, AgNPs, ZnONPs, ZnONPs/GO and AgNPs/GO nanocomposites.

Instrumentation

The modern Raman spectroscopy instrument contains four components namely: Detector (Photodiode array, CCD or PMT), Sample illumination system and light collection optics, Excitation source (Laser) and lastly Wavelength selector (Filter or Spectrophotometer). In this modern spectrophotometer most extensively Raman source is a laser sources similar to pulsed nitrogen laser, argon laser, He-Ne because of it is highly beam flux this is necessary as the Raman Effect is weak and high monochromatic nature. The required type of laser depends on the sample used and Raman technique. The sample is usually illuminated with a laser beam in the near infrared (NIR), visible (Vis) or ultraviolet (UV) range. The lens

collects scattered light and sends it through interference filter or spectrophotometer to achieve Raman spectrum of a sample. **(Khandpour., 2006)**

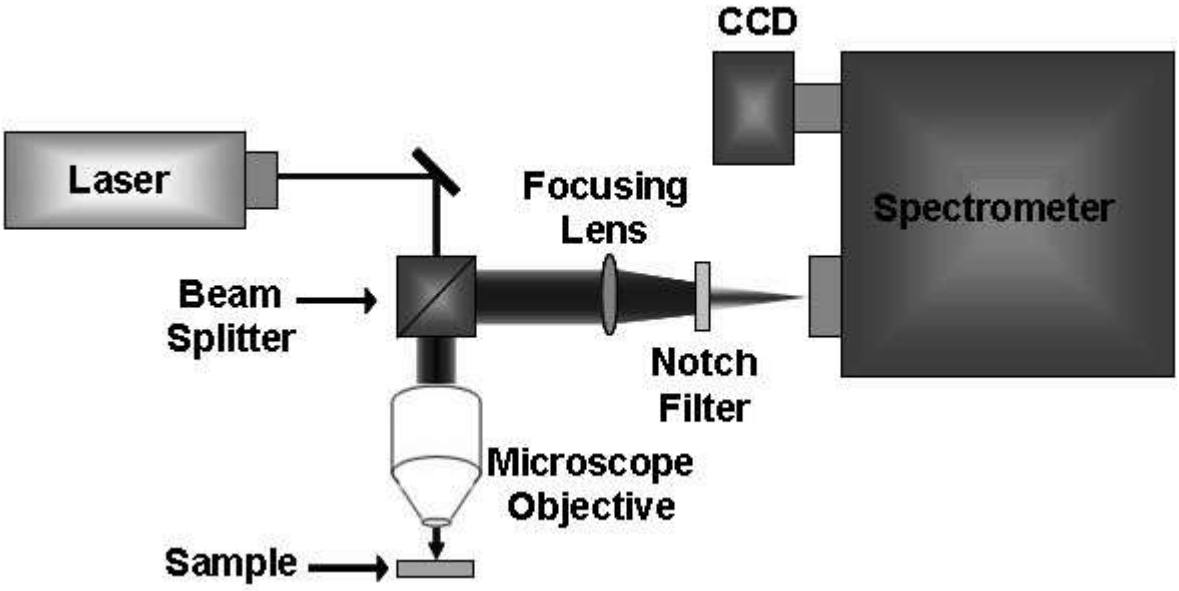

Figure 3.4 Schematic diagram of a Raman spectrometer. (Zabinski *et al*., 1994)

3.6.1.4 Fourier transform infrared spectroscopy (FTIR)

FTIR spectroscopy is a fast, non-destructive method with least sample preparation necessary. It allows the qualitative determination of compounds as the characteristic vibrational mode of each molecular group causes the appearance of bands in the FTIR spectrum at a specific frequency, which is further influenced by the surrounding functional groups. **(Vlachos *et al*., 2006)** FTIR spectroscopy is a technique that scientists use to determine the structures of molecules with the molecules' characteristic absorption of infrared radiation. Sample molecules selectively absorb radiation of specific wavelengths when they are exposed to infrared radiation that leads to change of dipole moment of sample molecules.

As a result, the sample molecules vibrational energy levels are transfer from ground state to excited state. The vibrational energy gap determines the frequency of the absorption peak. The number of absorption peaks is related to the number of vibrational freedom of the molecule. While the intensity of absorption peaks is related to the possibility of the transition of energy levels and the change of dipole moment. So, one can easily acquire abundant structure information of a molecule by just analyzing the infrared spectrum. This spectroscopy is very useful because it is capable to analyse sample in all phase; liquid, solid and gas. It commonly uses region of 4000 - 400 cm due to absorption radiation of inorganic ions and the organic compounds which are mostly within this region. **(Birkner and Wang., 2014)**

Instrumentation

FTIR interferometer consists of three basic spectrometer components shown in **Figure 3.5** and a detector. This type of instrument splits radiant beams and then generates an optical path difference recombines them in order to create repetitive interference signals that can be measured as a function of optical path difference by a detector. These interference signals that are created by interferometer, which contain infrared spectral information produced after they are passed through a sample. Michelson interferometer is the most frequently used interferometer. It consists of three active components; a fixed mirror, moving mirror and a beam splitter (**Figure 3.5**). These two mirrors are positioned perpendicular to each other and the beam splitter is a semi-reflecting which is often made by depositing a thin film of germanium onto a flat potassium bromide substrate. The radiation from the broadband IR source is collimated and directed into the interferometer, and impinges on the beam splitter. **(Thomas *et al*., 2014)**

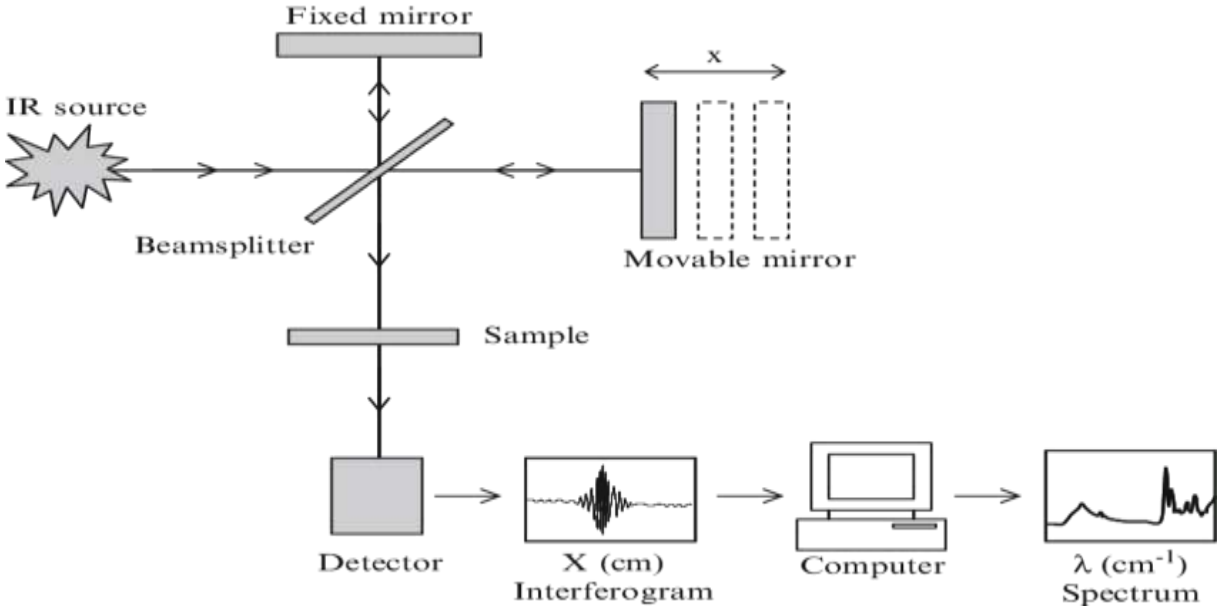

Figure 3.5: Schematic representation of the vital features of a Fourier transforms infrared spectrometer. (Ojeda and Dittrich., 2012)

3.6.1.5 X-Ray diffraction (XRD)

X-ray diffraction is an easiest method used to determine the shape and size of the unit cell for crystalline materials; additionally, it gives a huge quantity of information on crystals imperfections, phase change, texture and distribution of the grain size micro strain. **(Rahoui *et al*., 2016)** This technique is based on constructive interference of monochromatic X-rays and a crystalline sample, where cathode ray tube generates these X-rays and they are filtered to produce monochromatic radiation, collimated to concentrate, and directed toward the sample (**Figure 3.6**). One of advantage of using X-ray diffraction is that it is a non-destructive technique which penetrates from the surfaces into the bulk of the materials. **(Lindon *et al*., 2016)** Hence, it was used in this study for the characterization of GO, AgNPs, ZnONPs, ZnONPs/GO and AgNPs/GO nanocomposites

Instrumentation

Instrumentation of X-ray diffraction contains four major components such as: X-ray detector X-ray source, receiving optics and specimen stage as presented in **Figure 3.6**. The detector and source is associated with optics which makes them lie on the circumference of focusing circle and the sample stage at the center of the circle. Bragg's law is the root of XRD analysis. This law conveys possibility to create precise quantifications of experimental results in the determination of crystal structures. The angle between the Xray source and the plane of the specimen is θ, known as Bragg's angle and angle between the detector and the projection of X- ray is 2θ. XRD analysis is performed by mounting the sample holder and the powder assuming it consist of randomly oriented crystallites. X-rays are scattered by each atom in the sample, when a beam of X- ray is incident on the sample. If the scattered beams happen to be in the same phase, these interfere productively and one obtains the intensity maximum at that particular angle. The atomic planes from where the X-rays are scattered are referred to as reflecting planes. **(Sharma *et al*., 2012)**

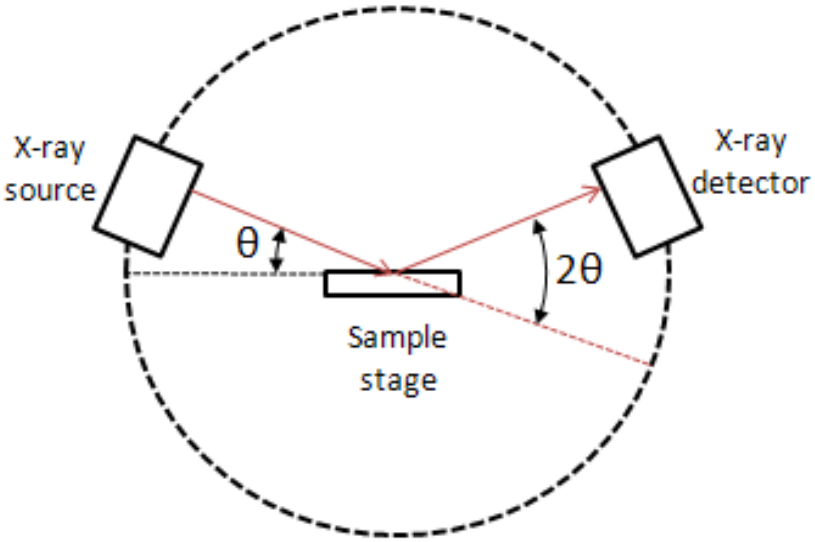

Fig. 3.6: Schematic diagram of a diffractometer. (Bunaciu et al., 2015)

3.6.2 Microscopic techniques

Microscopy techniques are very useful for determining the morphology of particles. Their advantage is that they can be ingredient specific when used for particle size analysis and are complementary to other particle sizing methods. Basically, microscopy is the most applicable method for determining the size of particles within some semi solid products, such as ointments and gels. On the other hand using microscopy for particle sizing can be challenging. Challenges that one can face are; the level of skill required by the operator and secondly deciding the sample size (number of particles) for accurate size analysis of the product. **(Kulkarni and Shaw., 2015)**

3.6.2.1 High resolution transmission electron microscopy (HRTEM)

High resolution transmission electron microscopy (HRTEM) is consistently useful to acquire images with atomic resolution. In HRTEM, a plane electron wave illuminates an electron-transparent specimen. The plane electron wave amplitude and phase is changed upon propagation through the object. In the process of image formation in HRTEM, the lens aberrations of the imaging lens system play a significant role. The attainable image contrast generally depends on the structure, elemental composition and thickness of the specimen as well as the selected imaging parameters. **(Hettler *et al*., 2016)** This microscopy can typically be used to study the growth of layers, their composition and defects in semiconductors. While the high resolution can be used to analyze the density, size, quality and shape of quantum dots, wells, and wires. **(Fulekar and Pathak., 2017)**

Instrumentation

Instrumentation of HRTEM consists of four parts: imaging system, electron source, sample holder and electromagnetic lens system as shown in **Figure 3.7**. The electromagnetic lenses and the metal apertures are tightly focused on the electron beam coming from the source. Only the electrons within a small energy range are allowed by the system to pass through, consequently the electrons in the electron beam will also pass through - defined energy. This beam falls on the sample placed in the holder, the electron beam then passes through the sample. The transmitted beam duplicates the patterns on the sample. This transmitted beam is projected onto a phosphor screen. **(Garg *et al*., 2010)** Nonetheless, in this work, images of HRTEM were recorded using a JEOL JEM 2100F High resolution transmission electron microscope, where the images were obtained by dispersing the powder samples in ethanol and ultrasonicate for 20 minutes; while for liquid samples were used as they are. Summing up, a drop of dispersion was coated onto the copper grid and HRTEM images were achieved.

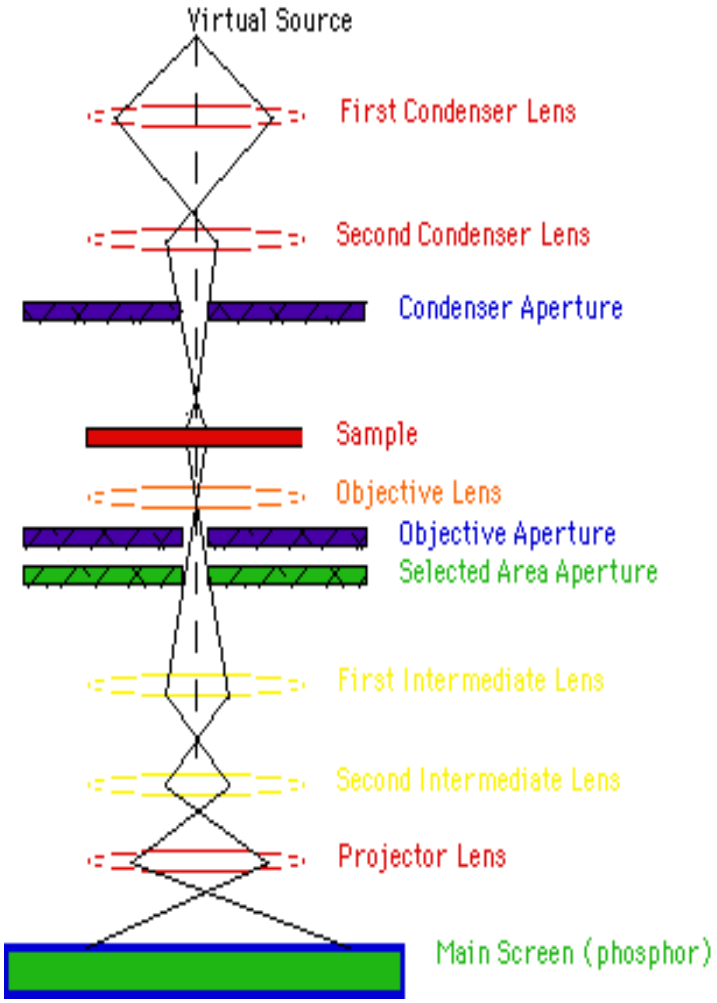

Figure 3.7: Schematic diagram of a High Resoluton Transmission Electron Microscope (HRTEM). (*https://ncmn.unl.edu/enif/microscopy/TEM.shtml*)

3.6.2.2 High resolution Scanning electron microscopy (HRSEM)

High resolution Scanning electron microscopy (HRSEM) is a microscope that scans a focused beam of electrons over a sample surface to produce an image. **(Scott., 2014)** These electrons in the beam interact with the sample and produce several signals that can be used to achieve information about the surface composition and topography. HRSEM is an electron microscopy, which is capable of much higher magnifications and has a better resolving power compared to the light microscope that allows it to see much smaller objects in finer detail.

(Carter and Shieh., 2015) In this study it was sucessfully used to attain information about the surface composition and topography of GO, ZnONPs/GO and AgNPs/GO nanocomposites.

Instrumentation

HRSEM schematic diagram is represented in **Figure 3.8**, where it shows an electron gun producing beam of electrons at the top of the microscope. This beam of electrons follows a vertical route through the microscope that is held within a vacuum. The beam moves through lenses and electromagnetic fields, which focus the beam down toward the sample. As soon as the beam hits the sample, X-rays and electrons are ejected from the sample. These backscattered electrons, X-rays and secondary electrons are then collected by detectors and converted into a signal that is sent to a screen that looks alike to a television screen. Thereafter the final image is produced. In this current research work, the samples were prepared by placing on powder sample on the carbon tape which was attached to the sample holder. Equipment that were used to study the surface morphology of the sample were JEOL JSM 6320F (FESEM) and F E I Quanta FEG 200 (HRSEM) **(Cheney., 2007)**

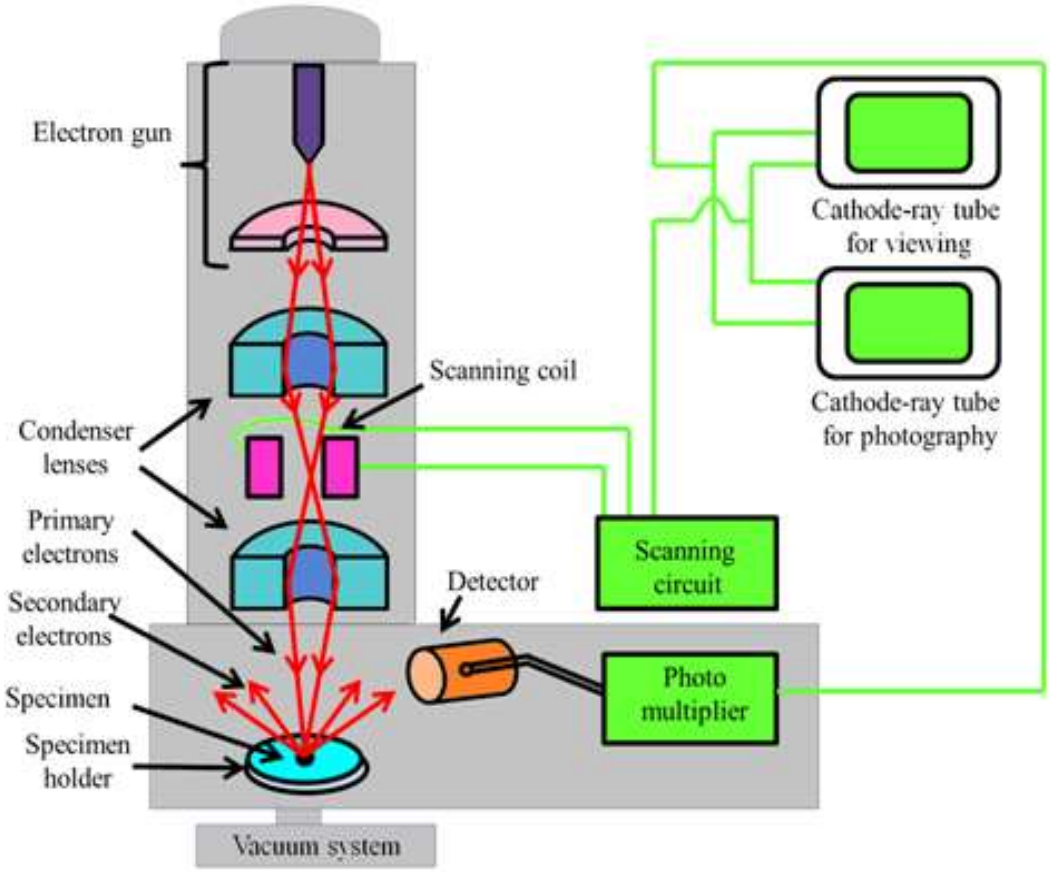

Figure 3.8: Schematic diagram of a High resolution Scanning Electron Microscope.

(*http://nptel.ac.in/courses/102103047/module6/lec34/1.html*)

3.6.2.3 Energy dispersive X-ray (EDX)

Energy dispersive X-ray (EDX) is an analytical device mainly used for chemical characterization. This type of microscopy relies on the investigation of a sample through interactions between matter and light where X-rays are analysed in this specific case. **(Rahoui *et al*., 2016)** EDX uses X-rays that are emitted from the sample thru bombardment by the electron beam to characterize the elemental composition of the analyzed volume (**Figure 3.9**). The technique measures the number of emitted X-rays as opposed to their energy using a detector. The X-ray energy is characteristic of the element from which the X-ray was emitted. A spectrum of the energy versus relative counts of the detected X-rays are

achieved and assessed for quantitative and qualitative determinations of the elements existing in the sampled volume. **(Ounsi *et al*., 2008)** In this study it was effectively used to determine existing elements in GO, AgNPs, ZnONPs, ZnONPs/GO and AgNPs/GO nanocomposites.

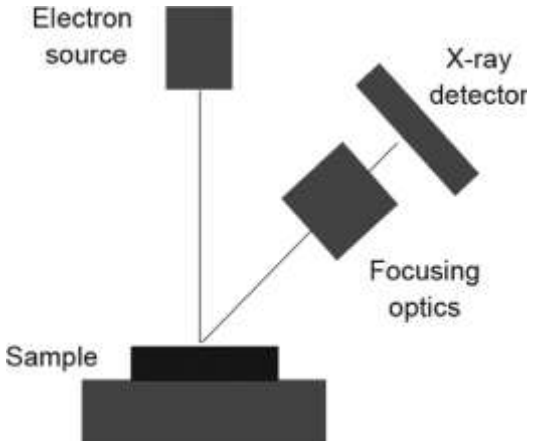

Figure 3.9: Schematic principle of energy dispersive X-ray. (Ounsi *et al*., 2008)

Instrumentation

The energy dispersive microscopy basic design is presented in **Figure 3.10**. In this microscopy X-ray passes through a thin beryllium window into a cooled reverse-biased lithium-drifted silicon detector. X-ray photon absorption in the detector produces a photoelectron, which in turn produces electron-hole pairs in the reverse-biased diode. The bias on the detector swept away these electron-holes pairs and then converts them into a voltage pulse by a charge sensing amplifier. The signal is further amplified and sent to a multichannel analyzer, where the pulses are sorted by voltage. The distribution by voltage can then be displayed and manipulated by the computer to identify peaks or quantification.

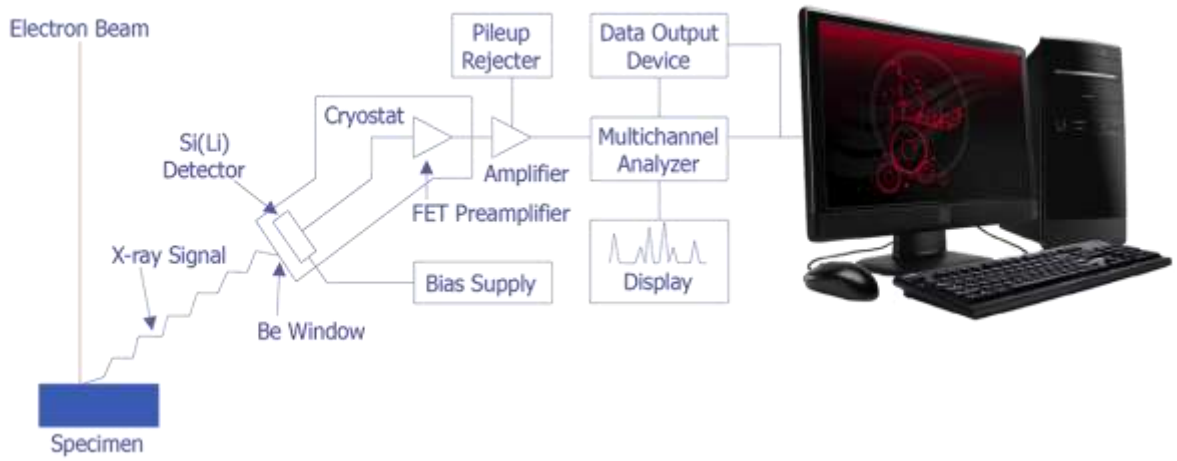

Figure 3.10: Schematic Representation of an energy-dispersive microscopy. (*https://www.semitracks.com/reference-material/failure-and-yield-analysis/failure-analysis-materials-characterization/energy-dispersive-x-ray-spectrometry.php)*

3.6.2.4 Atomic Force Microscopy (AFM)

Atomic force microscopy (AFM) is an important tool not only to attain high-resolution topographical images, but also to determine certain physical properties of samples, such as their composition and mechanical properties. This technique is versatile and that is reflected by the extensive range of sizes of the specimens that it can deal with, such as molecules, cells, atoms and molecular aggregates. **(de Pablo., 2011)** AFM usually is based around imaging probe that are very sharp, which is scanned over the surface of interest, generating a three-dimensional map. Its usefulness lies in its versatility, being capable to make measurements in both liquid and ambient environments, different to many other high-resolution imaging techniques. **(Johnson et al., 2017**)

Instrumentation

The AFM instrument is governed by three components as shown in **Figure 3.11** for imaging purposes. This tool operates by creating mechanical movement under an applied electric

potential using piezoelectric elements. These piezoelectric elements are then used to precisely move the AFM probe independently in three dimensions. In the X–Y direction the probe is raster-scanned across the sample, while the force of the interaction between the probe and the sample is measured by a force transducer, normally the cantilever on which the probe is mounted. A laser beam is focused onto the back of the cantilever. There is possibility for cantilever to be reflected back to a 4-quadrant photodiode detector. By assistance of this position sensitive photodiode, the bending of the cantilever can be measured accurately. The cantilever deflects according to the atomic force variations between sample and the tip thus the detector measures the deflection. The produced image is a topographical illustration of the sample surface. **(Wallace., 2012)**

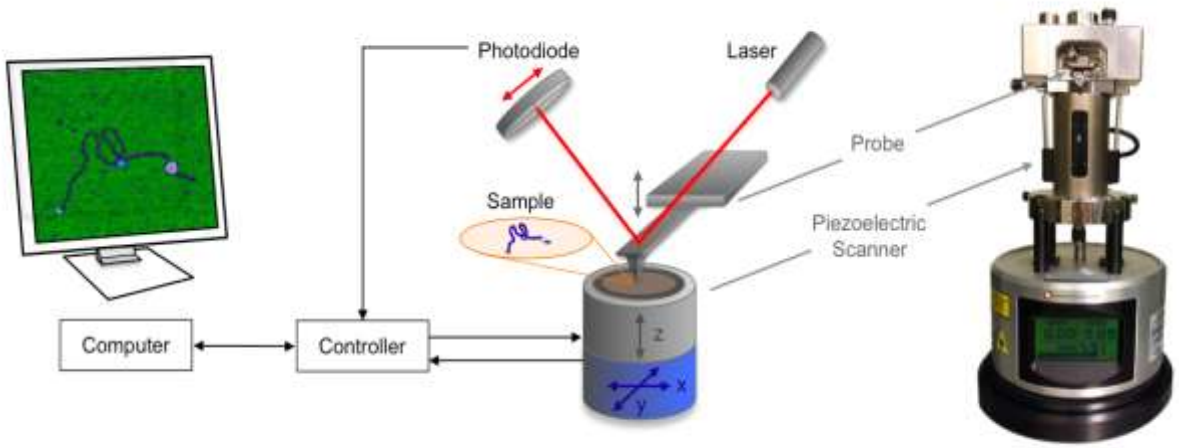

Figure 3.11: Schematic diagram of an Atomic Force Microscopy (AFM).

(*http://www.physics.emory.edu/faculty/finzi/research/afm.html*)

3.6.3 Electrochemical techniques

Electrochemical methods are very important tools used to study chemical and physical properties as a result of electrons through reduction and oxidation reactions. Advantage associated with these methods include cheapness and are effective in dealing with some of the most common extant pollutants, they also demonstrates to be greener alternative to several other forms of clean-up now available. Electrochemical methods are useful due to their environmental compatibility, safety, selectivity, energy efficiency, amenability to automation, versatility and cost effectiveness. **(Ngece., 2011)** These techniques are among the greatest extensively used current applications in medical diagnostics devices, waste treatment and environmental protection.

3.6.3.1 Cyclic Voltammetry (CV)

Cyclic voltammetry (CV) is the most popular and powerful electrochemical method frequently employed to investigate the oxidation and reduction processes of molecular species. CV is also helpful to study electron transfer initiated chemical reactions, which involves catalysis. It is a method that is regularly used to obtain qualitative information about electrochemical reactions that occur. It also offers a fast setting of reduction and oxidation potentials of the electroactive species. **(Elgrishi et al., 2017)** CV can also be used to acquire useful kinetic information of electrode reaction. Electrode reaction normally includes electron transfer reaction which is influenced by electrode potential. Electrode mechanism is investigated by voltammetry. The advantage of using this method includes its broad accessibility, it access wide theory for electrochemist as well as other field of specialists. Though, this method has some weaknesses which include the struggle to determine the

mechanism of the second of two or more closely spaced charge transfer reactions. **(Nicholson, 1965)**

Instrumentation

Potentiostat Set-up

Electrochemical measurements were done using Palm sens monitored on PSTrace software. For electrochemical analyses, conventional three electrode set up was used; as shown in **Figure 3.12**. These three electrodes system consisted of a 10 mL electrochemical cell and were immersed in an electrolyte solution. The electrodes used in this study were; platinum wire purchase from Sigma Aldrich which acted as a counter electrode (CE), glassy carbon working electrode (WE), with an area of 7.065 mm^2 purchased from BASi and a Ag/AgCl kept in 3 M NaCl also from BASi was the reference electrode (RE). The analytical grade nitrogen gas was used for degassing all the cell solutions was purchased from Afrox Company, South Africa.

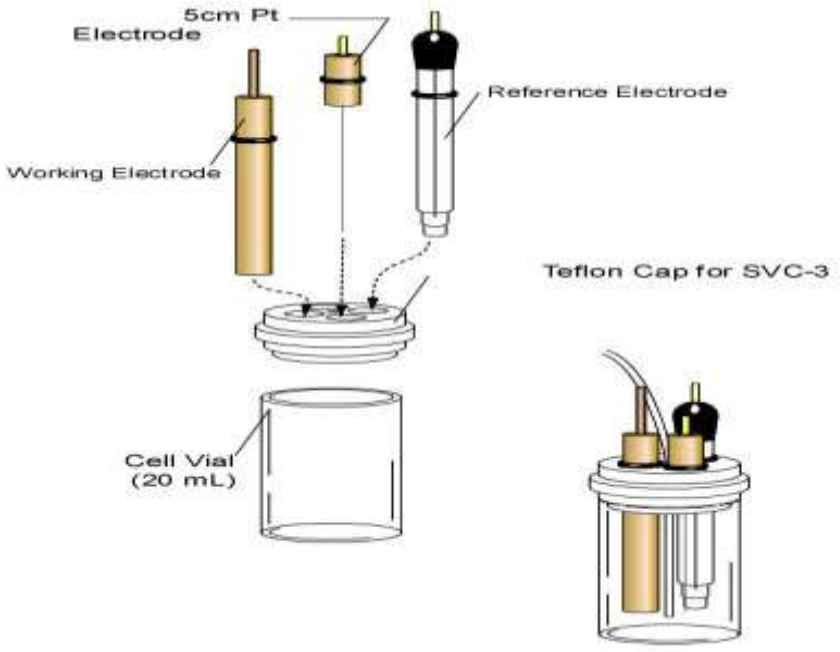

Figure 3.12: Set up of three electrode system.

(*www.ijcambria.com/VC-3.htm*)

Electrode Surface Preparation

Alumina micro polishing pads and powder (1 μm, 0.3 μm and 0.05 μm) were used to clean glassy carbon (GC) electrodes. The GC electrodes were polished using aqueous slurries of 1 μm, 0.3 μm and 0.05 μm alumina powder and were sequentially sonificated in ethanol for 15 min followed by deionised water. The polished electrodes were then checked their cleanness electrochemically 0.1M PBS at the scan rate of 50 mVs^{-1}.

3.6.4 Scattering techniques

Scattering techniques are a valuable tool that provide quantitative information on structure, shape and size of colloidal particles, subsequently they are based on interactions between particles and incident radiations (e.g., X-ray, neutrons or light) (**Pauw., 2013)**

3.6.4.1 Small-Angle X-ray Scattering (SAXS)

Small-angle X-ray scattering (SAXS) is a method used to study colloidal size particles in a sample. X-rays are normally scattered in this technique due to the elastic collision between sample and the X-rays. **(Flores-Villaseñor., 2015)** The scattering of X-rays are recorded at the angles ranging from 0.1 to 10 °C. The size and shape macromolecules, characteristic distances of partially ordered materials, pore sizes and structure can be determined from this analysis. This technique is non-destructive and for analysis, a least amount of samples are required. **(Borthakur *et al*., 2016)** SAXS also gives information on the electron density of

the sample relative to the solvent. Due to technical boundaries regarding the wavelength of the radiation relative to the overall particle size, SAXS procedures in principle provide a viewing window on the sample. The data then must be interpreted in terms of the density of the average particles observed. **(Qi., 2009)**

Instrumentation

Instrumentation of SAXS with a 2D (area) detector is shown in **Figure 3.13**. Occurring in this typical SAXS setup, a proper source emits a beam of X-rays which is monochromated and focused on special X-ray optics. A system of slits adjusts the size of the beam; thereafter the beam hits the sample and enters the flight path. The flight path, which has to be under vacuum due to air scatters the beam, provides the long distance between sample and detector that is crucial to detect X-rays scattered at small angles. Un-oriented samples produce a centrosymmetric pattern on the 2D detector, which is radially averaged to give the typical plots of diffracted intensity vs. scattering vector q (= $4\pi \sin\theta/\lambda$).

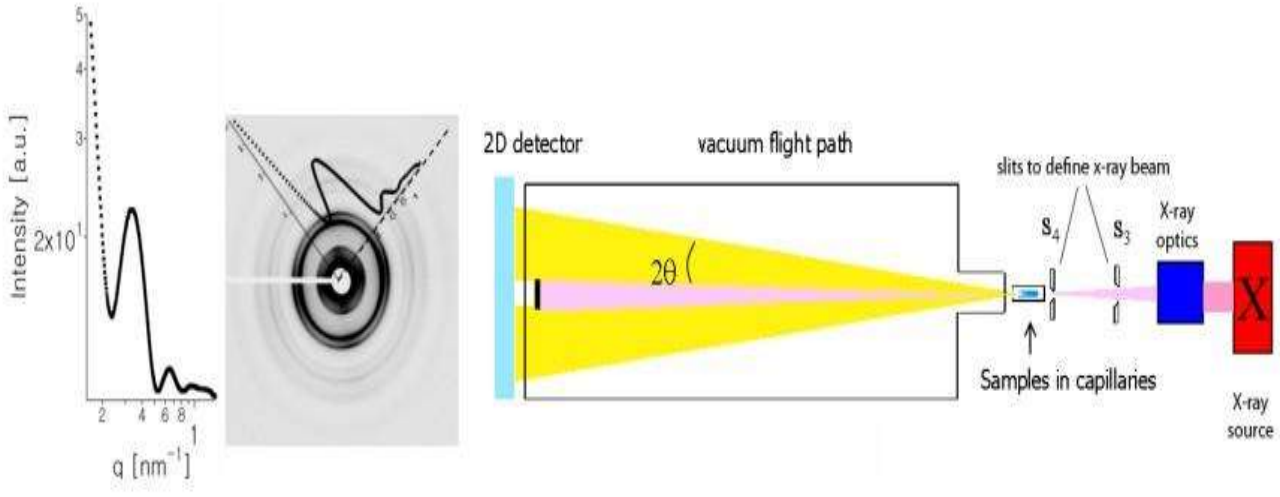

Figure 3.13: Schematic diagram of a Small-Angle X-ray Scattering (SAXS).

(*http://www.mrl.ucsb.edu/~safinyaweb/XRD.htm*)

3.7 References

Akaoğlu, C., 2017. Istanbul Technical University graduate school of science engineering and technology.

Beynon, R. and Easterby, J., 2004. Buffer solutions. Taylor & Francis.

Birkner, N. and Wang, Q., 2014. How an FTIR Spectrometer Operates. UC Davis ChemWiki.

Borthakur, P., Boruah, P.K., Sharma, B. and Das, M.R., 2016. Nanoemulsion: Preparation and its application in food industry. In Emulsions (pp. 153-191).

Bumbrah, G.S. and Sharma, R.M., 2016. Raman spectroscopy–Basic principle, instrumentation and selected applications for the characterization of drugs of abuse. Egyptian Journal of Forensic Sciences, 6(3), pp.209-215.

Bunaciu, A.A., UdriŞTioiu, E.G. and Aboul-Enein, H.Y., 2015. X-ray diffraction: instrumentation and applications. Critical reviews in analytical chemistry, 45(4), pp.289-299.

Carter, M. and Shieh, J.C., 2015. Guide to research techniques in neuroscience. Academic Press.

Cheney, B., 2007. Introduction to scanning electron microscopy. Materials Engineering department San Jose State University.

Collins, A., 2012. Nanotechnology cookbook: practical, reliable and jargon-free experimental procedures. Elsevier.

de Pablo, P.J., 2011. Introduction to atomic force microscopy. In Single Molecule Analysis (pp. 197-212). Humana Press.

Elgrishi, N., Rountree, K.J., McCarthy, B.D., Rountree, E.S., Eisenhart, T.T. and Dempsey, J.L., 2017. A Practical Beginner's Guide to Cyclic Voltammetry. Journal of Chemical Education, 95(2), pp.197-206.

Garg, N., Garg, K.L. and Mukerji, K.G., 2010. Laboratory manual of food microbiology. IK International Pvt Ltd.

Gullapalli, S. and Barron, A., 2010. Optical Characterization of Group 12-16 (II-VI) Semiconductor Nanoparticles by UV-visible Spectroscopy. Connexions.

Flores-Villaseñor, S.E., Peralta-Rodríguez, R.D., Ramirez-Contreras, J.C., Cortes-Mazatán, G.Y. and Estrada-Ramírez, A.N., 2016. Biocompatible microemulsions for the nanoencapsulation of essential oils and nutraceuticals. In Encapsulations (pp. 503-558).

Fulekar, M.H. and Pathak, B., 2017. Environmental Nanotechnology. CRC Press.

Hettler, S., Dries, M., Zeelen, J., Oster, M., Schröder, R.R. and Gerthsen, D., 2016. High resolution transmission electron microscopy with an electrostatic Zach phase plate. New Journal of Physics, 18(5), p.053005.

Hofmann, A., 2010. 12 Spectroscopic techniques: I Spectrophotometric techniques.

Instruments, P., 2012. Raman spectroscopy basics. Internet: http://content. piacton. com/Uploads/Princeton/Documents/Library/UpdatedLibrary/Raman_Spectroscopy_Basics. pdf.

Johnson, D., Oatley-Radcliffe, D.L. and Hilal, N., 2017. Atomic Force Microscopy (AFM). In Membrane Characterization (pp. 115-144).

Karoui, R. and Blecker, C., 2011. Fluorescence spectroscopy measurement for quality assessment of food systems—a review. Food and Bioprocess technology, 4(3), pp.364-386.

Khandpur, R.S., 2007. Handbook of analytical instruments. Tata McGraw-Hill Education.

Kulkarni, V.S. and Shaw, C., 2015. Essential Chemistry for Formulators of Semisolid and Liquid Dosages. Academic Press.

Lindon, J.C., Tranter, G.E. and Koppenaal, D., 2016. Encyclopedia of spectroscopy and spectrometry. Academic Press.

Marcano, D.C., Kosynkin, D.V., Berlin, J.M., Sinitskii, A., Sun, Z., Slesarev, A., Alemany, L.B., Lu, W. and Tour, J.M., 2010. Improved synthesis of graphene oxide. ACS nano, 4(8), pp.4806-4814.

Ngece, R.F., 2011. Nanoparticulate of silver-modified poly (8-anilino-1-naphthalene sulphonic acid) nanobiosensor systems for the determination of Tuberculosis treatment drugs (Doctoral dissertation, University of the Western Cape).

Nicholson, R. S. 1965. Theory and Application of Cyclic Voltammetry for Measurement of Electrode Reaction Kinetics. Analytical chemistry 37: 1351-1354.

Ojeda, J.J. and Dittrich, M., 2012. Fourier transform infrared spectroscopy for molecular analysis of microbial cells. In Microbial Systems Biology (pp. 187-211). Humana Press, Totowa, NJ.

Ounsi, H.F., Al-Shalan, T., Salameh, Z., Grandini, S. and Ferrari, M., 2008. Quantitative and qualitative elemental analysis of different nickel–titanium rotary instruments by using scanning electron microscopy and energy dispersive spectroscopy. Journal of Endodontics, 34(1), pp.53-55.

Qi, P.X., 2009. Studies of the biological function and structure of casein micelles, and future implications. In Dairy-Derived Ingredients (pp. 147-169).

Pauw, B.R., 2013. Everything SAXS: small-angle scattering pattern collection and correction. Journal of Physics: Condensed Matter, 25(38), p.383201.

PS, P.O.A.D. and Akaoğlu, C., 2017. Istanbul Technical University graduate school of science engineering and technology.

Rahoui, N., Jiang, B., Pan, H.T. and Huang, Y.D., 2016. Spectroscopy strategy for solid propellants quality control. Applied Spectroscopy Reviews, 51(5), pp.431-450.

Roberts, J., Power, A., Chapman, J., Chandra, S. and Cozzolino, D., 2018. The Use of UV Vis Spectroscopy in Bioprocess and Fermentation Monitoring. Fermentation, 4(1), p.18.

Rojas, F.S. and Ojeda, C.B., 2009. Recent development in derivative ultraviolet/visible absorption spectrophotometry: 2004–2008: A review. Analytica Chimica Acta, 635(1), pp.22-44.

Scott, K., 2014. Fabrication and Characterization of Magnetic Nanostructures.

Sharma, A. and Schulman, S.G., 1999. Introduction to fluorescence spectroscopy (Vol. 13). Wiley-interscience.

Sharma, R., Bisen, D.P., Shukla, U. and Sharma, B.G., 2012. X-ray diffraction: a powerful method of characterizing nanomaterials. Recent research in science and technology, 4(8).

So, P.T. and Dong, C.Y., 2001. Fluorescence spectrophotometry. e LS.

Sun, H., Yang, Y. and Huang, Q., 2011. Preparation and structural variation of graphite oxide and graphene oxide. Integrated Ferroelectrics, 128(1), pp.163-170.

Thomas, S., Thomas, R., Zachariah, A.K. and Mishra, R.K. eds., 2017. Spectroscopic Methods for Nanomaterials Characterization (Vol. 2). Elsevier.

Tissue, B.M., 2002. Ultraviolet and visible absorption spectroscopy. Characterization of Materials, pp.1-13.

Vallikkodi, M., 2018. Synthesis, growth and characterization of piperazinium p aminobenzoate and piperazinium p-chlorobenzoate nonlinear optical single crystals (Doctoral dissertation, ALAGAPPA UNIVERSITY).

Vlachos, N., Skopelitis, Y., Psaroudaki, M., Konstantinidou, V., Chatzilazarou, A. and Tegou, E., 2006. Applications of Fourier transform-infrared spectroscopy to edible oils. Analytica chimica acta, 573, pp.459-465.

Wallace, J.M., 2012. Applications of atomic force microscopy for the assessment of nanoscale morphological and mechanical properties of bone. Bone, 50(1), pp.420-427.

Zabinski, J.S., Donley, M.S., Prasad, S.V. and McDevitt, N.T., 1994. Synthesis and characterization of tungsten disulphide films grown by pulsed-laser deposition. Journal of materials science, 29(18), pp.4834-4839.

CHAPTER 4

Results and Discussion – Part 1

Summary

This chapter will illustrate and discuss the results obtained for physical and electrochemical properties of graphene oxide. Additionally, illustrated herein will be the characterization discussion of green synthesized silver nanoparticles as well as green synthesized zinc oxide nanoparticles. The discussions composed in this chapter are those received from the techniques namely; cyclic voltammetry (CV) for the electrochemical studies of grapheme oxide. Additionally, the surface morphological studies were achieved using High-Resolution Transmission Electron Microscopy (HRTEM), Atomic Force Microscopy (AFM) and High-Resolution Scanning Electron Microscopy (HRSEM). Finally, the elemental analyses were accomplished using Fourier Transform Infrared Spectroscopy (FTIR), Energy Dispersive X-Ray (EDS), Raman spectroscopy and X-Ray diffraction (XRD) while the electronic and optical properties were obtained using Ultraviolet Visible Spectroscopy (UV-vis), Photoluminescence Spectroscopy (PL) and Small-Angle X-ray Scattering (SAXS).

4.1 Characterization of graphene oxide (GO)

The graphite oxide (GrO) synthesized in this study was prepared by oxidizing purified natural flake graphite using a modified Hummers method. The graphene oxide (GO) was then prepared using graphite oxide exfoliated in distilled water subjected to ultrasonic waves. Henceforth, both graphene oxide and graphite oxide are discussed in detail in sections below where their difference, similarities and verification of their formation will also be discussed. All the analytical techniques mentioned in the summary above were employed in studying the variation in the structure after the oxidation of graphite and the change and new formation of functional groups formed after exfoliation. The techniques mentioned were also used to investigate the chemical and physical properties of the developed materials. **(Sun *et al*., 2011)**

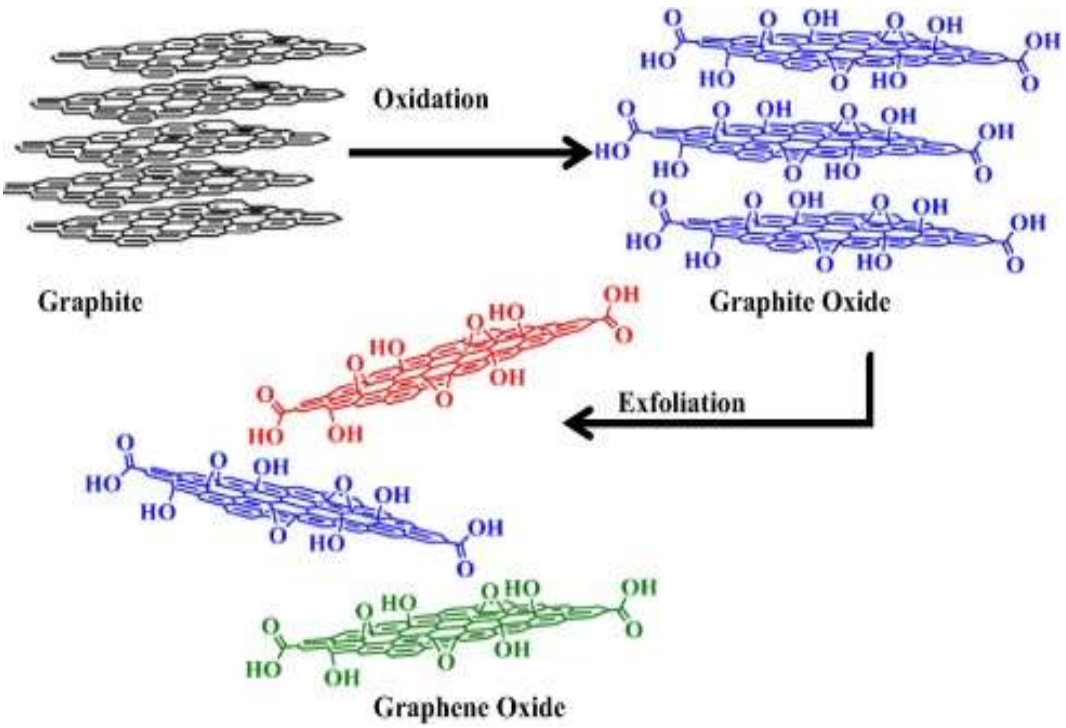

Figure 4.1: The three steps of preparing graphene oxide (GO) from graphite. (Ammaret *et al*,. 2016)

4.1.1 Spectroscopic characterisation of graphene oxide and graphite oxide

4.1.1.1 Fourier Transform Infrared spectroscopy (FTIR)

Figure 4.2 illustrates Fourier Transform Infrared (FTIR) spectra analyses that were performed to investigate the functional groups and the structures of graphite oxide (GrO) and graphene oxide (GO). Graphite oxide has shown an apparent adsorption band for the –OH at approximately 3319 cm^{-1} which is seen to be the most intense peak. Additionally, the following adsorption peaks were also observed a carboxyl C=O group at 1732.31 cm^{-1}, an aromatic C=C group at1617.19 cm^{-1}, an epoxy C–O group at 1389.11 cm^{-1} and an alkoxy C–O group at 1045.92 cm^{-1}. **(Gao., 2012)**

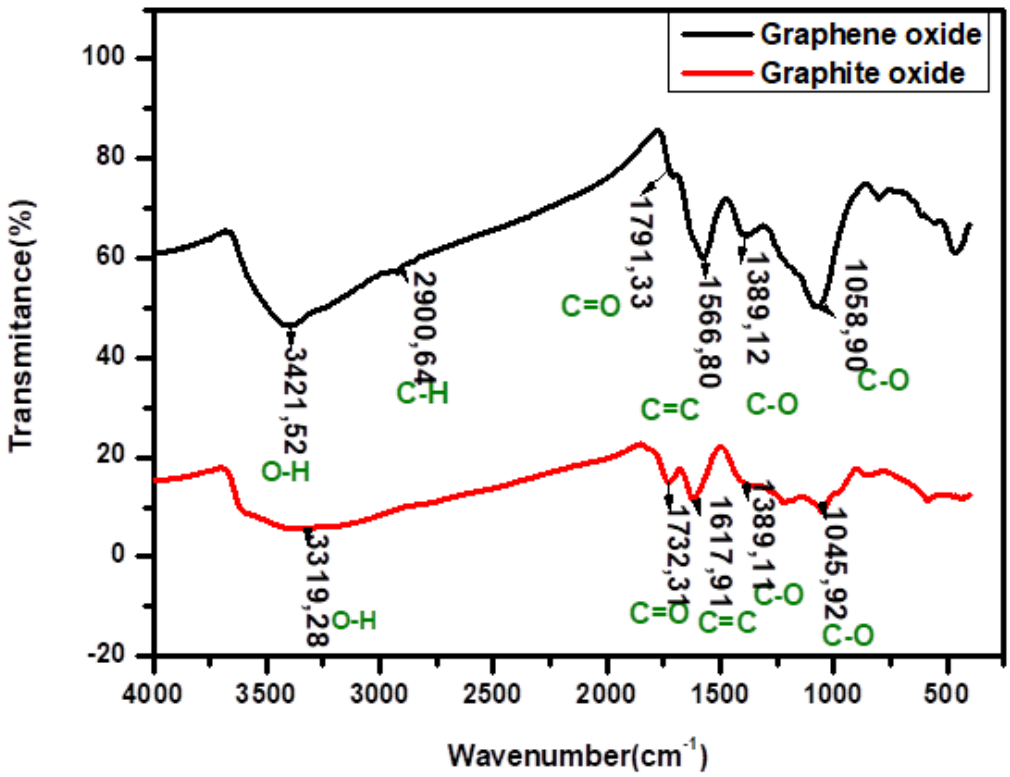

Figure 4.2: Fourier transform infrared spectrum of graphite oxide (GrO) and graphene oxide (GO).

On the other hand data received for graphene oxide has also shown apparent adsorption bands with larger wavenumbers as opposed to graphite oxide except in aromatic group C=C but they are still at a good range with elevated transmissions. Additionally, the data received also revealed adsorption bands of the hydroxy –OH group (at 3421.52 cm^{-1}) which was the most intense peak, a carboxyl C=O group at 1791.33 cm^{-1}, an aromatic C=C group at 1566.80 cm^{-1}, an epoxy C–O at 1389.12 cm^{-1} and an alkoxy C–O group at 1058.90 cm^{-1}. **(Kauppila., 2014)**

Consequently, the broad spectrum peak occurring within 3000–3500 cm^{-1}, at 3319 cm^{-1} is caused by the stretching vibration of –OH from graphite oxide resulting from adsorbed water molecules. This means that our sample was highly hygroscopic (capability of a product to react to the moisture content of the air by absorbing water vapour). **(Allada., 2016)** Hence the absorption peak at 1617 cm^{-1} is strong, based on the bending vibration of –OH in water molecules. The broad spectrum peaks between 3200–3700 cm^{-1} are caused by stretching vibration of water molecules. The absorption peak at 2900 cm^{-1} is caused by the anti-symmetric and symmetric stretching vibration of $=CH_2$, while the absorption peaks occurring at 1732 cm^{-1} and 1791cm^{-1} in the medium frequency area resultant from the stretching vibration of C=O of carboxylic acid and carbonyl groups at the edge of graphite oxide and graphene oxide. Finally, the absorption peaks at 1389 cm^{-1} and 1,110 cm^{-1} are caused by the stretching vibration of C-OH of alcohol and the vibration of C=O of carboxylic acid, respectively. **(Çiplak *et al*., 2015)**

Therefore the appearance of oxygen-containing functional groups such as C-O and C=O further confirmed that the graphite was certainly oxidized into graphite oxide and exfoliated to graphene oxide. The appearance of C=C groups illustrated that even though graphite had been oxidized into graphite oxide; the main structure of layer graphite was still retained.

4.1.1.2 Raman Spectroscopy

Figure 4.3 provides the Raman Spectroscopic analysis results of graphite oxide (GrO) and graphene oxide (GO). The spectrum peak displayed for graphite oxide at 1356 cm^{-1} is the D band peak which can be seen to be prominent, signifying the reduction in size of the in-plane sp^2 domains caused possibly by extensive oxidation. Graphite as expected displayed G band at 1593 cm^{-1} and a 2-D band at 2721 cm^{-1}. For graphene oxide the D band appears at 1341 cm^{-1} a peak is caused by double-resonance Raman scattering. The G band peak for GO occurs at 1581 cm^{-1} caused by doubly degenerated planar optical vibration of in-plane carbon atoms and a 2-D band at 2843 cm^{-1} . **(Kudin *et al*., 2008)**

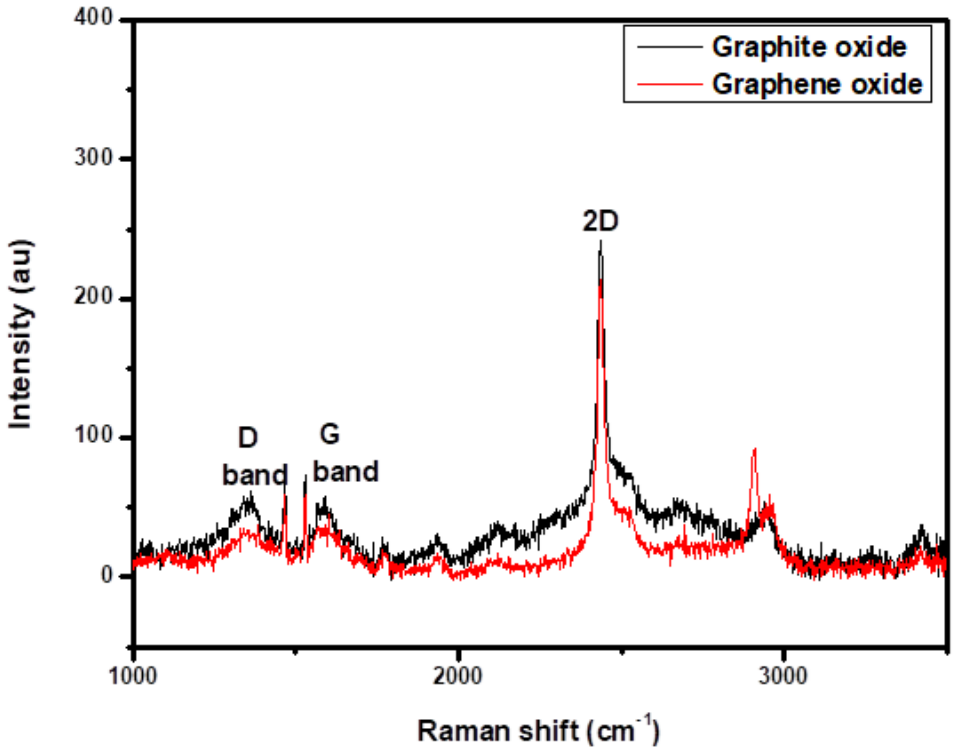

Figure 4.3: Raman spectrum of graphite oxide (GrO) and graphene oxide (GO).

Comparing the G and D band peak strength ratio between graphite oxide and graphene oxide, we find that the value of the latter is evidently lower than that of the former due to the reduced number of the sp^2 hybridized carbon atoms in the carbon layer plane and the degree of order of the structure is decreased when exfoliation occurs. Additionally, the 2-D band that appeared for both GrO and GO has a two peak profile, the intense $2D_1$ band and a $2D_2$ band which has a low energy shoulder. This splitting is caused by splitting of π electron dispersion energies produced by the interaction between the neighbouring graphitic planes. Moreover, the 2-D band position of graphene oxide is dispersive due to its double resonant origin. **(Jung *et al*., 2008)** It is also been noticed that the $2D_2$ band position depends on the number of layers and stacking order of the graphitic sample which in our study GrO has more layers than GO (AFM data analysis in later section will discuss at length) Hence, any modification of the graphitic surface is identified clearly via the $2D_2$ band. **(Kaniyoor and Ramaprabhu, 2012)**

The intensity ratio (I_D/I_G) of graphite oxide of D band and G band is about 0.952, while the intensity ratio of graphene oxide is 1.14 caused by the presence of unrepaired defects that remained after the removal of large amounts of oxygen-containing functional groups. **(Sun *et al*., 2011)** This intensity ratio value is compatible with most chemical reduction reports. The Raman spectrum of the materials compliments the XRD observed patterns (as seen below), for instance the changes of the structure during the exfoliation process from graphite oxide to graphene oxide.

4.1.1.3 X-Ray diffraction (XRD)

The XRD patterns of graphite oxide (GrO) and graphene oxide (GO) are illustrated in **Figure 4.4**. Graphite oxide displays a very strong 001 peak at 10.88 and a 002 peak at 31. 64° while GO shows a 001 peak at 11.30° and a 002 peak at 25.31°. After exfoliation to graphene oxide some of the oxygen-containing functional groups are removed and this causes an immediate shift to 25.31° on the graphene peak. This proposes that the conjugated graphene network (sp^2 carbon) is reconstructed during this process which is related with the ring-opening of the epoxides**. (Willemse., 2010)** Moreover, the decrease found from 8.7 Å to 13.1 Å of graphite oxide in the interplanar distance for the carbon layers has been attributed to the attachment of oxide functional groups to the graphite basal plane during oxidation reaction. Lastly, the graphite oxide most intense peak at $2\theta = 31.37^{o}$ (corresponding to a d-spacing of 8.7 Å) indicates the successful formation of GO.

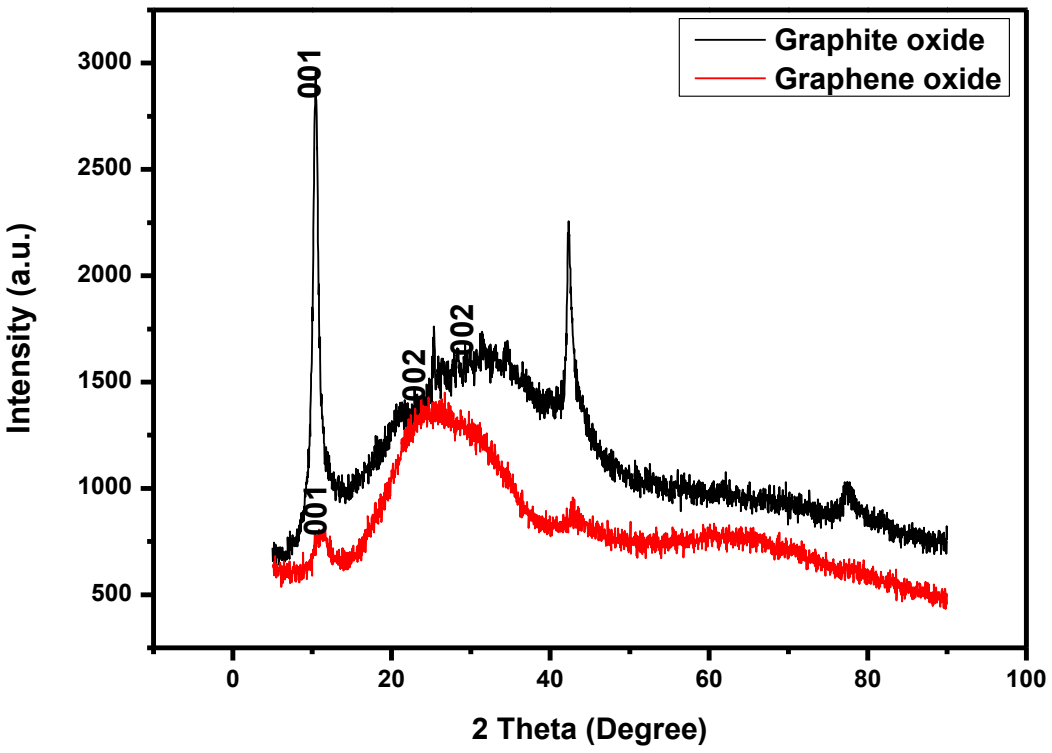

Figure 4.4: X-Ray diffraction spectrum of graphite oxide (GrO) and graphene oxide (GO).

4.1.1.4 Ultraviolet Visible Spectroscopy (UV-vis)

Figure 4.5 illustrates the ultraviolet-visible spectra of graphite oxide and graphene oxide. The spectrum of graphene oxide has a highest absorption peak at 208.70 nm while an absorption peak at 211.75 nm for graphite oxide was observed. This observed red shift occurs due to electronic configuration of graphite oxide when exfoliated to graphene oxide. Hence the highest absorption peaks are attributable to two types of electronic transitions, the first one being at 208.70 nm attributed to $\pi \rightarrow \pi^*$ to transition of aromatic C–C ring. The second absorption peak at 211.75 nm is attributed to $n \rightarrow \pi^*$ transition of C=O and C=C bonds that are embedded by intercalation and exfoliation on the graphene oxide. Hence, the ultraviolet-visible spectrum of graphene oxide illustrates the red shift at 211.75 nm. **(Liu., 2014)**

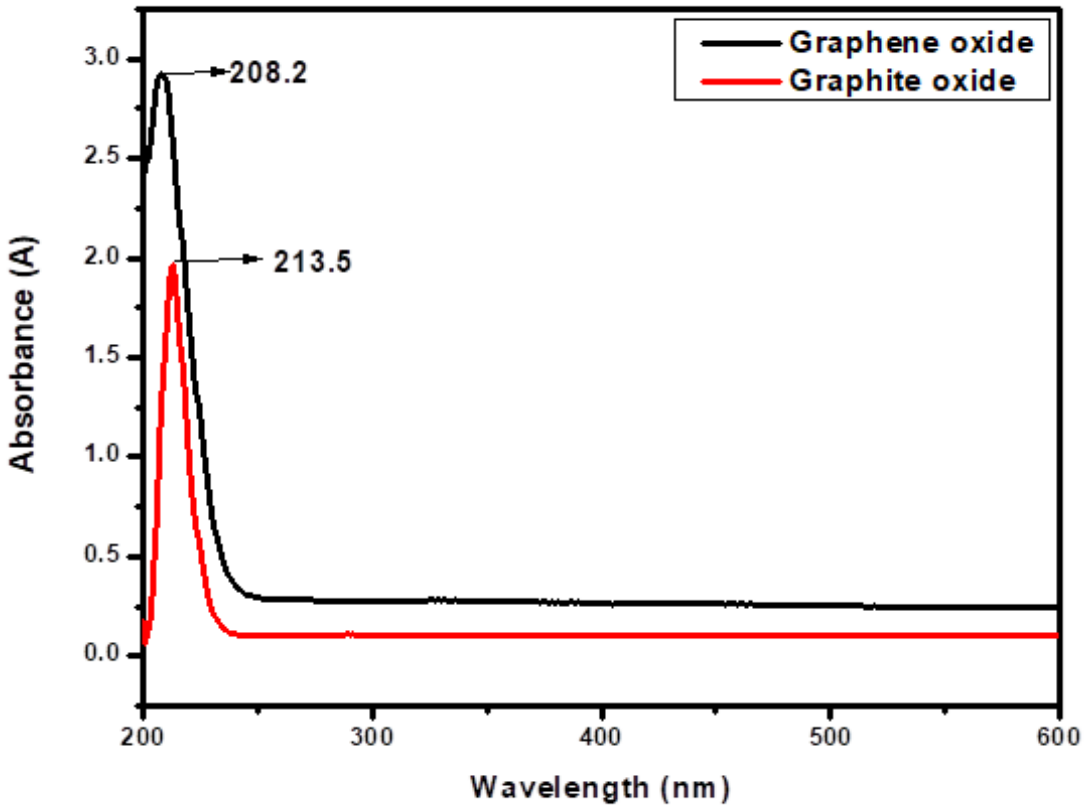

Figure 4.5: Ultraviolet-visible spectrum of graphite oxide (GrO) and graphene oxide (GO)

4.1.1.5 Photoluminescence Spectroscopy (PL)

Figure 4.6 shows photoluminescence excitation spectra for the emission wavelengths (λ_{em}) from 250 nm to 600 nm of graphite oxide (GrO) and graphene oxide (GO). The excitation wavelengths used was 490 nm and it was considered because it gave maximum and more linear emission spectra. The PL emission and excitation wavelengths were reproducible for graphite oxide indicating that the oxidation method was the determinant factor rather than the starting material. Previous studies have also presented similar emissions for GrO at around 342 nm and 407 nm and for GO which at around 334 nm and 435 nm upon different excitation wavelengths in the visible region.

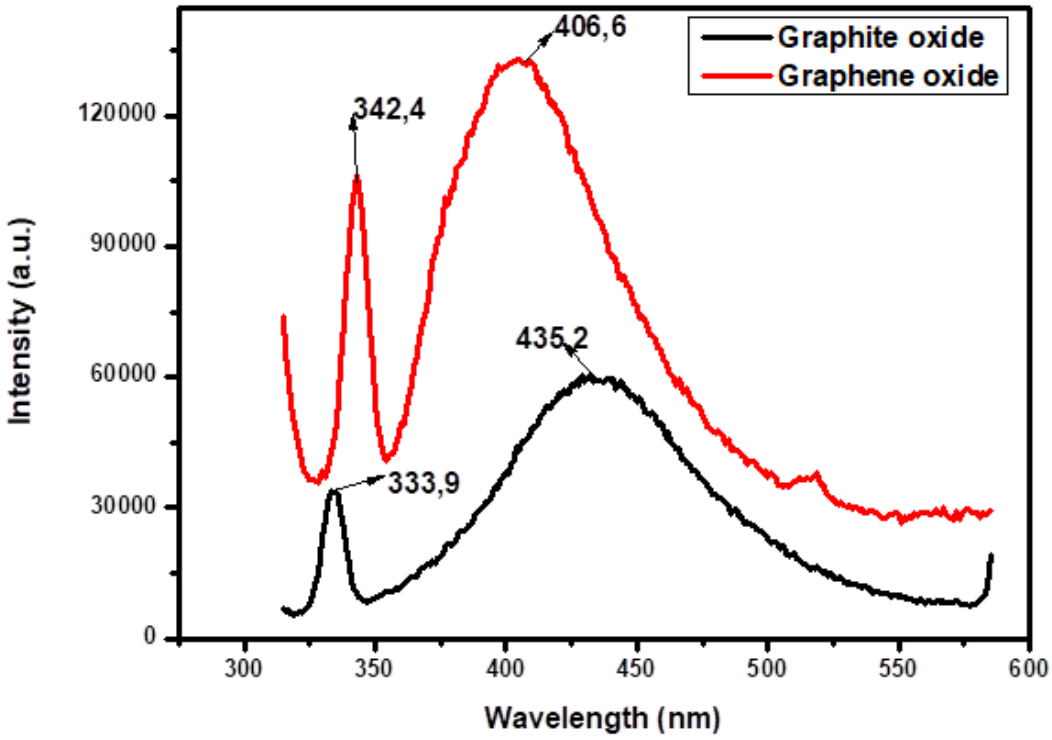

Figure 4.6: Photoluminescence spectrum of graphite oxide (GrO) and graphene oxide (GO).

The wavelength of emission was determined by the size of the sp^2 clusters within the sp^3 matrix in photoluminescence through local energy gap. The sp^2 cluster sizes < 1nm (~ 20 aromatic rings) resulted to emissions in the UV-visible region and those with smaller energy gaps >2 nm were accounted for red-to-NIR emission. The technique used for GO preparation appears to determine the amount and type of oxidation groups and hence act as the critical factor of the (PL excitation and emission wavelengths). Graphene oxide had larger emission peak intensities than graphite oxide due to its size (that is smaller than GrO when exfoliated) which relates to the stronger florescence intensity detected. Likewise variations in PL

emission correspond to the amplitude of the excitation spectrum are related to instrument detectivity **(Shukla and Saxena., 2011)**

4.1.2 Microscopic characterisation of graphene oxide and graphite oxide

4.1.2.1 High resolution transmission electron microscopy (HRTEM)

Figure 4.7 (a) and **(b)** shows HRTEM images for graphite oxide and graphene oxide. Their samples were prepared by pipetting the GrO and GO dispersion separately onto holey mesh grids. The HRTEM image of graphite oxide (**Figure 4.7(a)**) illustrates its graphitic structure as large thick dark flakes and also observed are large sheets that are situated on top of the grid resembling wavy silk veils. The sheets are entangled with one another and are not transparent. The structure of graphene oxide (**Figure 4.7(b)**) is different from that of graphite oxide (**Figure 4.7(a)**) because it appears smooth; flat with transparent layers on top of each other. Additionally, wrinkles and folding on the surface as well as the edges of the GO structure were observed. When graphene oxide was further studied at higher magnification it showed the more actual layers of graphene above 50 nm. **(Zhu *et al*., 2010)**

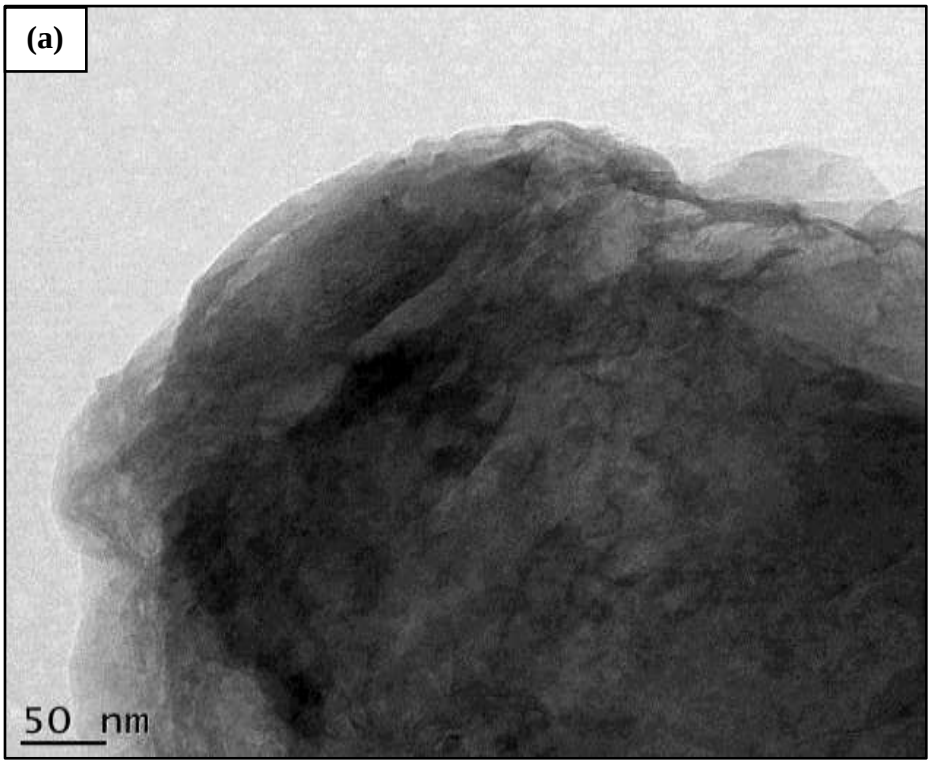

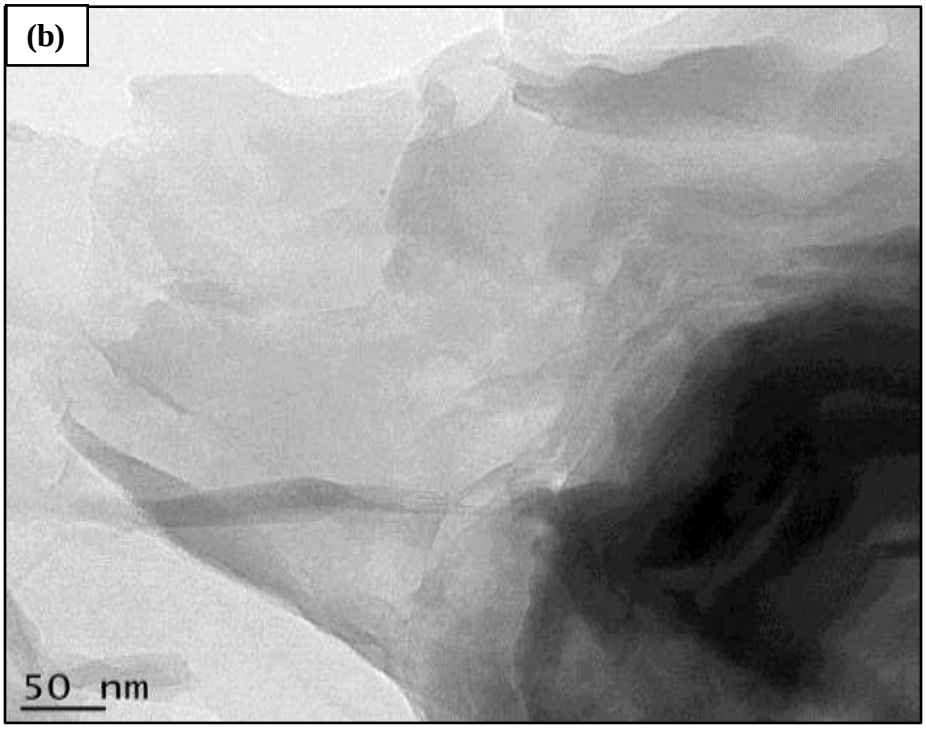

Figure 4.7: (a) HRTEM images of graphite oxide (GrO) and (b) HRTEM images of graphene oxide (GO).

4.1.2.1 High resolution Scanning electron microscopy (HRSEM)

The HRSEM images of graphite oxide (GrO) and graphene oxide (GO) are illustrated in **Figure 4.8 (a)** and **4.8 (b)**. The images were obtained by using High resolution Scanning Electron Microscopy regarding both graphite oxide and graphene oxide. The shape and size of the particles of both oxides (GrO ad GO) are dissimilar. GrO has more sheets than GO this is due to graphite that was certainly oxidized into graphite oxide and exfoliated to graphene oxide and hence the surface of graphite oxide is distinctly more developed. The structure of graphene oxide is smoother and flatter than that of graphite oxide and it shows a parallel arrangement of the respective layers. AFM also endorses this discussion.

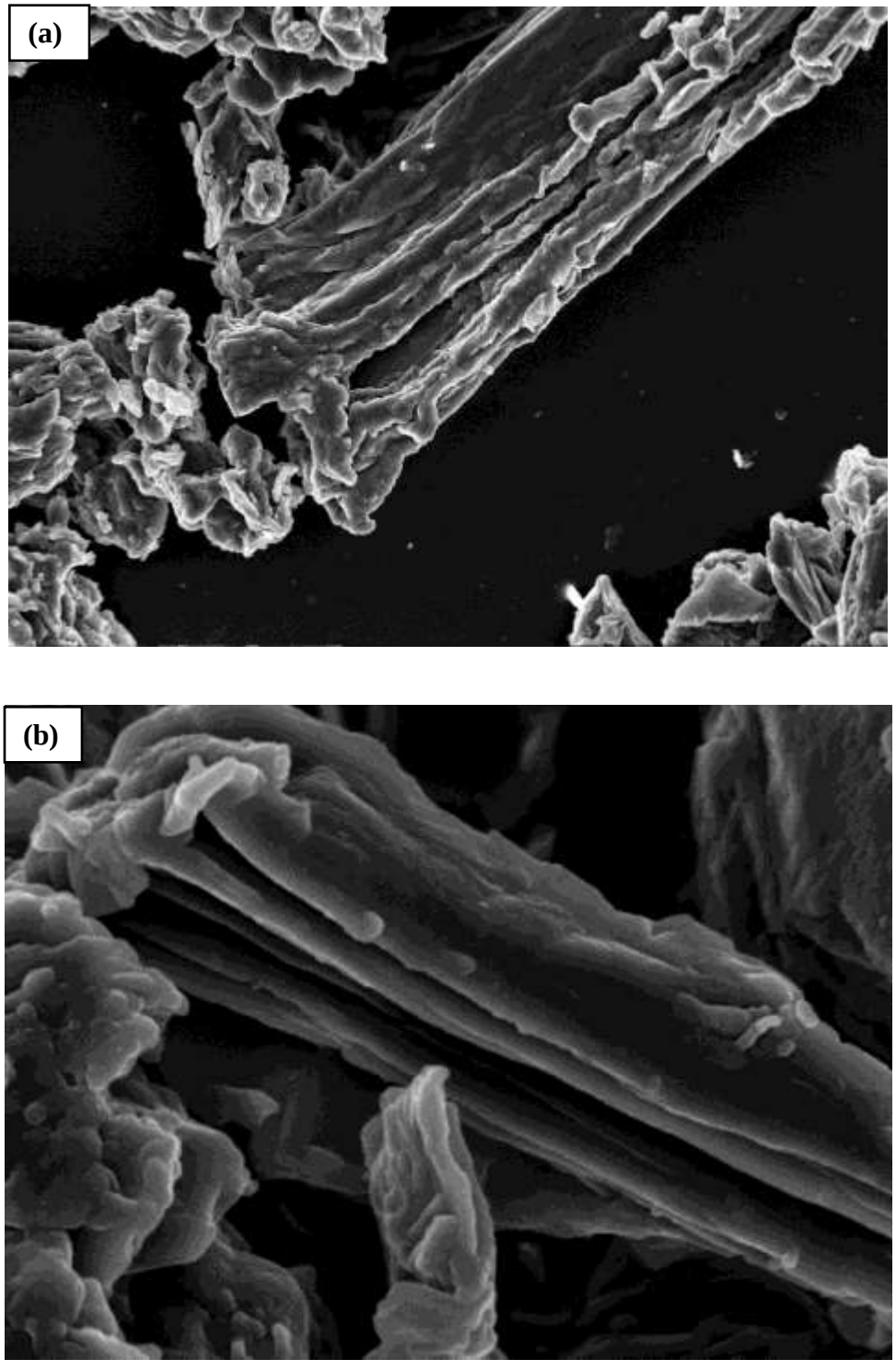

Figure 4.8: HRSEM images of (a) graphite oxide (GrO) and (b) graphene oxide (GO).

4.1.2.2 Energy dispersive X-ray (EDX)

Figure 4.9 (a) provides an elemental analysis of graphite oxide which was performed by Energy Dispersive X-ray (EDX) method. The percentages of the elements were determined from the intensity of the lines and are summarized in **Table 5.1**. From the chemical compositions obtained in the EDX spectra, it can be concluded that during the oxidation reaction of graphite, there was complete oxidation due to oxygen containing functional groups. The graphite oxide sheet obtained an enormous amount of oxygen containing functional groups for example, carboxylic acid group on the edge sites, hydrooxyl and epoxyl moieties on the basal plane. Other elements such as S, K and Mn were from the reagents used during the synthesis of graphite oxide.

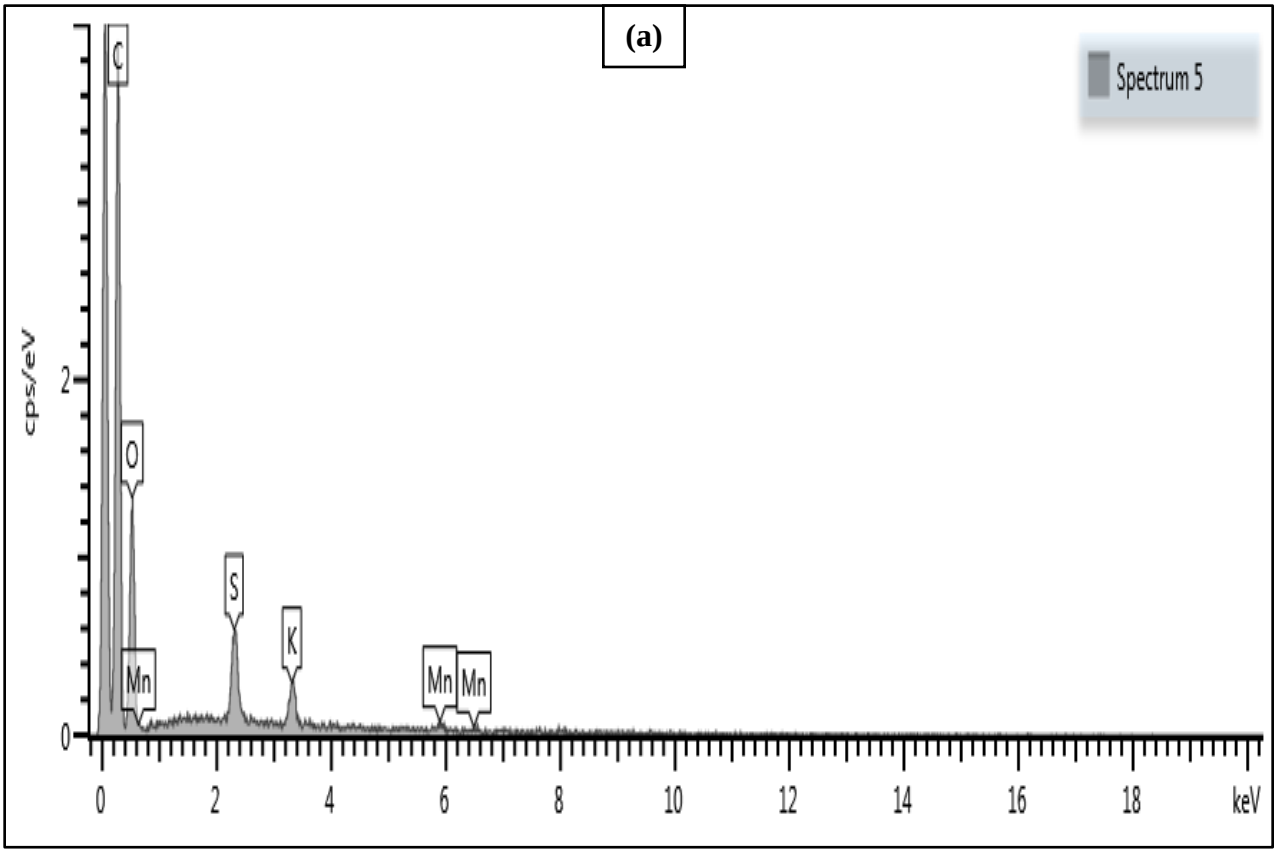

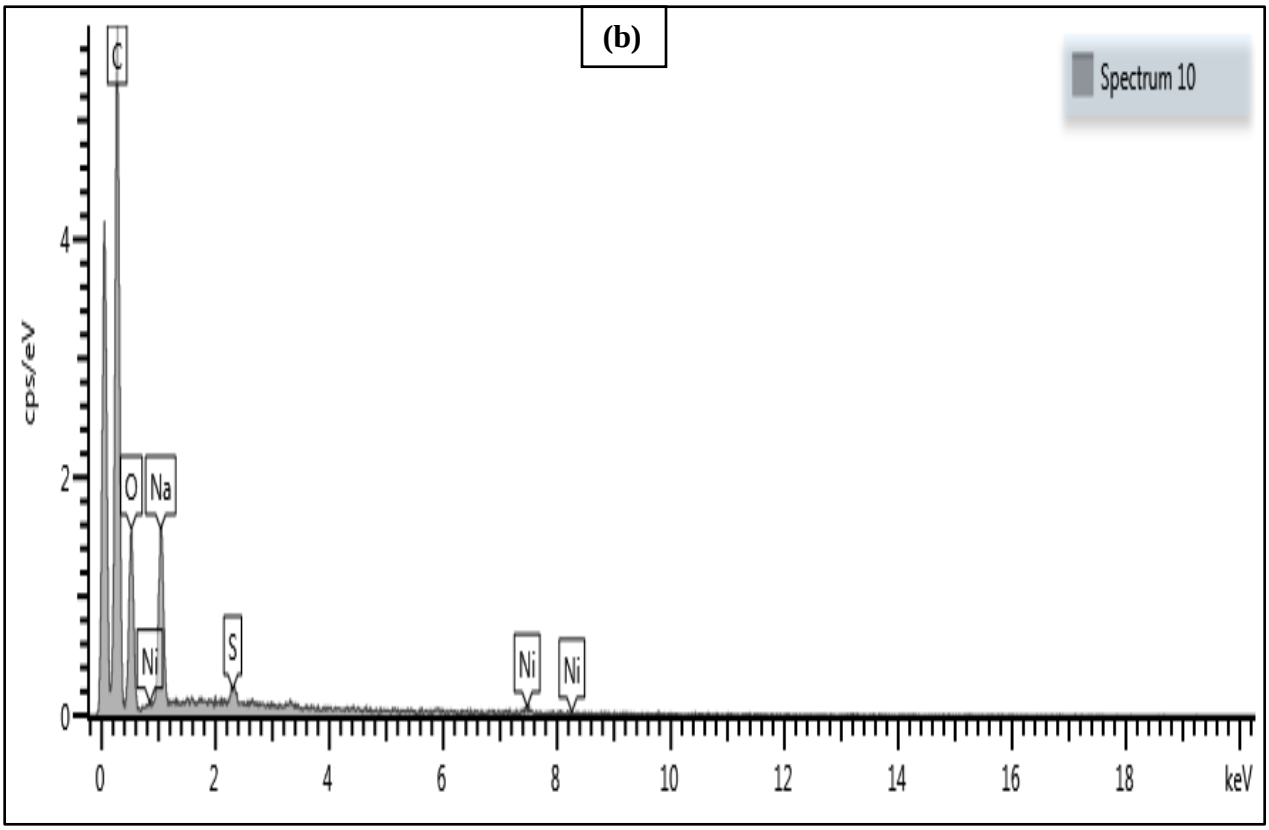

Figure 4.9: (a) Energy dispersive X-ray spectrum analysis of graphite oxide and (b) Energy dispersive X-ray analysis of graphene oxide.

Figure 4.9 (b) illustrates the elemental analysis of graphene oxide which was performed by Energy Dispersive X-ray (EDX) method. The percentages of the elements were determined from the intensity of the lines and are summarized in **Table 5.2** below.

Table 4.1 (a): Elemental composition of Graphite oxide.

Element	Weight percentage (%)	Weight percentage (%) Sigma
O	76.46	1.25
S	12.19	0.77
K	8.57	0.69
Mn	2.77	0.86
Total:	100	

Table 4.1 (b): Elemental composition of Graphite oxide (GO).

Element	Weight percentage (%)	Weight percentage (%) Sigma
O	48.7	1.19
Na	43.25	1.15
S	3.42	0.51
Ni	4.63	0.96
Total:	100	

From the chemical compositions obtained in the EDX spectrum, it can be determined that during the exfoliation reaction of graphite oxide some oxygen containing functional groups were removed. Hence, graphite oxide sheet obtained a fewer amount of oxygen containing functional groups. Other elements were from the reagents used during the exfoliation of graphite oxide.

4.1.2.3 Atomic Force Microscopy (AFM)

Atomic force microscopy (AFM) was also performed on graphite oxide and graphene oxide in order to characterize the degree of exfoliation. As of **Figure 4.10 (a)** graphite oxide seems to be well dispersed with wrinkles as well as numerous sheets were observed stacked on top of one another or together. For more analysis a certain part of graphite oxide pictures was enlarged and then studied using three-dimensional (3-D) view (**Figure 4.10 (a)**). Graphite oxide surface showed a bit roughness although layers could still be seen from the image. Also indicated was the cross sectional view of the graphite oxide that displays average thickness of GrO sheets as ~ 1.4 nm. AFM topography image of graphene oxide are represented in **Figure 4.10 (b)**. A flat and smooth graphene oxide sheets were observed and selected for further investigation using the 3-D view (**Figure 4.10 (b)**). The surface of graphene oxide was slightly rough and this could be caused by the less existence of some functional groups. Across the plain area of the sheet the cross sectional views an average thickness of 1.3 nm. **(Drewniak *et al*., 2016)** Thus AFM supported both HRTEM and HRSEM results in verifying the sheets of graphtite oxide which were more than graphene oxide due to more existence of some functional groups.

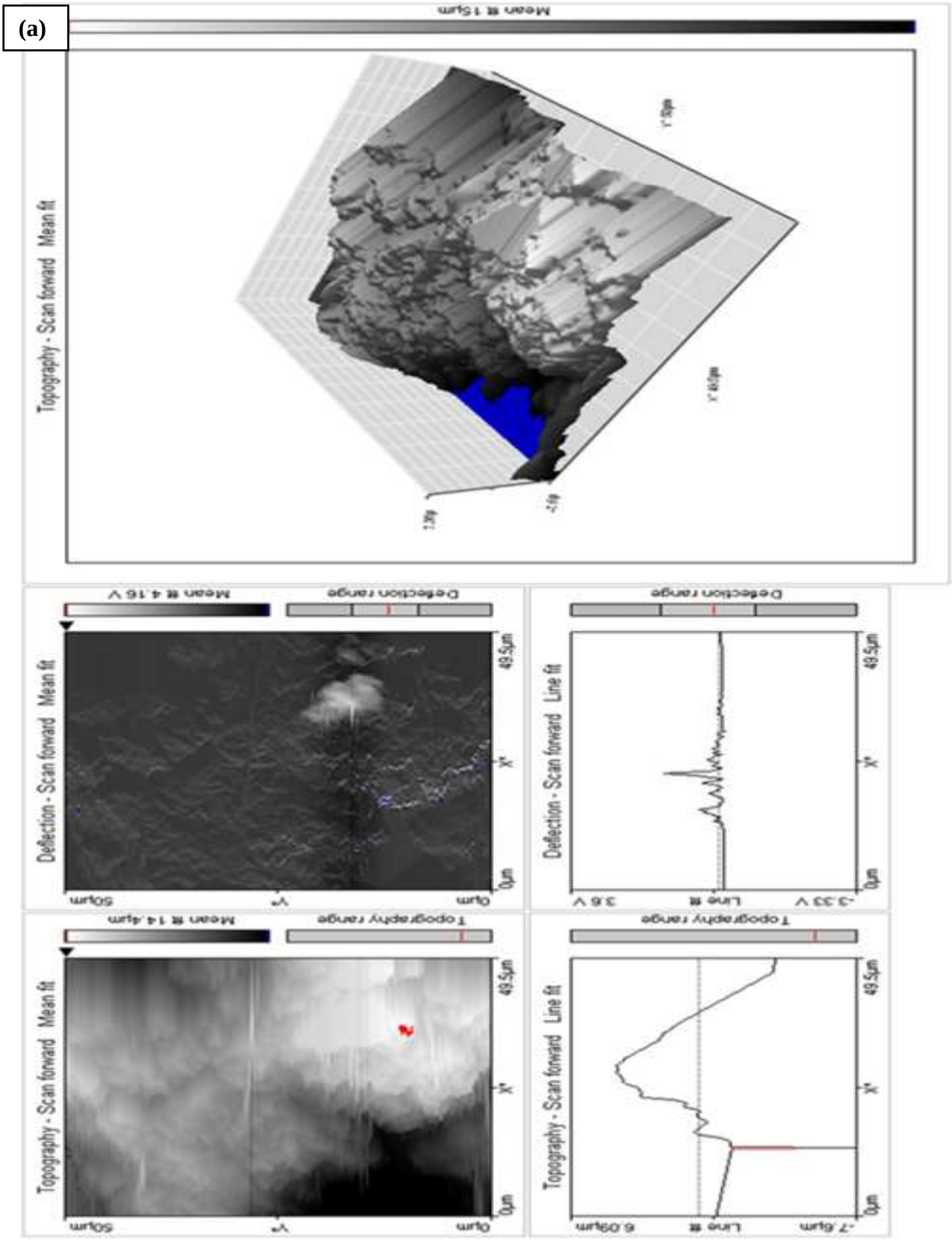
(a)
Topography - Scan forward Mean fit
Deflection - Scan forward Mean fit
Deflection - Scan forward Line fit
Topography - Scan forward Mean fit
Topography - Scan forward Line fit

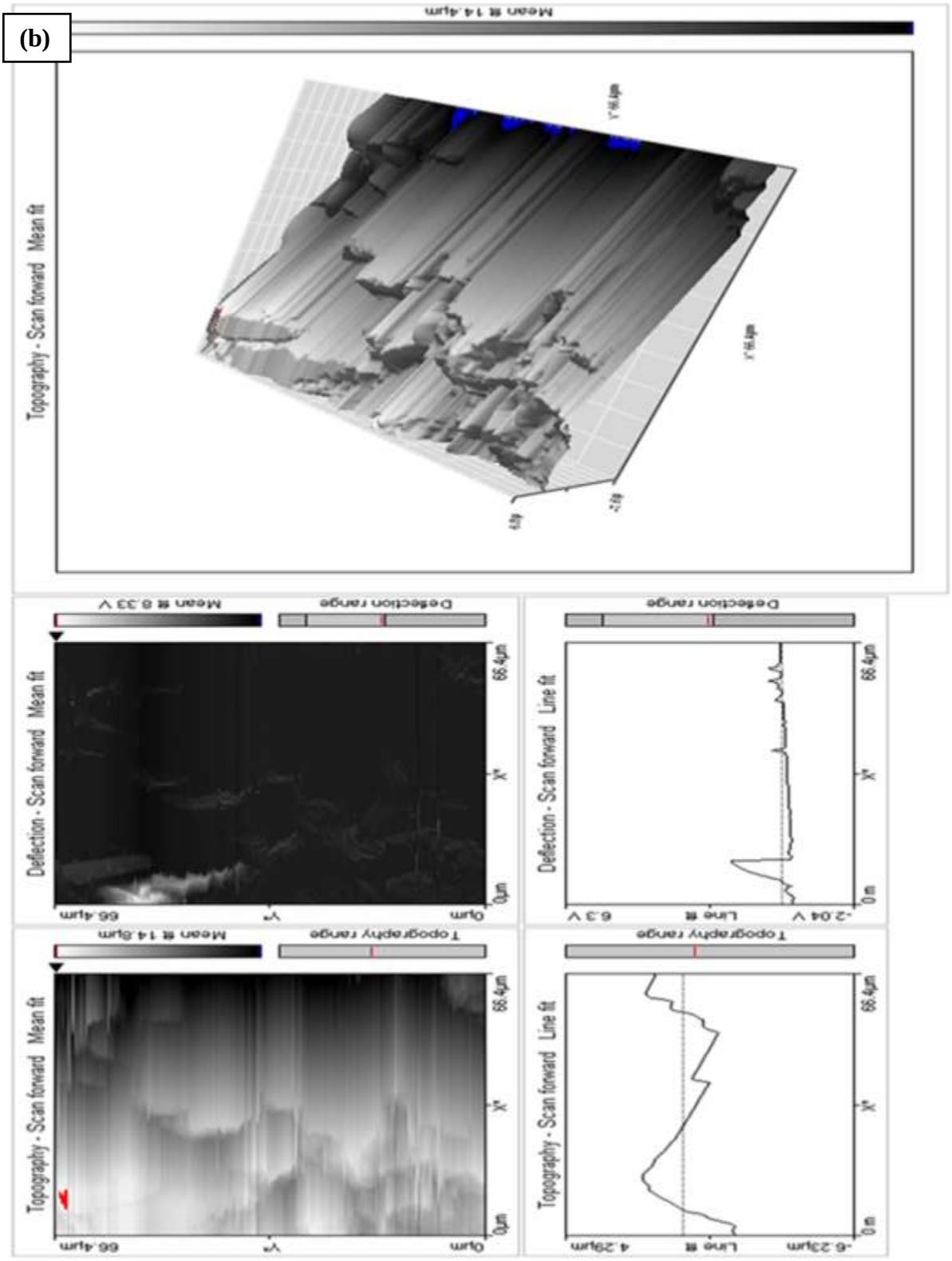

Figure 4.10: (a) Graphite oxide AFM topography image with 3-D representation and cross sectional analysis (b) Graphene oxide topography image with 3-D representation of the selected area and cross sectional analysis of the selected individual.

4.1.3 Electrochemical characterisation of graphene oxide and graphite oxide

4.1.3.1 Cyclic Voltammetry (CV)

Figure 4.11 illustrates the electrochemical response of graphite oxide (GrO) and graphene oxide (GO). Represented here are the bare glassy carbon electrode (**black curve**), graphite oxide on glassy carbon electrode (**red curve**) and graphene oxide attached on glassy carbon electrode (**blue curve**). As seen in the voltammogram different electrochemical responses were observed between graphite oxide and graphene oxide. GrO modified on glassy carbon electrodes indicated an increased peak current that is more than of GO suggesting more conductivity which could have been caused by large amounts of carbon−oxygen bonds contained by GrO. It has been proposed that the presence of a higher amount of oxygen functional groups on graphite oxide results in a slower electron transfer rate as well. Moreover, there is a slight shift in the potential which clearly indicates that there is electron transfer between the glassy carbon surface and GrO or GO. **(Ambrosi *et al*., 2014)**

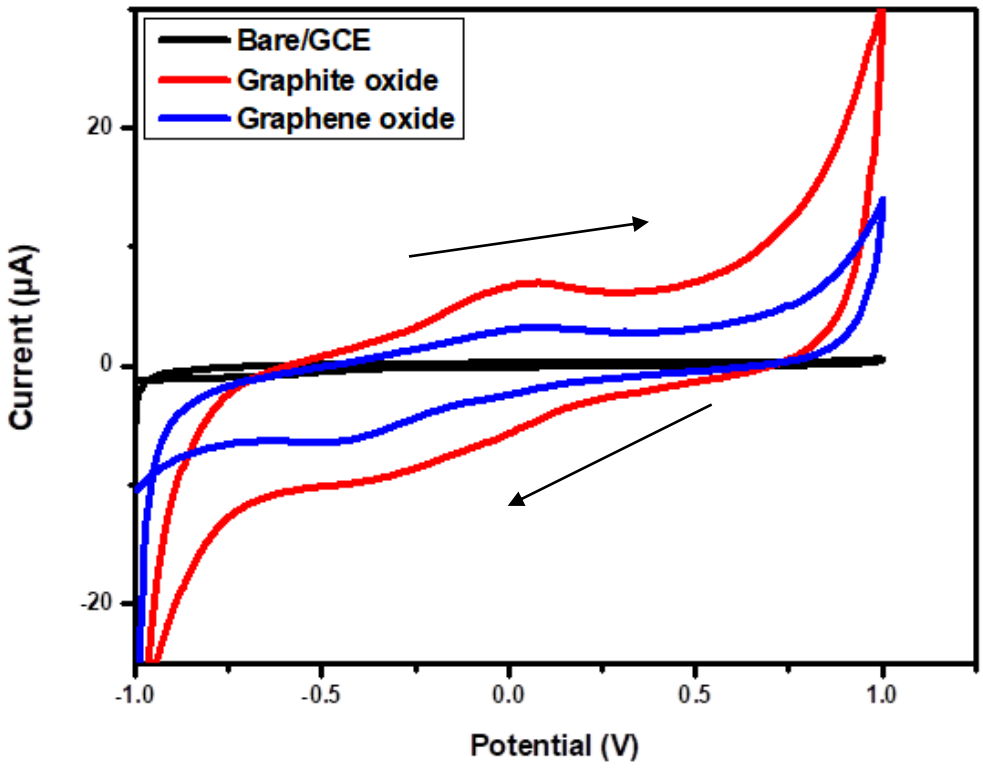

Figure 4.11: CV of bare Glassy carbon electrode (GCE) (black curve), Graphite oxide (red curve) and graphene oxide (blue curve) in phosphate buffer solution (pH 7.4) at 30 mV s^{-1}.

Additionally, the effect of scan rate on current peak was questioned by running a series of cyclic voltammogram at different scan rates from 10 to 100 mV s^{-1} (shown in **Figure 12**) where the chemically synthesized graphite oxide (**Figure 4.12 (a)**) and graphene oxide (**Figure 4.12 (b)**) where studied independently. The results shown by CV displays that the anodic peak current varies linearly with the scan rate and a shift in potential to more positive values with increasing scan rate was observed for each type material. This shows that these graphite oxide and graphene oxide are conductive while transferring electrons along the electrode surface. **(Thu *et al.*, 2018)**

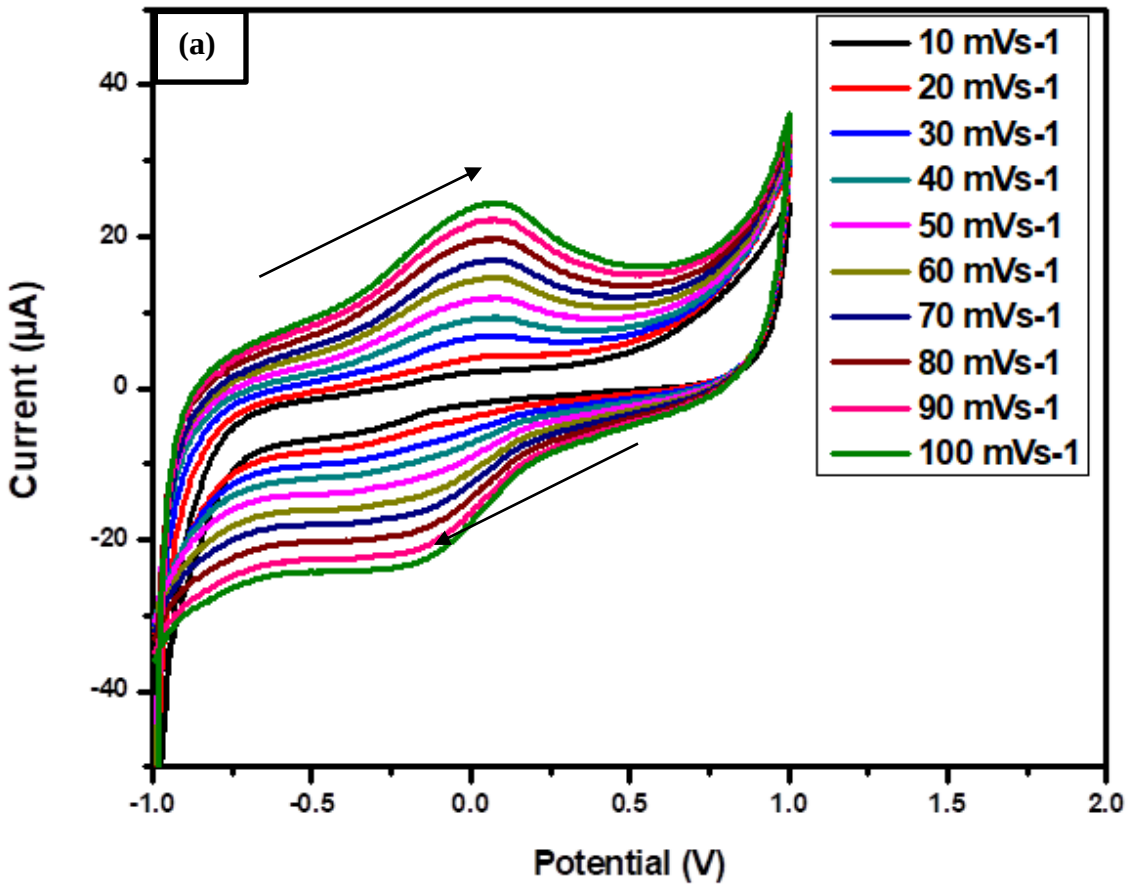
(a)
10 mVs-1
20 mVs-1
30 mVs-1
40 mVs-1
50 mVs-1
60 mVs-1
70 mVs-1
80 mVs-1
90 mVs-1
100 mVs-1
Current (µA)
Potential (V)
40
20
0
-20
-40
-1.0
-0.5
0.0
0.5
1.0
1.5
2.0

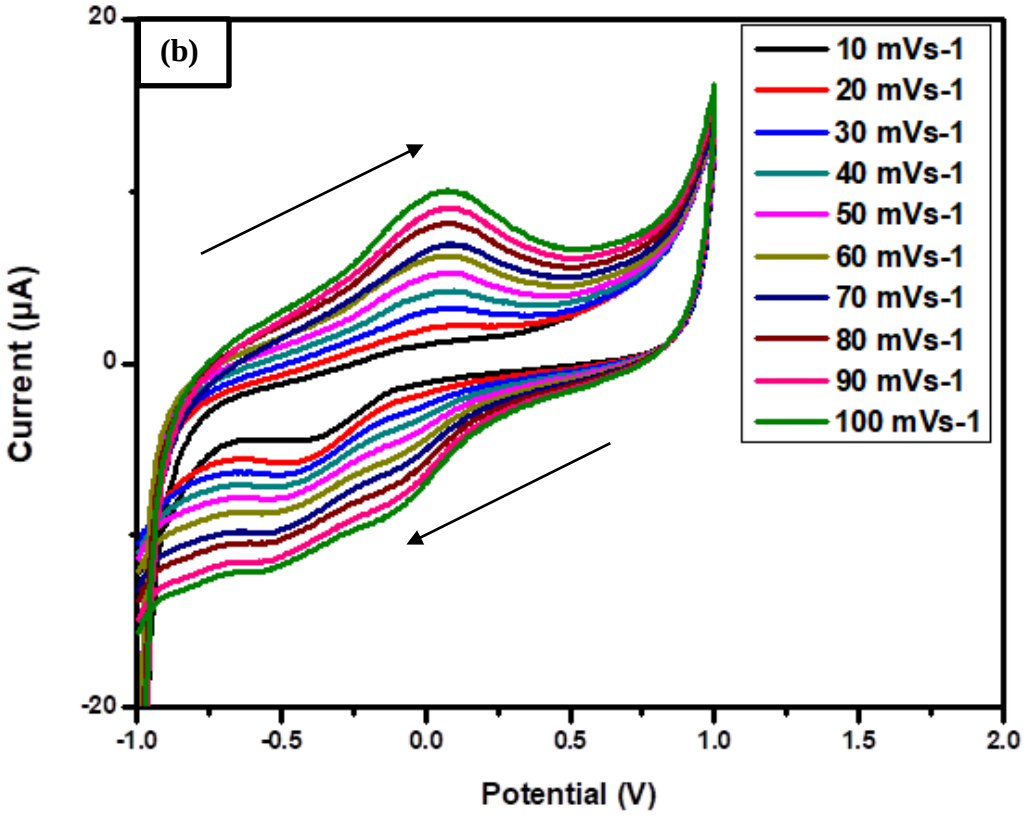

Figure 4.12: CV of graphite oxide (a) and graphene oxide (b) in 0.1 M phosphate buffer solution (pH 7.4) at 10-100 mV s^{-1}.

Additionally, a plot of log anodic current peak against the log scan rate was plotted for the graphite oxide where nearly a straight line with a linear regression I_{pa} (µA) = -0.0995*x*-0.3884 and a correlation coefficient r^2 = 0.9969 was determined as shown in **Figure 4.13 (a)**. A similar plot was plotted for graphene oxide as demonstrated in **Figure 4.13 (b)** where the linear regression was I_{pa} (µA) = -0.064*x*-0.4477 and the correlation coefficient was r^2= 0.9913. In both cases the plots indicate a clear sign of the dependence of anodic peak current on the scan rate. **(Peik-See *et al*., 2014)** Moreover, I_{pc} / I_{pa} of graphite oxide and graphene oxide was obtained to be ~1.4 and ~2.0 µA using current values obtained in **Figure 4.11**

confirming that both material performed as a stable redox species adsorbed on the electrode surface undergoing reversible electrochemistry as also confirmed by similar studies by **Wester. 2015 and Boikanyo, 2015.** The peak-to-peak separations (ΔE_p = [E_{pa} – E_{pc}]) was also determined for GrO to be 0.40 mV and for GO it was 0.60 mV at different scan rates; the results at 50 mVs^{-1} showed a lower ΔE_p than 57/n. Therefore the analysis of the peak-to-peak separation (ΔE_p) indicated a dependence on the scan rate demonstrating the electrochemical process to be classed as semi-reversible within the scan rates employed.

"However for a system be to reversible, the difference should be 57/n mV^{-1} at 25 ^{o}C, when this is true the rate of oxidation and reduction are equal. In addition, ΔE_p should be independent of scan rate and the current passed at reduction (I_{pa}) and oxidation (I_{pc}) should increase in proportion to scan rate. The values of I_{pa} and I_{pc} should be similar in magnitude. On the other hand, if the ratio of I_{pc} and I_{pa} is greater or less than one, this indicates a semi-reversible reaction which is dependent on scan rate" **(Tomás., 2017)**

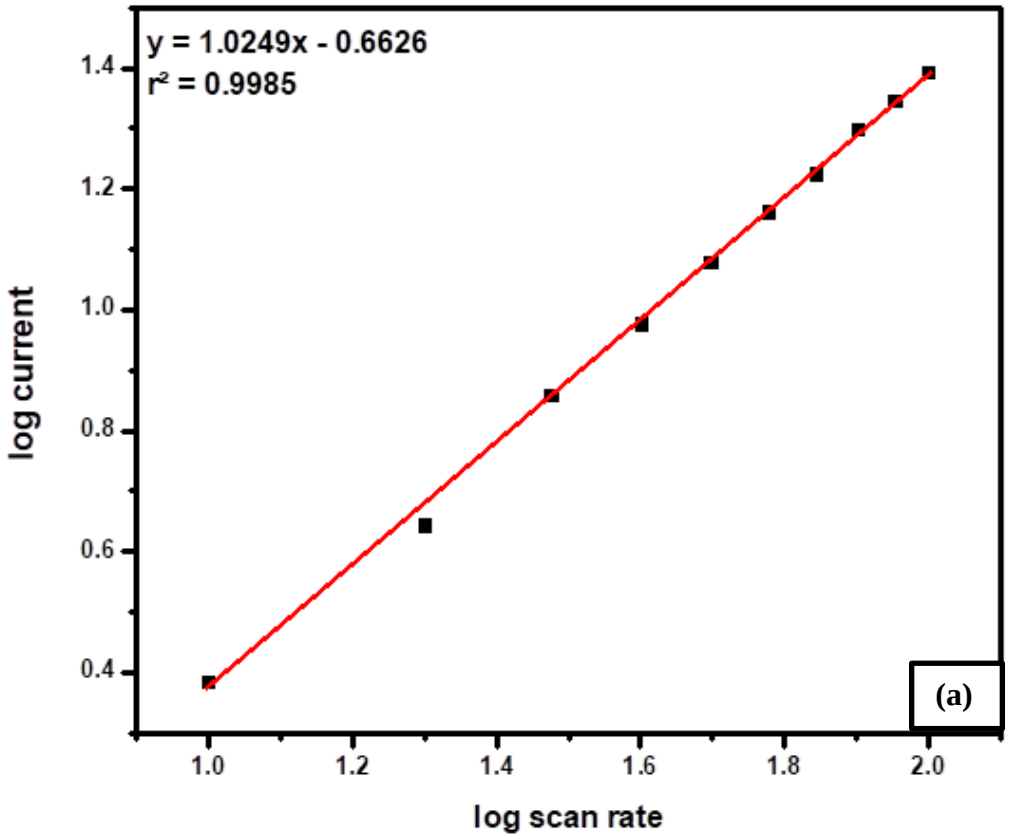
y = 1.0249x - 0.6626
r² = 0.9985
log current
log scan rate
1.4
1.2
1.0
0.8
0.6
0.4
1.0
1.2
1.4
1.6
1.8
2.0
(a)

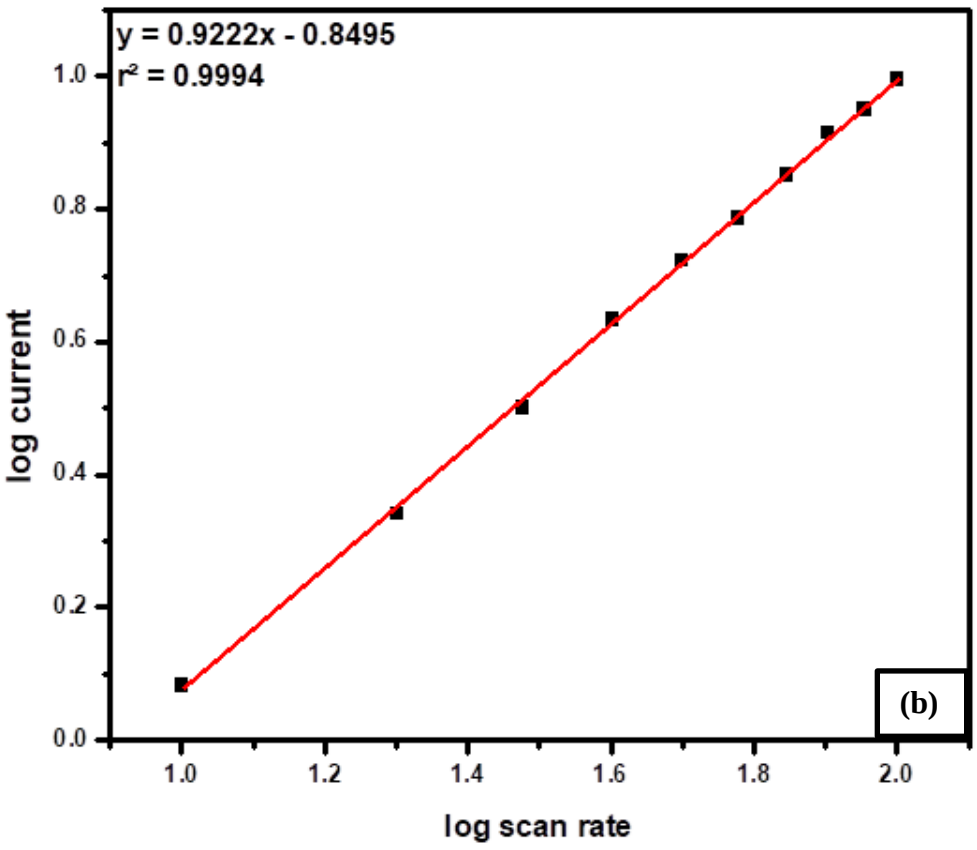

Figure 4.13: Plots of log current versus log scan rate of graphite oxide (a) and graphene oxide (b).

The surface concentration was also determined for graphite oxide and graphene oxide using Brown Anson equation (**Equation 4.1**). From the equation, F is the faraday constant (96485 C mol-^{1}), A is the surface area of the glassy carbon electrode (0.043 cm^{2}), n is the number of electron transferred (n = 2), υ is the scan rate (V s^{-1}), T is the operating absolute temperature of the system (25 ℃ T in 298 K), R is the gas constant (8.314 J mol-1 K^{-1}), Γ* represent the surface concentration of the GrO and GO (mol cm^{-2}) The surface concentration (Γ*) of graphite oxide resulted was calculated to be 1.4379 x 10^{-3} mol cm^{-2} and that of graphene oxide was calculated to be 6.6673 x 10^{-4} mol cm^{-2}. As projected, the surface concentration of

graphite oxide was a little higher than that of the graphene oxide which was resultant from the structure of the materials that has more functional groups.

$$\mathbf{I_p = n^2 F\ ^2 \Gamma^* A \nu / 4 R T} \qquad \textbf{(4.1)}$$

The Diffusion coefficient was also determined for GO and GrO using the Randel-Sevcik Equation (**Equation 4.2**) at 25 ^{O}C. A value of 7.3235 x 10^{-4} cm^2/s was determined for graphite oxide while a value of 6.6512 x 10^{-4} cm^2/s was determined for graphene oxide. As expected graphite oxide indicated a slightly faster coefficient than graphene oxide that resultant from the thick layers on the glassy carbon surfaces which impede the flow of electrons, thus supporting the surface concentration value determined above.

$$\mathbf{Ip = 268,600\ n^{3/2} AD^{1/2} C\nu^{1/2}} \qquad \textbf{(4.2)}$$

Apart from the synthesis of graphite oxide which led to graphene oxide (the focus of this work); this study also involved the synthesis of green method nanoparticles. The aim was geared at developing electroactive compites to use in sensor construction. Below is the discussion of the data received from those studies.

4.2 Green synthesized nanoparticles

The use of plant extract in the biosynthesis of nanoparticles (NPs) has been suggested as a possible substitute to classic methods namely; chemical and physical methods due to their eco-friendly approach. In this study, the biosynthesis of silver nanoparticles (AgNPs) and zinc oxide (ZnONPs) by both "microwave irradiation" (MI) and "conventional heating" (CH) procedures has been reported. Spherical and stable nanoparticles were produced using silver nitrate for AgNPs and zinc nitrate for ZnONPs using a mixture of tomato and apple extract as a precursor.

The tomato and apple extract acted as capping and reducing agents for the generation of both AgNPs and ZnONPs. The morphological, structural and colloidal properties of the as-synthesized nanoparticles have been confirmed by Fourier transform Infrared (FTIR) and Energy Dispersive X-ray (EDX). In comparison with the conventional method, the microwave irradiation is more advantageous because of the nanoparticles are synthesised in a short reaction time owing to the high heating rate and therefore accelerating the reaction rate. Yet, the disadvantage of using MI is that it is not cost effective and challenging to maintain the equipment is very expensive. However, both the techniques; CH and MI led to the synthesis of nearly identical nanoparticles with respect to size and shape according to the results discussed below from UV-vis, TEM and SAXspace techniques. **(Jafarirad *et al.*, 2016)** The use of both methods was to ascertain which of the two methods would produce highly electroactive nanoparticles as this is an imperative quality when developing sensors. Additionally, the chosen one will also be compared to chosen zinc oxide nanoparticles also synthesized using both methods. The idea is to ascertain which of these four sets of nanomaterials superior, stable and electroactive enough to be applied towards

sensor/biosensor development. Discussions below will indicate which of these nanomaterials is ideal for this specific application.

4.2.2 Green synthesized silver nanoparticles (AgNPs)

4.2.2.1 Spectroscopic characterisation of silver nanoparticles (AgNPs)

4.2.2.1.1 Fourier transform infrared spectroscopy (FTIR)

In this study FTIR analysis gave a clear indication of the functional groups involved in the CH and MI synthesis of silver nanoparticles (AgNPs). **Figure 4.14** illustrates the FTIR analysis of tomato and apple extract mediated synthesized nanoparticles. FTIR analysis of apple and tomato showed a broad peak at 3908 cm^{-1} corresponding to O-H stretch of phenols, intermediate peak attained at in the range of 2220 and 2124 cm^{-1} corresponded to C-H stretch of alkanes, the peak at 1898 cm^{-1} signified the presence of the C=O stretch of conjugated aldehydes, the medium peak obtained at 1720 and 1542 cm^{-1} corresponds to C=C stretch of unsaturated ketones and the O-H bend of alcohol respectively.

The FTIR analysis of conventional green synthesized silver nanoparticles (black) represented a broad peak at 3444 cm^{-1} corresponded to O-H stretch of phenols, intermediate peaks attained at 2742 and 2410 cm^{-1} demonstrated the presence of C-H stretch of alkanes, a medium broad peak at 1624 cm^{-1} corresponded to N-H bend of amine, a weak peak at 1376 cm^{-1} representing the C-H bend of alkane and a medium peak at 1060 cm^{-1} corresponded to C-O stretch of alkanes.

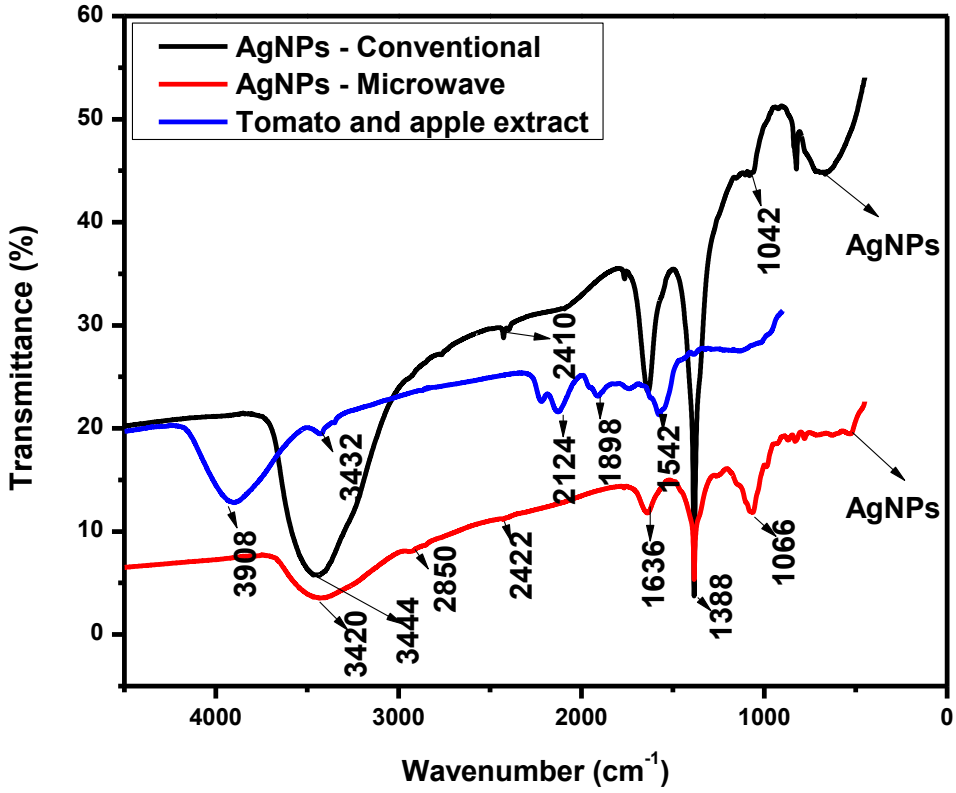

Figure 4.14: Fourier transform infrared spectrum (FTIR) of conventional green synthesized silver nanoparticles (black line) microwave green synthesized silver nanoparticles (red line) and Tomato and apple extract (blue line).

The FTIR spectrum analysis of the microwave green synthesized silver nanoparticles (red) illustrates a band at 3420 cm^{-1} resulting from the O-H stretch while the band at 1388 cm^{-1} is due to O-H bending. Intermediate peaks attained at 2850 and 2422 cm^{-1} demonstrated the presence of C-H stretch of alkanes, a medium broad peak at 1636 cm^{-1} corresponded to N-H bend of amine, a weak peak at 1388 cm^{-1} represented the C-H bend of alkanes and a medium peak at 1066 cm^{-1} corresponded to C-O stretch of alkane.

The characteristic peaks of Ag nanoparticles are ascribed to the absorption bands in the range 400-800 cm^{-1} in the FTIR spectrum of both green conventional heating and green microwave irradiation synthesized Ag. Weak peaks obtained at 662 cm^{-1} (CH) and 542 cm^{-1} (MI) correspond to C-H bend of alkynes. The disappearance of C=O stretch of aldehyde in nanoparticle showed the absorbance of this band in the nanoparticle. Therefore, it could be concluded that aldehyde groups has assisted in nanoparticle synthesis. **(Agarwal *et al*., 2018)**

4.2.2.1.2 Ultraviolet Visible Spectroscopy (UV-vis)

Figure 4.15 illustrates UV–vis spectra of silver nanoparticles (AgNPs) which is synthesized using conventional heating and microwave irradiation methods. The absorption peak intensity of the dispersion obtained by conventional method was lower as seen at 213.1 to 214.4 nm for the microwave irradiation. This shift in wavelength and high peak indicate that the size of silver nanoparticles in microwave heating is smaller and has a higher density compared to those developed using conventional heating which reflected a more uniform size distribution. The obtained concentration of silver nanoparticles (AgNPs) by conventional heating and microwave irradiation were 0.102 and 0.136 mg/L, respectively, confirming a high density of silver nanoparticles produced by the microwave irradiation method which confirmed the observation in the UV–vis spectra (**Figure 4.15**). **(Noroozi *et al*., 2012)**

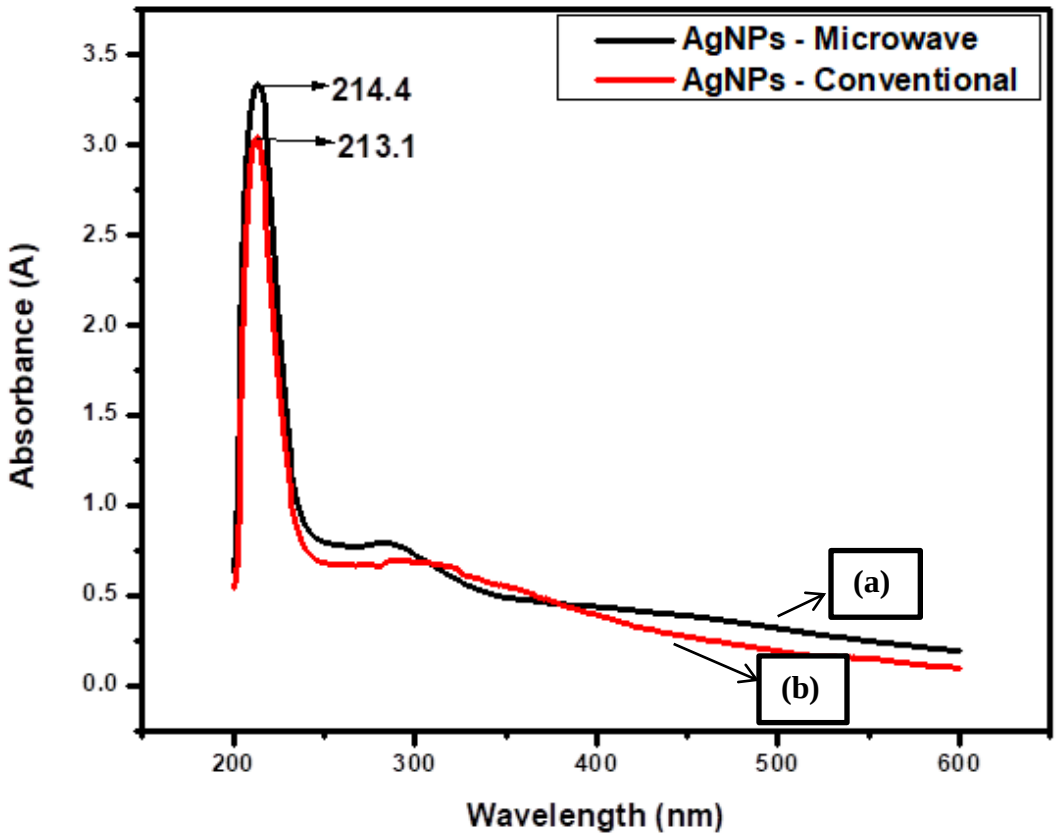

Figure 4.15: Ultraviolet-visible spectrum of (a) microwave green synthesized silver nanoparticles and (b) conventional green synthesized silver nanoparticles.

4.2.2.2 Microscopic characterisation of silver nanoparticles (AgNPs)

4.2.2.2.1 High resolution transmission electron microscopy (HRTEM)

The High resolution transmission electron microscopy (HRTEM) micrographs of the MI and CH synthesized silver nanoparticles (AgNPs) were conducted as shown in **Figure 4.16** in order to access some insight into the size distribution and the morphology of the achieved AgNPs. It is evidently shown from the HRTEM images that the AgNPs are well dispersed and there are almost no aggregates of these nanoparticles observed. Previous studies reported that the morphology of the heating-synthesized AgNPs is oval or spherical shape. **(Santra *et al.*, 2014)** In this work we found the common spherical and oval shapes but the particles sizes

differed for MI and CH methods showing that some AgNPs can contain stacking faults randomly and multiple twins inside these particles. Also, it was found that the size distribution of AgNPs varied with different methods of synthesis.

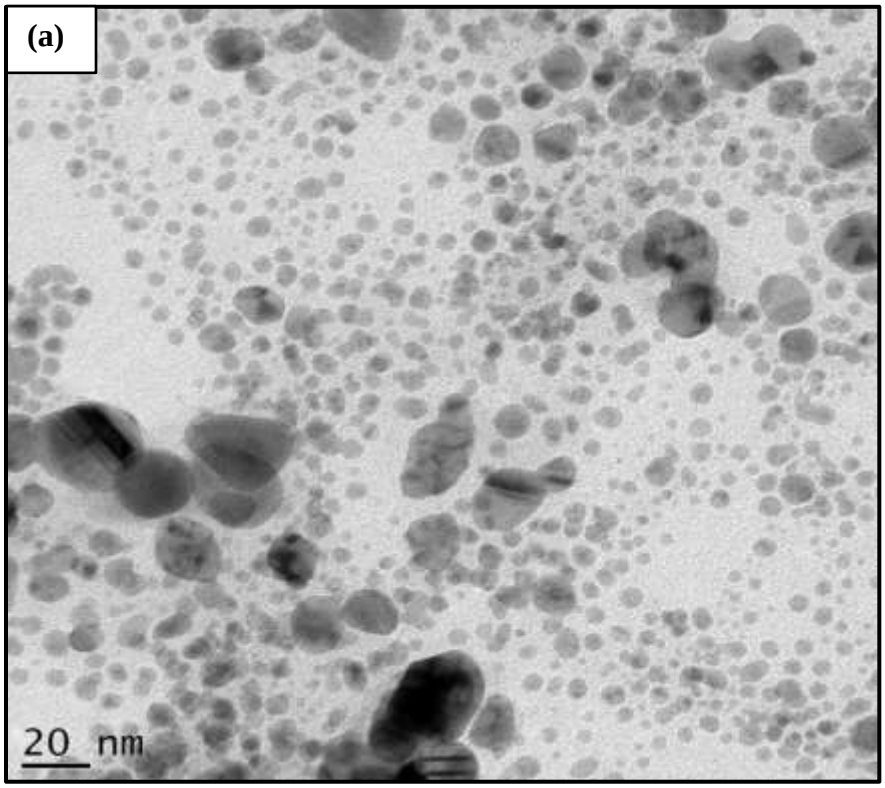

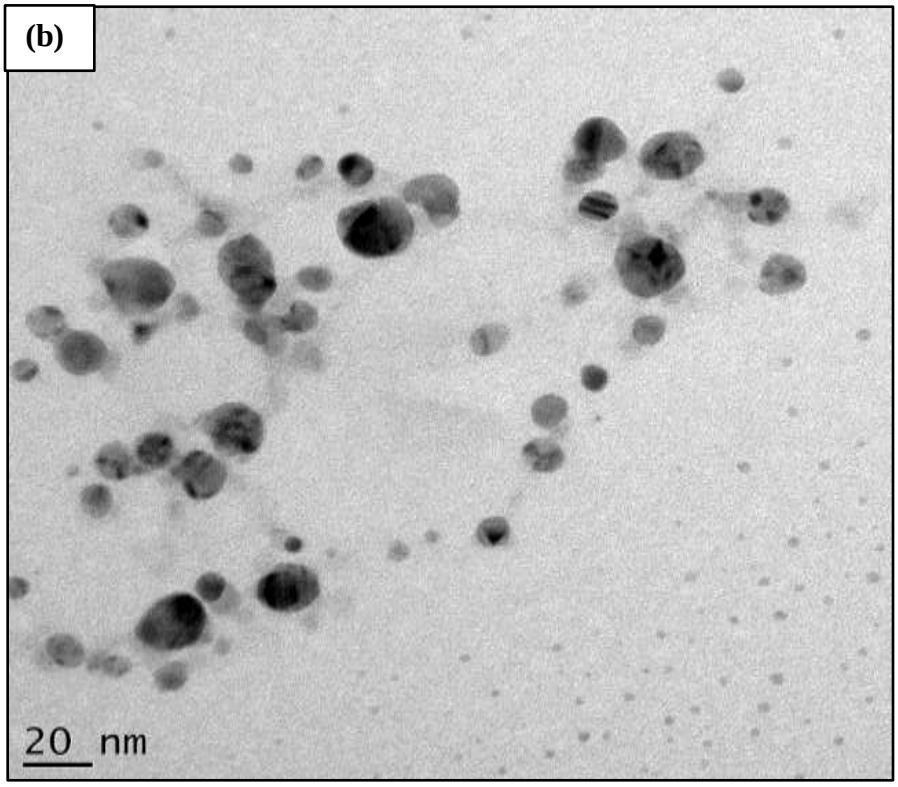

Figure 4.16: HRTEM images of (a) microwave green synthesized silver nanoparticles and (b) conventional green synthesized silver nanoparticles.

In **Figure 4.17**, the histogram evidently shows that the silver nanoparticles obtained from the CH (**Figure 4.17 (a)**) have a higher standard deviation of 12.67 nm compares to those produced with the MI method (**Figure 4.17 (b)**) where a value of 8.71 nm was determined. The silver nanoparticles produced by MI are decrementing in size attributed to the effectiveness of the electromagnetic field in heating the polarizing water molecules. With CH, the solvent was heated through convention and conduction so that there can be a large temperature distribution within the solvent. Prompt heating by MI produced a narrow size distribution of silver nanoparticles as opposed to those synthesized conventionally.

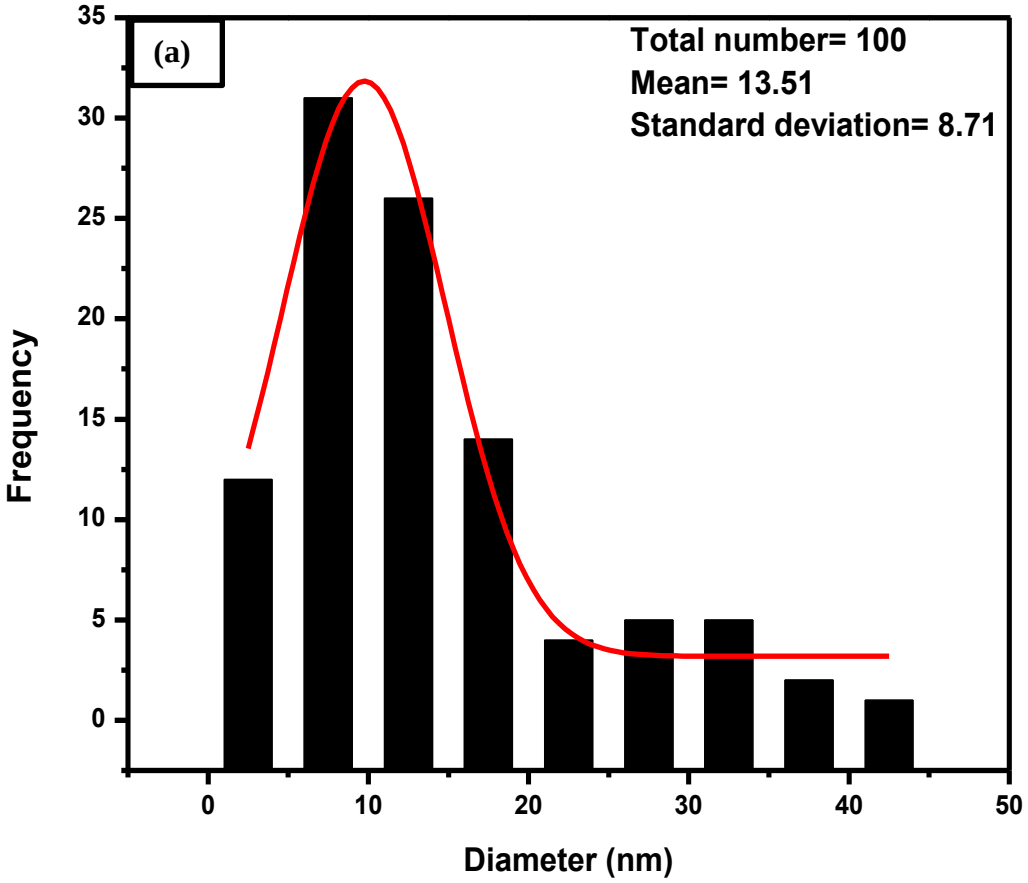
(a)
Total number= 100
Mean= 13.51
Standard deviation= 8.71
Frequency
Diameter (nm)
0
5
10
15
20
25
30
35
0
10
20
30
40
50

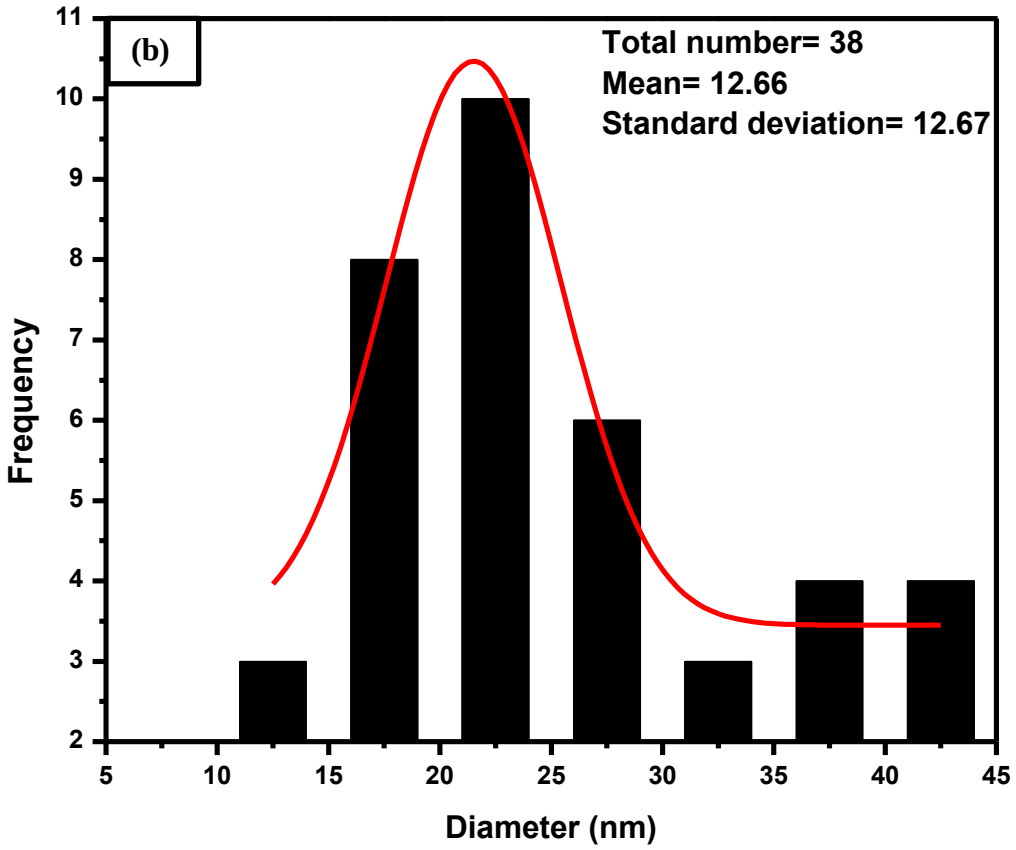

Figure 4.17: Particle size distribution of (a) microwave green synthesized silver nanoparticles and (b) conventional green synthesized silver nanoparticles.

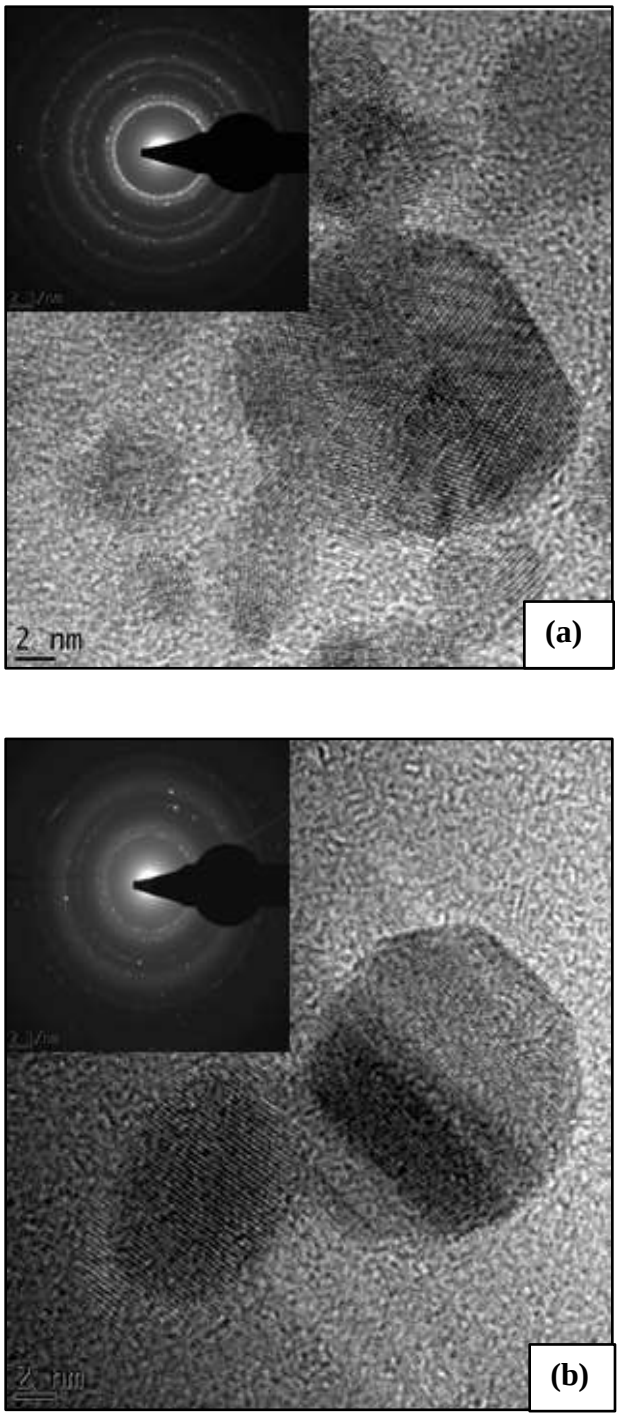

Figure 4.18: (a) Conventional green synthesized silver nanoparticles (AgNPs) and (b) microwave green synthesized silver nanoparticles (AgNPs) at 2.1 nm scale view. Insert SAED pattern.

The selected area electron diffraction (SAED) pattern in the insert of **Figure 4.18** illustrated distinct bright rings that confirm the superior orientation of nanocrystals instead of uneven ones which can be indexed to the oval and spherical structure of Ag with phase purity. The AgNPs with such structure are more appropriate for the immobilization of biomolecules and they are known to further enhance the performance of biosensors. **(Haider *et al*., 2018).**

4.2.2.2.2 Energy dispersive X-ray (EDX)

The elemental composition of both conventional green synthesized AgNPs (**Figure 4.19 (a)**) and microwave green synthesized AgNPs (**Figure 4.19 (b)**) was studied using energy dispersive X-ray (EDX) spectroscopy. For conventional green synthesized AgNPs, the presence of phosphorus (P) element was due to the mineral phosphorus in apple and tomato extract that is reported to improve the antioxidant activity of extracts and the levels of amino acids and polyphenols (**Shi et al., 2014)**. The EDX of the conventional green synthesized AgNPs and microwave green synthesized AgNPs revealed that the most abundant element to be Ag indicating the formation of the nanoparticles. The EDX spectra both presented the presence of copper (Cu) which is as a result of the copper grid used throughout the sample preparation proceeding to analyses.

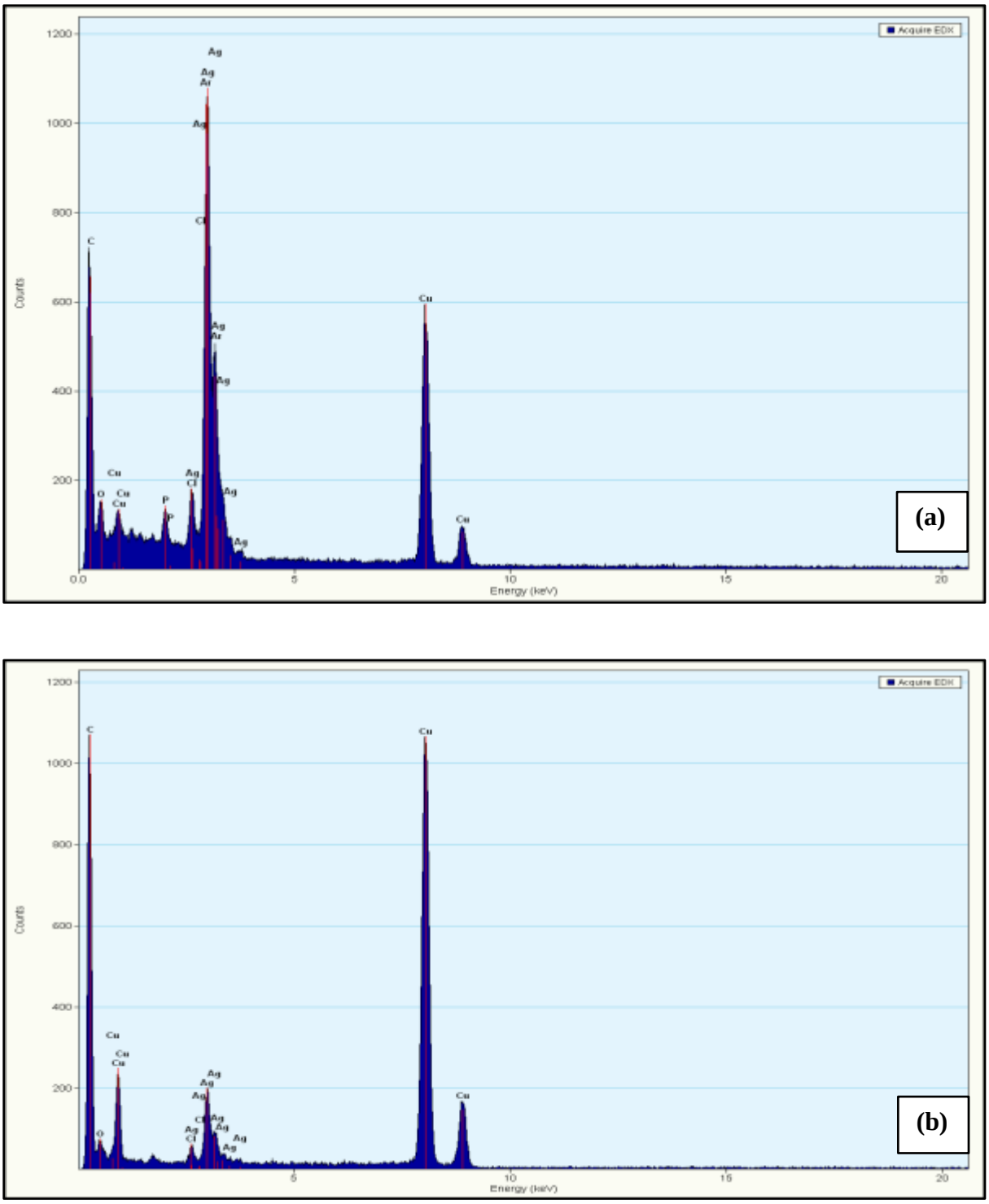

Figure 4.19: Energy dispersive X-ray spectrum analysis of (a) conventional green synthesized silver nanoparticles (AgNPs) and (b) microwave green synthesized silver nanoparticles (AgNPs).

4.2.2.3 Electrochemical characterisation of silver nanoparticles (AgNPs)

4.2.2.3.1 Cyclic Voltammetry (CV)

Figure 4.20 shows the electrochemical response of silver nanoparticles (AgNPs) which were synthesized using two different methods; Microwave Irradiation (MI) and Conventional Heating (CH). Denoted here is the bare glassy carbon electrode (black), microwave green synthesized silver nanoparticles (Red) and conventional green synthesized silver nanoparticles (Blue) evaluated in 0.1 M PBS buffer, pH 7.4. The potential window from -1.0 to 1.0 V was used at a scan rate of 30 mV/s. **Figure 4.20** illustrates a well-defined redox couple; a cathodic and anodic peak for the silver nanoparticles. These results prove that the AgNPs show a different redox response compared to the bare glassy carbon electrode.

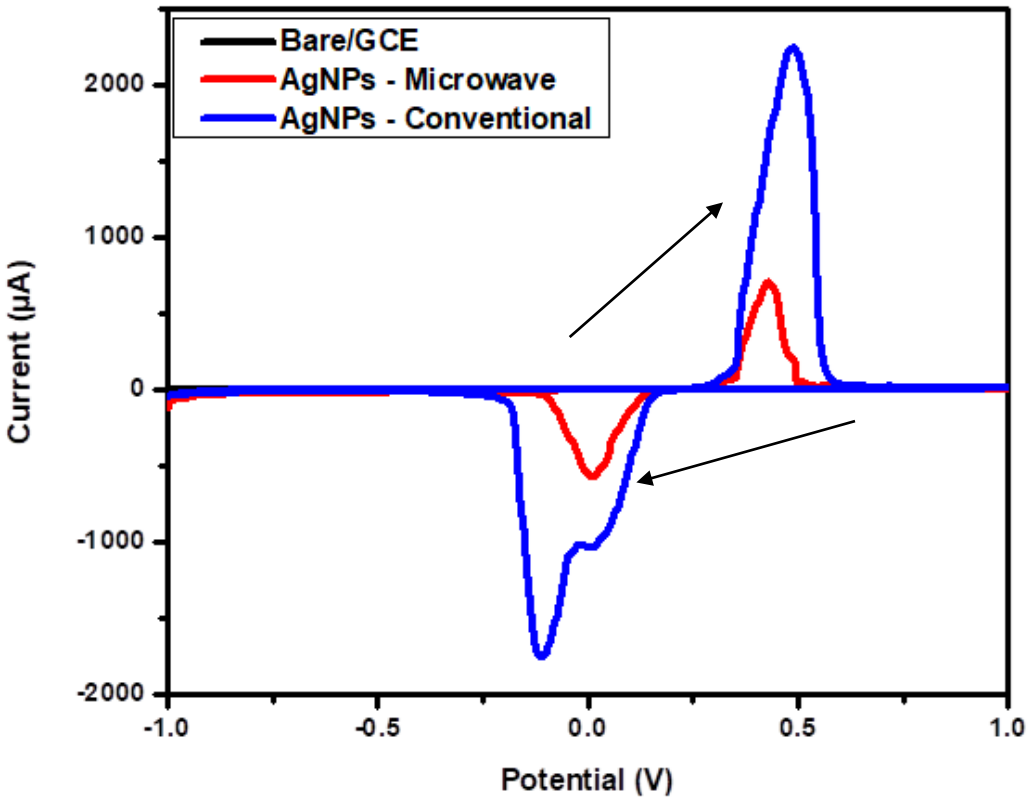

Figure 4.20: CV of bare glassy carbonelectrode (black curve), MI silver nanoparticles (red curve) and CH silver nanoparticles (blue curve) in phosphate buffer solution (pH 7.4) at 30 mV s^{-1}.

Upon increasing the scan rates **Figure 4.21 (a)** and **(b)**, the cathodic current peaks increased linearly and cathodic potential peaks shifted to positive potentials for both MI and CH synthesized silver nanoparticles. The corresponding cathodic peak denotes the conversion of Ag^{+}/Ag. The anodic current peaks also increased linearly with the scan rate and shifted slightly towards the positive potentials. The shift that occurred in anodic peaks indicated the expected electrochemical activity of the nanoparticles. **(Prabhu *et al*., 2016)**

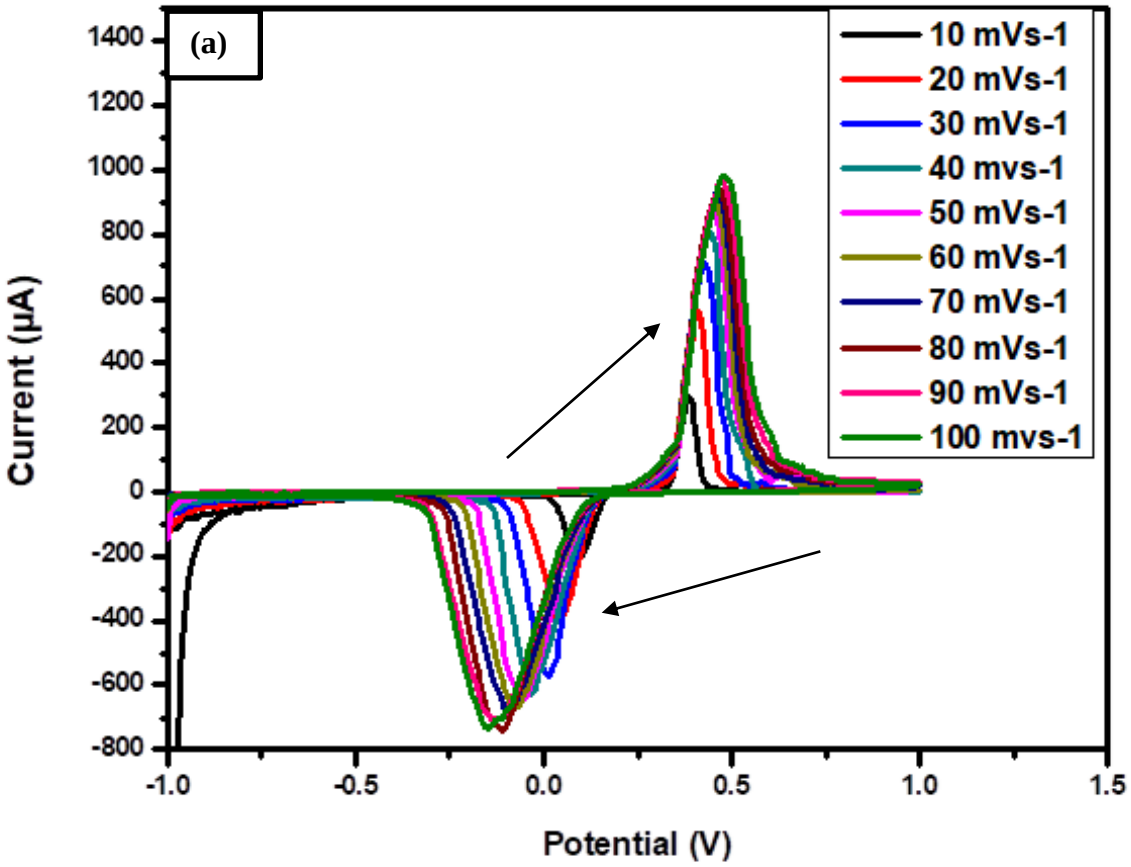

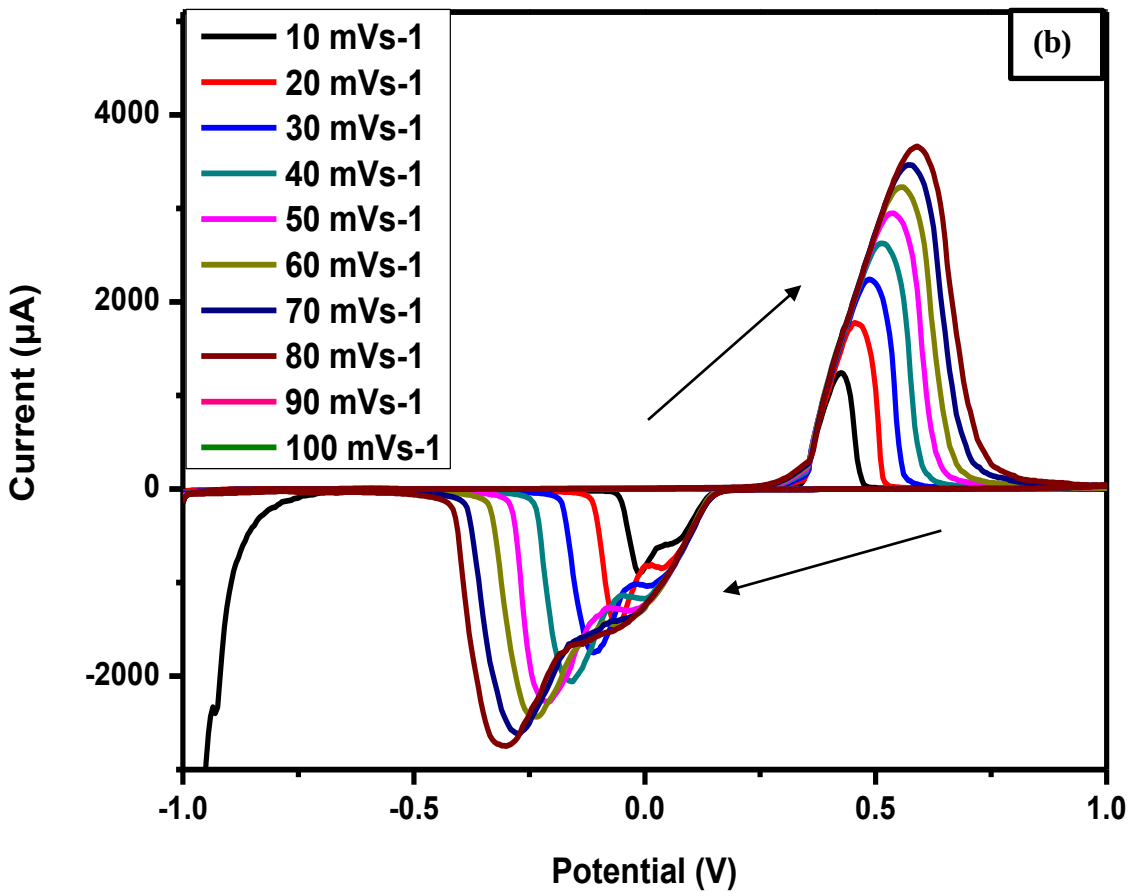

Figure 4.21: CV of (a) microwave green synthesized silver nanoparticles and (b) conventional green synthesized silver nanoparticles in 0.1 M phosphate buffer solution (pH 7.4) at 10-100 mV s^{-1}.

Furthermore, the peak-to-peak separations (ΔE_p = [E_{pa} – E_{pc}]) for microwave green synthesized silver nanoparticles and conventional green synthesized silver nanoparticles were calculated at different scan rates; the results at 50 mVs^{-1} were 1.49 × 10^3 µA (MI) and 5.18 × 10^3 (CH) µA. The analysis of the peak-to-peak separation (ΔE_p) confirmed that the peak currents were diffusion-controlled because when increasing the scan rate, the magnitude of the peak current increased, demonstrating the electrochemical process classified as Quasi-

reversible since ΔE_p was determined to be larger than the value of 57/n mV associated with reversible process at 25 ºC within the scan rates employed. **(Raoof *et al*., 2006)** Moreover, the surface concentration of the electrode (Γ) was also determined using Brown Anson equation (**Equation 4.1**).The surface concentration of the microwave green synthesized AgNPs was 1.4746 x 10^{-1} mol cm^{-2} and for the conventional green synthesized AgNPs was determined to be4.6098 x 10^{-1} mol cm^{-2}.

From the cyclic voltammograms of modified glassy carbon electrode surfaces with AgNPs at various scan rates (**Figure 22 (a) and (b)**), the relationships of the anodic and cathodic peak potentials with the scan rate were applied to calculate the electrochemical parameter such as diffusion coefficient (α) (**Equation 4.2**). The Randles-Sevcik's equation shown in **Equation 4.2** was also used in the calculation of the diffusion coefficient. The diffusion coefficient value for the microwave green synthesized AgNPs was determined to be 7.3228 x 10^{-4} cm^2/s and that for the conventional green synthesized AgNPs was determined to be 7.5275 x 10^{-4} cm^2/s. This clearly demonstrated that the conductivity of the microwave green synthesized AgNPs is slight better than conventional green synthesized AgNPs. These results confirmed that the microwave green synthesized nanoparticles where more suitable towards the fabrication of sensors or biosensors. **(Mohan *et al*., 2016)**

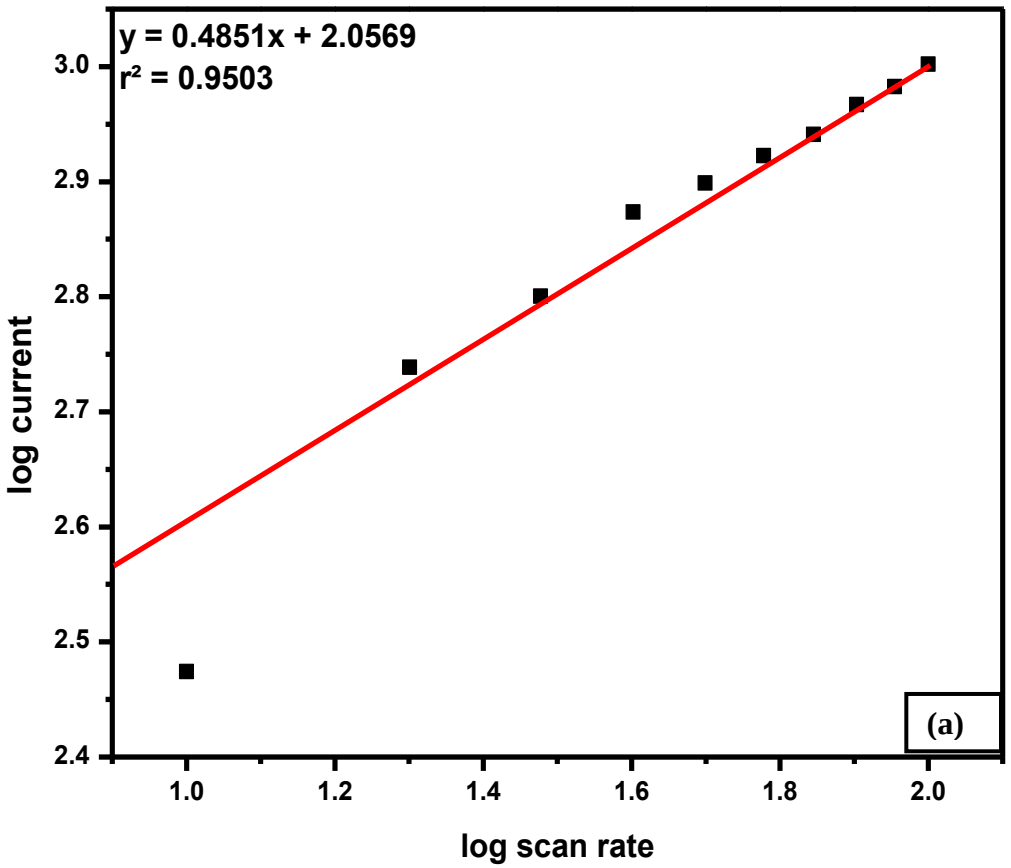
y = 0.4851x + 2.0569
r² = 0.9503
log current
log scan rate
3.0
2.9
2.8
2.7
2.6
2.5
2.4
1.0
1.2
1.4
1.6
1.8
2.0
(a)

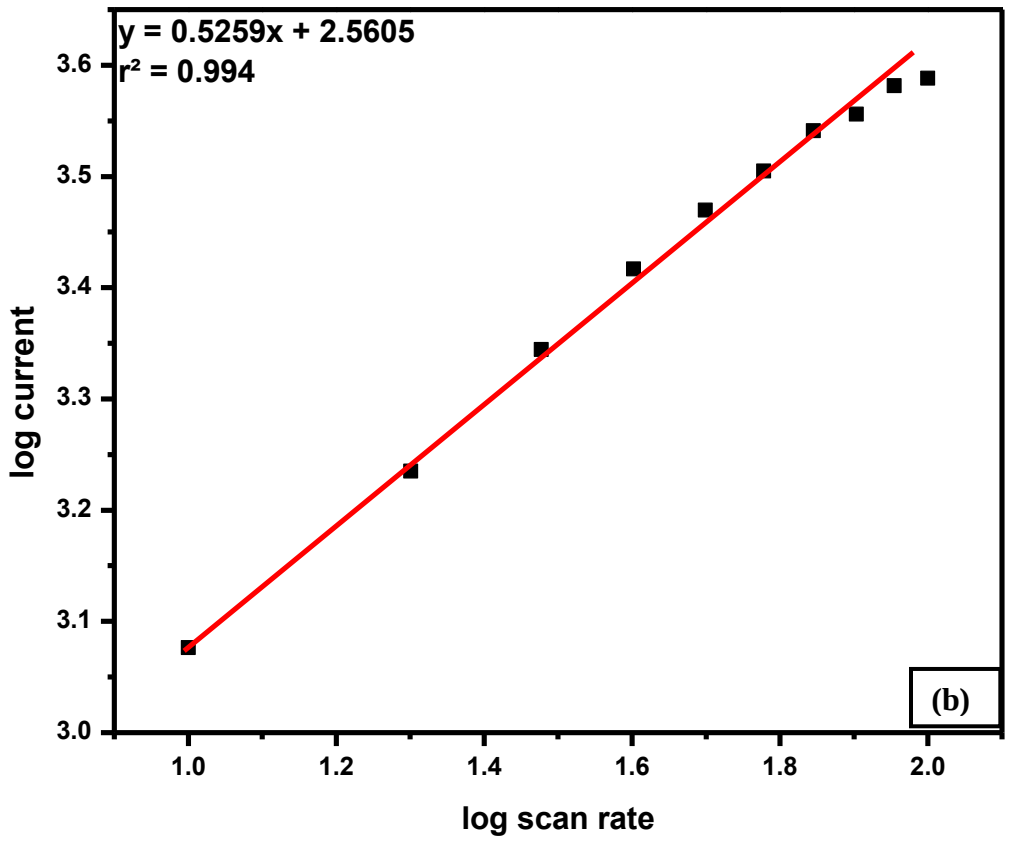

Figure 4.22: Plots of log current versus log scan rate of (a) microwave green synthesized silver nanoparticles and (b) conventional green synthesized silver nanoparticles.

4.2.2.4 Scattering characterisation of silver nanoparticles (AgNPs)

4.2.2.4.1 Small-Angle X-ray Scattering (SAXS)

The Small-Angle X-ray Scattering (SAXS) intensity distribution of the microwave irradiated (MI) green synthesized silver nanoparticles (black) and the conventional heated (CH) green synthesized silver nanoparticles (red) was obtained and together with their corresponding particle size distribution are shown in **Figure 4.23 (a)** and **(b)**, respectively. The average particle sizes of AgNPs synthesized are found to be 4.6 for MI and 4.4 nm for CH respectively. The values for the particle sizes attained using SAXS analyses are found to be smaller than that of HRTEM for both MI and CH. That could be due to the effective crystallite size and the geometric diameter coupled to the fact that this proves that these nanoparticles have different sizes as indicated in HRTEM above. (**Yan *et al*., 2014**)

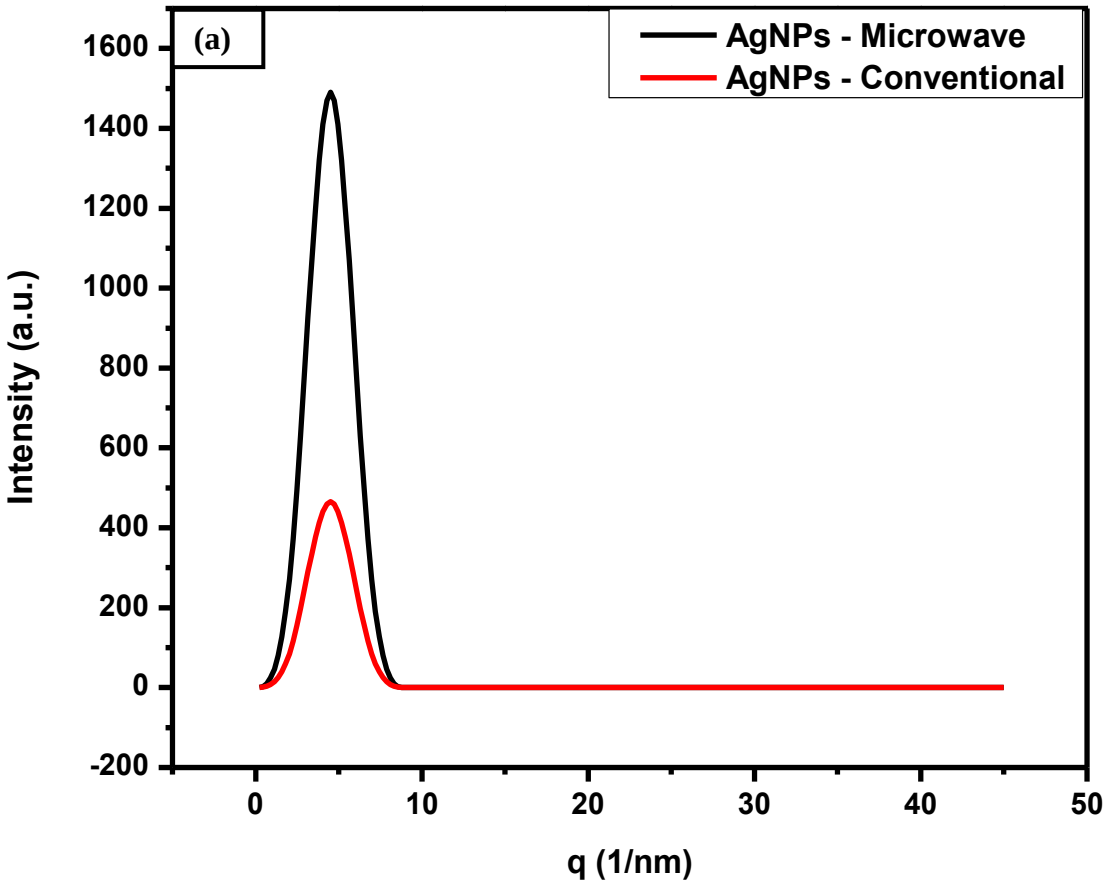
(a)
AgNPs - Microwave
AgNPs - Conventional
Intensity (a.u.)
1600
1400
1200
1000
800
600
400
200
0
-200
0
10
20
30
40
50
q (1/nm)

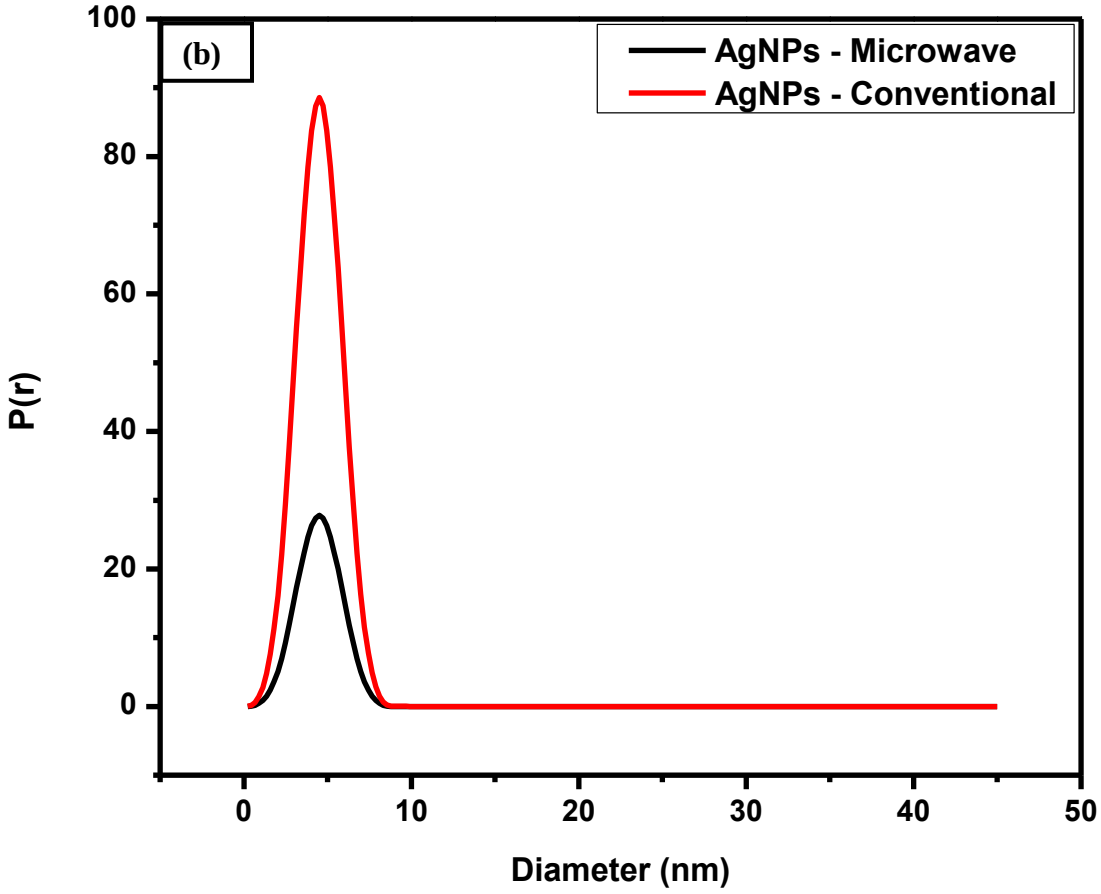

Figure 4.23: The SAXS (a) intensity distribution of microwave green synthesized silver nanoparticles (black line) and conventional green synthesized silver nanoparticles (red line) obtained and their corresponding (b) particle size distribution.

4.2.3 Green synthesized zinc oxide nanoparticles (ZnONPs)

4.2.3.1 Spectroscopic characterisation of zinc oxide nanoparticles (ZnONPs)

4.2.3.1.1 Fourier transform infrared spectroscopy (FTIR)

Generally, the stability of nanoparticles is very significant for their applications. Hence they are normally stabilized with capping agents such as plant extracts and surfactants. In this study the nanoparticles produced namely; zinc oxide nanoparticles (ZnONPs) were seen to be stable due to situ bio-capping by the residues of tomato and apple extract which are observed in the FTIR characterization (**Figure 4.24**). FTIR analysis of apple and tomato showed a broad peak at 3908 cm-1 corresponding to O-H stretch of phenols, intermediate peak attained at in the range of 2220 and 2124 cm^{-1} corresponded to C-H stretch of alkanes, the peak at 1898 cm-1 signified the presence of the C=O stretch of conjugated aldehydes, the medium peak obtained at 1720 and 1542 $cm^{-}1$ corresponds to C=C stretch of unsaturated ketones and the O-H bend of alcohol respectively. Additionally, in tomato and apple extract there is the presence of metabolites such as fatty acids, proanthocyanidins, carotenoids, carotenoids, sugars, phenolic acids, tannins, pectin, flavonoids and fruit acids malic acid, ascorbic acid and citric metabolites that are capable at possessing antioxidant activities. **(Jafarirad *et al*., 2016)** The biocapping occurrence may possibly be because of the presence of metabolites such as carboxylic acids (like ascorbic acid) and phenolic which adhered to the surface of zinc oxide nanoparticles (ZnONPs).

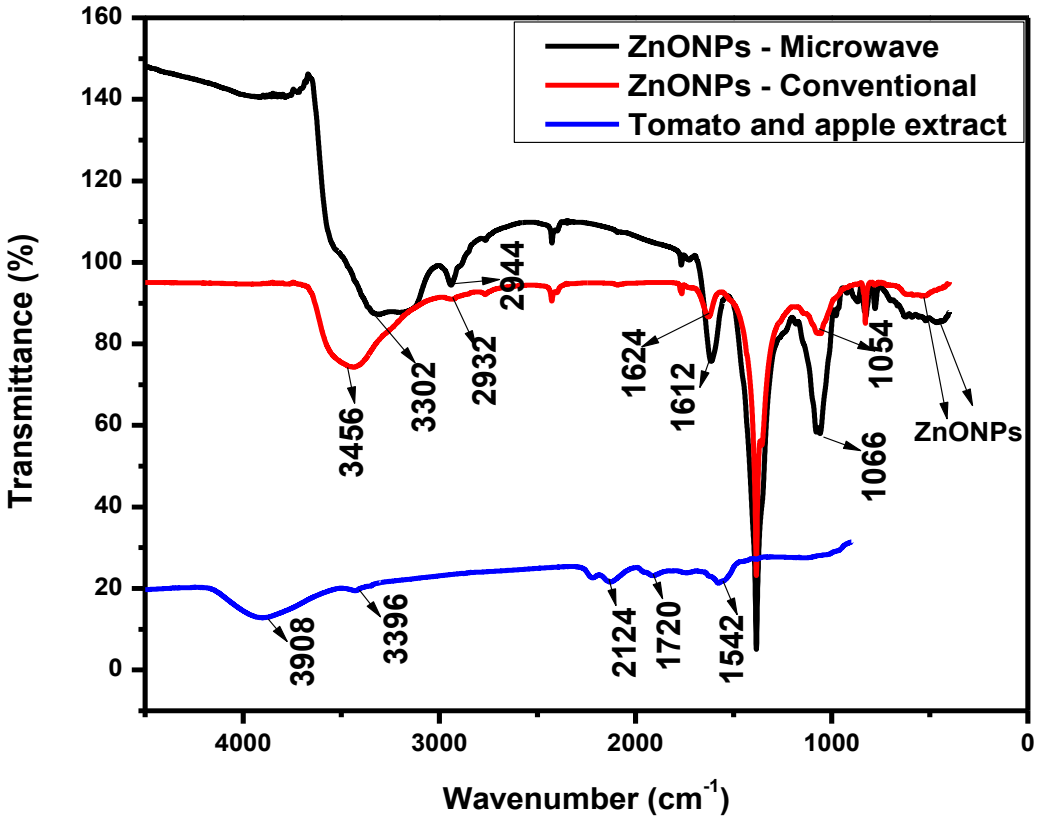

Figure 4.24: Fourier transform infrared spectrum of conventional green synthesized zinc oxide nanoparticles (red line) microwave green synthesized zinc oxide nanoparticles (black line) and Tomato and apple extract (blue line).

The spectrum achieved evidently indicates ZnONPs absorption bands on 460 and 530 cm^{-1} for conventional heating (CH) and microwave irradiation (MI), respectively. Additionally, the bands at 1054 cm^{-1} (CH) and 1066 cm^{-1} (MI) correspond to C-O stretching modes of esters. The band at 2944 cm^{-1} (MI) and 2932 cm^{-1} (CH) is attributed to C-H stretching. The synthesized ZnONPs possess peaks at 1624 cm^{-1} (CH) and 1612 cm^{-1} (MI) which shows C=O of esters. In the FTIR spectrum of synthesized ZnONPs, the characteristic peak at 3456

cm^{-1} (CH) and 3302 cm^{-1} (MI) corresponds to the hydroxyl group. The characteristic corresponding peaks of hydroxyl groups at 3908 cm^{-1} and the appearance of a carbonyl peak at 1880 cm^{-1} implies the oxidation process of tomato and apple extract. Therefore, the presence of extract as capping agents in the matrix of ZnONPs is confirmed. **(Agarwal *et al.*, 2017)**

4.2.3.1.2 Ultraviolet Visible Spectroscopy (UV-vis)

The unique properties of nanomaterials are caused by the size of the materials where in most circumstances they cannot be experimented in their bulk counterparts. Henceforward, exploring the size development of semiconducting nanomaterials has become very important. However, a characterization technique that is widely used to study the optical properties of nanomaterials as well as their particle size and distribution is Ultraviolet Visible Spectroscopy (UV-vis) as shown by the results in **Figure 4.25**. The results illustrate the UV properties of the differently synthesized ZnONPs. The absorption spectrum of conventional green synthesized zinc oxide nanoparticles has shown a red-shifted maximum at 237 nm (**Figure 4.25 (b)**) compared to the absorption spectra of the microwave green synthesized zinc oxide nanoparticles at 216 nm (**Figure 4.25 (a)**); confirming a smaller particle sizes of the microwave synthesized nanoparticles. Bulk ZnONPs has been reported to show a peak around 281 nm. **(Panda *et al.*, 2017)** However, the sharp absorption peak in the spectra of the conventional green synthesized zinc oxide nanoparticles might be due to the poly-dispersed nature of the nanoparticles as seen in the below section.

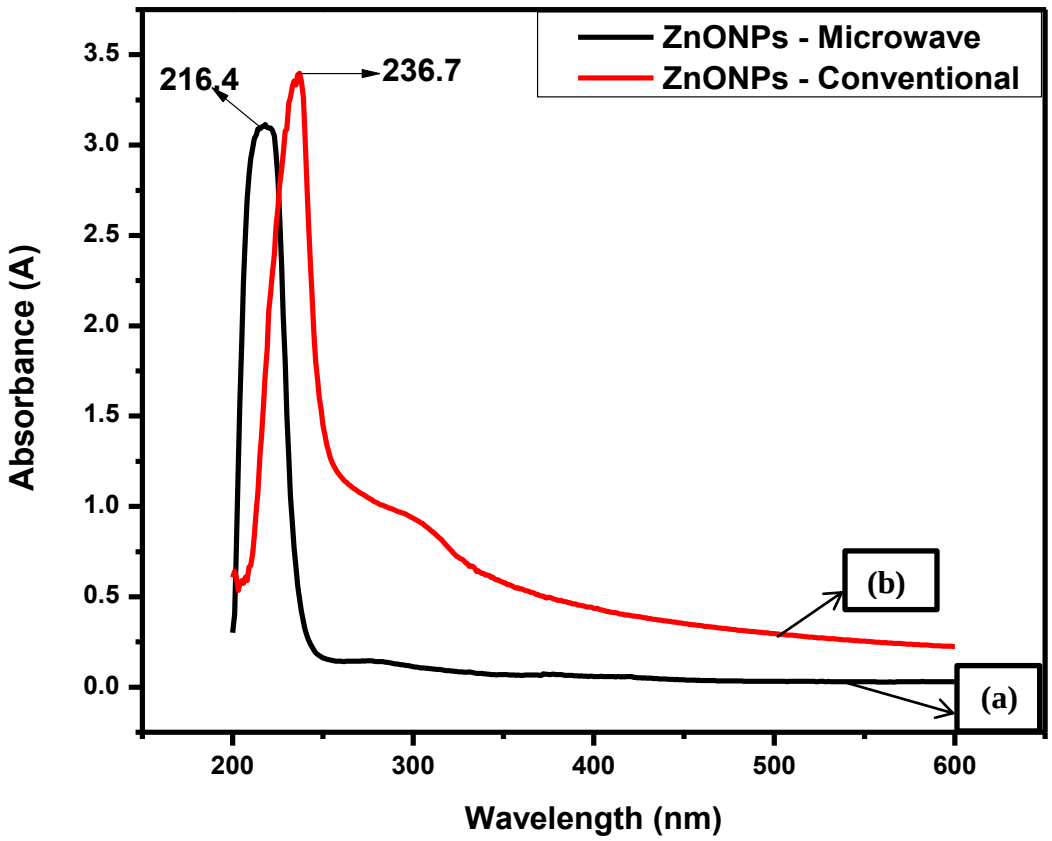

Figure 4.25: Ultraviolet-visible spectrum of (a) microwave green synthesized zinc oxide nanoparticles and (b) conventional green synthesized zinc oxide nanoparticles.

4.2.3.2 Microscopic characterisation of zinc oxide nanoparticles (ZnONPs)

4.2.3.2.1 High resolution transmission electron microscopy (HRTEM)

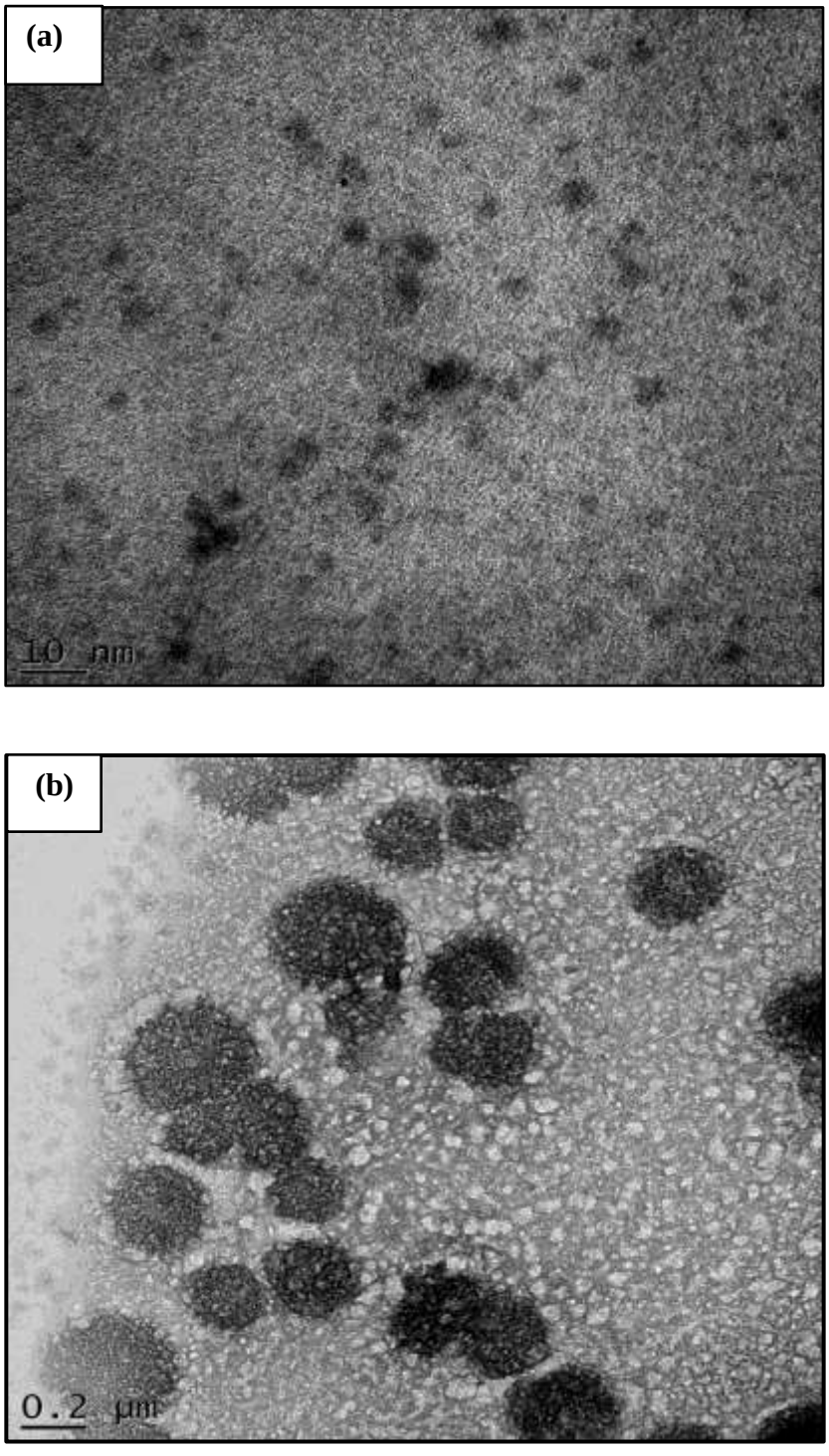

Figure 4.26: HRTEM images of (a) microwave green synthesized zinc oxide nanoparticles and (b) conventional green synthesized zinc oxide nanoparticles.

The definite evidence of size, shape and structure of both the microwave green synthesized zinc oxide nanoparticles (**Figure 4.26 (a)**) and conventional green synthesized zinc oxide nanoparticles (**Figure 4.26(b)**) were observed using HRTEM whose images are shown at (a) 10 nm and (b) 0.2 nm scale view. The microwave green synthesized zinc oxide nanoparticles appeared to be oval and spherical as seen in **Figure 4.26 (a)** and their size of approximately 5 nm as shown in **Figure 4.27 (a)** was confirmed from numerous random particles. In **Figure 4.26** it was observed that the conventional green synthesized zinc oxide nanoparticles were not as poly-dispersed as the microwave green synthesized zinc oxide nanoparticles. However, the particle size distribution confirmed that the standard deviation of the microwave green synthesized zinc oxide nanoparticles to be 3.48 nm respectively and conventional green synthesized zinc oxide nanoparticles appeared to be rod-shape with a higher standard deviation of 9.34 nm. The huge difference in standard deviation of ZnONPs is be due to the particle sizes shown in HRTEM images; the MI synthesized ZnONPs were smaller compared to those of CH synthesized ZnONPs.

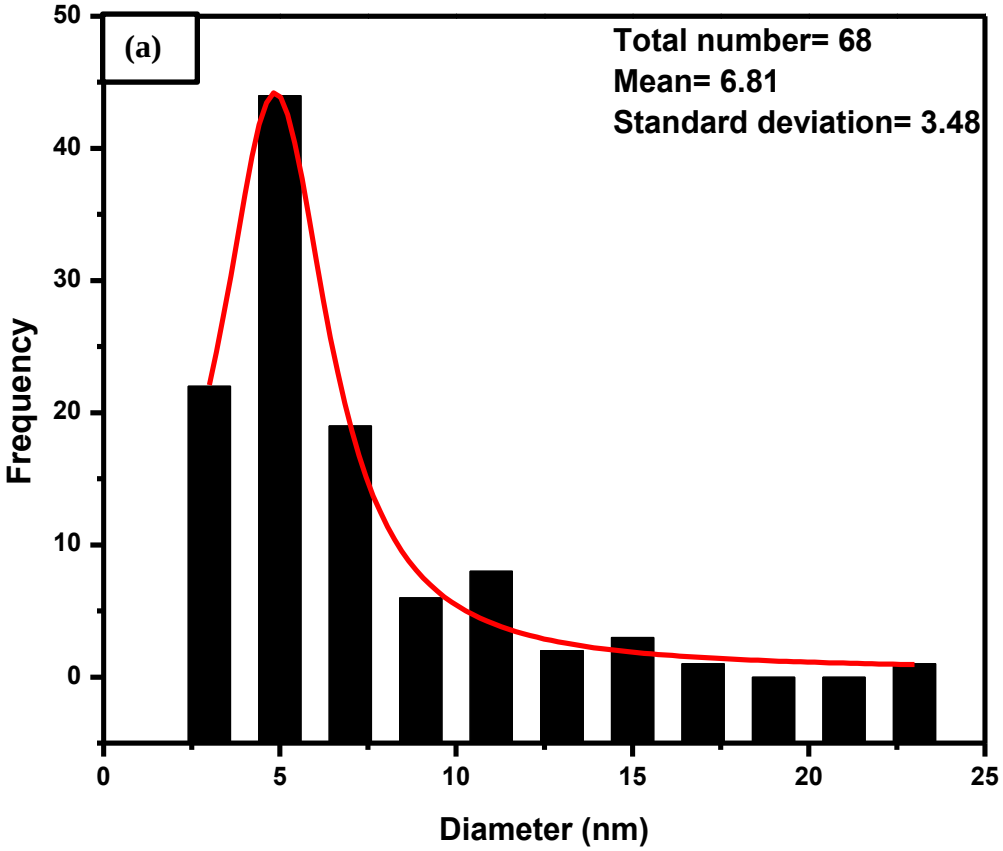
(a)
Total number= 68
Mean= 6.81
Standard deviation= 3.48
Frequency
Diameter (nm)
0
10
20
30
40
50
0
5
10
15
20
25

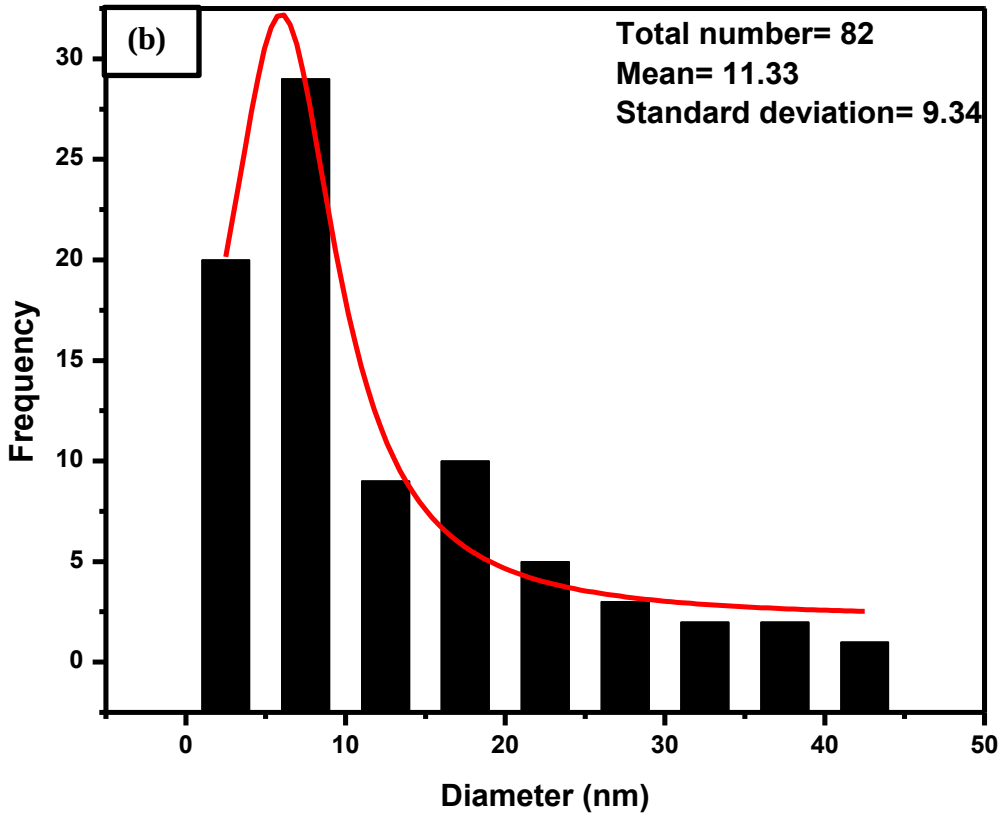

Figure 4.27: Particle size distribution of (a) microwave green synthesized zinc oxide nanoparticles and (b) conventional green synthesized zinc oxide nanoparticles.

The selected area electron diffraction (SAED) pattern in the insert of **Figure 4.28 (a)** and (**b)** illustrates distinctive bright rings which endorse the preferential orientation of nanocrystals instead of irregular ones that are indexed to the hexagonal structure of ZnONPs with phase purity. The ZnONPs with such rings are more suitable for the immobilization of biomolecules and have a larger ratio of surface to volume; leading to enhancement on performance of biosensors.

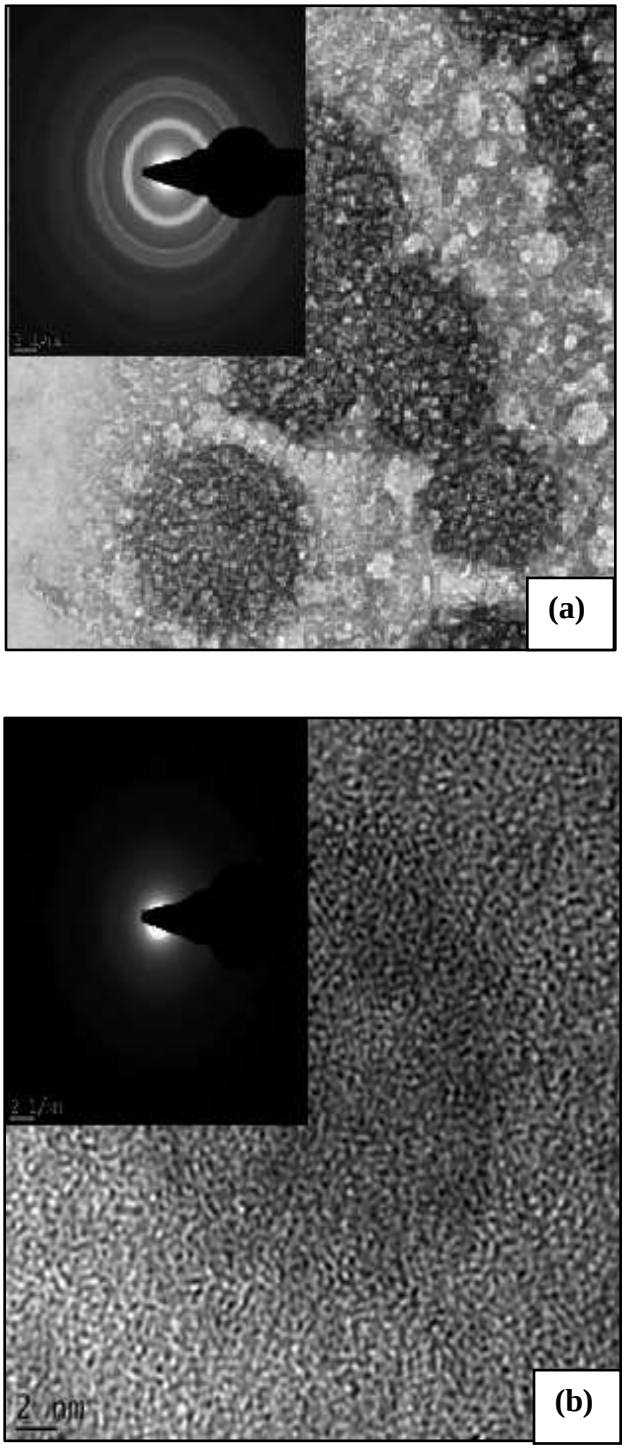

Figure 4.28: Conventional green synthesized silver nanoparticles (ZnONPs) (a) and microwave green synthesized silver nanoparticles (ZnONPs) (b) at 2.1 nm scale view. Insert SAED pattern

4.1.1.1.1 4.2.2.1.3 Energy dispersive X-ray (EDX)

The presence of oxygen, zinc and other elements contained in zinc oxide nanoparticles (ZnONPs) were confirmed by Energy dispersive x-ray spectrum analysis (EDX) pattern shown in **Figure 4.29**. The signal for copper (Cu) element in the EDX spectra was due to the copper grid used in the process of HRTEM analysis. Furthermore EDX spectra showed a signal of some elements (Se, SI and Te) in the conventional green synthesized zinc oxide nanoparticles (ZnONPs) (**Figure 4.29 (b)**) which might be impurities and the carbon element shown in both spectrums is typically seen in the organic substances attached to the ZnONPs due to phytochemicals in the extract. The oxygen and zinc for microwave green synthesized zinc oxide nanoparticles (ZnONPs) and conventional green synthesized zinc oxide nanoparticles (ZnONPs) had the highest counts, which indicated that zinc nanoparticles were successfully obtained.

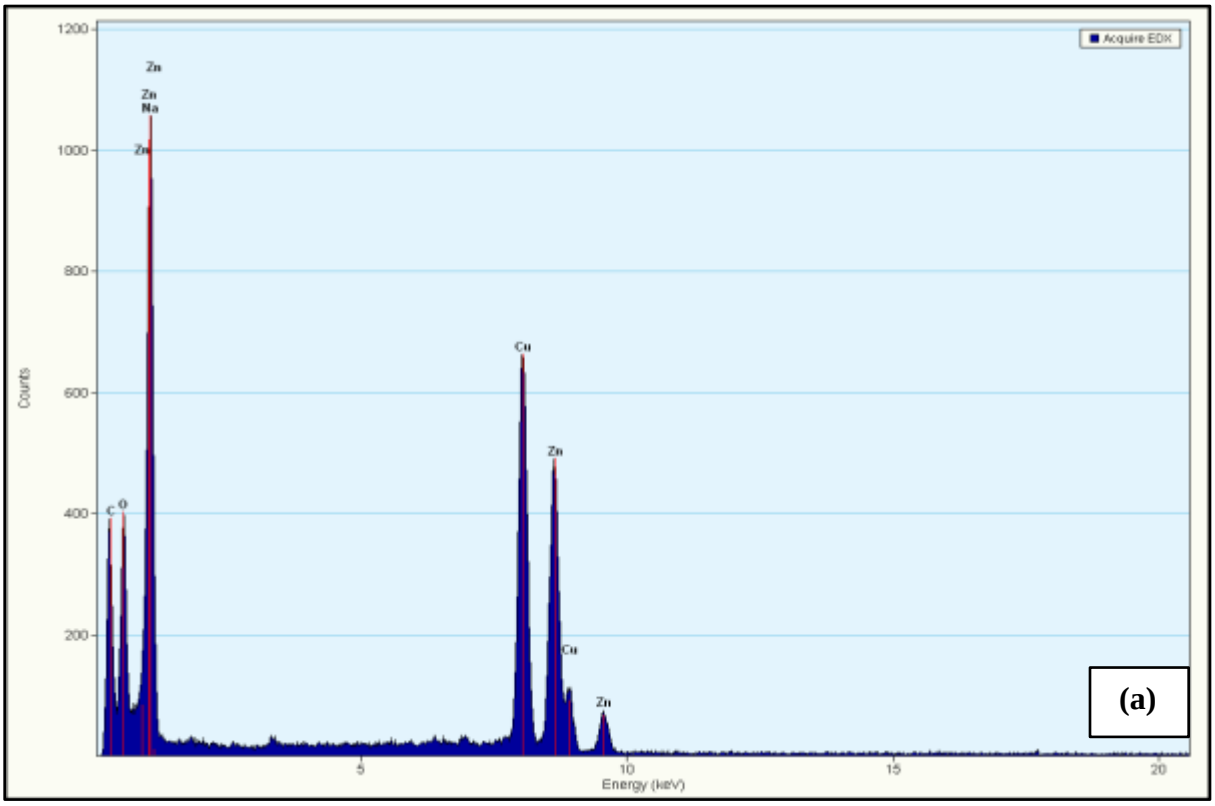

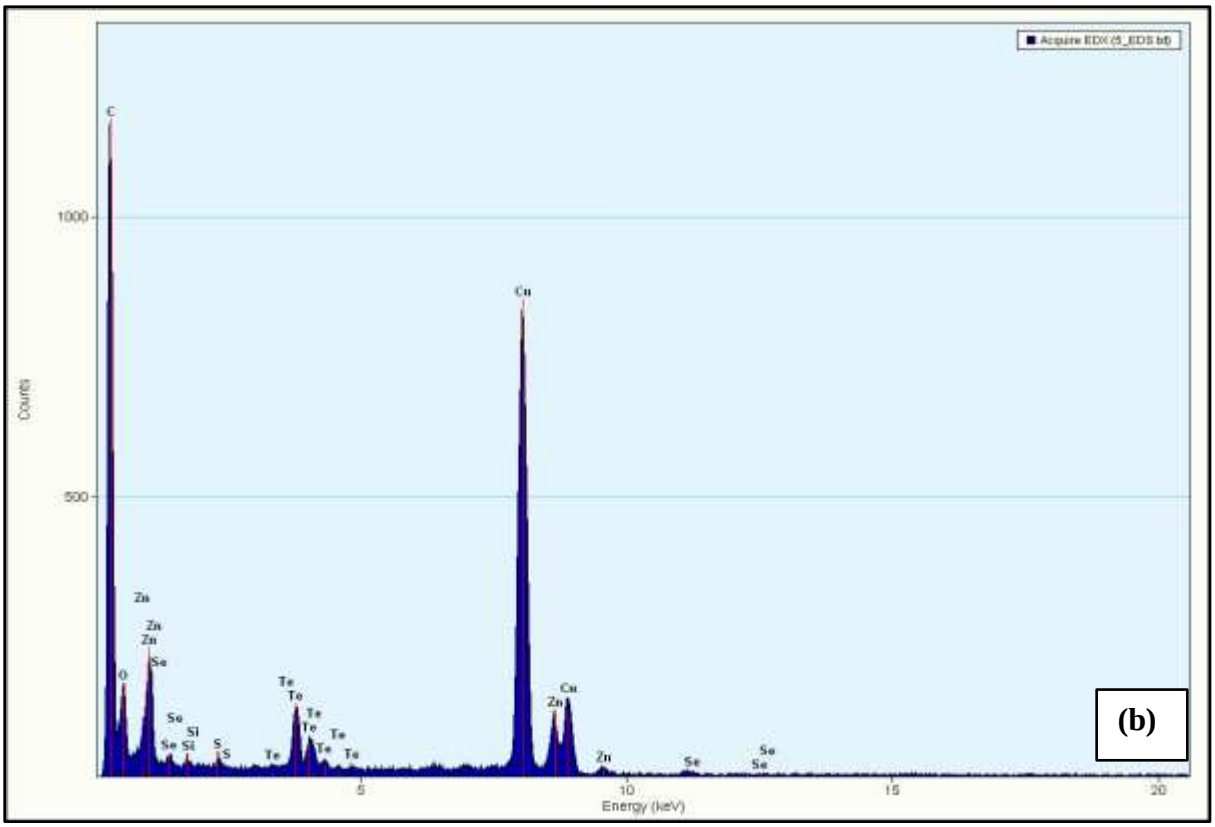

Figure 4.29: Energy dispersive X-ray spectrum analysis of (a) microwave green synthesized zinc oxide nanoparticles (ZnONPs) and (b) conventional green synthesized zinc oxide nanoparticles (ZnONPs).

4.2.3.3 Electrochemical characterisation of zinc oxide nanoparticles (ZnONPs)

4.2.3.3.1 Cyclic Voltammetry (CV)

Cyclic voltammetry (CV) is a unique and the most useful electro-analytical technique for the study of redox behaviours of electroactive species. In this part of this study it was used to investigate the electrochemical properties of zinc oxide nanoparticles which were synthesized using different methods and characterized in PBS solution (pH 7.4) and adsorbed onto the glassy carbon electrode. CV was employed over a potential range from -1 to +1 V. In **Figure 4.30** the voltammogram illustrates a bare glassy carbon electrode (GCE) (black), microwave irradiation (MI) green synthesized zinc oxide nanoparticles (red) and conventionally heated (CH) green synthesized zinc oxide nanoparticles (blue) at a potential scan rate of 30 mVs^{-1}. The CV behavior of MI synthesized ZnONPs showed one oxidation peak at 0.2195 V while CH synthesized ZnONPs showed one reduction peak at 0.1831 V.

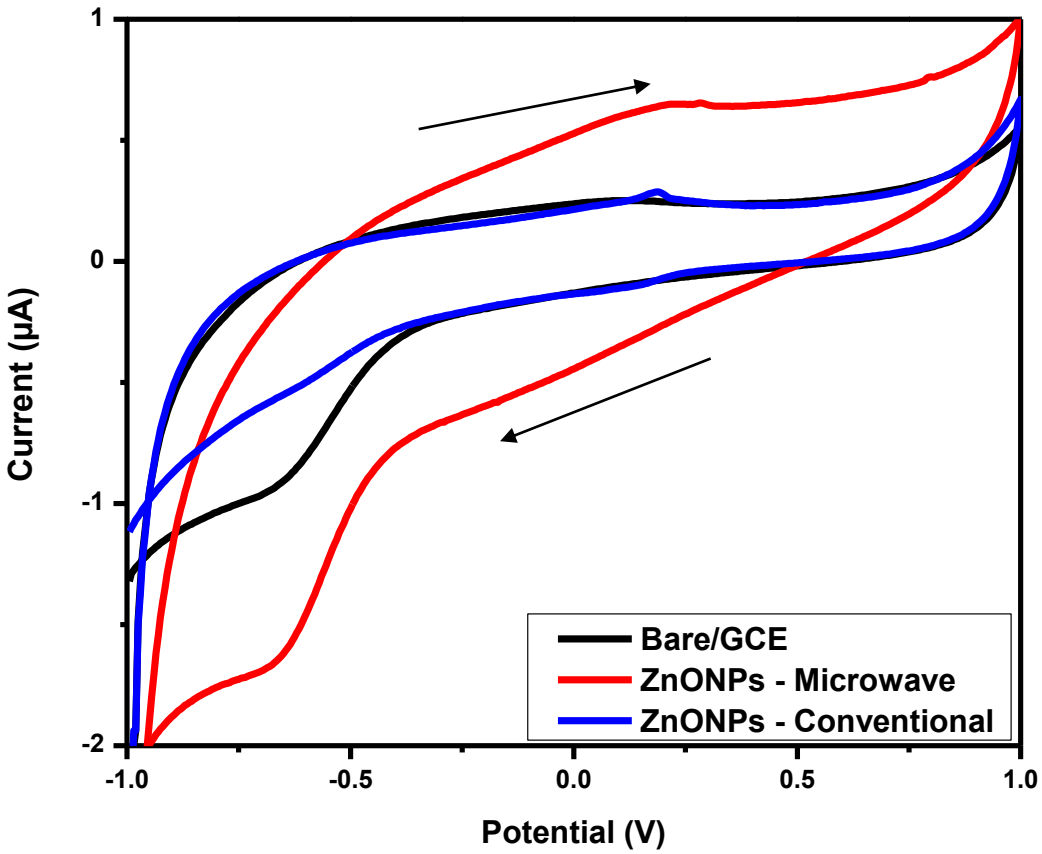

Figure 4.30: CV of bare glassy carbon electrode (GCE) (black curve), microwave green synthesized zinc oxide nanoparticles (red curve) and conventional green synthesized zinc oxide nanoparticles (blue curve) in phosphate buffer solution (pH 7.4) at 30 mV s^{-1}.

The glassy carbon electrodes modified by ZnONPs were found to perform better in comparison to bare glassy carbon electrode as shown in **Figure 4.30**. This suggested that the presence of ZnONPs improves the relative electron transfer. Both the ZnONPs synthesized using different methods showed enhanced peak current than the bare glassy carbon electrode which indicated that the modified electrodes could be further used in the application of electrochemical sensors. Additionally, ZnONPs anodic peak current in **Figure 4.31 (a**) and

(b) increased with increasing scan rate. **(Matinise *et al.*, 2017)** The effects of scan rate on current peaks were interrogated by running a series of voltammograms at different scan rates from 10 mVs^{-1} to 100mVs^{-1}.

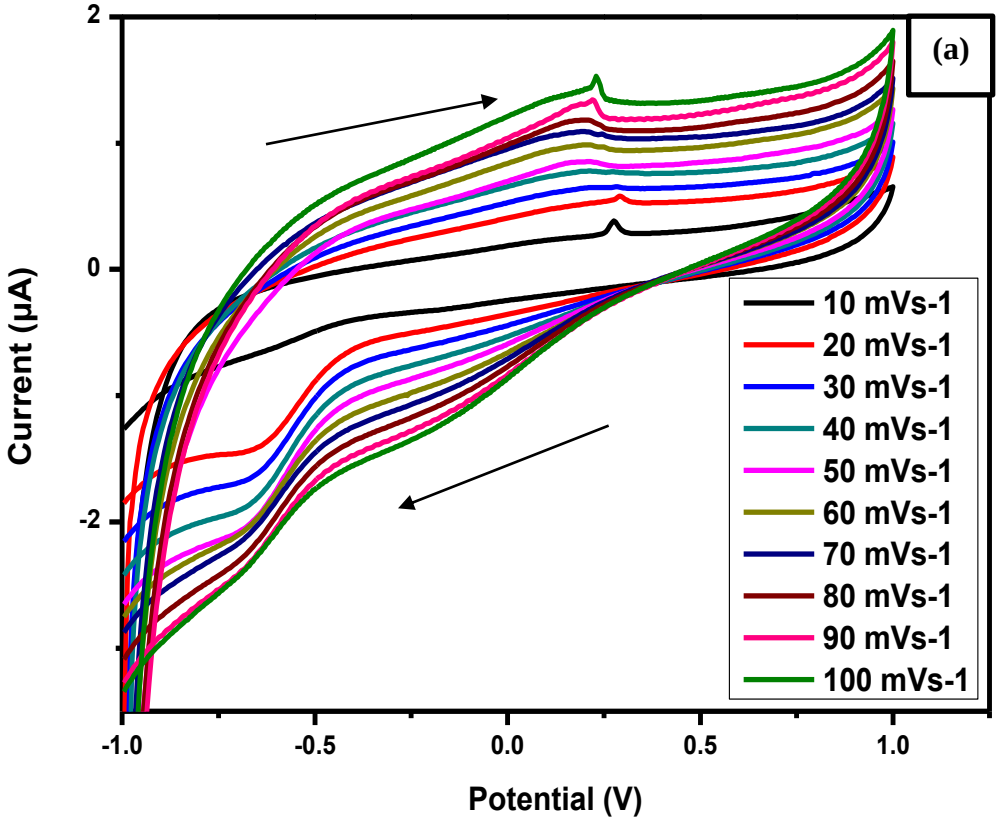

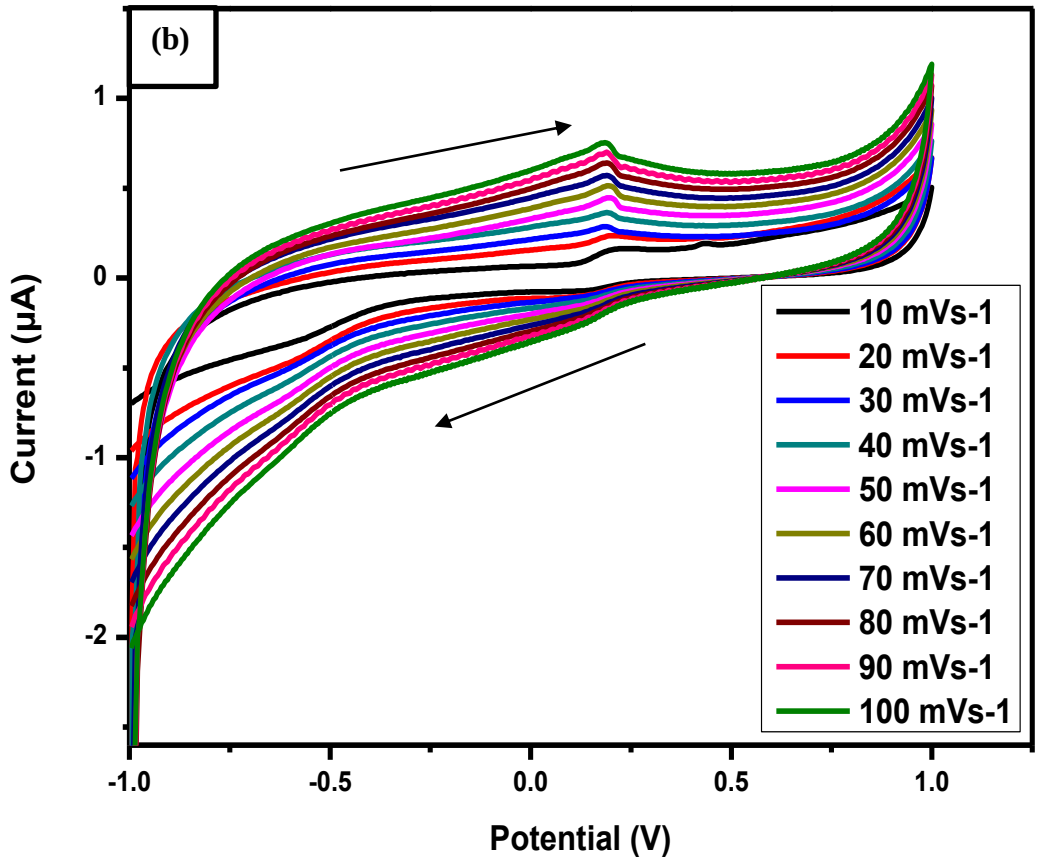

Figure 4.31: CV of (a) microwave green synthesized zinc oxide nanoparticles and (b) conventional green synthesized zinc oxide nanoparticles in 0.1 M phosphate buffer solution (pH 7.4) at 10-100 mV s^{-1}.

The plot of log anodic current peak against log scan rate was plotted for the microwave green synthesized zinc oxide nanoparticles where nearly a straight line with a linear regression I_{pa} (µA) = 0.6084x - 1.0756 and a correlation coefficient r^2= 0.9835 was determined as seen in **Figure 4.32 (a)**. The same plot was plotted for the conventional green synthesized zinc oxide nanoparticles as demonstrated in **Figure 4.32 (b)** where the linear regression and correlation coefficient were determined to be I_{pa} (µA) = -0.6876*x* - 1.5143 and r^2 = 0.977 respectively.

Consequently, in both circumstances the plots illustrated a clear sign of the dependence of anodic peak current on scan rate. From these plots, the surface concentration of these ZnONPs was determined using the Brown Anson equation (**Equation 4.1**). The system for both nanoparticles were irreversible indicated by $I_{pa}/I_{pc} \neq 1$ (I_{pa}/I_{pc} valuses for conventional green synthesized zinc oxide nanoparticles was 0.2686 µA and 0.6475 µA for the microwave green synthesized zinc oxide nanoparticles).The surface concentration of the of microwave green synthesized zinc oxide nanoparticles was determined to be 1.3359 x 10^{-4} mol cm^{-2} and for the conventional green synthesized zinc oxide nanoparticles it was determined to be 5.7148 x 10^{-5} mol cm^{-2}. As anticipated, the surface concentration of the microwave green synthesized zinc oxide nanoparticles is slightly higher than that of conventional green synthesized zinc oxide nanoparticles due to the longer time the reaction took to reach the desired temperature.

Moreover, the irreversible Randel-Sevcik equation was used to determine the diffusion coefficient of ZnONPs. A value of 7.322 x 10^{-4} cm^2/s was determined for the microwave green synthesized zinc oxide nanoparticles while a value of 7.8501 x 10^{-4} cm^2/s was determined for the conventional green synthesized zinc oxide nanoparticles. As also anticipated, the microwave green synthesized zinc oxide nanoparticles showed a slightly more rapid coefficient resulting from the finely layered nanoparticles on the glassy carbon surfaces thus supporting the reduced surface concentration value determined above. For the conventional green synthesized zinc oxide nanoparticles the opposite is true.

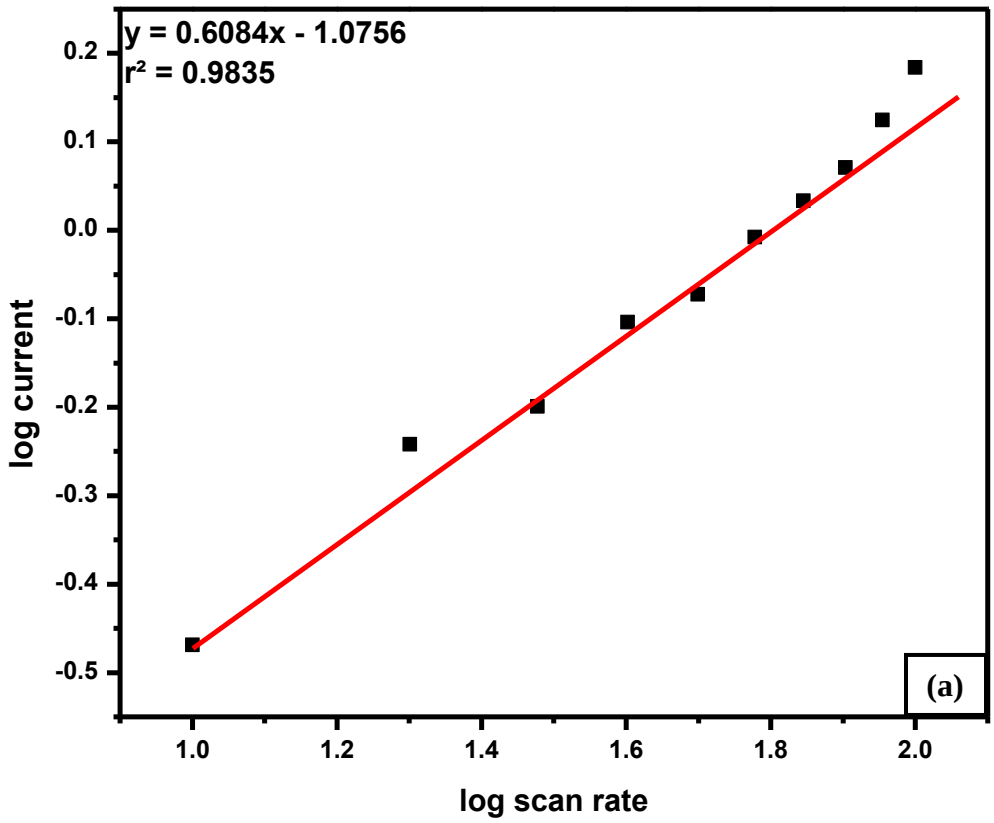
y = 0.6084x - 1.0756
r² = 0.9835
0.2
0.1
0.0
-0.1
-0.2
-0.3
-0.4
-0.5
log current
1.0
1.2
1.4
1.6
1.8
2.0
log scan rate
(a)

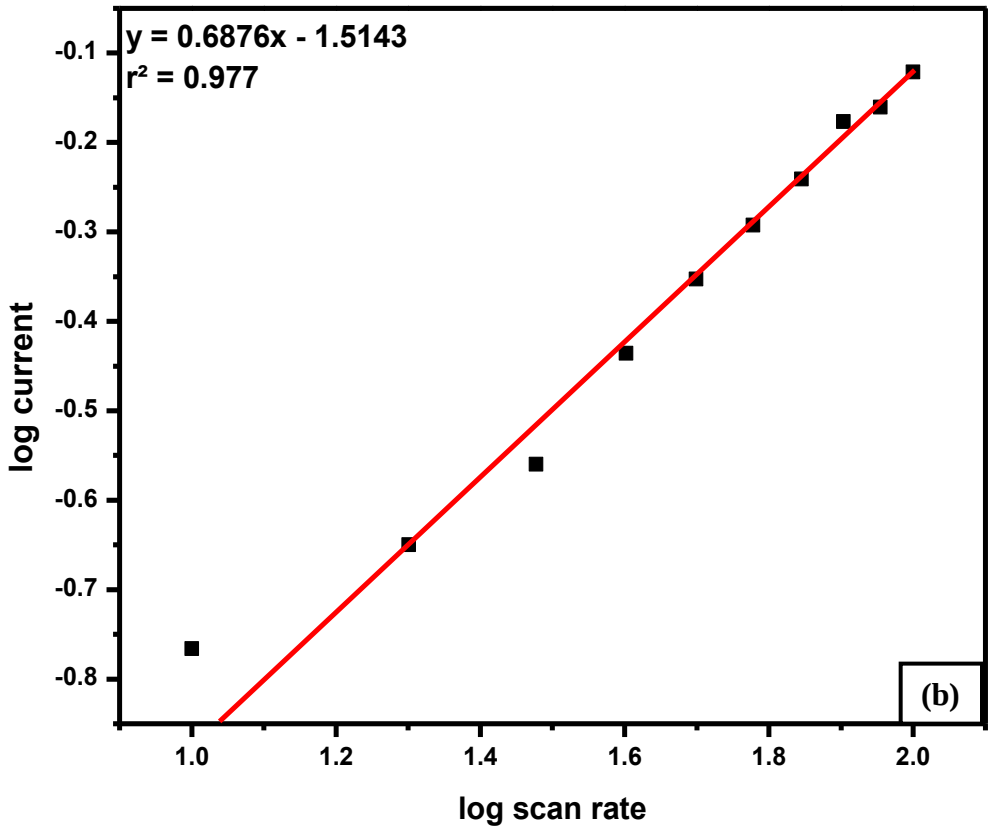

Figure 4.32: Plots of log current versus log scan rate of (a) microwave green synthesized zinc oxide nanoparticles and (b) conventional green synthesized zinc oxide nanoparticles.

4.2.3.4 Scattering characterisation of zinc oxide nanoparticles (ZnONPs)

4.2.3.4.1 Small-Angle X-ray Scattering (SAXS)

Small-angle X-ray scattering (SAXS) is one of the greatest techniques to study particle size distribution of nanoparticles. As it is recognized, that particle size distribution is an essential feature of nanomaterials. In **Figure 2.33** SAXS illustrates the determined intensity distribution of microwave irradiated (MI) green synthesized zinc oxide nanoparticles (black) and conventional heated (CH) green synthesized zinc oxide nanoparticles (red) and their corresponding particle size distribution. The average particle sizes of ZnONPs synthesized are found to be 73.22 (MI) and 80.85 nm (CH), respectively. The biosynthesized ZnONPs using CH and MI methods are reported to usually having sizes between 25 - 204 nm and 21 - 243 nm respectively indicating that our study has reported values withing the expected values. **(Jafarirad *et al*., 2016)** The values for the particle sizes accomplished using SAXS analyses in this particular case were found to be larger than that of HRTEM for both MI and CH. This is due to the effective crystallite size and the geometric diameter coupled to the fact that these nanoparticles have different sizes as indicated in HRTEM above. **(Yan *et al*., 2014)**

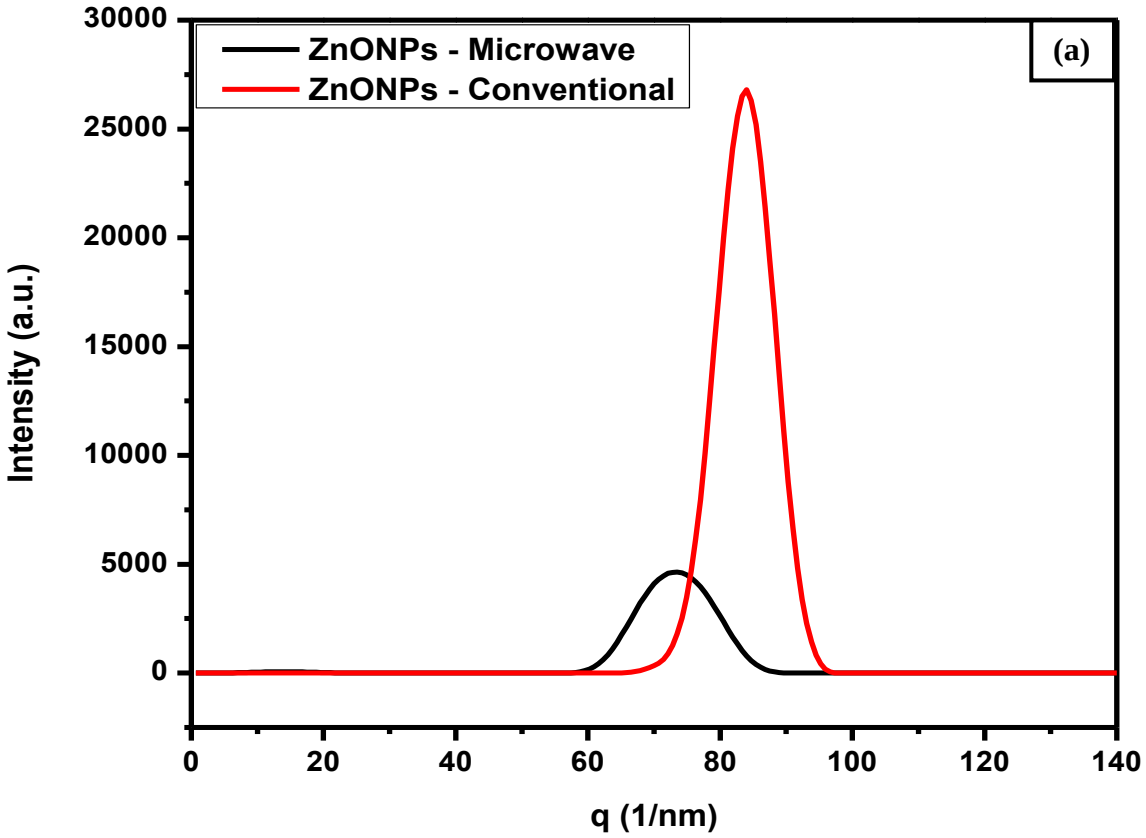
ZnONPs - Microwave
ZnONPs - Conventional
(a)
Intensity (a.u.)
30000
25000
20000
15000
10000
5000
0
0
20
40
60
80
100
120
140
q (1/nm)

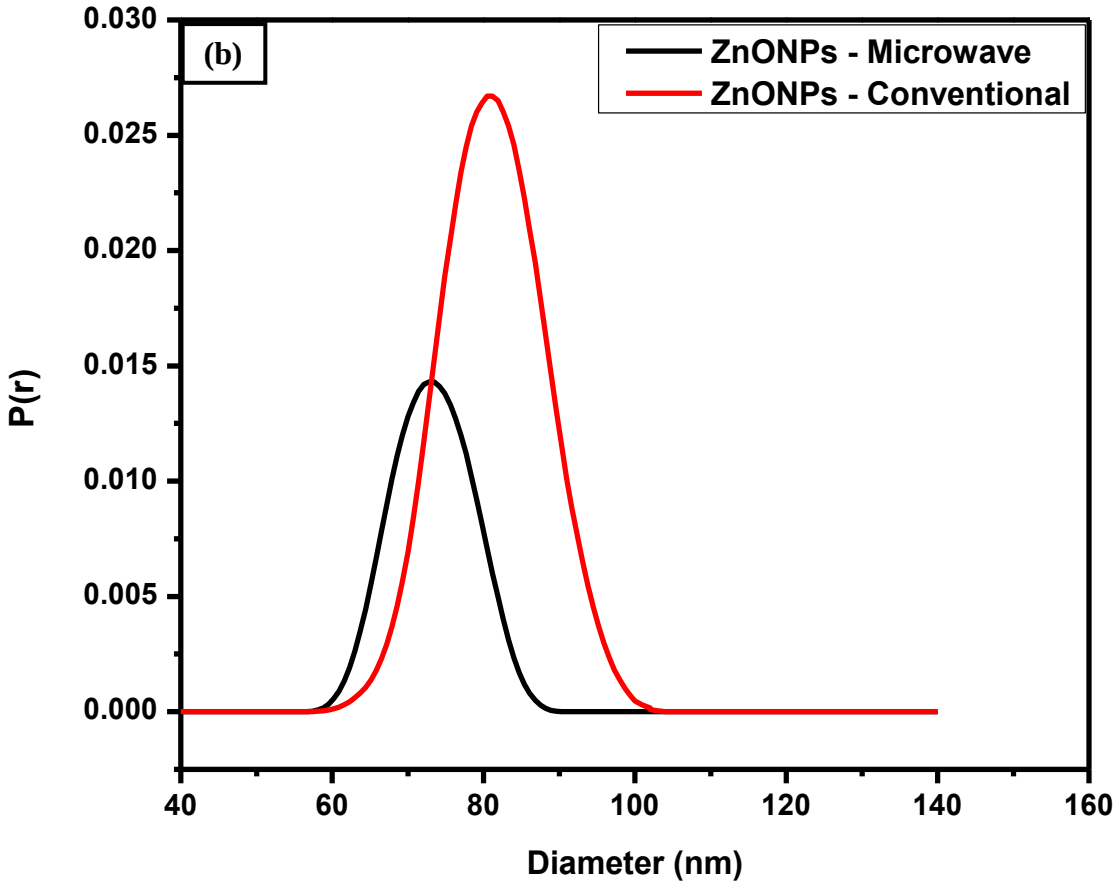

Figure 4.33: The SAXS (a) intensity distribution of microwave green synthesized zinc oxide nanoparticles (black) and conventional green synthesized zinc oxide nanoparticles (red) obtained and (b) their corresponding particle size distribution.

4.3 References

Agarwal, H., Kumar, S.V. and Rajeshkumar, S., 2018. Antidiabetic effect of silver nanoparticles synthesized using lemongrass (cymbopogon citratus) through conventional heating and microwave irradiation approach. Journal of Microbiology, Biotechnology & Food Sciences, 7(4).

Agarwal, H., Kumar, S.V. and Rajeshkumar, S., 2017. A review on green synthesis of zinc oxide nanoparticles–An eco-friendly approach. Resource-Efficient Technologies.

Allada, R., 2016. Hygroscopicity Categorization of Pharmaceutical Solids by Gravimetric Sorption Analysis: A Systematic Approach. *Asian Journal of Pharmaceutics (AJP): Free full text articles from Asian J Pharm*, *10*(04).

Ambrosi, A., Chua, C.K., Bonanni, A. and Pumera, M., 2014. Electrochemistry of graphene and related materials. Chemical reviews, 114(14), pp.7150-7188.

Ammar, A., Al-Enizi, A.M., AlMaadeed, M.A. and Karim, A., 2016. Influence of graphene oxide on mechanical, morphological, barrier, and electrical properties of polymer membranes. Arabian journal of chemistry, 9(2), pp.274-286.

Boikanyo, D., 2015. Electrochemical study of pyrene using glassy carbon electrode modified with metal-oxide nanoparticles and a graphene oxide/multi-walled carbon nanotubes nanoplatform (Doctoral dissertation).1

Çiplak, Z., Yildiz, N. and Çalimli, A., 2015. Investigation of graphene/Ag nanocomposites synthesis parameters for two different synthesis methods. Fullerenes, Nanotubes and Carbon Nanostructures, 23(4), pp.361-370.

Drewniak, S., Muzyka, R., Stolarczyk, A., Pustelny, T., Kotyczka-Morańska, M. and Setkiewicz, M., 2016. Studies of reduced graphene oxide and graphite oxide in the aspect of their possible application in gas sensors. Sensors, 16(1), p.103.

Gao, W., 2012. Graphite oxide: Structure, reduction and applications (Doctoral dissertation, Rice University).

Haider, A.J., Haider, M.J. and Mehde, M.S., 2018, May. A review on preparation of silver nano-particles. In AIP Conference Proceedings (Vol. 1968, No. 1, p. 030086). AIP Publishing.

Jafarirad, S., Mehrabi, M., Divband, B. and Kosari-Nasab, M., 2016. Biofabrication of zinc oxide nanoparticles using fruit extract of Rosa canina and their toxic potential against bacteria: a mechanistic approach. Materials Science and Engineering: C, 59, pp.296-302.

Jung, I., Dikin, D.A., Piner, R.D. and Ruoff, R.S., 2008. Tunable electrical conductivity of individual graphene oxide sheets reduced at "low" temperatures. Nano letters, 8(12), pp.4283-4287.

Kaniyoor, A. and Ramaprabhu, S., 2012. A Raman spectroscopic investigation of graphite oxide derived graphene. Aip Advances, 2(3), p.032183.

Kauppila, J., 2014. Graphene from Graphite by Chemical and Physical Techniques.

Kudin, K.N., Ozbas, B., Schniepp, H.C., Prud'Homme, R.K., Aksay, I.A. and Car, R., 2008. Raman spectra of graphite oxide and functionalized graphene sheets. Nano letters, 8(1), pp.36-41.

Matinise, N., Fuku, X.G., Kaviyarasu, K., Mayedwa, N. and Maaza, M., 2017. ZnO nanoparticles via Moringa oleifera green synthesis: physical properties & mechanism of formation. Applied Surface Science, 406, pp.339-347.

Mohan, S., Okumu, F., Oluwafemi, O., Matoetoe, M. and Arotiba, O., 2016. Electrochemical behaviour of silver nanoparticle-MWCNTs hybrid nanostructures synthesized via a simple method.

Noroozi, M., Zakaria, A., Moksin, M.M., Wahab, Z.A. and Abedini, A., 2012. Green formation of spherical and dendritic silver nanostructures under microwave irradiation without reducing agent. International journal of molecular sciences, 13(7), pp.8086-8096.

Panda, K.K., Golari, D., Venugopal, A., Achary, V.M.M., Phaomei, G., Parinandi, N.L., Sahu, H.K. and Panda, B.B., 2017. Green synthesized zinc oxide (ZnO) nanoparticles induce oxidative stress and DNA damage in Lathyrus sativus L. root bioassay system. Antioxidants, 6(2), p.35.

Peik-See, T., Pandikumar, A., Nay-Ming, H., Hong-Ngee, L. and Sulaiman, Y., 2014. Simultaneous electrochemical detection of dopamine and ascorbic acid using an iron oxide/reduced graphene oxide modified glassy carbon electrode. Sensors, 14(8), pp.15227-15243.

Prabhu, A., Shankar, K., Muthukrishnan, P. and Kathiresan, A., 2016. Electrochemical Studies of Biosynthesized Silver Nanoparticles by using Setaria verticillata Plant. Journal of Advanced Chemical Sciences, pp.302-304.

Raoof, J.B., Ojani, R., Beitollahi, H. and Hosseinzadeh, R., 2006. Electrocatalytic oxidation and highly selective voltammetric determination of L-cysteine at the surface of a 1-[4-(ferrocenyl ethynyl) phenyl]-1-ethanone modified carbon paste electrode. Analytical sciences, 22(9), pp.1213-1220.

Santra, T.S., Tseng, F.G.K. and Barik, T.K., 2014. Biosynthesis of silver and gold nanoparticles for potential biomedical applications—a brief review. Journal of Nanopharmaceutics and Drug Delivery, 2(4), pp.249-265.

Senthilkumar S.R. And Sivakumar T., Green Tea (Camellia Sinensis) Mediated Synthesis Of

Zinc Oxide (ZnO) Nanoparticles and Studies on Their Antimicrobial Activities., International Journal of Pharmacy and Pharmaceutical Sciences, 2014, 6(6) pg 461-465.

Shi, Y., Jiang, L., Zhang, L., Kang, R. and Yu, Z., 2014. Dynamic changes in proteins during apple (Malus x domestica) fruit ripening and storage. Horticulture research, 1, p.6.

Shukla, S. and Saxena, S., 2011. Spectroscopic investigation of confinement effects on optical properties of graphene oxide. Applied Physics Letters, 98(7), p.073104.

Sun, H., Yang, Y. and Huang, Q., 2011. Preparation and structural variation of graphite oxide and graphene oxide. Integrated Ferroelectrics, 128(1), pp.163-170.

Thu, N.T.A., Duc, H.V., Hai Phong, N., Cuong, N.D., Hoan, N.T.V. and Quang Khieu, D., 2018. Electrochemical Determination of Paracetamol Using Fe3O4/Reduced Graphene-Oxide-Based Electrode. Journal of Nanomaterials, 2018.

Tomás, R., 2017. Electrochemical sensing directly in bodily fluids–a move towards point of care and in vivo analysis.

Wester, N., 2015. Tetrahedral amorphous carbon–graphene hybrid electrode for detection of dopamine.

Willemse, C.M., 2010. Nanocomposite-graphene based platform for heavy metal detection (Doctoral dissertation, University of the Western Cape).

Yadav, R., Mishra, R. and C. Pandey, A., 2009. Particle size distribution study by small-angle X-ray scattering technique and photoluminescence property of ZnO nanoparticles. Journal of Experimental Nanoscience, 4(2), pp.139-146.

Yan, S., Wu, Z., Yu, H., Gong, Y., Tan, Y., Du, R., Chen, W., Xing, X., Mo, G., Chen, Z. and Cai, Q., 2014. Time-resolved small-angle X-ray scattering study on the growth behavior of silver nanoparticles. The Journal of Physical Chemistry C, 118(21), pp.11454-11463.

Zhang, K., Ai, S., Xie, J. and Xu, J., 2017. Comparison of direct synthesis of silver nanoparticles colloid using pullulan under conventional heating and microwave irradiation. Inorganic and Nano-Metal Chemistry, 47(6), pp.938-945.

Zhu, Y., Murali, S., Cai, W., Li, X., Suk, J.W., Potts, J.R. and Ruoff, R.S., 2010. Graphene and graphene oxide: synthesis, properties, and applications. Advanced materials, 22(35), pp.3906-3924.

CHAPTER 5

Results and Discussion – Part 2

Summary

In the progress of the development of biosensors, nanocomposites have drawn an extraordinary attention due to their unique properties which allows them to perform as exceptional materials for the immobilization of biomolecules and their rapid electron transfer in the performance of effective biosensors. This segment of the study reports on green synthesized zinc oxide nanoparticles using graphene oxide (ZnONPs/GO) and green synthesized silver nanoparticles with graphene oxide (AgNPs/GO) nanocomposites as an application for development of biosensors. As part of characterizing these nanocomposites, Fourier Transform Infra-Red spectroscopy (FTIR), Raman spectroscopy and Energy Diffraction X-Ray (EDX) were used to determine the structural and elemental compositions of these nanocomposites while ultraviolet-visible spectroscopy (UV-Vis) was used to determine the electron transitions present in these nanocomposites. Moreover, the morphology of these nanocomposites were studied by High-Resolution Scanning Electron Microscopy (HRSEM) and High- Resolution Transmission Electron Microscopy (HRTEM). Lastly, electrochemical studies were also conducted to study their conductivities and the suitability of these nanocomposites to be applied in the fabrication of nanocomposites.

5.1 Green synthesized AgNPs/GO and/or ZnONPs/GO nanocomposites

This study demonstrates the electrochemical and physical characterization of nanocomposites based on silver nanoparticles or zinc oxide nanoparticles with graphene oxide synthesized by a green and a low cost approach using a mixture of tomato and apple extract as a reducing and stabilizing agent. This part of this study was carried out using the conventional heating (CH) method using mainly green materials, although in chapter 4 the microwave irradiation (MI) method synthesized nanoparticles showed better results and were initially chosen to be used in the nanocomposite synthesis. Consequently when the synthesis was attempted, several issues were experienced several times which included; the deposition of potassium permanganate in the MI equipment and enhanced when it is irradiated with microwaves, Furthermore, the MI method again was conducted with a lower content of sulphuric acid related with the Hummers method obtaining graphene oxide in the nanocomposites which had low defect contents. **(Ibarra-Hernández *et al*., 2018)** Using graphene oxide in MI was problematic even other researchers exhibited some toxic qualities though the nanoparticles seem to show no problem.

Thereafter this lead to the successful fabrication of both nanocomposites; AgNPs/GO and ZnONPs/GO using CH methods followed by a comparison made between them using spectroscopical, morphological and electrochemical techniques to investigate which one was effective and suitable in the fabrication of biosensors. Thus, FTIR data illustrated functional groups that were present in nanoocomposites while the XRD data confirmed the formation of highly pure crystal of Ag or Zn on GO. The HRTEM images demonstrated that that spherical ZnONPs or AgNPs of an average size of 4 nm are uniformly deposited onto GO sheets. The energy dispersive X-ray spectra (EDX) of nanocomposites indicated the presence of Zn, Ag and GO. While on the other hand, the electrochemical investigations revealed the

conductivity of these nanocomposites. Other techniques that were also used will be clarified below.

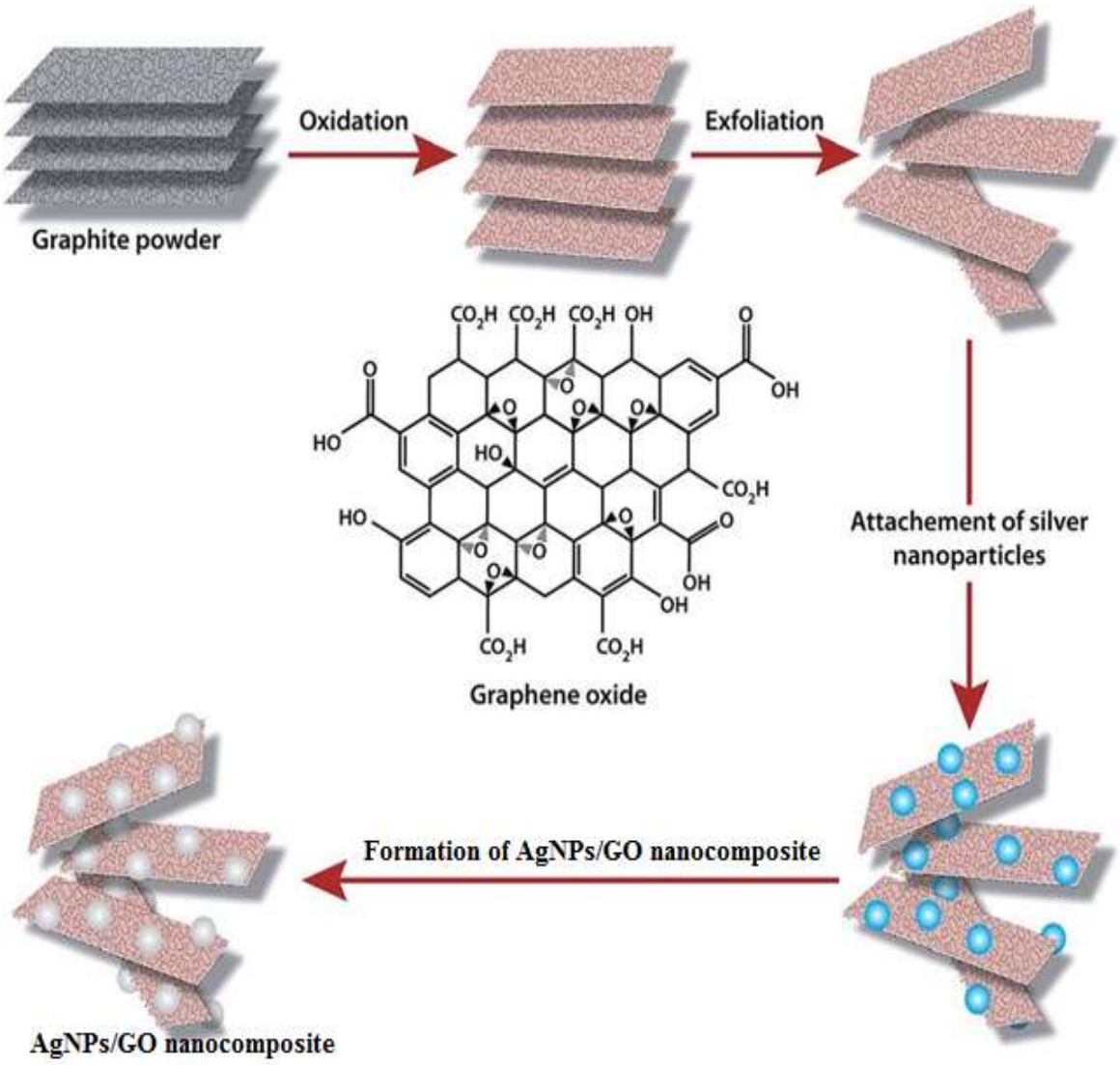

Figure 5.1: Schematic diagram demonstrating the preparation steps of AgNPs/GO nanocomposites. (Roy *et al*., 2015)

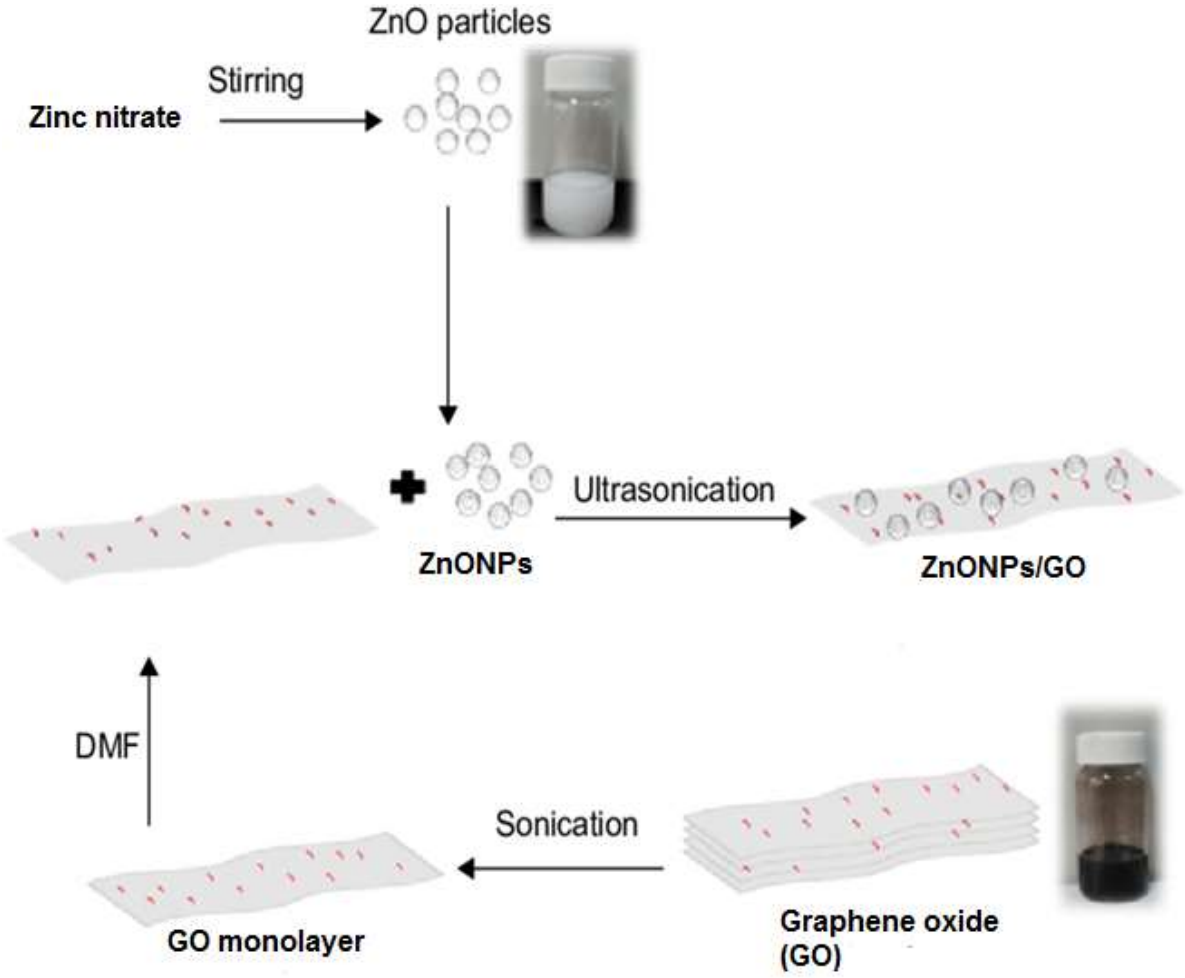

Figure 5.2: Schematic diagram illustrating the preparation steps of ZnONPs/GO nanocomposites. (Zhong and Yun,. 2015)

5.1.1 Spectroscopic characterisation of AgNPs/GO and/or ZnONPs/GO nanocomposites

5.1.1.1 Fourier transform infrared spectroscopy (FTIR)

Figure 5.3 illustrates the Fourier Transform Infra-Red (FTIR) spectra of green synthesized ZnONPs/GO and AgNPs/GO nanocomposites using a CH method. In this segment of study or AgNPs. Analyzing the results showed that the ZnONPs/GO nanocomposite obtained consists of zinc oxide nanoparticles decorated on graphene oxide sheets. The broad peak at 3431 cm^{-1} in the FTIR spectrum of the ZnONPs/GO nanocomposite is attributed to the O–H stretching vibration of absorbed water molecules. The peaks at 1074, 1234, 1560 cm^{-1} are assigned to C=O stretching, sp^2 hybridized C=C groups, C–O stretching, O–H deformation and C–OH stretching, respectively. Also in the spectrum a peak at 452 cm^{-1} corresponds to the hexagonal nature of ZnO. **(Azarang., 2017)** this particular technique is carried out to investigate the interactions between GO and ZnONPs

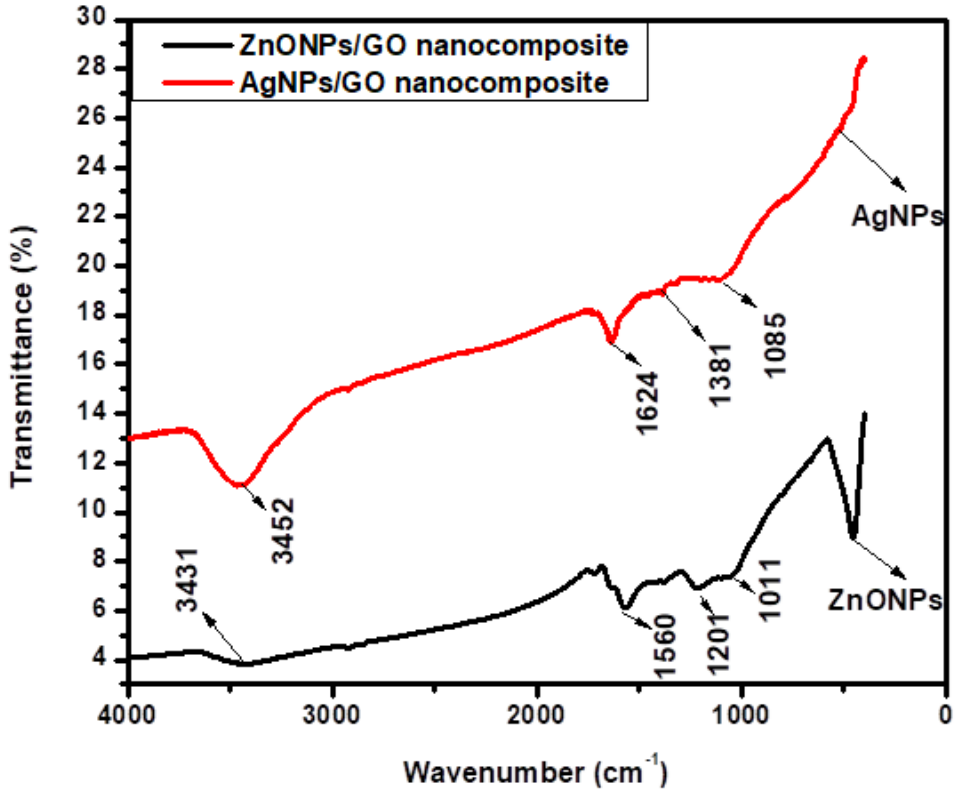

Figure 5.3: Fourier transform infrared spectrum of green synthesized ZnONPs/GO and AgNPs/GO nanocomposites.

However for the AgNPs/GO nanocomposite, the FTIR spectrum shows similar peaks at 1095, 1381, 1634 cm^{-1} which are relatively strong compared to those of ZnONPs/GO. The absorption peak for AgNPs/GO at 3452 cm^{-1} is also attributed to the O–H stretching vibration. The absorption band at 1560 cm^{-1} for ZnONPs/GO and at 1633 cm^{-1} for AgNPs/GO is attributed to the skeletal vibration of the graphene sheets. These results evidently prove that GO was successfully exfoliated and that there is a strong interactions between AgNPs or ZnONPs with the remaining surface hydroxyl groups. **(Shao *et al*., 2015)**

5.1.1.2 Ultraviolet Visible Spectroscopy (UV-vis)

Ultraviolet Visible Spectroscopy (UV-vis) was used to study the electronic transitions of the green synthesized ZnONPs/GO and AgNPs/GO nanocomposites (**Figure 5.4**). The UV-vis spectrum of AgNPs/GO showed typical characteristics features such as a shoulder at 213.9 nm corresponding to a π–π* plasmon peak. AgNPs/GO was confirmed by UV-visible spectra that there are AgNPs attached to the layers of graphene oxide by showing a typical characteristic peak that was consistent with the surface plasmon resonance phenomena of AgNPs formulation as shown in **Figure 4.15**, while GO showed a typical peak around 208 nm (**Figure 4.5**) corresponding to the C=C aromatic bonding. **(Gurunathan and Kim., 2017)**

The UV–vis absorption spectrum of ZnONPs/GO revealed a characteristic absorption peak at a wavelength of 205.6 nm, which was assigned to the intrinsic band gap absorption of π–π*, owing to the electron transitions to the conduction band from the valence band. It is clearly seen that the peak position of the UV–vis spectra of ZnONPs/GO has been affected by the absorption contribution from both ZnONPs and GO through the modification of the fundamental process of electron–hole pair formation. Therefore, from the spectrum in **Figure 5.4** the presence of AgNPs/GO compared to ZnONPs/GO has an increased light absorption range and intensity which is beneficial to the biosensor performance due its higher wavelength. **(Azarang *et al*., 2014)** The position and intensity of these nanocomposites vary depending on the concentration of the solvent used, sonication time and several other factors.

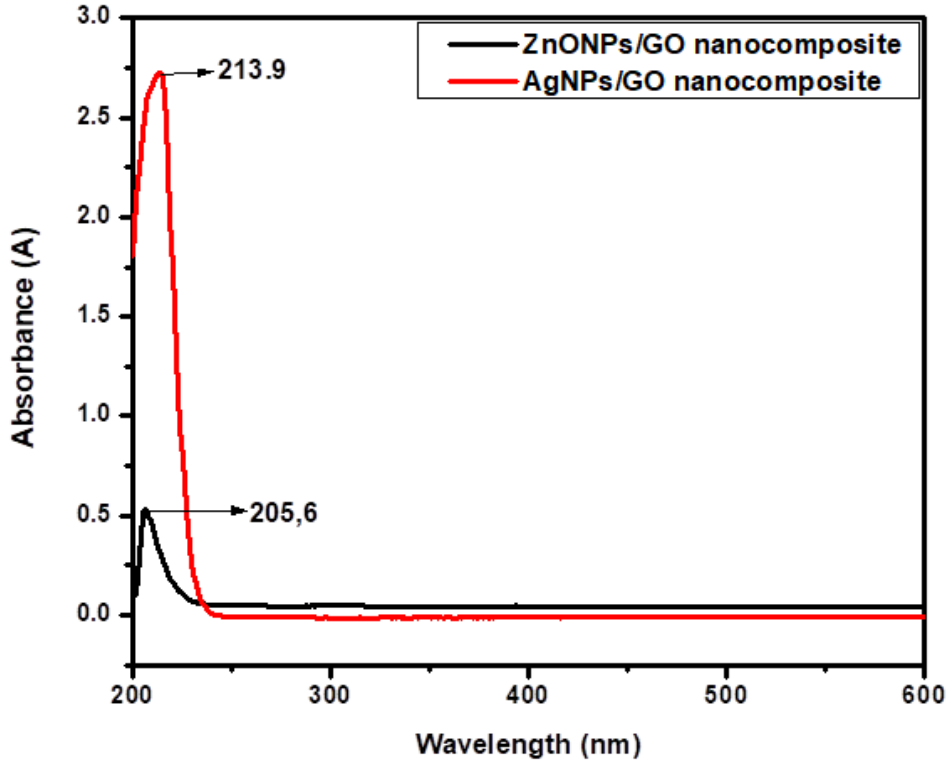

Figure 5.4: Ultraviolet-visible spectrum of green synthesized ZnONPs/GO and AgNPs/GO nanocomposites.

5.1.1.3 Raman Spectroscopy

Raman spectroscopy is one of most non-destructive and powerful techniques to extract useful information about nanocomposites. In this part of this study it was used to characterize green synthesized ZnONPs/GO and AgNPs/GO nanocomposites, respectively. **Figure 5.5** illustrates the Raman spectra that were obtained after characterization. There are two main peaks that were observed by both nanocomposites namely; D and G. The D band arises due to disorder at edges of graphene, while the G band is due to in-phase vibrations of the graphene lattice. **(Ferrari. and Basko., 2013)** The Raman spectroscopy was performed to characterize the electronic and structural properties of AgNPs/GO, which showed the two characteristic D and G bands at approximately 1347 cm^{-1} and 1608 cm^{-1}, respectively. The G

band narrates to the tangential stretching mode of the E_2g phonon of the sp^2 carbon atom and the D band offers evidence on the breathing mode of the κ-point. **(Gurunathan *et al*., 2015)**. However, in the case of ZnONPs/GO the D and G bands were found to be at 1339 and 1577 cm^{-1}, which are due to zinc oxide nanoparticles anchored onto the GO surface. The intensity ratio in Raman spectrum of ZnONPs/GO was found to be 1.17 while that of AgNPs/GO was found to be 1.19.

A decrease in the intensity of the D peak with respect to the G peak was observed, that is the decrease in intensity ratio (1.17) in ZnONPs/GO compared to AgNPs/GO (1.19) indicated that there was a different restoration of the sp^2 network on the surface of graphene oxide and a reduction of nanoparticles (ZnO or Ag). Therefore, from Raman spectra, it is observed that there is an attachment of ZnO or Ag onto the GO matrix leading to partial restoration of the sp^2 network. Both these results are consistent with previous reports on the Raman spectra of AgNPsGO **(Gurunathan *et al*., 2017)** and that of ZnONPs/GO. **(Jilani and Banerji., 2014)**

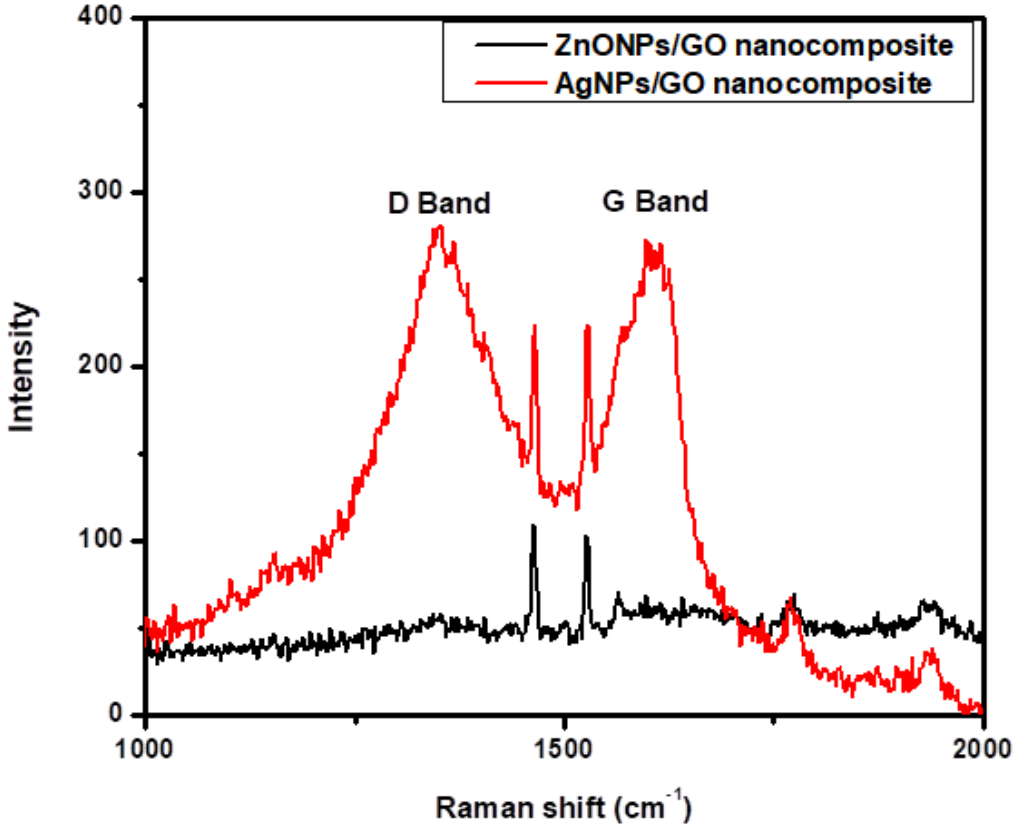

Figure 5.5: Raman spectrum of green synthesized ZnONPs/GO and AgNPs/GO nanocomposites.

5.1.1.4 X-Ray diffraction (XRD)

X-Ray diffraction (XRD) is a suitable technique for determining crystalline structure and interlayer distances. **Figure 5.6** illustrates XRD patterns of both green synthesized ZnONPs/GO and AgNPs/GO nanocomposites. For the ZnONPs/GO nanocomposite the appearance of characteristic diffraction peaks are illustrated by the red line curve. The ZnO nanoparticles present in ZnONPs/GO corresponds to the (100), (002), (101), (102), (110), (103), and (112) planes. All these diffraction peaks confirm the crystalline ZnO has a hexagonal quartzite structure and the sharp diffraction peak that appears at $2\theta = 10.16°$ is a confirmation of presence of GO. The XRD pattern of the ZnONPs/GO nanocomposite is

similar to previous studies results. **(Zhong and Yun,. 2015)** Moreover, the disappearance of the (001) reflection of GO in the XRD pattern of ZnONPs/GO is attributed to the intercalation of ZnONPs that impaired the regular stack of graphene oxide. **(Hosseini and Babaei., 2017)**

XRD pattern for AgNPs/GO nanocomposite had peak values which shifted at about 38.2°, 44.2°, 64.6° and 77.5° which were allocated to the (111), (200), (220) and (311) crystal lattice planes of face-cantered cubic (fcc) silver nanoparticles respectively whereas, the peak of graphene oxide disappeared due to the metal nanoparticles that are attached onto the inlayers which led to sheeting the signals of GO peaks. Evidently, the sharp peak at 38.2° confirmed that the nanoparticles are composed of pure crystalline silver. **(Vi and Lu., 2017)** Thus, from the XRD results it can be confirmed that both nanocomposites were successfully obtained.

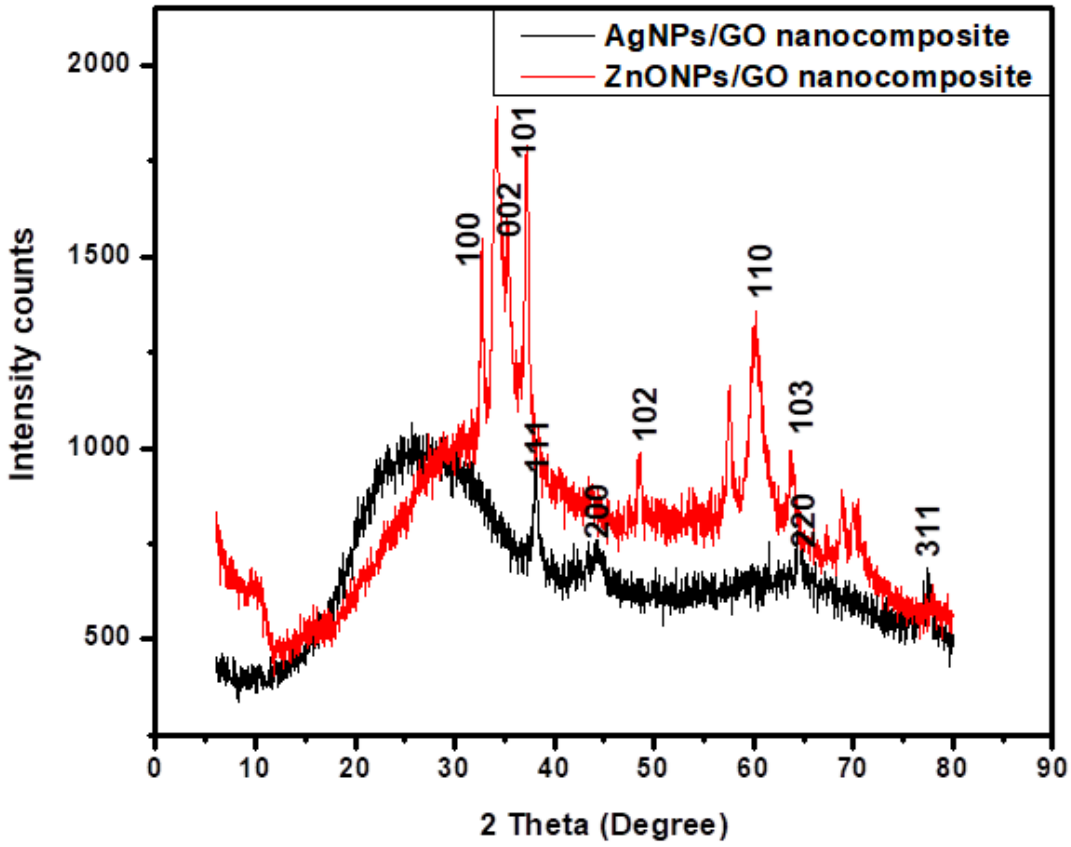

Figure 5.6: X-Ray diffraction spectrum of green synthesized ZnONPs/GO and AgNPs/GO nanocomposites.

5.1.2 Microscopic characterisation of AgNPs/GO and/or ZnONPs/GO nanocomposites

5.1.2.1 High resolution transmission electron microscopy (HRTEM)

The representative HRTEM images of AgNPs/GO and ZnONPs/GO nanocomposite are shown in **Figure 5.7 (a) and (b)**, respectively. In both images large GO sheets with dimension in the nanometers range were found positioned on the top of the grid where rippled silk waves and transparent appearances where demonstrated. In the case of the HRTEM image of ZnONPs/GO (**Figure 5.7 (a)**), the dark spots on the GO flake are attributed to the presence of ZnONPs. As a result, the image proves that the nanoparticles ZnO and nanosheet GO are present in the nanocomposite. Whereas from the HRTEM image

of AgNPs/GO (**Figures 5.7 (b)**) the GO sheets are observed with few crumpled silk waves while the oval or spherical shape AgNPs are spotted on the graphene oxide sheets.

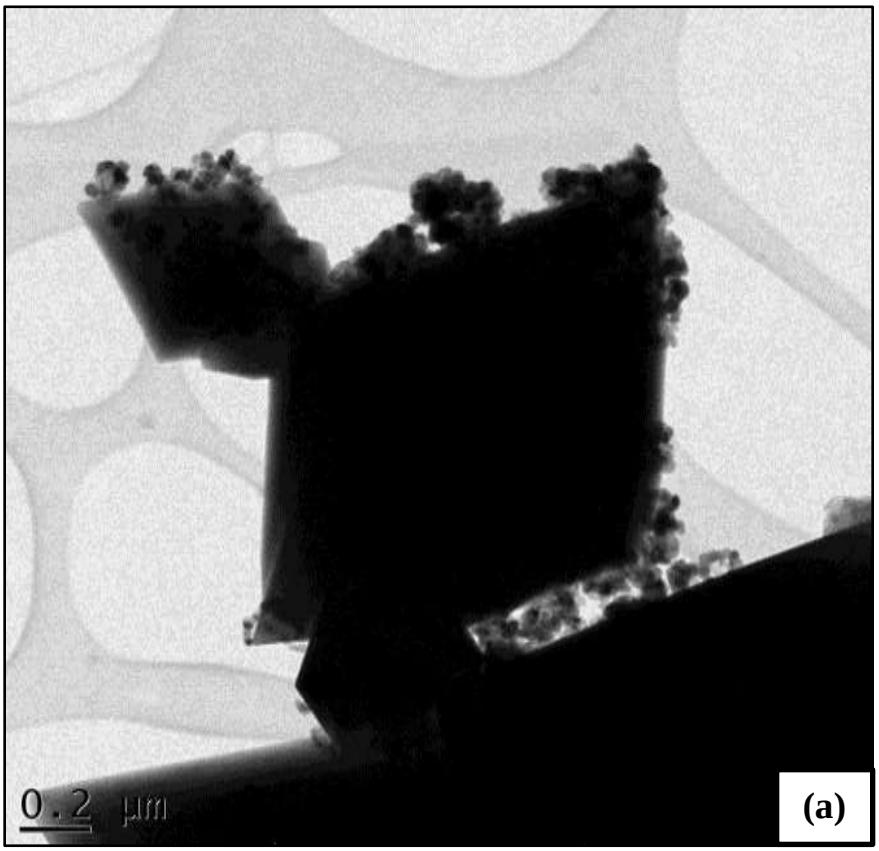

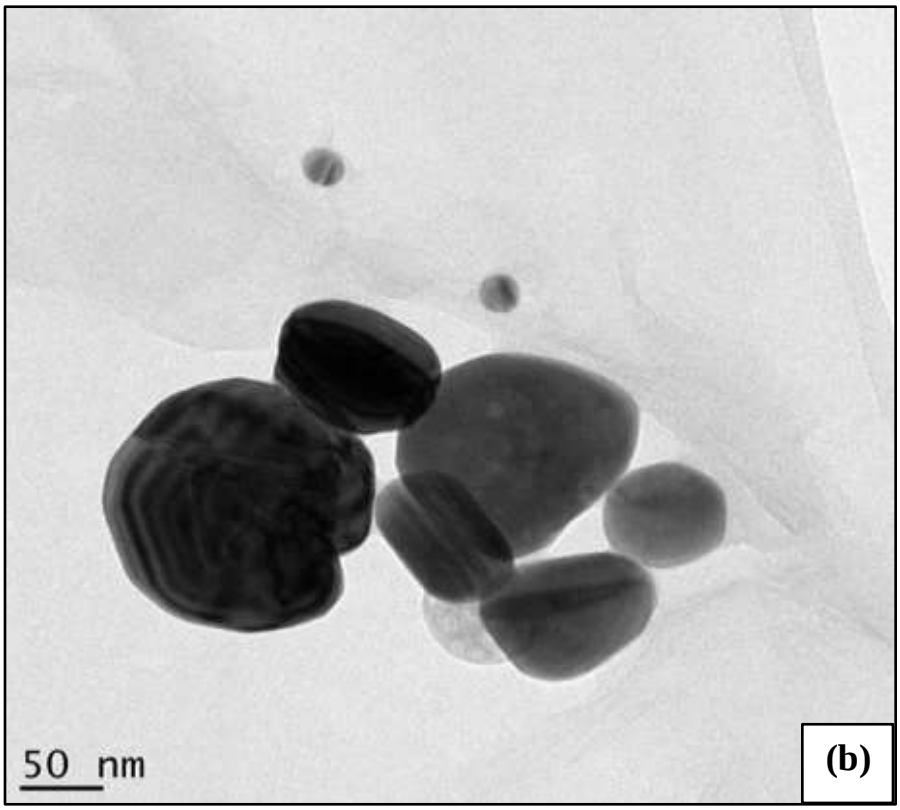

Figure 5.7: HRTEM images of green synthesized (a) ZnONPs/GO and (b) AgNPs/GO nanocomposites.

5.1.2.2 High resolution Scanning electron microscopy (HRSEM)

To further study the particle size and surface morphology of AgNPs/GO and ZnONPs/GO nanocomposies, HRSEM images were obtained as shown in **Figure 5.8 (a) and (b)**. In the HRSEM images of ZnONPs/GO (**Figure 5.8 (b)**) the nanoparticles of zinc oxide were dispersed and uniformly covered on the graphene oxide sheets and it was observed that some ZnONPs had been agglomerated. ImageJ software (The software that was developed to allow better image analysis and enhancement) was used to investigate the diameter of ZnONPs present in the nanocomposite. The nanoparticles were obtained to be less than 100 nm as

expected**,** comparable in other studies had nanoparticles with diameter around 98.3 and 89.01 nm **(Hosseiniand Babaei., 2017)** and they were very similar in size to the nanoparticles obtained before of MI and CH method which also had diameter less than 100 nm as shown before, hence our findings are within acceptable values.

In case of AgNPs /GO (**Figure 5.8 (b)**), the graphene oxide sheets had AgNPs randomly distributed and well separated from each other. ImageJ was also used in this instance to determine the particles size of AgNPs present in the AgNPs/GO nanocomposite. Consequently, the examined particles sizes were between 10 and 100 nm as expected **(Chook *et al*., 2012)** and also to the nanoparticles obtained before of MI and CH method.

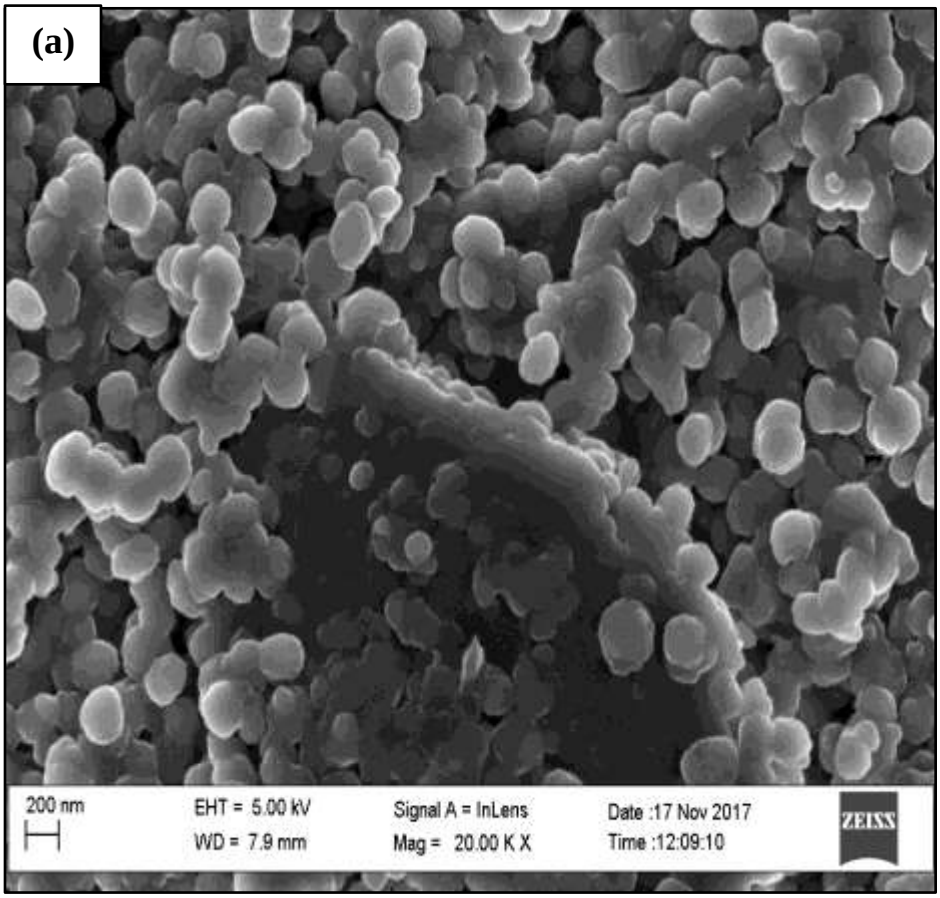

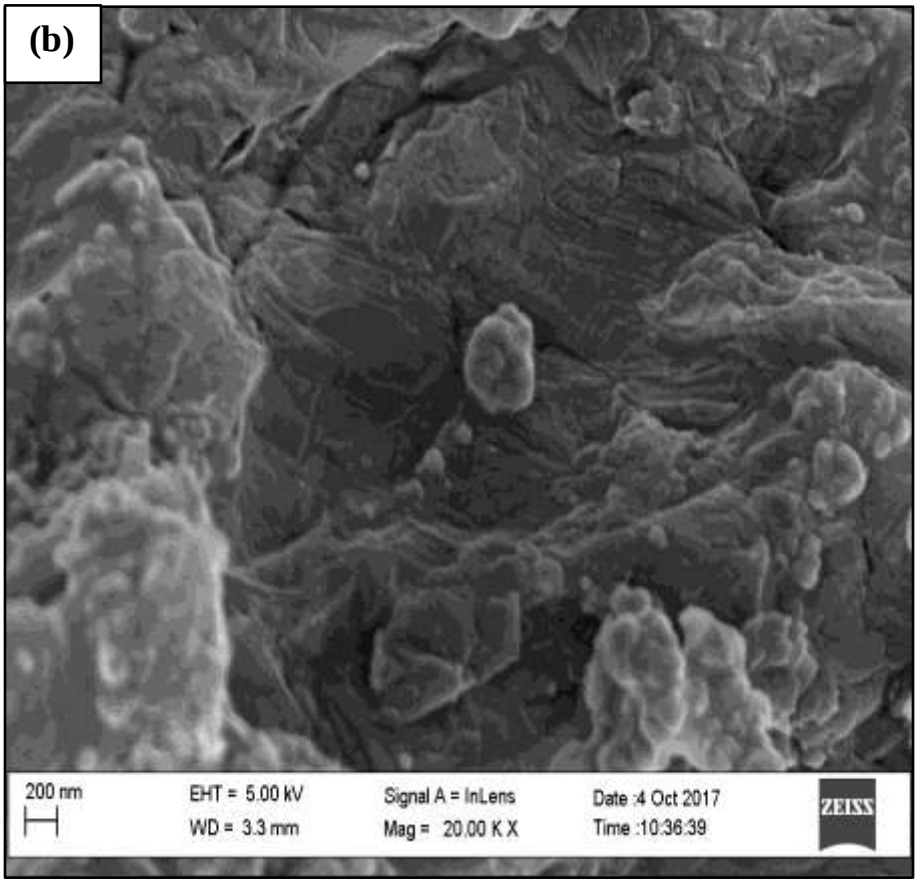

Figure 5.8: HRSEM images of green synthesized (a) ZnONPs/GO and (b) AgNPs/GO nanocomposites.

5.1.2.3 Energy dispersive X-ray (EDX)

Energy-dispersive X-rays spectroscopy (EDX) was used to detect the elemental composition of the green synthesized AgNPs/GO nanocomposite. **Figure 5.9 (a)** illustrated an EDX spectrum for AgNPs/GO which clearly indicated the Ag peak indicating thepresence of silver nanoparticles therein the sample.

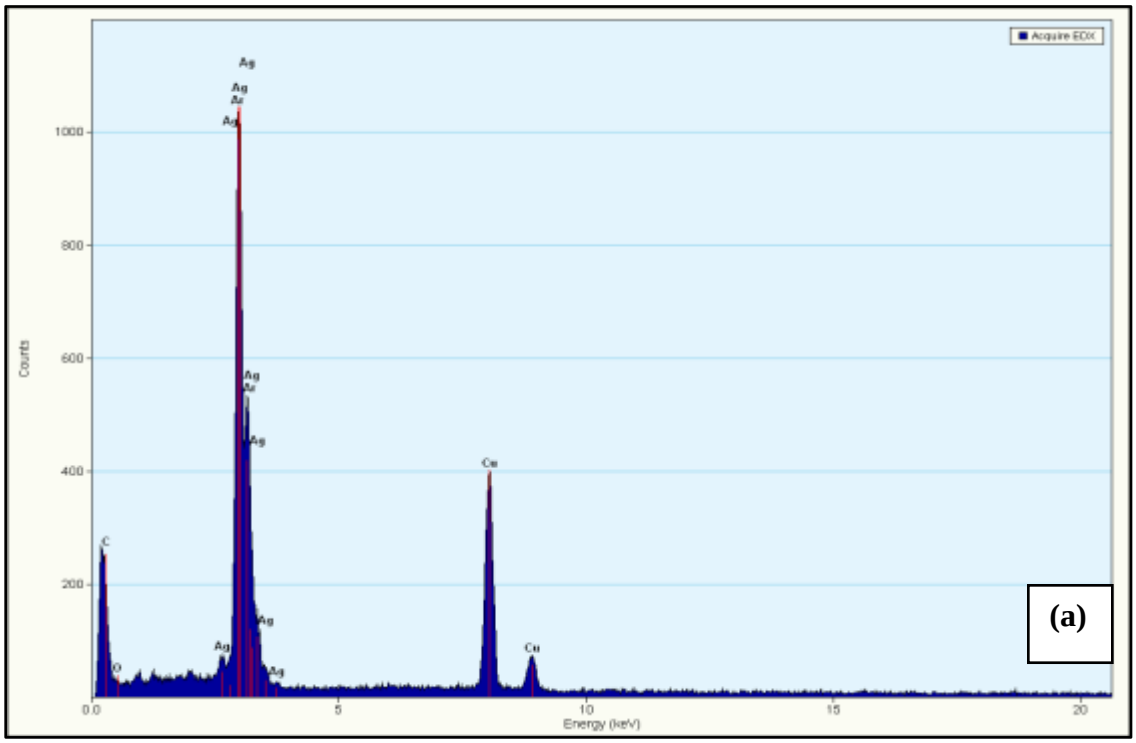

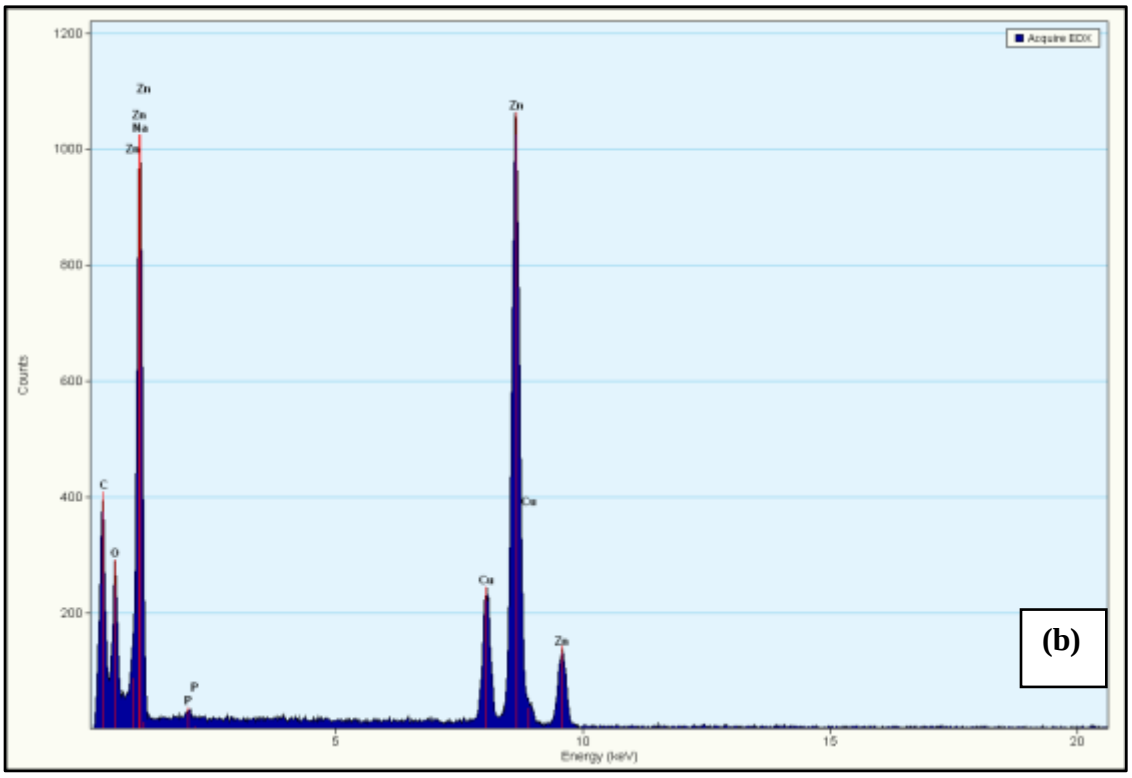

Figure 5.9: (a) Energy dispersive x-ray spectrum analysis of green synthesized AgNPs/GO nanocomposite and (b) Energy dispersive x-ray spectrum analysis of green synthesized ZnONPs/GO nanocomposites.

The elements that were present and their percentage are shown in **Table 5.1**. The oxygen (O) peak was from graphene oxide present in the nanocomposite and presence of copper (Cu) results copper grid used throughout for sample preparation to precede the analyses. **Figure 5.9 (b)** demonstrates the elemental analysis of ZnONPs/GO nanocomposites which was performed by the Energy Dispersive X-ray (EDX) technique. The weight percentage and weight percentage stigma detected where those of C, O and Zn elements apart from the element Cu used to coat the samples. All the elements detected were present in ZnONPS/GO nacomposites during synthesis. The percentages of the elements were determined from the intensity of the lines and are summarized in **Table 5.2 (b)**

Table 5.1 (a): Elemental composition of AgNPs/GO nanocomposite.

Element	Weight percentage (%)	Weight percentage sigma (%)
C	19.02	2.77
O	23.07	3.66
Ag	57.9	3.66
Total:	100	

Table 5.2 (b): Elemental composition of ZnONPs/GO nanocomposite.

Element	Weight percentage (%)	Weight percentage sigma (%)
O	16.2	0.58
Na	10.43	1.81
Zn	73.37	1.56
Total:	100	

5.1.3 Electrochemical characterisation of AgNPs/GO and/or ZnONPs/GO nanocomposites

5.1.3.1 Cyclic Voltammetry (CV)

The electrochemical response of green synthesized AgNPs/GO nanocomposites and green synthesized ZnONPs/GO nanocomposites are illustrated in **Figure 5.10**. Represented here is a bare glassy carbon electrode (black curve), green synthesized AgNPs/GO nanocomposite (red curve) and green synthesized ZnONPs/GO nanocomposite (blue curve) evaluated in 0.1 M PBS, pH7.4 buffer at a scan rate 30 mV/s at a potential window from -1000 to 1000 mV. The potential window demonstrates a well-defined redox couple anodic and cathodic peak for both nanocomposites. The results shown in **Figure 5.10** proves that ZnO/NPs and AgNPs/GO have a different redox response compared to the bare GCE; the cathodic current peaks of nanocomposites increased linearly to cathodic potential peaks while anodic current peaks on the other side also increased linearly to potential peak which shifts slightly towards the positive potentials. The shift occurring in anodic peaks shows an electrochemical activity of nanocomposites. **(Arfin and Rangari ., 2018)**

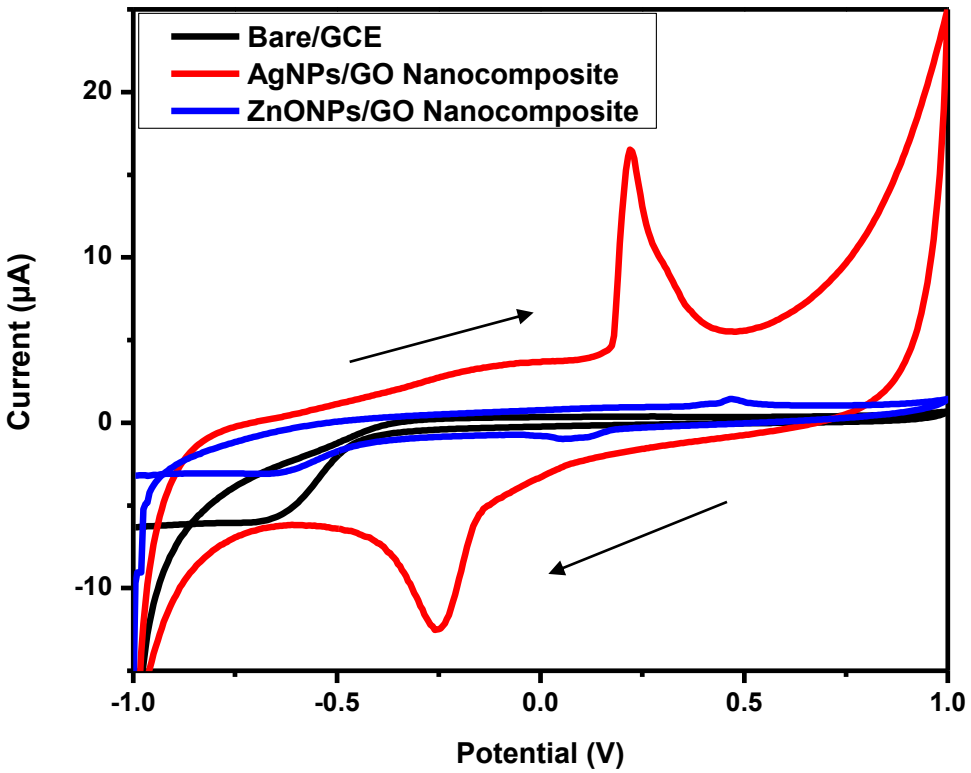

Figure 5.10: CV of bare Glassy carbon electrode (GCE) (black curve), green synthesized AgNPs/GO nanocomposite (red curve) and green synthesized ZnONPs/GO nanocomposite (blue curve) in phosphate buffer solution (pH 7.4) at 30 mV s^{-1}.

Moreover, the effect of scan rate on the peak current was examined by running a series of cyclic voltammograms at different scan rates from 10 to 100 mV s^{-1} as shown in **Figure 5.11 (a) and (b)** where the green synthesized AgNPs/GO nanocomposite and green synthesized ZnONPs/GO nanocomposite where studied independently. The results presented by CV displays that the anodic peak current varies linearly with the scan rate and a shift in potential to more positive values with increasing scan rate was observed for each type of material. This

is clearly indicates that these nanocomposites were conductive while transferring electrons with the electrode surface.

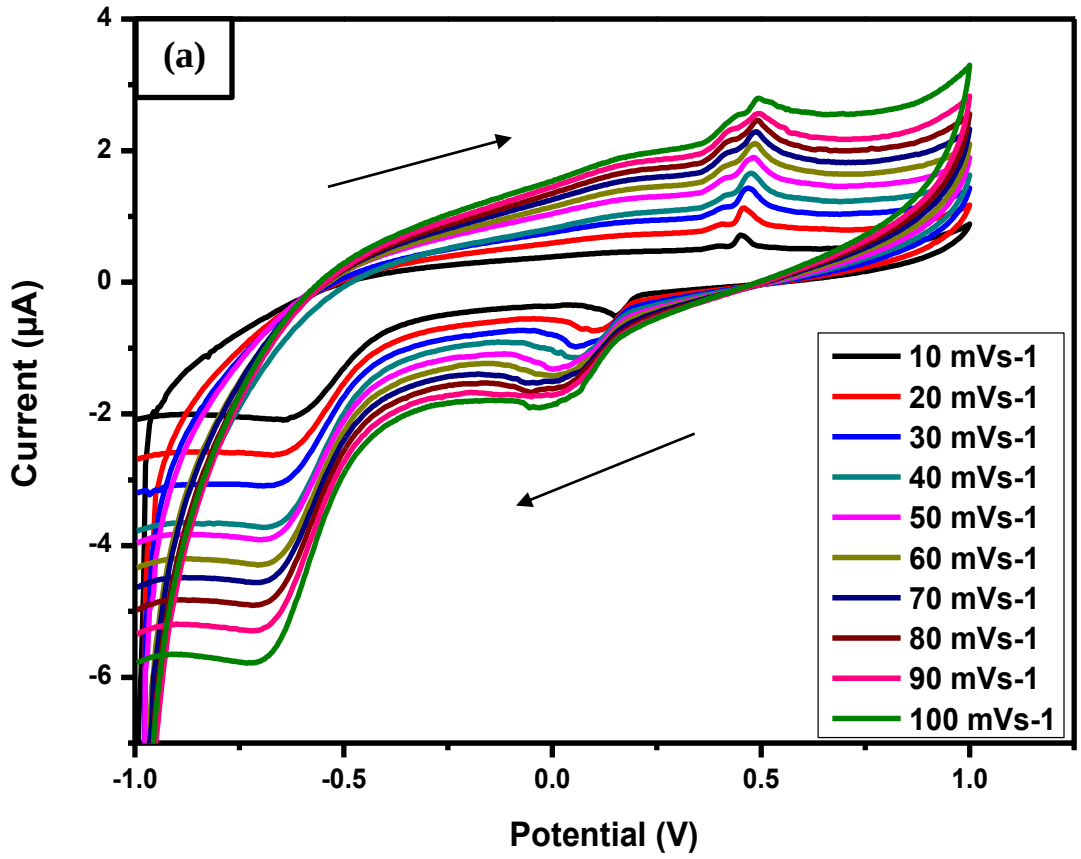

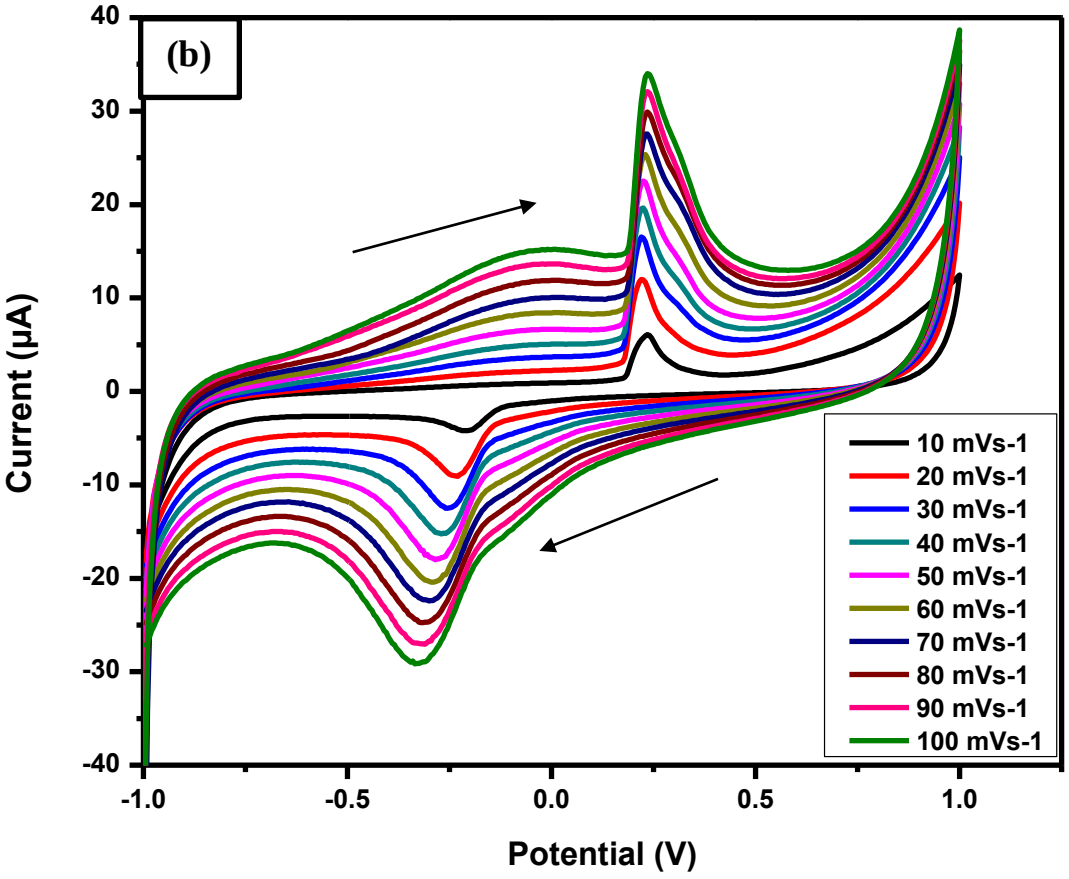

Figure 5.11: CV of green synthesized ZnONPs/GO nanocomposite (a) and green synthesized AgNPs/GO nanocomposite (b) in 0.1 M phosphate buffer solution (pH 7.4) at 10-100 mV s^{-1}.

The performance of cyclic voltammetry on these nanocomposites at different scan rates led to the preparation of linear plots as shown in **Figure 5.12** whose slopes provide additional information about redox properties. The slopes of plots of log scan rate versus log current were used to identify adsorption controlled or diffusion controlled processes. **Figure 5.12 (a)**, gave a linear equation of $y = 0.6071x - 0.7595$ with a correlation coefficient $r^2 = 0.9955$ for the green synthesized ZnONPs/GO nanocomposite and for the green synthesized AgNPs/GO

attached on the GCE a linear equation of y = 0.7341x + 0.0873 was determined with a correlation coefficient r^2 = 0.9865. These results show that the electron transfer reaction was controlled by the adsorption of the nanocomposite on the surface of the glassy carbon electrode as confirmed by the slopes of these plots. Additionally, the analysis of the peak-to-peak separation (ΔEp) were determined and confirmed that the peak currents were diffusion-controlled in both nanocomposites (AgNPs/GO and ZnONPs/GO) because when increasing the scan rate. The magnitude of the peak current increased demonstrating the electrochemical process classified as quasi-reversible since ΔE_p was determined to be larger than the value of 57/n mV associated with reversible process at 25 ºC within the scan rates employed. **(Raoof *et al*., 2006)**

Furthermore, the Brown Anson equation (**Equation 5.1)** was used to determine the surface concentration Γ^* (mol cm^{-2}) of the green synthesized AgNPs/GO nanocomposite and the green synthesized ZnONPs/GO nanocomposite. From the equation, F is the faraday constant (96485 C mol^{-1}), A is the surface area of the glassy carbon electrode (0.043 cm^2), n is the number of electron transferred, υ is the scan rate (V s^{-1}), T is the operating absolute temperature of the system (25 °C T in 298 K), R is the gas constant (8.314 J mol^{-1} K^{-1}), Γ* represent the surface concentration of the AgNPs/GO and ZnONPs/GO (mol cm^{-2}) The surface concentration (Γ*) of green synthesized AgNPs/GO nanocomposite was established to be 7.1854 x 10^{-3} mol cm^{-2} while that of the green synthesized ZnONPs/GO nanocomposite was determined to be 5.8645 x 10^{-4} mol cm^{-2}. This indicated that the AgNPs/GO nanocomposite is much denser than the ZnONPs/GO nanocomposite hence showing an elevated surface concentration value.

$$I_p = n^2 F^2 \Gamma^* A \nu / 4 R T \quad (5.1)$$

Similarly to the previous chapter, the diffusion coefficient of the green synthesized AgNPs/GO nanocomposite and green synthesized ZnONPs/GO nanocomposite was determined using the Randel-Sevcik Equation (**Equation 5.2**). For the green synthesized AgNPs/GO nanocomposite a value of 1.6213 $x10^{-4}$ cm^2/s was determined and a value of 1.5979 $x10^{-4}$ cm^2/s was determined for the green synthesized ZnONPs/GO nanocomposite. As predicted the value observed for the green synthesized AgNPs/GO nanocomposite is slightly higher than that observed for the ZnONPs/GO nanocomposite. This means that AgNPs/GO allows efficient transfer of electrons hence it was be chosen for the fabrication of the biosensors of interest in this study.

$$I_p = 268, 600\, n^{3/2} A D^{1/2} C \nu^{1/2} \quad (5.2)$$

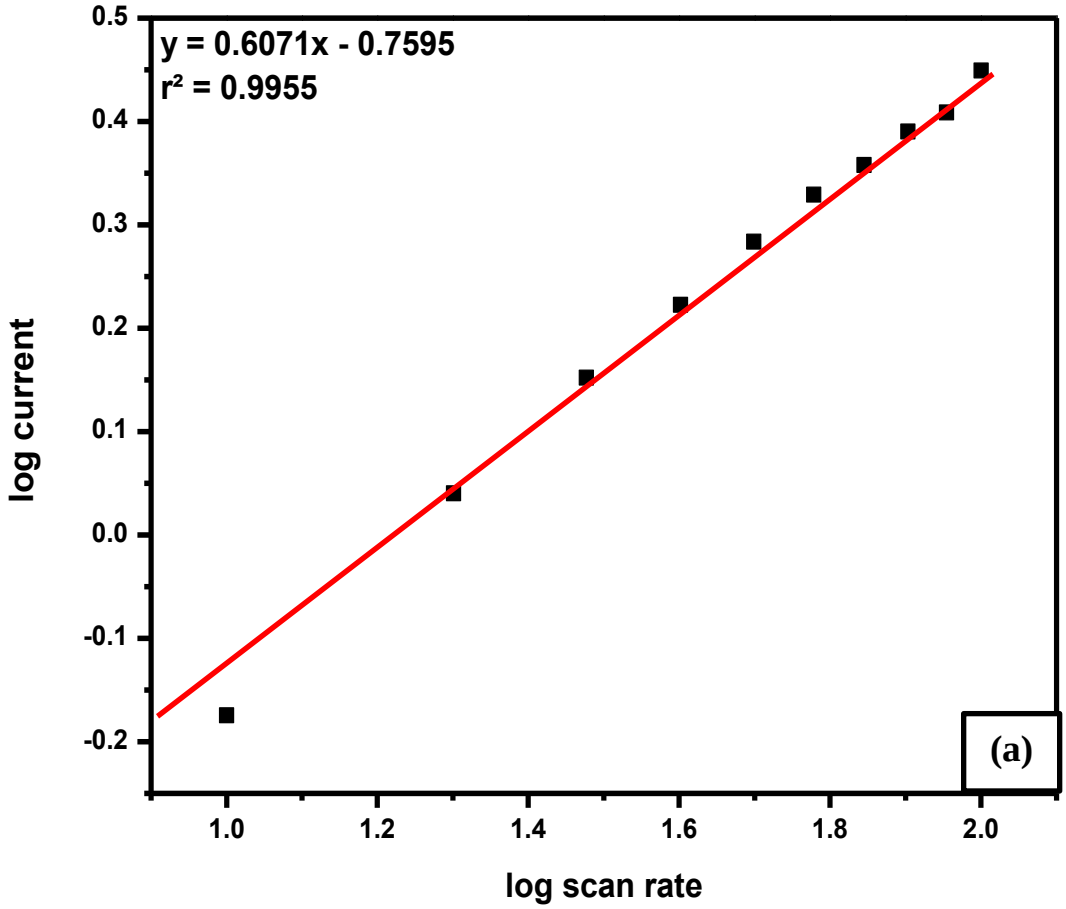
y = 0.6071x - 0.7595
r² = 0.9955
log current
log scan rate
(a)
0.5
0.4
0.3
0.2
0.1
0.0
-0.1
-0.2
1.0
1.2
1.4
1.6
1.8
2.0

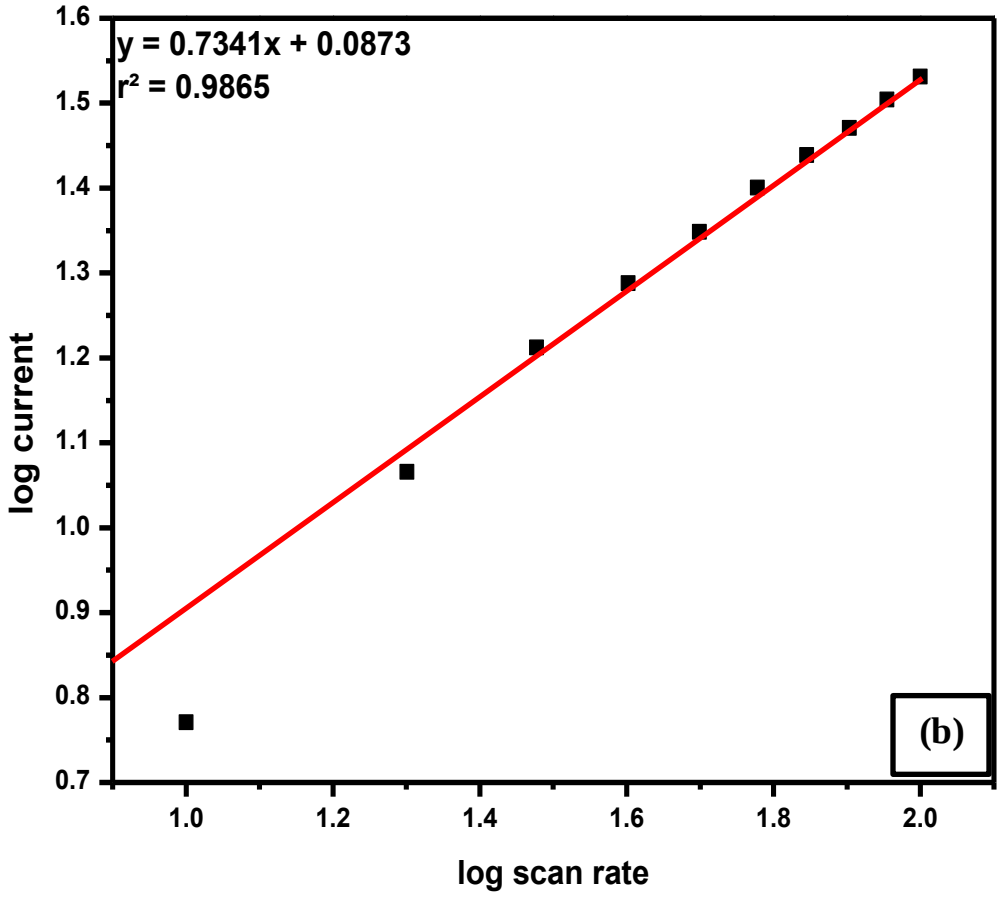

Figure 5.12: Plots of log current versus log scan rate of (a) green synthesized ZnONPs/GO nanocomposite and (b) green synthesized AgNPs/GO nanocomposite.

5.2 References

Arfin, T. and Rangari, S.N., 2018. Graphene oxide–ZnO nanocomposite modified electrode for the detection of phenol. Analytical Methods, 10(3), pp.347-358.

Azarang, M., 2017. Zinc oxide nanoparticles-based reduced graphene oxide composites for photocatalytic and photovoltaic applications (Doctoral dissertation, University of Malaya).

Azarang, M., Shuhaimi, A., Yousefi, R., Golsheikh, A.M. and Sookhakian, M., 2014. Synthesis and characterization of ZnO NPs/reduced graphene oxide nanocomposite prepared in gelatin medium as highly efficient photo-degradation of MB. Ceramics International, 40(7), pp.10217-10221.

Chook, S.W., Chia, C.H., Sarani, Z., Ayob, M.K., Chee, K.L., Neoh, H.M. and Huang, N.M., 2012. Silver nanoparticles-graphene oxide nanocomposite for antibacterial purpose. In Advanced Materials Research (Vol. 364, pp. 439-443). Trans Tech Publications.

Ferrari, A.C. and Basko, D.M., 2013. Raman spectroscopy as a versatile tool for studying the properties of graphene. Nature nanotechnology, 8(4), p.235.

Gurunathan, S. and Kim, J.H., 2017. Graphene oxide–silver nanoparticles nanocomposite stimulates differentiation in human neuroblastoma cancer cells (SH-SY5Y). International journal of molecular sciences, 18(12), p.2549. (a)

Gurunathan, S., Hyun Park, J., Choi, Y.J., Woong Han, J. and Kim, J.H., 2016. Synthesis of graphene oxide-silver nanoparticle nanocomposites: an efficient novel antibacterial agent. Current Nanoscience, 12(6), pp.762-773. (b)

Gurunathan, S., Han, J.W., Park, J.H., Kim, E., Choi, Y.J., Kwon, D.N. and Kim, J.H., 2015. Reduced graphene oxide–silver nanoparticle nanocomposite: a potential anticancer nanotherapy. International journal of nanomedicine, 10, p.6257. (c)

Hosseini, S.A. and Babaei, S., 2017. Graphene oxide/zinc oxide (GO/ZnO) nanocomposite as a superior photocatalyst for degradation of methylene blue (MB)-process modeling by response surface methodology (RSM). Journal of the Brazilian Chemical Society, 28(2), pp.299-307.

Ibarra-Hernández, A., Vega-Rios, A. and Osuna, V., 2018. Synthesis of Graphite Oxide with Different Surface Oxygen Contents Assisted Microwave Radiation. Nanomaterials, 8(2), p.106.

Jilani, S.M. and Banerji, P., 2014. Graphene Oxide–Zinc Oxide Nanocomposite as Channel Layer for Field Effect Transistors: Effect of ZnO Loading on Field Effect Transport. ACS applied materials & interfaces, 6(19), pp.16941-16948.

Roy, I., Rana, D., Sarkar, G., Bhattacharyya, A., Saha, N.R., Mondal, S., Pattanayak, S., Chattopadhyay, S. and Chattopadhyay, D., 2015. Physical and electrochemical characterization of reduced graphene oxide/silver nanocomposites synthesized by adopting a green approach. RSC Advances, 5(32), pp.25357-25364.

Shao, W., Liu, X., Min, H., Dong, G., Feng, Q. and Zuo, S., 2015. Preparation, characterization, and antibacterial activity of silver nanoparticle-decorated graphene oxide nanocomposite. ACS applied materials & interfaces, 7(12), pp.6966-6973.

Vi, T.T.T. and Lue, S.J., 2016, November. Preparation of silver nanoparticles loaded graphene oxide nanosheets for antibacterial activity. In IOP Conference Series: Materials Science and Engineering (Vol. 162, No. 1, p. 012033). IOP Publishing.

Zhong, L. and Yun, K., 2015. Graphene oxide-modified ZnO particles: synthesis, characterization, and antibacterial properties. International journal of nanomedicine, 10(Spec Iss), p.79.

CHAPTER 6

Results and Discussion - Part 3

Summary

This chapter provides a detailed description of the fabrication of the biosensors used for the respective detection of the tuberculosis treatment drugs namely; Ethambutol and Pyrazinamide. Herein is also an in-depth discussion of the electrochemical properties of the developed silver nanoparticles graphene oxide nanocomposite (AgNPs/GO) attached onto Cytochrome P450-2D6 (CYP2D6) enzyme modified on glassy carbon electrode (GCE). Moreover, this segment of this study discusses the detection of Ethambutol and Pyrazinamide using the fabricated biosensors.

6.1 Fabrication and electrochemical studied of AgNPs/GO/CYT2D6/GCE biosensors

According to the results obtained in the previous chapter pertaining to the comparison between the nanocomposites; AgNPs/GO and ZnONPs/GO, it was clearly revealed that AgNPs/GO showed a good degree of dispersion as well as size distribution. HRSEM and HRTEM images also presented high loaded nanocomposites which exhibited a morphology very similar to previous studies such as; **Li *et al*., 2013**, **Rajabathar *et al*., 2017** and **Soroush *et al*., 2015** as compared to ZnONPs/GO. According to electrochemical analysis it was demonstrated that the conductivity of this nanocomposite was slightly higher and consequenty more stable hence its electrochemical properties are good for the fabrication of the biosensors of interest.

A sensitive and a simple electrochemical method was proposed for the determination of pyrazinamide (PZA) and ethambutol (EMB). For the first time silver nanoparticle graphene oxide nanocomposite immobilised with cytochrome P450-2D6 (AgNPs/GO/CYT2D6) modified on glassy carbon electrode (GCE) is reported for the determination of pyrazinamide (PZA) and ethambutol (EMB) using the cyclic voltammetry (CV) technique. The projected modified electrode indicated strong electrocatalytic activity towards the above mentioned drugs with higher peak enhancement than that of the unmodified electrodes. From these results it was evident that the proposed electrode showed good catalytic activity towards PZA and EMB as illustrated in **Figure 6.1**. Further discussions pertaining to the respective detection of the drugs of interest are elaborated on below.

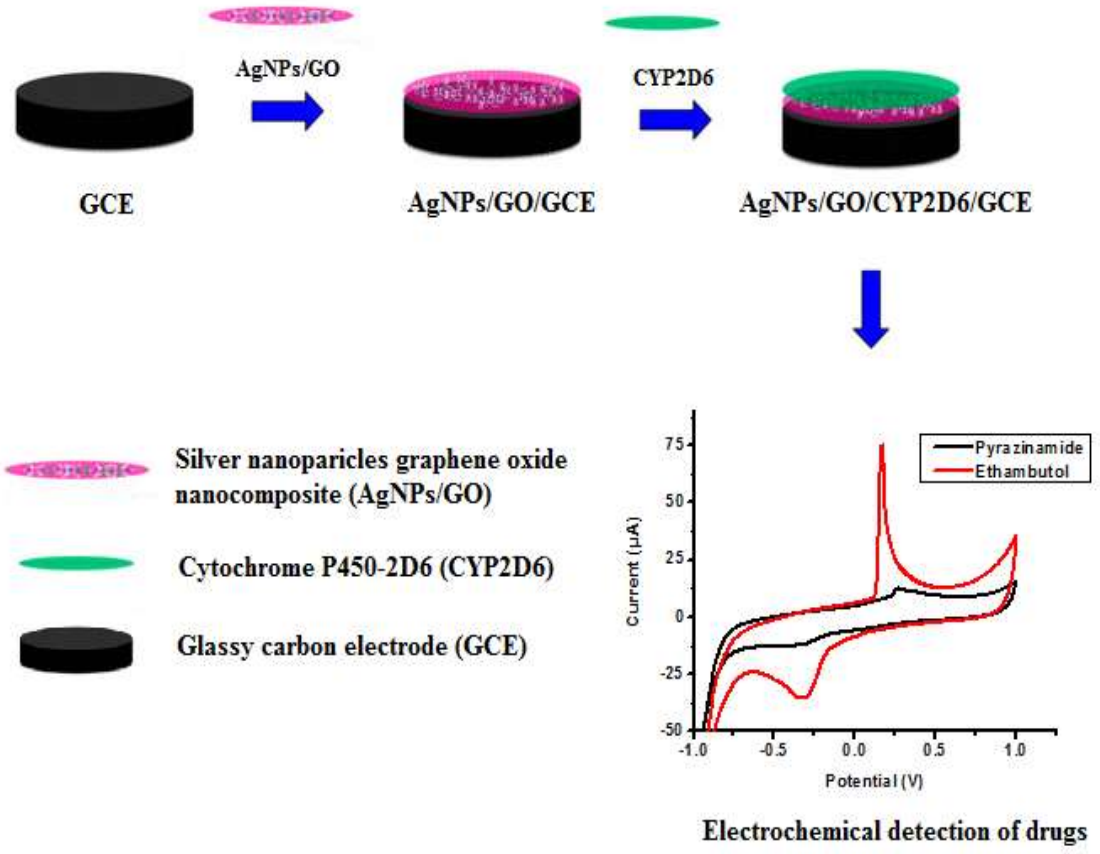

Figure 6.1: Schematic diagram of Fabrication of AgNPs/GO/CYT2D6/GCE and Electrochemical detection of EMB and PZA.

6.1.1 Amperometric characterization of AgNPs/GO/CYT2D6/GCE biosensor

Cytochrome P450-2D6 (CYP2D6) enzyme was immobilized onto AgNPs/GO nanocomposites by drop coating 5 µL of 10 µg/µL enzyme onto a dried AgNPs/GO/GCE modified electrode. Following the immobilization of the enzyme it was fundamental to access whether the enzyme was attached onto the nanocomposite or not and to ascertain whether or not the resultant biosensor possessed the necessary electro-activitity. As seen in **Figure 6.2** the immobilisation of the enzyme saw a reduction in the current response as opposed to the voltammogram depicting only the platform. It can be clearly seen that the enzyme mealy reduced the current but did not hinder the performance of the platform. Cyclic voltammetry (CV) was used for this study at the potential window of -1000 mV to 1000 mV at different scan rates (10 mVs^{-1} to 120 mVs^{-1}). **Figure 6.3** illustrates the CV voltammogram of the characterization at 20, 40, 60, 80, 100 and 120 mVs^{-1}, where one redox couple was observed for the CYP2D6 electron transition. The redox peak towards the more positive potentials (0.30 V) is attributed to the enzymes ($Fe^{3+/}Fe^{2+}$) transition while the AgNPs/GO(Ag(0)/Ag(1)) transition is not fully defined**. (Ngece., 2011)**

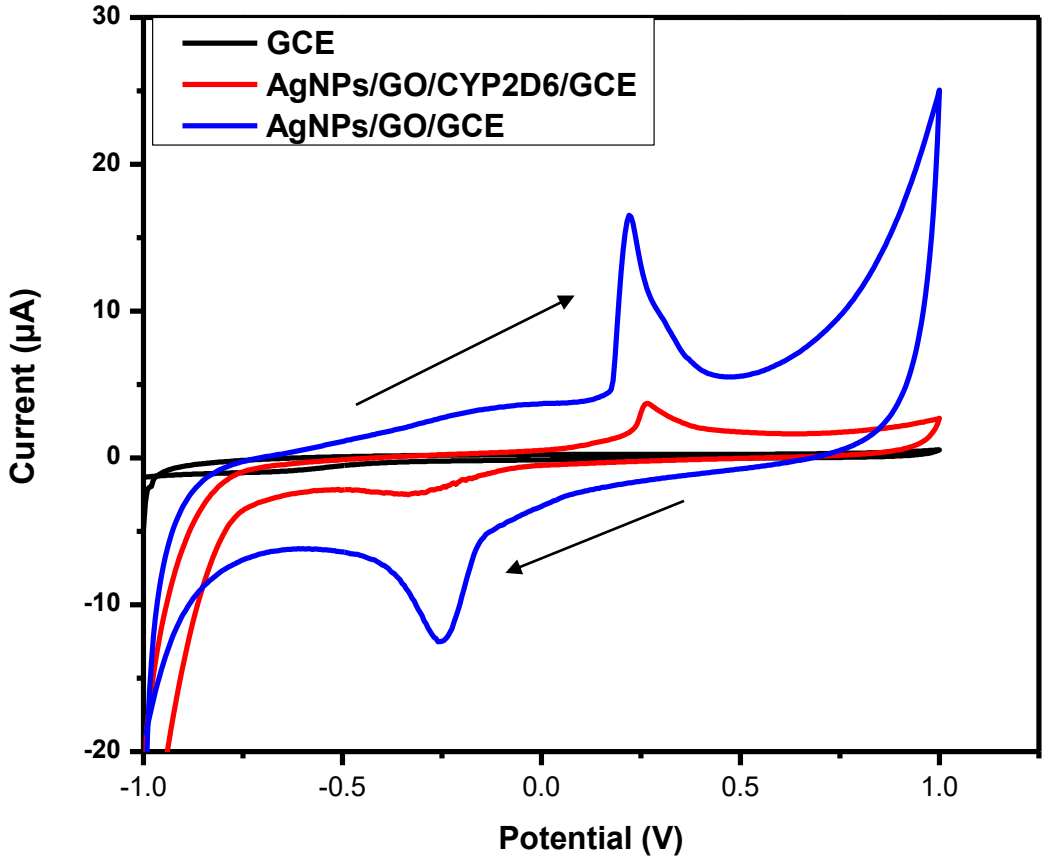

Figure 6.2: CV of bare glassy carbon electrode (GCE) (black), AgNPs/GO/CYT2D6/GCE (red) and AgNPs/GO/CYT2D6/GCE (blue) in phosphate buffer solution at 50 mVs^{-1}.

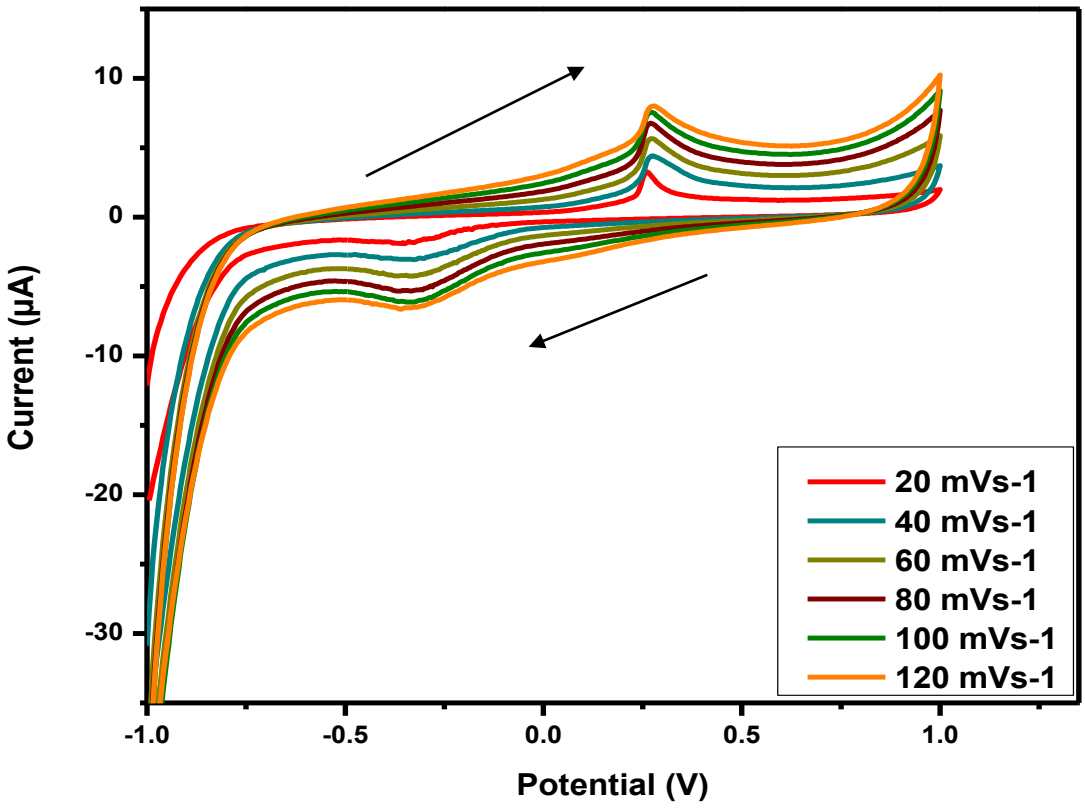

Figure 6.3: CV of AgNPs/GO/CYT2D6/GCE in 0.1 M phosphate buffer solution (pH 7.4) at 20-120 mV s^{-1}.

The plot of log anodic current peak against log scan rate was plotted for the AgNPs/GO/CYT2D6/GCE and a nearly straight line with a linear regression of I_{pa} (µA) = 0.5337x – 0.1982 and a correlation coefficient of r^2= 0.9956 was determined as shown in **Figure 6.4**.

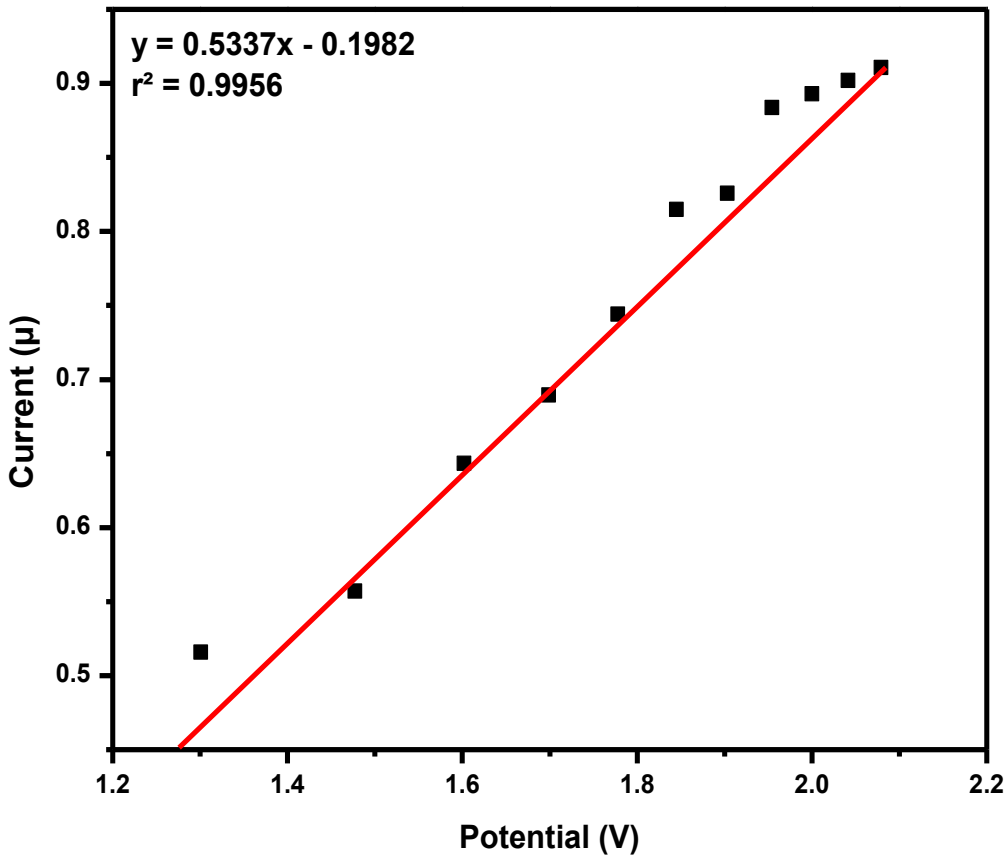

Figure 6.4: Plots of log current versus log scan rate of AgNPs/GO/CYT2D6/GCE.

The plot illustrated a clear sign of the dependence of anodic peak current on scan rate. Additionally, from this plot the surface concentration of AgNPs/GO/CYT2D6/GCE was determined using the Brown Anson equation (**Equation 6.1**). The analysis of the peak-to-peak separation (ΔE_p) which was 3.15 mV confirmed that the peak currents were diffusion-controlled because when increasing the scan rate, the magnitude of the peak current increased demonstrating the electrochemical process classified as quasi-reversible within the scan rates employed. **(Tomás., 2017)** The surface concentration of AgNPs/GO/CYT2D6/GCE was determined to be 1.122 x 10^{-3} mol cm^{-2} and as expected, the surface concentration of

AgNPs/GO/CYT2D6/GCE is slightly lower as compared to that of AgNPs/GO/GCE which was determined to be 7.1854 x 10^{-3} mol cm^{-2} before the attachment of the enzyme; as there are so many layers of materials attached to the electrode.

$$\mathbf{I_p = n^2 F^2 \Gamma^* A \nu / 4 R T} \qquad \mathbf{(6.1)}$$

Moreover, the Randel-Sevcik equation (**Equation 6.2**) was used to determine the diffusion coefficient of AgNPs/GO/CYT2D6/GCE; where a value 4.7909 x 10^{-4} cm^2/s was determined. As also expected, the AgNPs/GO/CYT2D6/GCE platform also produced impressive data. From these results it is quite evident that AgNPs/GO/CYT2D6 modified on glassy carbon electroded provided more surface area and definitely plays a crucial role in the electrocatalytic activity for detection of pyrazinamide and ethambutol.

$$\mathbf{I_p = 268,600\, n^{3/2} A D^{1/2} C \nu^{1/2}} \qquad \mathbf{(6.2)}$$

6.2 Influence of pH and effect of scan rate

The influence of the pH in the enzyme modified nanocomposites on glassy carbon electrode (GCE) towards studying the biotransformation of PZA and EMB have been evaluated before in previous studies **Cheemalapati *et al*., 2014**, and **Chokkareddy., 2018** in various buffer solutions (pH 3 to 10) (data not shown). For both of these drug studies, the pH chosen was 7.4 and the solution was used throughout the biotransformation studies. Additionally, the effect of scan rate on the peak current was also studied for the electrocatalytic activity of EMB and PZA using the enzyme modified nanocomposites on glassy carbon electrode (GCE) in deoxygenated PBS pH 7.4 in order to investigate the nature of the electrode process taking place on the modified electrode. **Cheemalapati *et al*., 2014**, and **Chokkareddy., 2018**. The chosen scan rate was 50 mVs^{-1} due to good conductivity and consistent results it gave for the drugs as compared to other scan rates.

6.3 The electrochemical behaviours of PZA and EMB at AgNPs/GO/CYT2D6/GCE

The electrochemical behaviours of ethambutol (EMB) and pyrazinamide (PZA) at AgNPs/GO/CYT2D6/GCE and bare GCE were investigated using cyclic voltammetry (CV). **Figure 6.5** illustrated the cyclic voltammograms of 100 µM of EMB and **Figure 6.6** that of 50 µM PZA that were initially added in pH 7.4 PBS at a scan rate of 50 mV s^{-1} for AgNPs/GO/CYT2D6/GCE (red) and bare GCE (black) under nitrogen saturated condition (5 minutes purged).

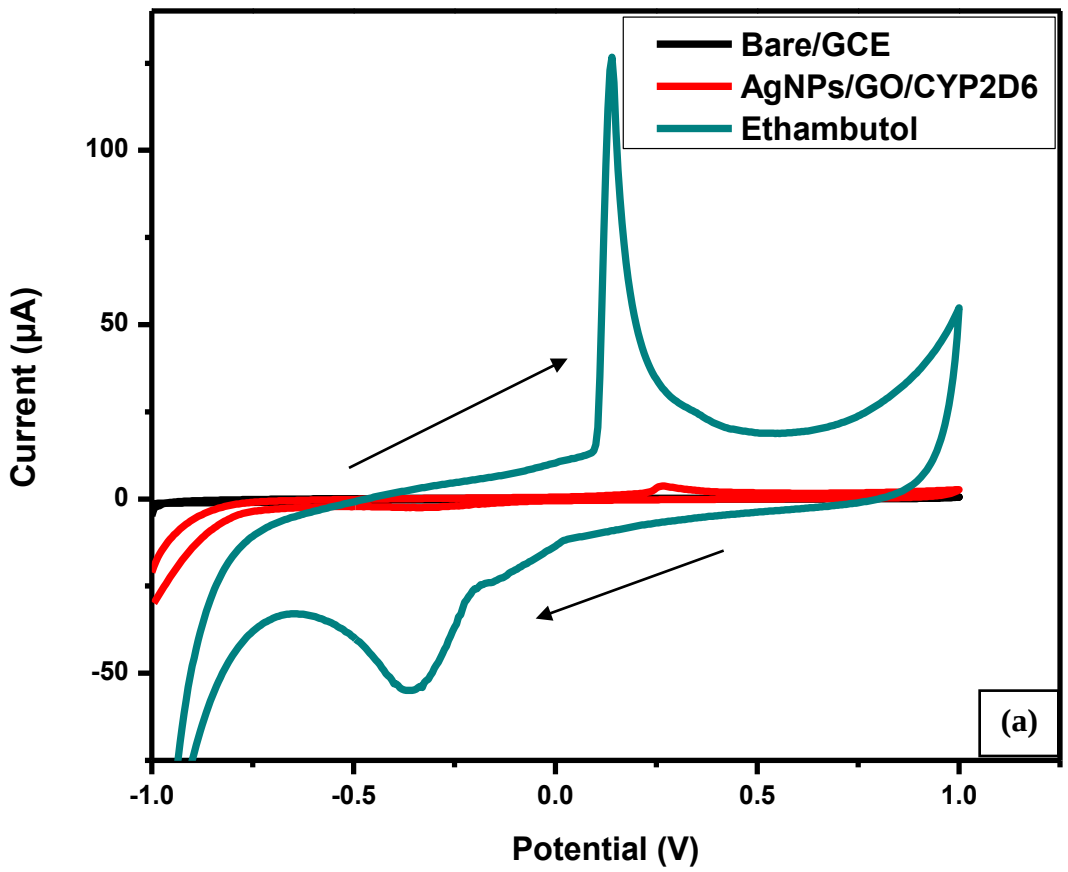

Figure 6.5: CV of bare glassy carbon electrode (GCE) (black), AgNPs/GO/CYT2D6 (red) and 100 µM of ethambutol (light green) in phosphate buffer solution (pH 7.0) at 50 mVs^{-1}.

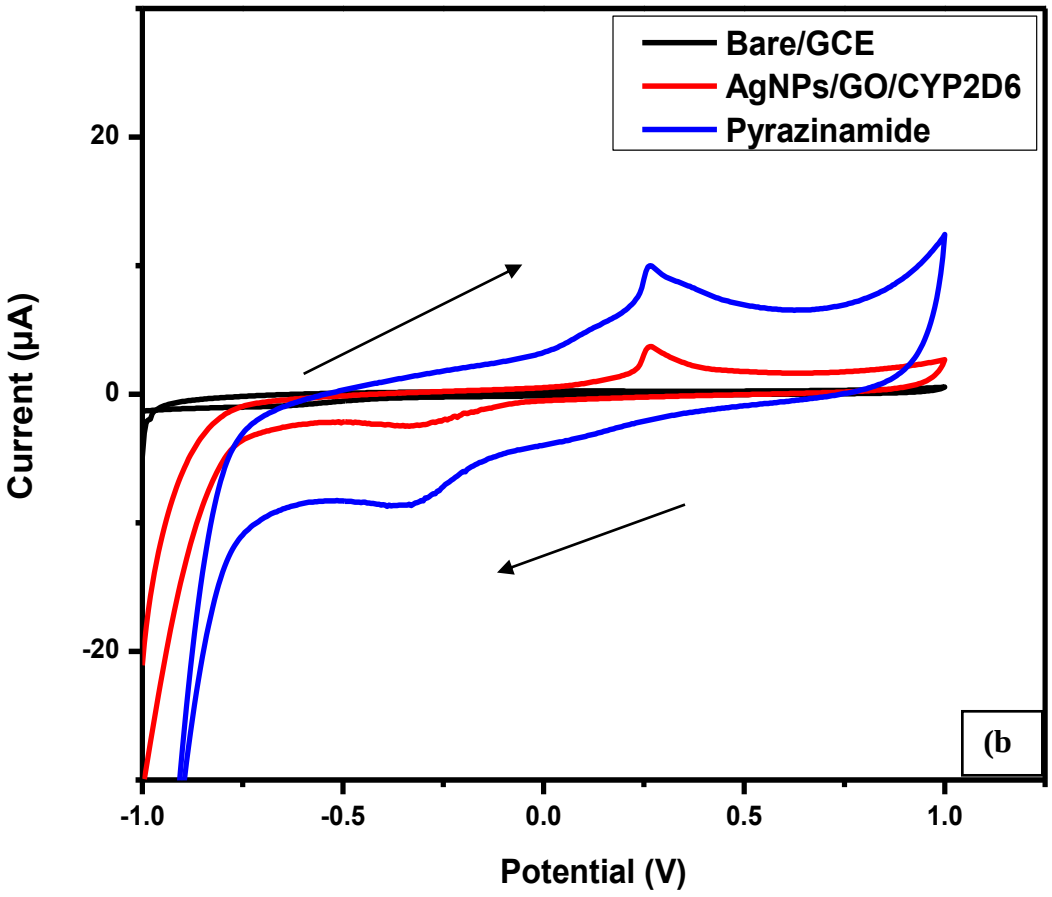

Figure 6.6: CV of bare glassy carbon electrode (GCE) (black), AgNPs/GO/CYT2D6 (red) and 50 µM of pyrazinamide (blue) in phosphate buffer solution (pH 7.0) at 50 mVs^{-1}.

For the AgNPs/GO/CYT2D6/GCE the oxidation of EMB and PZA were observed at 0.14 and 0.36 V, respectively. Furthermore I_{pa} of PZA and EMB were almost several folds more than the bare GCE and AgNPs/GO/CYT2D6/GCE due to the nanocomposite's nature of being more stable and having more surface area due to the presence of the enzyme (CYP2D6)

which possesses amino acids and carboxylic active sites in its structure further enhancing the conductance at the surface of the nanocomposite**. (Bostick *et al*., 2018)**

6.4 Electrochemical detection of EMB and PZA at AgNPs/GO/CYT2D6/GCE by CV

Cyclic voltammetry was employed in the detection of the drugs of interest and from the responses received the linear ranges and detection limits for the drugs was also determined. The CV voltammograms were recorded at a constant time interval of 3 minutes with nitrogen bubbling before the start of each experiment. The respective responses of the AgNPs/GO/CYT2D6 biosensor towards EMB and PZA were investigated in pH 7.4, 0.1 M phosphate buffer solution under anaerobic conditions at 50 mV s^{-1}. A redox wave was observed on the CV voltammogram when the stock solutions of EMB and PZA were added independently and thus the oxidation current increased remarkably with increasing EMB concentration shown in **Figure 6.7** and PZA concentration shown in **Figure 6.8**.

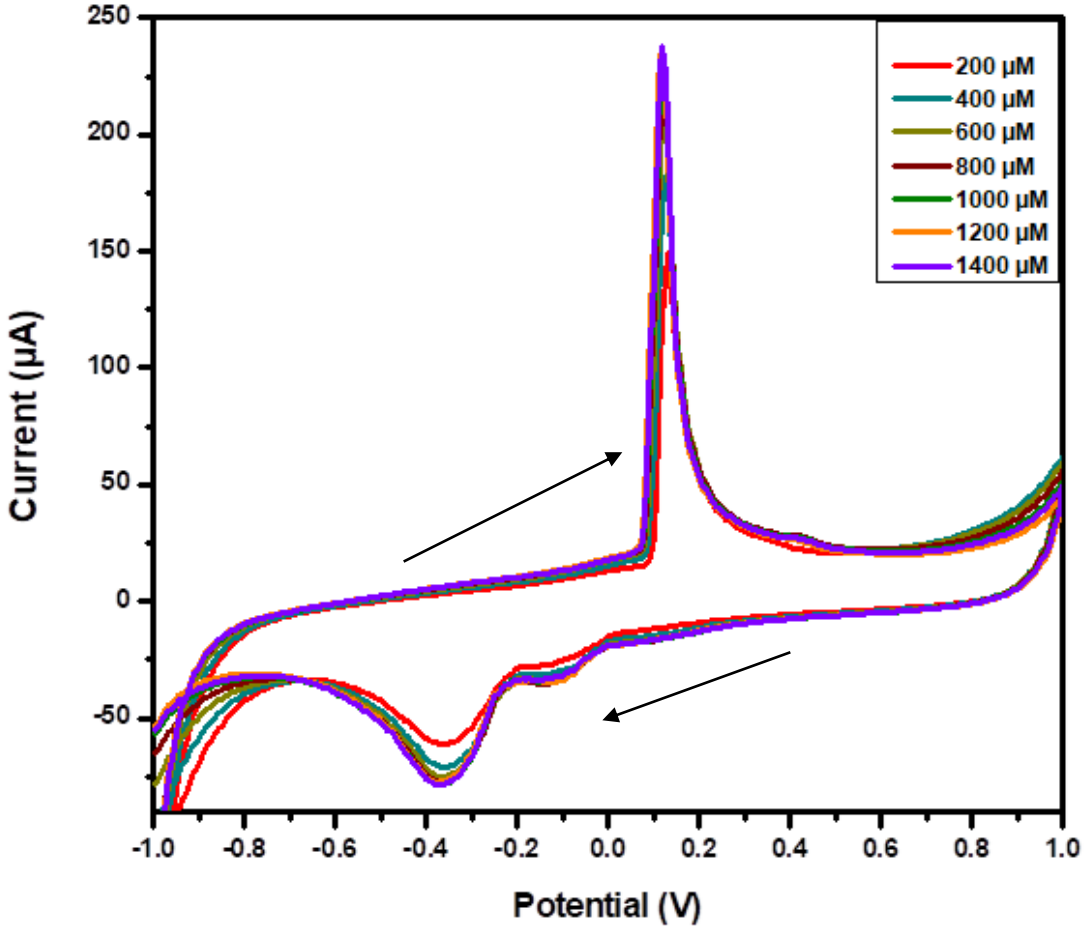

Figure 6.7: CV Characterization of AgNPs/GO/CYT2D6/GCE detecting EMB in 0.1 M PBS (pH 7.0) at 50 mV s^{-1} (with only selected voltammograms illustrated).

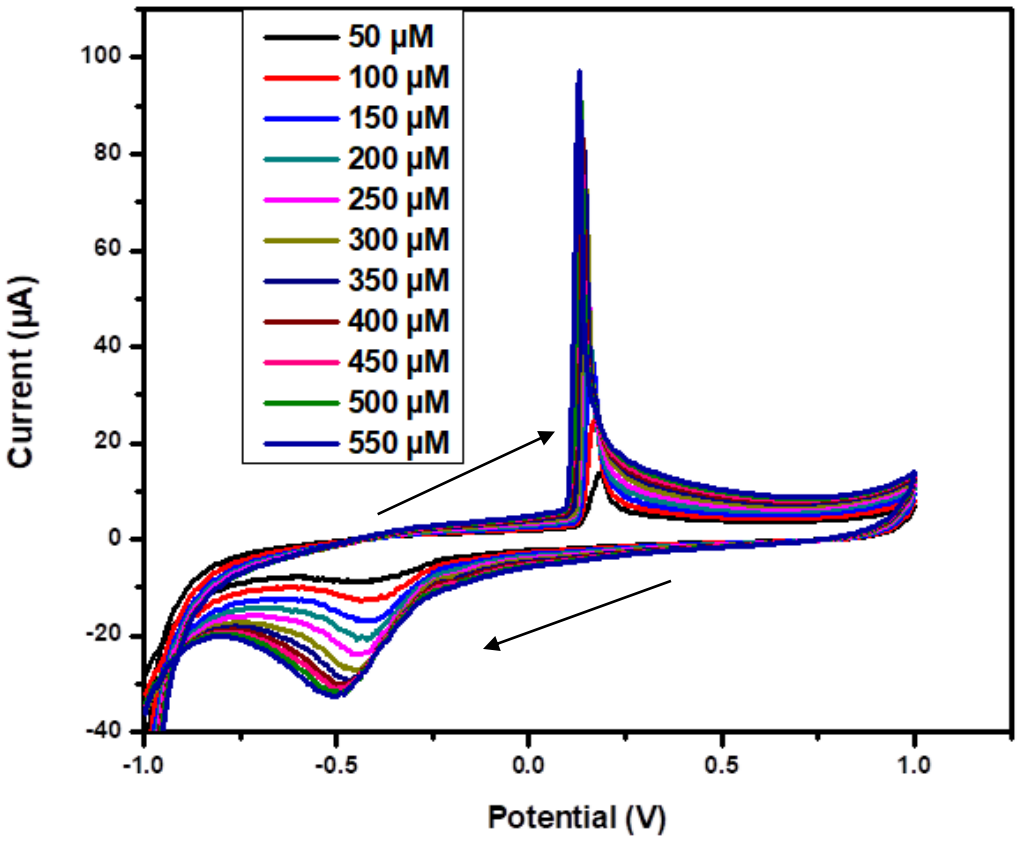

Figure 6.8: CV Characterization of AgNPs/GO/CYT2D6/GCE detecting PZA in 0.1 M PBS (pH 7.4) at 50 mV s^{-1}.

The response upon independently detecting EMB and PZA using the developed nanosensors led to a calibration curve; with a detection range of 50 - 1600 µM and a sensitivity of 0.0748 µA/µM for EMB as shown in **Figure 6.9;** while for PZA a detection range of 50 - 550 µM was studied and a sensitivity of 0.1715 µA/µM was determined as represented in **Figure 6.10**. This shows that a responsive and comfortable environment was made by the AgNPs/GO/CYT2D6/GCE biosensor for the successful biocatalytic reaction to take place. The calibration curves resulted in Michaelis-Menten profiles for each drug biotransformation studued. This resulted in the parameters I_{MAX} and K_M being determined and assigned the

values 0.2383 mA and 0.1464 mM (0.0299 mg/mL) for EMB whereas for PZA I_{MAX} was 0.0973 mA and K_M was 0.0138 mM (1.6989 x 10^{-3} mg/mL).

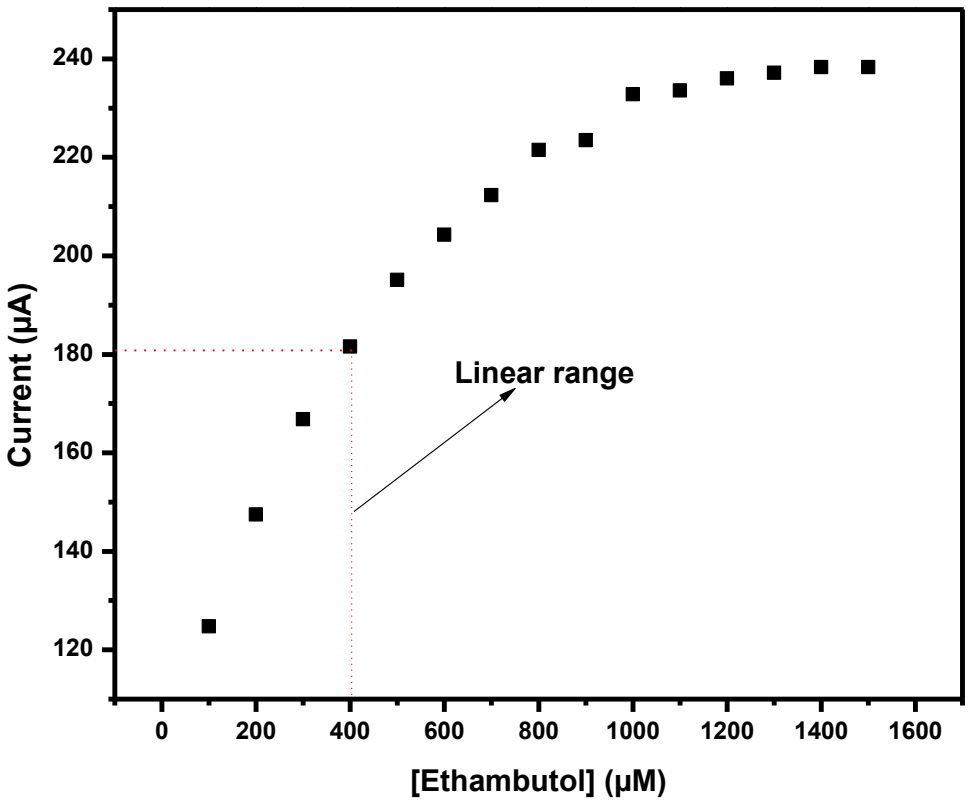

Figure 6.9 (a): Calibration curve of ethambutol for the of AgNPs/GO/CYT2D6/GCE biosensor.

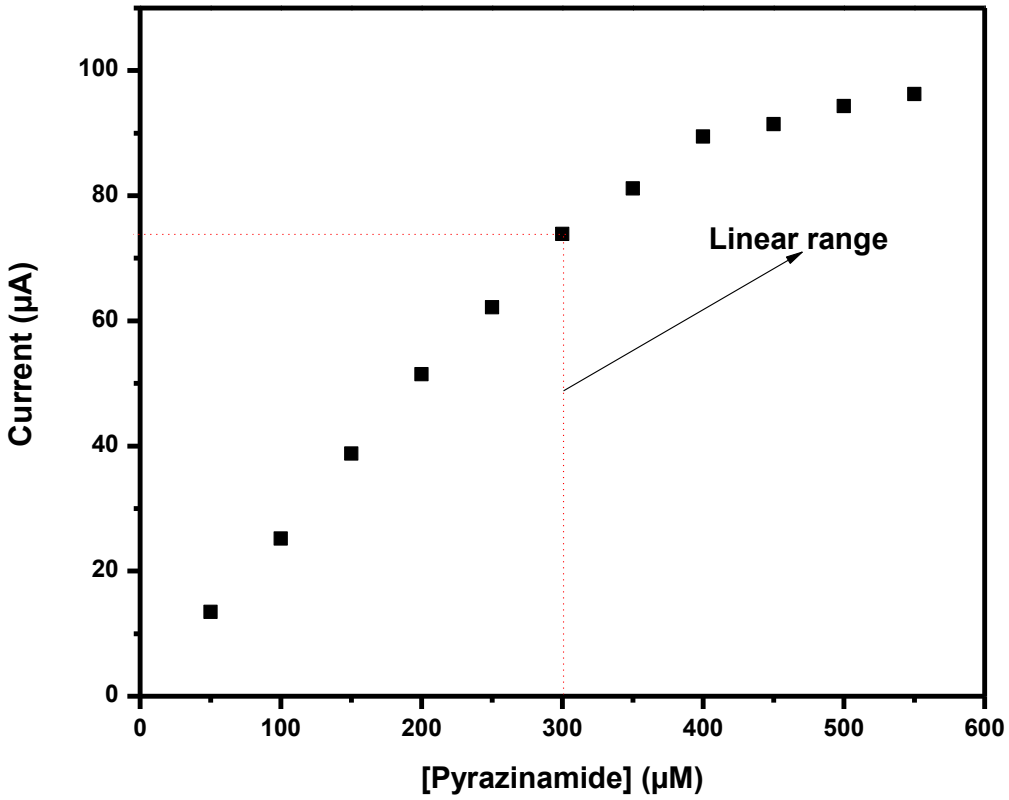

Figure 6.10: Calibration curve of pyrazinamide for the of AgNPs/GO/CYT2D6/GCE biosensor.

6.5 Stability and reproducibility

The stability and reproducibility of the AgNPs/GO/CYT2D6/GCE was also investigated in this section of this study. The modified electrode was stored at 4 ^{0}C using pH 7.4, 0.1 M phosphate buffer solution as electrolyte for one week where the current response obtained for the detection of EMB retained more than 80 % of its original response for the AgNPs/GO/CYT2D6/GCE biosensor. Thereafter the relative standard deviation (R.S.D) was then determined for five successive measurements of each 50 μM EMB and 100 μM PZA were 3.6 % and 2.9 % respectively. The results received from these experiments showed that the current responses only decreased by an average of less than 15 % signifying that the biosensors indicated in this study have long-term stability.

6.6 Method validation for the proposed method

According to the manuscript of **Cheemalapati *et al*., 2014** the specificity, limit of detection (LOD) and limit of quantitation (LOQ) were calculated. The LOD and LOQ are essentially two main performance characteristics in method validation. They are terms used to refer to the smallest concentration of an analyte that can be dependably measured by an analytical procedure.

Detection limit (LOD)

For the detection limit (LOD) calculation, initially the slope value (S) was calculated from the linear calibration curve. The linearity that was accomplished by the response of obtained current versus concentrations of ethambutol (EMB) and pyrazinamide (PZA) was plotted and then used to calculate the linear regression equation. Furthermore, standard deviation (σ) was

also calculated for the biosensor responses. The LOD was calculated using the ICH guidelines equation (**Equation 6.3**). **(Shrivastava and Gupta., 2011)**

The detection limit **(LOD) = 3.3 σ/S** **(6.3)**

Where, S is the slope of the calibration curve and σ is the standard deviation of the response. The obtained LOD value for EMB was 0.6791 x 10^{-2} nM and for PZA it was determined to be 0.2962 x 10^{-2} nM. The obtained LOD results for both these drugs indicated that the method used in this study is great and is within the desired range. Even other studies that have been developed for ethambutol determination where relatively similar data was acquired gave such as **Lima *et al*., 2016** who reported a novel methodology using an amperometric sensor for ethambutol determination with a LOD of 0.0437 mM and **Ngece., 2011** who conveyed studies using a bioelectrochemical sensor for determination of ethambutol with a LOD of 0.7 mM. For pyrazinamide there are studies that have been developed for its determination as well such as **Devadas *et al*., 2015** who reported an electrochemical sensor for determination of pyrazinamide with a LOD of 3.28 μM.

This study has determined lower LOD similar to these previously reported studies shown in the table below demonstrating a good indication that the developed biosensors have potential of being used in real human samples. The most commonly reported maximum observed plasma concentration (C_{max}) value of EMB found in plasma is < 2 mg/mL in adults and a very low C_{max} (<1 mg/mL) is common in children (after 10 hours of administration) mainly in South African irrespective of their CYP2D6 genotype. **(Zhu *et al*., 2004)** However, it has been reported that the maximum plasma concentration (C_{max}) for PZA is >35 μg/ml (after 24 hours of administration). **(Alsultan *et al*., 2017** Coupled to the low LOQ values determined for each drug as discussed below, it is evidently clear that the LOD values received are below

the maximum plasma concentrations reported for these drugs confirming their ability for future use in plasma. **Table 6.1** illustrates the superiority of the developed biosensors as compared to previouslt developed biosensors.

Table 6.1: Comparison studies for TB drug biosensors

Platform	**Linear range (µM)**	**LOD (µM)**	**Reference**
Tyrosine (Tyr) modified glassy carbon electrode for electrochemical determination of Ethambutol drug.	20 – 1000 µM	6.93 µM	Cheemalapati *et al.*, 2014
Determination of pyrazinamide using a poly-histidine modified electrode	10 – 100 µM	0.57 µM	Bergamini *et al.*, 2013
Sensing graphene oxide/poly-arginine-modified electrode for electrochemical determination of pyrazinamide drug.	25 – 1600 µM	3.28 µM	Devadas *et al.*, 2015
Glassy carbon electrode fabricated with ZnONPs and reduced graphene for the determination of ethambutol	2 - 32 µM	0.0214 µM	Chokkareddy, R., 2018
l-Cysteine (poly(l-Cys)) on a glassy carbon electrode (GCE) for electrochemical determination of pyrazinamide drug.	0.476 - 51.2 µM	0.113 µM	Ferraz *et al.*, 2016
Graphene-silver/zinc oxide nanoparticulate phenotype biosensors for ethambutol and pyrazinamide	*100 µM – 300 µM (pyrazinamide)* *50 µM – 400 µM (ethmabutol)*	*0.8975 x 10^{-2} nM (pyrazinamide)* *0.02057 nM (ethambutol)*	*Current Study*

Quantification limit (LOQ)

The Quantification limit (LOQ) was also calculated in this study using **Cheemalapati *et al*., 2014** manuscript. The following equation was used;

Quantification limit **(LOQ) =10 σ/S** **(6.4)**

Where, S is the slope of the calibration curve and σ is the standard deviation of the response. The obtained LOQ values that were calculated were found to be for PZA 0.8975 x 10^{-2} nM and 0.02057 nM for EMB respectively. From both these results; PZA and EMB it is clear evident that the biosensors developed in this study can be successfully used in human samples. These results are illustrative of a good biosensor that can detect actual low drug concentrations among tuberculosis patients.

6.7 References

Alsultan, A., Savic, R., Dooley, K.E., Weiner, M., Whitworth, W., Mac Kenzie, W.R., Peloquin, C.A. and Tuberculosis Trials Consortium, 2017. Population pharmacokinetics of pyrazinamide in patients with tuberculosis. Antimicrobial agents and chemotherapy, pp.AAC-02625.

Bergamini, M.F., Santos, D.P. and Zanoni, M.V.B., 2013. Electrochemical behavior and voltammetric determination of pyrazinamide using a poly-histidine modified electrode. Journal of Electroanalytical Chemistry, 690, pp.47-52.

Bostick, C.D., Mukhopadhyay, S., Pecht, I., Sheves, M., Cahen, D. and Lederman, D., 2018. Protein bioelectronics: a review of what we do and do not know. Reports on Progress in Physics, 81(2), p.026601.

Cheemalapati, S., Devadas, B., Chen, S.M., Ali, M.A. and Al-Hemaid, F.M., 2014. Electrochemical determination of selected antihypertensive and antituberculosis drugs at a tyrosine-modified electrode. Analytical Methods, 6(17), pp.6774-6782.

Chokkareddy, R., 2018. *Fabrication of sensors for the sensitive electrochemical detection of anti-tuberculosis drugs* (Doctoral dissertation).

Devadas, B., Cheemalapati, S., Chen, S.M., Ali, M.A. and Al-Hemaid, F.M., 2015. Highly sensing graphene oxide/poly-arginine-modified electrode for the simultaneous electrochemical determination of buspirone, isoniazid and pyrazinamide drugs. Ionics, 21(2), pp.547-555.

Ferraz, B.R.L., Leite, F.R.F. and Malagutti, A.R., 2016. Simultaneous determination of ethionamide and pyrazinamide using poly (l-cysteine) film-modified glassy carbon electrode. Talanta, 154, pp.197-207.

Li, Z., Zhou, Z., Yun, G., Shi, K., Lv, X. and Yang, B., 2013. High-performance solid-state supercapacitors based on graphene-ZnO hybrid nanocomposites. Nanoscale research letters, 8(1), p.473.

Lima, A.E.B., Luz Jr, G.E., Batista, N.C., Longo, E., Cavalcante, L.S. and Santos, R.S., 2016. Determination of ethambutol in aqueous medium using an inexpensive gold microelectrode array as amperometric sensor. Electroanalysis, 28(5), pp.985-989.

Ngece, R.F., 2011. *Nanoparticulate of silver-modified poly (8-anilino-1-naphthalene sulphonic acid) nanobiosensor systems for the determination of Tuberculosis treatment drugs* (Doctoral dissertation, University of the Western Cape).

Rajabathar, J.R., Shukla, A.K., Ali, A. and Al-Lohedan, H.A., 2017. Silver nanoparticle/r-graphene oxide deposited mesoporous-manganese oxide nanocomposite for pollutant removal and supercapacitor applications. International Journal of Hydrogen Energy, 42(24), pp.15679-15688.

Shrivastava, A. and Gupta, V.B., 2011. Methods for the determination of limit of detection and limit of quantitation of the analytical methods. Chronicles of Young Scientists, 2(1), p.21.

Soroush, A., Ma, W., Silvino, Y. and Rahaman, M.S., 2015. Surface modification of thin film composite forward osmosis membrane by silver-decorated graphene-oxide nanosheets. Environmental Science: Nano, 2(4), pp.395-405.

Tomás, R., 2017. Electrochemical sensing directly in bodily fluids–a move towards point of care and in vivo analysis.

Zhu, M., Burman, W.J., Starke, J.R., Stambaugh, J.J., Steiner, P., Bulpitt, A.E., Ashkin, D., Auclair, B., Berning, S.E., Jelliffe, R.W. and Jaresko, G.S., 2004. Pharmacokinetics of ethambutol in children and adults with tuberculosis. The International Journal of Tuberculosis and Lung Disease, 8(11), pp.1360-1367.

CHAPTER 7

Conclusion and Recommendations

Summary

This chapter revisits the definite objectives of this study to report whether the aims of this dissertation were attained and it also give an overview of the accomplishments and inadequacies of the study. An exertion is made to summarize the entire work of the thesis. Most importantly the conclusions and the recommendations for future work are reported.

7.1 Conclusions

This study reported a novel and simple nanobisensor which has been developed and characterized for detection of tuberculosis treatment drugs; ethambutol and pyrazinamide. The first specific objective of this study was to synthesis graphene oxide using Hummers method and this task was successfully achieved as it served as the foundation for the rest of the tasks to follow. The results of graphite oxide and graphene oxide were investigated regarding their physical and chemical properties. The investigations were accomplished using High-Resolution Scanning Electron Microscopy and Atomic Force Microscopy techniques to prove that the surfaces of graphite oxide and graphene oxide were evidently developed. During preparation, the ultrasonic waves that were involved when exfoliation took place separating various functional groups from graphite oxide, resulting to an alteration of the chemical composition of the obtained graphene oxide. These changes were confirmed by Energy Dispersive X-Ray which measured the amount of oxygen in the graphene oxide. Some alterations in functional groups and structure of the materials were confirmed by Fourier Transform Infrared Spectroscopy, Raman's Spectrometry, Small Angle X-Ray and X-Ray diffraction. Investigations on electron flow and sensitivity based on graphene oxide were also performed using electrochemistry. Thereafter, it was expected that the possibility of using graphite oxide for nanobisensors is boundless.

Secondly, green synthesized nanoparticles; silver and zinc oxide nanoparticles were synthesized through microwave irradiation and conventional heating, spherical nanoparticles were obtained. The methods were then later compared for both zinc oxide and silver nanoparticles to verify which one would produce highly electroactive nanoparticles as this is an imperative quality when developing nanocomposite for a sensors. Microwave irradiation method was then initially chosen for continuation of the study for synthesis of

nanocomposites however due some toxic qualities that were exhibited by graphene oxide in both the nanocomposite; AgNPs/GO and ZnONPs/GO conventional heating method became a moderate replacement. Thirdly, green synthesized nanocomposite; AgNPs/GO and ZnONPs/GO were also synthesized by means of conventional heating as mentioned above. They were later also compared because only the one that showed a good degree of dispersion as well as size distribution and that also demonstrated good electrochemical properties for fabrication of biosensor was chosen. AgNPs/GO nanocomposite showed all those characteristics hence it was chosen. Characterization of the nanoparticles and nanocomposite were obtained by means of Fourier Transform Infra-Red spectroscopy, Raman spectroscopy and Energy Diffraction X-Rray, Ultraviolet-visible spectroscopy, High-Resolution Scanning Electron Microscopy and High Resolution Transmission Electron Microscopy.

The nanocomposite indicated a stable platform for the immobilization of the enzyme cytochrome P450-2D6 (CYP2D6). The AgNPs/GO nanocomposite served as a point of attachment for the enzyme as well as an efficient electron mediator between the redox centre of CYP2D6 and the glassy carbon electrode surface. Cyclic voltammetry showed good conductivity with respect to the newly formed platform thus indicating their potential application in biosensor development. The results obtained confirmed that the AgNPs/GO/CYP2D6/GCE biosensor was successful in the oxidative catalysis of pyrazinamide and ethambutol into respective water soluble materials. The resultant catalytic current responses were amperometrically monitored by cyclic voltammetric technique where an increase in current was observed for the separate analytes namely; ethambutol and pyrazinamide. Moreover from the calibration curve that were plotted, linear ranges were established in which sensitivity of the drugs, limit of detection and limit of quantitation were determined. The sensitivities of the biosensors (EMB = 0.0748μA/μM and PYR = 0.1715

μA/μM) showed lower sensitivities compared to previous studies concerning the biotransformation of these drugs. Michaelis-Menten kinetics was used to determine the values of I_{MAX} and K_M of the biosensor dectecting TB drugs. The apparent Michaelis-Menten constants showed the biosensors to have limit of detection (LOD) and quantification (LOQ) withinin the biosensor linear range and had high affinity for the respective drugs, thus making the biosensor system appropriate for the determination of the respective analytes in serum.

7.2 Professional recommendations for future work

The subsequent aspects of the biosensor for the determination of tuberculosis treatment drugs (pyrazinamide and ethambutol) showed in this study permit further investigations.

1. Further work needs to be done to improve the green synthesis of nanocomposite through plant extracts, especially nanocomposites that has graphene oxide.

2. It is suggested that another method is required to develop the AgNPs/GO nanocomposite in order to improve electroactivity so that nanocomposite can perhaps be able to immobilize numerous biological components.

3. It is also proposed that a wide pH range yet closed aligned of phosphate buffer solution is required in order to determine whether the detection limits can be further improved.

4. Another important factor to consider about future work pertaining to these biosensors is to ensure that the platforms are able to carry out the envisaged spectroelectrochemical studies and not only the reported electrochemical studies only. Various factors

contributed to this shortfall where the main issues was instability during the spectrochemical studies which resulted in focusing on the the electrochemical studies only.

5. Another suggestion is to practicality detect biological samples (blood plasma and serum and urine) using the developed biosensors and to study ethambutol and pyrazinamide.